NUMERICAL INVESTIGATION OF THE INFLUENCE OF AN IMPINGING SHOCK WAVE AND HEAT TRANSFER ON A DEVELOPING TURBULENT BOUNDARY LAYER

Muhammad Farrukh Shahab

THÈSE

Pour l'obtention du grade de

DOCTEUR DE L'ÉCOLE NATIONALE SUPÉRIEURE de MÉCANIQUE et d'AÉROTECHNIQUE

(Diplôme National - Arrêté du 7 août 2006)

École Doctorale : Sciences et Ingénierie en Matériaux, Mécanique, Energétique et Aéronautique

Spécialité : Mécanique des Milieux Fluides et Acoutique

Présentée par

Muhammad Farrukh Shahab

ETUDE NUMERIQUE DE L'INFLUENCE DE L'IMPACT D'UNE ONDE DE CHOC ET D'UN TRANSFERT DE CHALEUR SUR UNE COUCHE LIMITE EN DEVELOPPEMENT

– – – – – – – – – – – – – –

NUMERICAL INVESTIGATION OF THE INFLUENCE OF AN IMPINGING SHOCK WAVE AND HEAT TRANSFER ON A DEVELOPING TURBULENT BOUNDARY LAYER

Directeur de thèse : **Pierre Comte**
Co-encadrants : **Thomas B. Gatski**
Guillaume Lehnasch

Soutenue le 12 décembre 2011
Devant la Commission d'Examen

JURY

N. A. Adams	Professeur, TUM, Munich	Rapporteur
C. Tenaud	Directeur de Recherche CNRS, LIMSI, Orsay	Rapporteur
B. Aupoix	Directeur de Recherche, ONERA, Toulouse	Examinateur
J. -P. Dussauge	Directeur de Recherche CNRS, IUSTI, Marseille	Examinateur
T. B. Gatski	Directeur de Recherche CNRS, PPRIME, Poitiers	Examinateur
E. Garnier	Ingénieur, ONERA, Meudon	Examinateur
G. Lehnasch	Maître de Conférences, PPRIME, Poitiers	Examinateur

Dedication

This thesis is dedicated to my parents, for their love, endless support and encouragement. To my sister and brother, who never left my side and are very special to me. It is also dedicated to my lovely fiancée whose continuous support and love means alot to me.

Acknowledgements

I am deeply grateful to my thesis director Dr. Pierre Comte (late) who gave me the opportunity to excel in the field of research under his great supervision and for all the enormous support that he had provided during the time frame. May his soul rest in peace, with his death i have lost a great mentor.

The thesis was co-directed by Dr Thomas B. Gatski and Dr. Guillaume Lehansch. I would like to express my deep and sincere gratitude to Dr. Thomas B. Gatski as his wide knowledge and logical way of thinking have been of great value for me. His extensive guidance and encouragement throughout the course of my PhD helped me alot to complete this task quite comfortably. I warmly thank Dr. Guillaume Lehnasch for his detailed and constructive comments, and for his important support throughout this work.

My sincere thanks to all the jury members, specially the reviewers Dr. Nikolaus A. Adams and Dr. Christian Tenaud, who honored me by accepting and approving my research work. I would also like to express my deep sense of gratitude to the invited member Dr. Xavier Gloerfelt.

In addition during the course of my PhD i also worked over the ANR project SPICEX, i would like to thanks all the members of the project who were undoubtedly a great source of knowledge to me and it was really a great experience that i worked with all those intelligent minds.

The financial support of Higher Education Commission (HEC), Pakistan, is gratefully acknowledged and i would like to present a special thanks to IDRIS (high performance computing centre, CNRS, France) for computing resources provided.

I acknowledge the support of my colleagues for many discussions and help to sort out the problems that I went through during my research tenure at L'institut Pprime. I would also like to appreciate the help and the gentle behavior of all personnel of CEAT/LEA/ENSMA, Poitiers.

Last but not the least my family whose love and prayers gather me everywhere.

Résumé

Dans l'optique de développer à terme des modèles pertinents et in fine améliorer le design de véhicules supersoniques, cette étude propose une analyse détaillée de l'influence d'un choc et d'un transfert de chaleur sur la structure de la turbulence au sein d'une couche limite supersonique. La stratégie numérique utilisée repose sur des simulations numériques directes des équations de Navier-Stokes à l'aide de schémas WENO et compact d'ordre élevé. Le développement complet de la couche limite est simulé à l'aide d'un forçage amont à la paroi afin de s'assurer du plus haut degré de réalisme dans la zone d'étude. Des conditions de séparation naissante et deux conditions thermiques de paroi (adiabatique et refroidie) sont considérées. L'analyse se concentre sur l'altération des caractéristiques moyennes et turbulentes à travers la zone d'interaction et au sein de la zone de relaxation, sur la base de profils moyens et de paramètres intégraux. L'amplification anisotrope des variables turbulentes est quantifiée tandis que les évènements turbulents associés à la modification de la structure globale sont identifiés. La forte modification des champs thermiques moyens et turbulents par le refroidissement est mise en exergue, notamment la diminution significative des quantités turbulentes à travers la couche. Par ailleurs, la réduction à la fois des longueurs d'influence amont, de séparation et de relaxation est mise en évidence.

Mots clés : Simulation numérique directe, Ecoulement supersonique, Couche limite turbulente, Ondes de choc, Transfert de chaleur, Décollement des écoulements

Abstract

As a prerequisite for relevant model development and improvement of design methodologies for supersonic vehicles, this study aims at investigating the influence of wall heat-transfer and shock interaction on the turbulence structure of supersonic boundary layers. The numerical strategy relies on the full resolution of three-dimensional compressible Navier-Stokes equations by means of state-of-art high-order WENO and compact schemes. A fully-developed turbulent boundary layer is simulated by means of upstream wall perturbations triggering the transition in order to dispose of fully-reliable data upstream of the analysis region. Incipient separation conditions and two different wall thermal boundary conditions (adiabatic and cold) are considered. The analysis focuses on the evolution of mean and turbulent flow properties along the interaction region and in the relaxation region downstream of the shock-system. The strong influence of the mean pressure gradient is quantified through the analysis of mean flow profiles and boundary layer integral parameters. The anisotropic amplification of turbulent quantities through the interaction region is characterized and the turbulent events associated with the modification of the turbulence structure of the perturbed boundary layer are identified. The mean and turbulent thermal fields are shown to be strongly modified by the wall cooling which significantly dampens more particularly the turbulent thermal quantities levels across the boundary layer. In addition, a reduction of the upstream influence and separation lengths by the wall cooling are evidenced along with a faster recovery process downstream of the shock-system.

Keywords : Direct numerical simulation, Supersonic flow, Turbulent boundary layer, shock waves, Heat transfer, Separated flows

Contents

Nomenclature

Δx^+,Δy^+,Δz^+ grid spacing in wall unit scaling in three-dimensional space (x, y and z respectively)

Δ total energy thickness parameter

δ boundary layer thickness

δ^* compressible displacement thickness

δ_ω^l boundary layer thickness based on the vorticity measure at each streamwise station

δ_ω^o boundary layer thickness based on the vorticity measure at reference station

δ_i^* incompressible displacement thickness

δ_{ij} Kronecker delta

ϵ, ϵ_I, ϵ_d total dissipation, inhomogeneous dissipation, dilatational dissipation

ϵ_{th} dissipation rate of temperature variance

γ ratio of specific heats

κ von Kàrmàn constant

μ dynamic viscosity

∇P pressure gradient

ν kinematic viscosity

$\overline{\rho'\rho'}$ density variance

$\overline{p'p'}$ pressure variance

$\overline{u_i'T'}$ Reynolds-averaged turbulent heat flux vector

$\overline{u_i'u_j'}$ Reynolds-averaged turbulent stress tensor

$\overline{u}_c^+$ van Driest transformed velocity

$\Phi_{\alpha\alpha}$ One-dimensional power spectrum of a given variable α

ρ density

H shape factor

σ_{ij} stress tensor

$\tau_{ij} = \widetilde{u_i''u_j''}$ Favre-averaged turbulent stress tensor

θ compressible momentum thickness

θ_i incompressible momentum thickness

$\tilde{U}_{tmax}$ velocity at the point of temperature extremum

$\widetilde{t''t''}$ static temperature variance

$\widetilde{Tt''Tt''}$ total temperature variance

$\widetilde{u_i''T''}$ Favre-averaged turbulent heat flux vector

a_1, a_2, a_3, a_4, a_5 turbulent stress ratios

A_i, P_{Ti}^1, P_{Ti}^2, Φ_{Ti}, ϵ_{Ti}, D_{Ti}, C_{Ti} advection, production due to mean temperature and velocity gradients, production due to fluctuating strain rate field, pressure scrambling, turbulent viscous-thermal dissipation, turbulent and viscous-thermal transport, compressibility terms in transport equation of heat flux vector

A_K, P_K, Π_K, T_K, D_K, ϵ_K, M_K advection, production, pressure dilatation, turbulent transport, viscous diffusion, dissipation, mass-flux terms in turbulent kinetic energy equation

B_q heat flux parameter

$b_{ij} = \tau_{ij}/\tau_{ii} - \delta_{ij}/3$ turbulent stress anisotropy tensor

c speed of sound

C_τ maximum shear stress coefficient

C_f coefficient of friction (skin-friction)

E total energy

$F(u'_i)$ flatness factors

F_c incompressible to compressible transformation function for C_f

F_{Re_θ} incompressible to compressible transformation function for Re_θ

H compressible shape factor

H total enthalpy

H_i incompressible shape factor

J equilibrium shape parameter

$K = \tau_{kk}/2$ turbulent kinetic energy

K_{th} thermal potential energy

L_x,L_y,L_z Length of computational domain in three-dimensional space (x, y and z respectively)

L_{sep} separation length

L_{ui} upstream influence length

M Mach number

M_τ friction Mach number

N_x,N_y,N_z number of grid points in three-dimensional space (x, y and z respectively)

p static pressure

Pr molecular Prandtl number

Pr_m	mixed Prandtl number
Pr_t	turbulent Prandtl number
$Pr_{t(HSRA)}$	turbulent Prandtl number extracted from Huang Strong Reynolds Analogy
q_j	heat flux vector
R	mean reattachment point
R	turbulent time scale ratio between thermal and velocity field
r	recovery factor
$R_{\alpha\alpha}$	Two-point correlation of a given variable α
R_{u_1t}	correlation coefficient between streamwise velocity and temperature
$R_{u_1u_2}$	correlation coefficient between streamwise and wall-normal velocity components
R_{u_2t}	correlation coefficient between wall-normal velocity and temperature
Re	Reynolds number
Re_θ	Momentum thickness Reynolds number
Re_x	Reynolds number based on streamwise (x) length
S	mean separation point
$S(u_i')$	skewness factors
S_{ij}	rate-of-strain tensor
T	static temperature
T_t	total temperatur
u_τ	friction velocity
U_e	boundary layer edge velocity
u_j	velocity vector
W_{ij}	skew-symmetric part of the velocity gradient tensor

X^{*},X^{**} normalized streamwise coordinates

x_i space coordinates vector

x_{imp} impingement position of incident shock

X_{re} streamwise coordinate of reattachment point

X_{sep} streamwise coordinate of mean separation point

Subscripts

∞ free-stream conditions

∞, bi free-stream values before (upstream) interaction

$adia$ values for adiabatic wall conditions

aw adiabatic wall conditions

i incompressible values

iso values for isothermal (cold) wall conditions

r adiabatic recovery conditions

w wall values

Superscripts

$'$ Reynolds variable fluctuations

$''$ Favre variable fluctuations

$*$ dimensional quantities, quantities in terms of semi-local scaling

$+$ quantities in terms of wall unit scaling

$\bar{\ }$ Reynolds averaged quantities

$\tilde{\ }$ Favre averaged quantities

List of Figures

List of Tables

Chapter I

Introduction

In high-speed aeronautical applications, a better understanding of the characteristics of the compressible turbulent boundary layers is essential for improving the efficiency of a wide range of aeronautical systems. In comparison with the incompressible regime, where a great deal of study has already been conducted, the problem in the compressible regime is not as yet fully well-understood and requires more thorough and accurate analysis. In high-speed flow configurations shocks, are likely to appear and an interaction with the turbulent boundary layer leads to highly complex unsteady interaction mechanism that significantly alters the characteristics of the boundary layer. The level of flow dynamic complexity further increases when these perturbed boundary layers are subjected to heat transfer effects. Clearly a detailed analysis of these effects would be quite useful in further understanding the dynamics of the compressible turbulent boundary layer.

The occurrence of shock/turbulent boundary layer (SWBLI) phenomenon often leads to undesirable effects, such as maximum mean and fluctuating pressures, thermal loads, dynamic loads due to the shock unsteadiness, flow separation and drag increment. These effects can possibly degrade the performance of the air- and space-vehicles, or if these are of an aggravated nature, can possibly have some detrimental effects on the structural integrity of the system. The characteristics of these types of interactions are mainly dependent on the Mach number, the shock angle, the nature of the incoming flow and the flow geometry. Despite the large set of experimental, numerical and theoretical studies that have been attempted to quantify the dynamic features of this problem and which are certainly a valuable addition to the understanding of this complex interaction mechanism, broad based research is ongoing in order to enhance our understanding about features that are not yet fully understood. Some of these features, such as the unsteady motion of the shock, mean flow modification and turbulence amplification induced by the shock distortion have been extensively studied. To a lesser extent, studies involving other important issues like the characterization of structure of turbulence, unsteady heating loads, separation and reattachment detection criteria for three-dimensional separations and even more complicated dynamics like the effects introduced by the generation of turbulent mixing layers as a result of the interaction have been undertaken in order to have a detailed and through understanding of the phenomenon.

The aim of the present study is to investigate, by means of direct numerical simulations, the influence of the wall heat transfer and/or shock interaction on the structure of turbulence in supersonic boundary layers. A better understanding of the interaction mechanism may assist us in improving the design of air- and space-vehicles and also guide us in developing new and improved turbulence models that are able to replicate the real physics of the flow. The emphasis is placed on understanding the evolution of the mean and turbulent flow properties along the interaction region.

The effects of two different thermal boundary conditions, adiabatic and isothermal (cold) wall on the characteristics of a compressible turbulent boundary layer at Mach 2.25 have been investigated. For the isothermal cold wall case, a temperature ratio of $T_w/T_{aw} = 0.67$ has been selected, and the choice was made similar to the ones observed in compressible channel flow simulations. The study is then extended to include the mutual influence of two different thermal wall boundary conditions and an impinging shock ($8°$, incipient separation condition, $P_2/P_1 = 1.6$).

In these type of studies, the turbulence is often (artificially) sustained through approximation methods (e.g. rescaling-recycling technique or synthetic eddy method, etc.) that can possibly bias the flow properties. One of the unique feature of the present study is that the turbulence is developed from instabilities imposed upstream in a laminar region and allowed to develop the full spatial simulation through a progressive transition from laminar to turbulent state.

The development of robust and accurate numerical methods for shock/turbulence interaction problems is the subject of particularly active ongoing research. However, it is worth noting that the most advanced methods proposed in literature are still rather computationally expensive and/or require a delicate tunning of the numerical parameters as a function of the flow considered. The development of such improved numerical tools is outside of the scope of our priority objectives. In the present study, the numerical tools employed are based on (yet perfectible) mature approaches available ($7th$-order WENO , $4th$-order compact, $4th$-order Runge-Kutta along with standard grid resolution for wall-bounded flows) which leads to a reasonable numerical compromise.

The present thesis is organized as follows:

Chapter II provides a detailed survey of the studies that have been performed on the subject of shock/turbulent boundary layer interaction.

Chapter III describes, the numerical simulation methodology and includes the description of spatial discretization and time integration techniques along with the method of generation of the inflow turbulence.

Chapter IV, presents a detailed statistical analysis of the results for the base flow simulations, i.e., the simulation of turbulent boundary layers without shocks. The base simulations are validated against other numerical and experimental results and the effect of adiabatic and isothermal(cold) wall boundary conditions on the velocity and the thermal field of the flow are reported.

Chapter V, deals with the direct simulations of turbulent boundary layers with the impinging oblique shocks. This chapter discusses the evolution of perturbed boundary layers downstream of the central interaction region(i.e; downstream of the incident shock), with a specific emphasis on discovering the extent to which the flow is relaxed back when compared to the characteristics of an undisturbed boundary layer. Similar to the no-shock case, the influence of wall-cooling on the interaction properties in comparison to the adiabatic wall conditions is the basis of the analysis.

Chapter VI, presents with an increasing degree of flow dynamics complexity, the details of the mean and turbulent field modification in the central interaction region (i.e., the region bounded by the legs of the incident and reflected shock and its immediate vicinity).

Chapter VII provides some general conclusions and future perspectives.

Chapter II

Bibliographic Review

II.1 Historical Background: At a Glance

The presence of a shock was originally considered to be an imaginary concept, until Mach (1887) proved the physical existence of shocks and observed, for the first time, the appearance of bow and trailing-edge shocks around a bullet in a supersonic experiment using the shadowgraph technique (Fig. II.1). Since then, there have been numerous experimental studies of shocks (Humble 2008 [16][1]). Probably the first published work on SWBLI was by Ferri (1940) [17] who made experimental observations of an airfoil in a high-speed wind tunnel (Adamson and Messiter (1980) [18] and Dolling (2001) [19]). Shortly afterwards, the studies performed by Donaldson (1944) [20], Liepmann (1946) [21], Fage and Sargent (1947) [22], Ackeret et al. (1947) [23], Allen et al. (1947) [24] discussed the sensitive nature of such interactions on the state of an incoming boundary layer at transonic speeds.

Despite the fact that the earlier studies regarding SWBLI had provided some valuable information, it was difficult to isolate the specific effects induced by the shock, because other parameters had an added effect (e.g. curved surfaces, transonic speeds, streamwise pressure gradient). In an effort to improve the understanding of the phenomenon, most of the studies in late 1940's and in early 1950's were performed at supersonic speeds and on more simplified geometrical configurations (Bardsley and Mair (1951) [25], Barry et al. (1951) [26], Liepmann et al. (1952) [27], Gadd and Holder (1952) [28], Johannesen (1952) [29], Donaldson and Lange (1952) [30], Gadd et al (1953) [31], Holder et al. (1955) [32]). In these studies, the effects produced by the variation of the Mach number, Reynolds number, strength of shock and the incoming state of the boundary layer were analyzed and reported (Dolling (2001) [19]). In 1957 Chapman et al. [4] developed the concept of "free-interaction" through an extensive

[1] In this chapter, the dates are intentionally added with citations to mention the relative chronological order of different studies

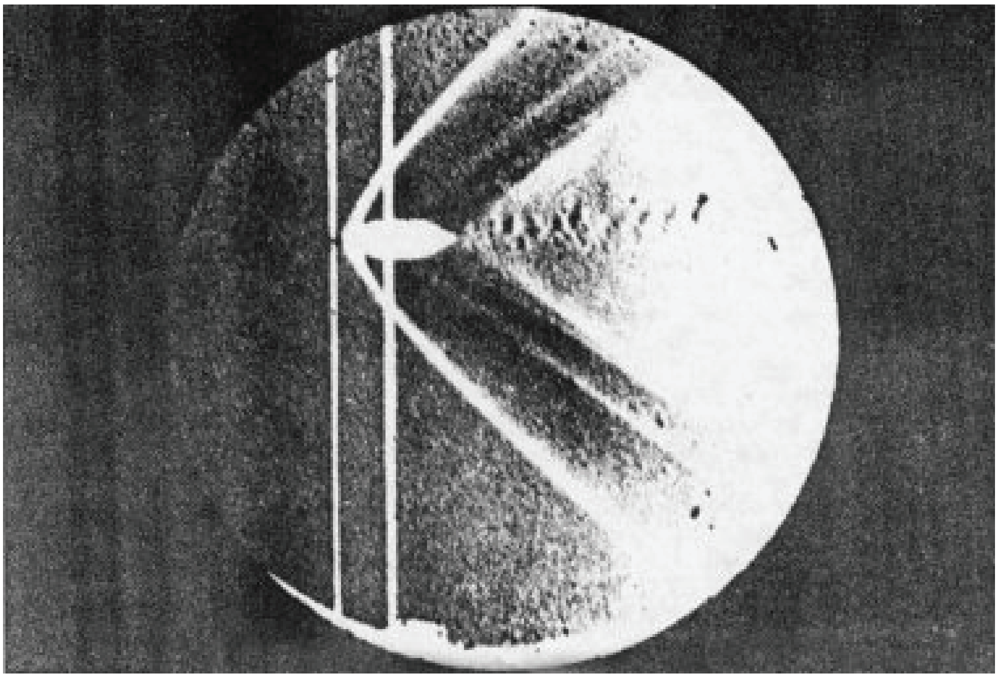

Figure II.1 – Historic photograph by Ernst Mach(1887), that allowed for the visualization of shocks for the first time. From Anderson(1999) [1].

set of experiments on laminar, transitional and turbulent boundary layer interactions with shocks (induced by different sources: ramp, step, or incident oblique shocks), and concluded that certain characteristics of the separated flow (e.g. pressure rise at separation, streamwise interaction extent) were found to be universal in nature and didn't depend on the mode of inducing separation (see Pearcey (1961) [33] for a summary of the studies of 1950's and earlier). Stewartson and Williams (1969) [34] and Neiland (1969) [35], formulated an asymptotic theory of viscous-inviscid interaction, commonly called the "triple-deck theory" and on the basis of this explained the separation of a supersonic laminar boundary layer through free interaction. With the availability of high-frequency pressure transducers in the mid-1960s, the unsteady aspect of the SWBLI was taken into account and the experiments performed by Kistler (1964) [36] were the first reported studies that explored the unsteady behavior of the shock-induced turbulent separation upstream of a forward-facing step and found that low-frequency, large-scale pulsations are characteristic of such interactions. New and more sophisticated measurement techniques have been devised and now used for the detailed investigation of the considered phenomenon. Significant efforts have also been made for the development of advanced numerical tools that can simulate such flows with a certain level of confidence. For a detailed overview of the subject, the reviews contained in Green (1970) [37], Korkegi (1971) [38], Stanewsky (1973) [39], Hankey and Holden (1975) [40], Adamson and Messiter (1980) [18], Délery and Marvin (1986) [41], Settles and Dolling (1992) [42], Dolling (2001) [19], Knight et al. (2003) [43] and more recent ones by Smits and Dussauge (2006) [44], Edwards (2008) [45] and Gatski and Bonnet (2009) [46] are recommended.

II.2 Types of SWBLI

One can classify the interactions of the shock with boundary layers into two broad categories (Délery and Marvin (1986) [41], Délery and Dussauge (2009) [3]), namely:

1. Two-Dimensional Interactions: The two-dimensional basic configurations include the interaction of the boundary layer with the following shock-systems.

    - separation shocks produced in front of the compression corners
    - impinging-reflecting oblique shock-system
    - normal shocks
    - shock-system developed in-front of the forward facing steps
    - reattachment shock-system formed behind the rearward facing steps
    - compressive discontinuities produced due to the pressure jumps

2. Three-Dimensional Interactions: The interactions produced around the following obstacles are example of three-dimensional interactions

    - swept wedges
    - blunt fins

As outlined in the Introduction the present study investigates the characteristics of the interaction of an impinging oblique shock/turbulent boundary layer interaction. In addition, because of some phenomenal similarities, the details about the compression corner interactions are also included. These selected configurations have also been taken into account by many of the experimental and numerical studies on the subject and can be effectively used for both validation and analysis of the current results.

II.2.1 Compression Ramps

The classical problem of boundary layer flow over a compression ramp has been the subject of extensive research in the domain of SWBLI for more than half a century. Various studies have helped to elucidate the different aspects of the problem (Ardonceau (1984) [47], Smits and Muck (1987) [8], Andreopoulos and Muck (1987) [48], Kuntz et al.(1987) [49], Selig et al. (1989) [9], Erengil and Dolling (1991) [50], Adams (2000) [51], Beresh et al. (2002) [11], Fletcher et al. (2004) [52], Ganapathisubramani et al. (2007) [53], Bookey et al. (2005) [54], Wu and Martin (2007,2008) [14], [55]).

In most of the aerodynamic related problems these types of flow-fields are usually encountered due to the discontinuous change in body geometry and flap related deflections. A discontinuous change in the wall inclination towards the flow gives rise to the compressive disturbances which accumulate in the formation of a shock. Depending on the inclination angle β of the compression ramp (which defines the intensity level of the pressure gradient in the flow direction), it may result in the formation of a separation bubble, which is confined between the walls of the ramp and the separated shear layer. Fig. II.2 shows the conceptual diagram of the compression ramp flows with and without flow separation (adapted from Arnal and Délery (2004) [2]).

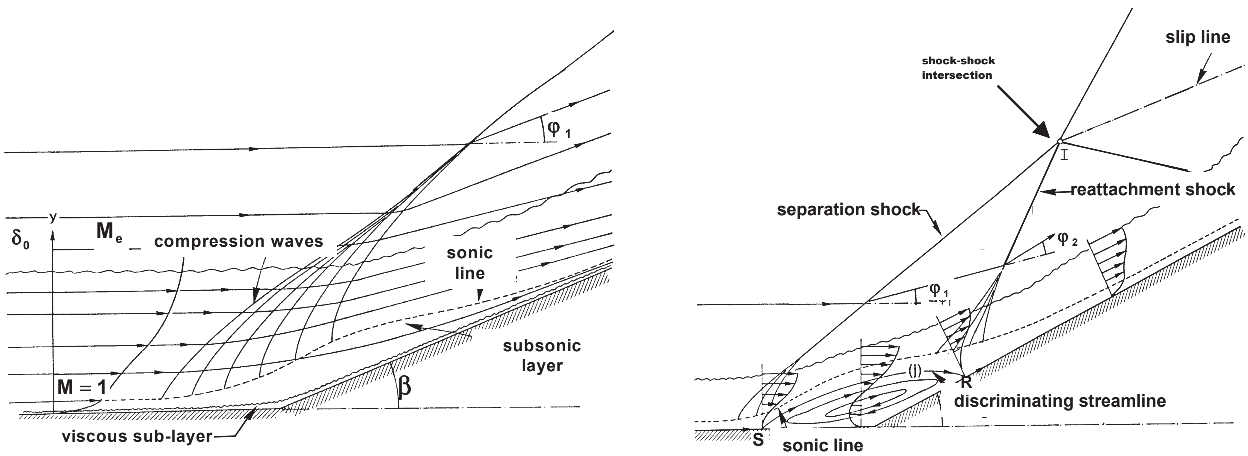

(a) Without Separation **(b)** With Separation

Figure II.2 – The shock boundary layer interaction mechanism over a compression ramp: (a) Without Separation; (b) With Separation. Adapted from Arnal and Délery (2004) [2].

The extent to which the presence of the perturbation is felt upstream of the inviscid shock origin is also dependent on the ramp inclination angle β. The upstream influence is generated by the subsonic part of the boundary layer because of its differential elliptic characteristics, the information can be transmitted in both upstream and downstream directions. Moreover, the nature of the flow determines the thickness of the subsonic layer and the wall-relative position of the origination of the shock within the boundary layer. At high Mach and Reynolds numbers, the boundary layer behaves more inviscid (rotational) in nature and the lower momentum deficit leads to a very thin subsonic layer. In this case, the shock originates from a region very close to the wall and undergoes a rapid interaction that is characterized by an interaction in which viscous forces are negligible as compared to the pressure and inertial forces.

For the cases with separation (Fig. II.2b), a second shock (the reattachment shock) is generated near the reattachment of the shear layer to the inclined ramp, as the flow is turned parallel to the wall. The separation and reattachment shocks intersect at some distance from the wall in the inviscid region at the triple point I which leads to the formation of two new refracted shocks downstream of this point and an intermediate state (slip line) appears between these two shocks so that the inviscid flow structure remains compatible above and below the triple point I.

II.2.2 Oblique Impinging Shock

These types of interactions are produced when a planar oblique shock, initiated by an external deflection source, impinges on a flat surface (boundary layer) and then reflects back with an oblique angle. In high-speed aeronautical applications, these interactions are representatives of the processes that take place at the intakes of scramjet and ramjet engines. Because of the practical importance and academic interest (in comparison with compression ramps, the study of such type of interactions removes the effects induced by the compression ramp curvature), this problem has been widely researched in recent times. A detailed review of the earlier work on two-dimensional impinging oblique shock interactions is found in Green(1970) [37] while the more recent reviews with details about the new advancement and understanding of the mechanism are reported in Délery and Marvin (1986) [41], Smits and Dussauge (2006) [44]. The studies conducted by Back and Cuffel (1976) [56], Deleuze (1995) [10], Laurent (1996) [57], Garnier et al. (2002) [58], Bookey et al. (2005) [54], Humble (2008) [16], Priebe et al. (2009) [15], Piponniau et al. (2009) [59] and Touber and Sandham (2009) [60] are some of the recent major experimental and numerical contributions.

As in the case of the compression corner, on the basis of the shock strength the mean flow mechanism of these interactions can be subdivided into two classes: interaction without separation (Fig. II.3a) and interaction with separation (Fig. II.3b).

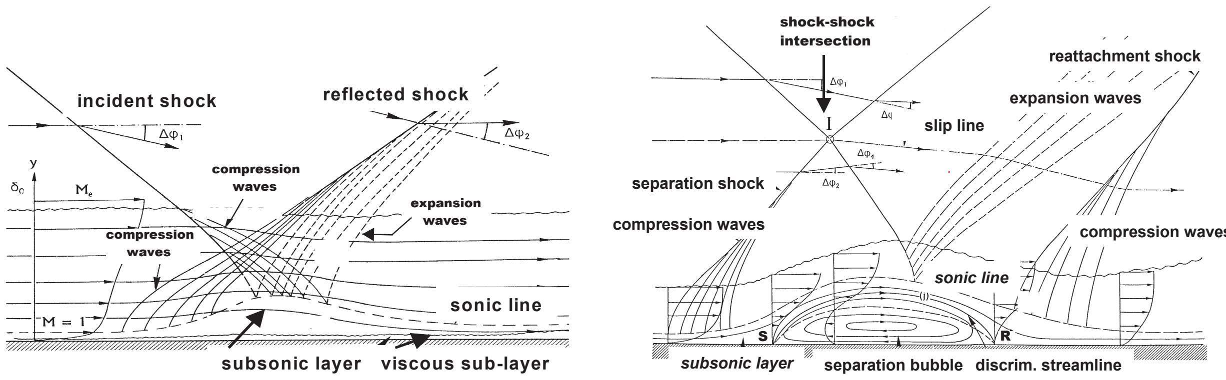

(a) Without Separation **(b)** With Separation

Figure II.3 – The shock boundary layer interaction mechanism induced by an impinging oblique shock: (a) Without Separation; (b) With Separation. Adapted from Arnal and Délery [2].

In the unseparated case, the pressure gradient imposed by the incident shock is not sufficient to cause the boundary layer to separate. A schematic representation of the interaction of an incident oblique shock with the boundary layer is shown in Fig. II.3a. In order to understand the interaction mechanism the flow-field can be divided into three regions:

- Region 1: Flow region upstream of the interaction
- Region 2: Central interaction region
- Region 3: Flow region downstream of the interaction(relaxation zone)

In the first region, the undisturbed boundary layer of thickness δ_o meets the reflected shock. The disturbance initiated by the penetrated incident shock is transmitted upstream through the subsonic part of the boundary layer, which is very close to the wall, and indicated by the dashed line in Fig. II.3a. The influence of the shock-system is therefore felt upstream of its inviscid origin (see Fig. II.4) with the extent of upstream influence mainly dependent on the strength of the shock and on the nature of the incoming flow. Turbulent boundary layers have velocity profiles that are characterized by a lower velocity deficit (large momentum transfer occurs between adjacent layers) as compared to the laminar boundary layer. This suggests that in turbulent boundary layers the subsonic layers found are relatively smaller as compared to laminar boundary layers and the upstream influence of the disturbances is relatively shorter.

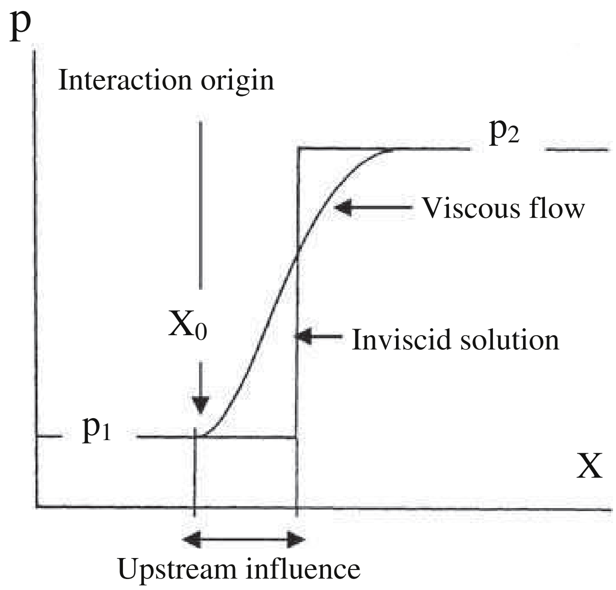

Figure II.4 – Mean wall-pressure distribution for a SWBLI, demonstrating the influence of shock upstream of its inviscid origin. From Délery and Dussauge (2009) [3]

As the flow proceeds further towards the central interaction region, the subsonic layer of the boundary layer starts experiencing the effect of the pressure gradient and the streamlines within the subsonic layer show a diverging pattern that results in a thickening of the layer. This thickening of the subsonic layer of the boundary layer generates the outgoing compression waves that rapidly coalesce to form the reflected shock. As the incident shock propagates through the inviscid rotational part of the boundary layer, it undergoes a decrease in the local Mach number that affects the strength of the shock and hence the incident shock is curved, and its intensity becomes vanishingly small when it reaches the sonic line. As the strength of the shock weakens, it start dispersing into compression waves that upon reaching the sonic line, reflect back in the form of expansion waves.

Downstream of the interaction region, the perturbed boundary layer undergoes a recovery process. The subsonic portion of the boundary layer now begins to contract, and the inner part of the boundary layer accelerates in order to adjust itself according to the new unstrained conditions. A downstream “relaxation length” of a few boundary layer thicknesses is required to return the boundary layer properties to the initial state upstream of the interaction. The extent of the relaxation length is dependent on the strength of the shock and on the nature of the incoming flow.

Now consider the case of an interaction in which the pressure gradient associated with the incident shock is strong enough that the boundary layer separates from the surface. The resulting wave pattern is much more complicated than its unseparated counterpart. A schematic representation of the separated case is shown in Fig. II.3b. A regional topology similar to that of the unseparated case is employed for the explanation of the interaction mechanism.

Starting with the region upstream of the shock-system, the undisturbed incoming boundary layer intersects with the shock-system and then separates at the point where the pressure gradient is large enough to detach the boundary layer from the surface. Due to the higher streamwise pressure gradient, the upstream influence of the disturbance, initiated by the penetration of the incident shock is felt over a larger streamwise extent when compared to an unseparated interaction. When considering the flow behavior during separation at a supersonic Mach number, it is important to mention the concept of "free interactions" presented by Chapman et al. in 1957 [4]. They suggested that any phenomenon near separation which is independent of the object shape does not depend on the downstream conditions but will be determined solely by the conditions upstream of the separation. In a more explicit manner, free interaction theory suggest that, for the case of laminar and turbulent supersonic interactions, the pressure rise during separation and the extent of the interaction region are entirely dependent on the flow properties at the interaction onset.

Proceeding toward the central interaction region, the boundary layer undergoes separation at the point "S", which is located well upstream of the point where the incident shock would meet the surface in the case of a perfect fluid. As a consequence of the boundary layer detaching from the surface, a recirculation region forms downstream of the separation point, and a shear layer develops between the recirculating fluid and the subsonic forward moving stream. Along the shear layer, through the action of viscous forces, a momentum transfer occurs between the low-momentum fluid in the reversed flow region and the higher-momentum fluid stream outside of the recirculation bubble. With the streamwise development of the shear layer, the low momentum fluid accelerates up to a point where it acquires enough momentum to overcome the pressure gradient and reattaches to the surface (designated by the point "R"). The streamwise distance between the reattachment point and the separation point is known as the "separation length". It is a well known fact, that the pressure rise at the separation depends solely on the upstream conditions and is not influenced by the downstream conditions (free interaction theory), which indicates that an increase in the strength of the incident shock will eventually suggest a greater pressure rise at the reattachment. Moreover, an increase in the pressure gradient necessitates an upstream displacement of the separation point in order to permit a longer acceleration phase of the fluid in the shear layer. This necessitates an explanation of the fact that the incident shock with a stronger strength leads to the longer separation length. The pressure rise at the separation is an after-effect of the formation of the reflected shock due to the coalescence of compression waves. This reflected shock intersects with the incident shock in the outer inviscid stream which results in the emanation of two refracted shocks and a slip line (the intersection point is designated by point "I" in Fig. II.2b). After intersecting with the reflected shock, the refracted part of the incident shock is bent because of the entropy gradient downstream of the reflected shock and the compression waves generated by the thickening of the boundary layer. Afterwards, the refracted incident shock penetrates the boundary layer and is reflected from the sonic line as an expansion wave.

Downstream of the reattachment, the induced compression waves coalesce to form a reattachment shock. The flow has now passed through a series of complicated flow patterns both inside and outside of the boundary layer and undergoes a recovery process farther downstream. The effect of the interaction on the recovering boundary layer is therefore less pronounced, and the mean and turbulent properties of the boundary layer may take $\mathcal{O}(10)$ undisturbed boundary layer thicknesses to fully recover.

II.3 Salient Features of SWBLI

The discussion in the present section provides a brief overview of the key elements that describe the flow evolution in SWBLI. As a result of SWBLI, the mean field and the turbulence dynamics are affected significantly. Since the first observation of SWBLI, a myriad of experimental and numerical studies have been performed to quantify the dynamic characteristics of the complex phenomenon. The existing literature on SWBLI is vast and diverse, so it is not possible to identify all of these studies within the length of this discussion, however the most relevant studies in advancing the understanding about the essential dynamics of such interactions are highlighted in Table II.1. Each study involved an investigation of different features of SWBLI Instead of presenting the key observations of different authors based on the nature of a specific characteristic of the interaction, the key observations found in the different experiments and numerical simulations are presented in chronological order, so that multiple repetitions of the same citation can be avoided.

II.3.1 Experimental Contributions

The evolution of the skin friction (coefficient of friction C_f) and the streamwise mean static pressure distribution at the surface are the basic elements that determine the lateral extent of

Table II.1 – Some important studies concerning SWBLI

Reference	Interaction type[a]	Mach number	Measurement technique / Numerical tool[b]	Ramp or shock generator angle
Experimental Studies				
Chapman et al. (1957) [4]	CR,IS,CS,FFS	Variable	SPM,ShV,OFV	Variable
Law (1974) [61]	CR,IS	2.96	SPM,ShV,OFV	25°CR, 12.27°IS
Back and Cuffel (1976) [56]	IS	3.5	PTM	8.4°
Settles et al. (1979) [6]	CR	2.95	PTM,SPM,ShV,OFV	8°,16°,20°,24°
Dolling and Murphy (1983) [7]	CR	2.9	SPM,ShV	24°
Ardonceau (1984) [47]	CR	2.25	SPM,HWA,LDA	8°,13°,18°
Smits and Muck (1987) [8]	CR	2.9	HWA	8°,16°,20°
Kuntz et al. (1987) [49]	CR	2.94	LDV	8°,12°,16°,20°,24°
Andreopoulos and Muck (1987) [48]	CR	2.84	SPM	16°,20°,24°
Selig et al. (1989) [9]	CR	2.84	SPM,HWA	24°
Erengil and Dolling (1991) [50]	CR	5.0	SPM	28°
Deleuze (1995) [10]	IS	2.28	LDV	8°
Laurent (1996) [57]	IS	2.28	HWA	8°
Beresh et al. (2002) [11]	CR	5.0	SPM,PIV	28°
Bookey et al. (2005) [54]	CR,IS,SP	2.9,8.0	SPM,FRS,OFV	8°CR,24°CR,12°IS,10°SF
Haddad (2005) [62]	IS	2.28	SPM,HWA,LDA,PIV	7.1°,8°,8.8°,9.5°
Ganapathisubramani et al. (2007) [53]	CR	2.0	PLS,PIV	20°
Humble (2008) [16]	IS	2.1	HWA,PIV	8°
Piponniau (2009) [63]	IS	2.28	StV,PIV	4° to 9.5°
Souverein (2010) [64]	IS	1.7,2.3	ScV,HWA,PIV	5.5°,6°,8°,9.5°
Numerical Studies				
Hunt and Nixon (1995) [65]	CR	3.0	LES	24°
Adams (2000) [51]	CR	3.0	DNS	18°
Garnier (2000) [66]	IS	2.3	LES	8°
Stolz et al. (2001) [67]	CR	3.0	LES	18°
Rizzetta and Visbal (2002) [68]	CR	3.0	LES	8°,16°,20°,24°
Dubos (2005) [69]	IS	2.3	LES	8°
Bookey et al. (2005) [70]	CR,IS	2.9	DNS	24°CR,12°IS
Pirozzoli et al. (2005) [71]	IS	2.25	DNS	8°
Loginov (2006) [72]	CR	2.95	LES	25°
Wu and Martin (2008) [55]	CR	2.9	DNS	24°
Priebe et al. (2009) [15]	IS	2.9	DNS	12°
Touber and Sandham (2009) [60]	IS	2.3	LES	8°
Hadjadj et al. (2010) [73]	IS	2.28	LES	8°
Morgan et al. (2010) [74]	IS	2.05	LES	8°

[a] CR=Compression Ramp, IS=Impinging Shock, CS= Curved Surfaces, FFS= Forward Facing Step, SF= Sharp Fin
[b] SPM= Surface Pressure Measurements, ShV= Shadowgraph Visualization, ScV= Schlieren Visualization, StV= Stereoscopic Visualization, OFV= Oil Flow Visualization, PTM= Pitot Tube Measurements, HWA= Hot Wire Anemometry, LDA/LDV= Laser Doppler Anemometry/Velocimetry, PIV= Particle Image Velocimetry, FRS= Filtered Rayleigh Scattering, PLS= Planar Laser Scattering, LES= Large Eddy Simulation, DNS= Direct Numerical Simulation

the interaction region. Through an extensive set of experiments in laminar, transitional and turbulent flows, Chapman et al. (1957) [4] developed the concept of "free-interaction" (see the previous section for an explanation) and showed that when an appropriate scaling for pressure and interaction length was employed, the pressure distribution through the separation zone for different model configurations and for different Reynolds numbers collapsed on the same curve (Fig. II.5a). In reviews by Green (1970) [37], Charwat (1970) [75], Stanewsky (1973) [39] and Délery and Marvin (1986) [41], the similarity of the interaction properties between different flow configurations (e.g. between compression corners and incident shocks, forward facing steps and spoilers) has been studied in detail and provides a validation of the free-interaction concept. The experiments performed by Law (1974) [61], as reported by Shang et al. (1976) [5] have observed, for a turbulent flow at Mach 2.96, that the general characteristics of the interaction induced by an impinging oblique shock and compression corner are nearly identical, provided that the deflection angle of the compression corner is twice that of the impinging shock generator angle. Fig. II.5b adapted from Shang et al. (1976) [5] shows the comparison of the wall-pressure distribution between interactions induced by a 25° compression ramp and an impinging oblique shock at 12.27°.

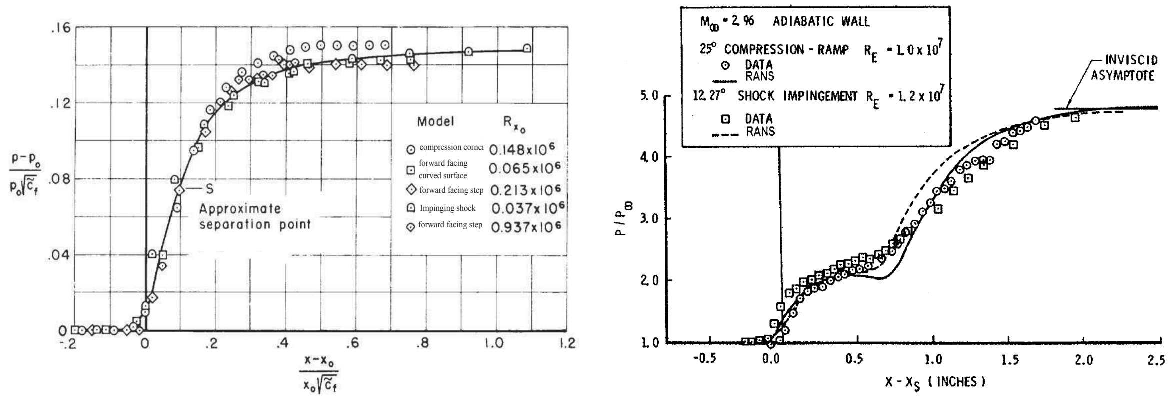

(a) **(b)**

Figure II.5 – (a): Wall-pressure distribution for laminar separation for various model configurations and Reynolds number at $M = 2.3$. From Chapman et al. (1957) [4],(b): Wall-pressure distribution along the entire interaction region for a compression corner(25°) and an impinging oblique shock(12.27°) configurations. Adapted from Shang et al. (1976) [5]

However, according to Smits and Dussauge (2006) [44], the free-interaction concept generally holds well for the case of laminar flows, but for the case of turbulent flows the collapse of data for different configurations is not impressive, and indicates a more significant dependence on the downstream boundary conditions. The reason for this discrepancy may lie in the fact that the free-interaction theory is based on a stationary flow concept and does not take into account the non-stationary motion of the shock.

Back and Cuffel (1976) [56] shed some light on the properties of SWBLI under the influence of different surface temperature conditions. The experiments conducted by them discussed the effects of surface wall cooling ($T_w/T_t = 0.44$) and surface heating ($T_w/T_t = 1.1$, T_w and T_t designate wall and stagnation temperature respectively) on the interaction flow-fields induced by an 8.4° impinging shock. A noticeable effect of surface cooling on the velocity and temperature flow-fields, the shock interaction structure and size of the separation bubble was observed. It was indicated that the size of the separation region was significantly decreased with surface cooling and the curve of the pressure rise in the interaction region was also very much steeper when compared to the heated wall condition.

The study reported by Settles et al. (1979) [6] presented the detailed surface and mean flow-field measurements for four different compression corner cases ranging from the attached to separated conditions. The development of a flow over the surface in the interaction region was analyzed by means of surface streak patterns, from which the progressive increase in the extent of the interaction region and the three-dimensional character of the flow were identified (Fig. II.9). As a consequence of the interaction, a significant retardation of the flow was observed in the mean velocity profiles. Moreover, the extent to which the flow recovered downstream of the interaction was also discussed.

Dolling and Murphy (1983) [7], measured the pressure fluctuations over a 24° compression corner at Mach 3 to quantify the unsteadiness of the shock. Large amplitude pressure fluctuations were observed in the interaction region, reaching their peak levels near the separation and reattachment positions (Fig. II.7). Close to the separation shock structure, the pressure signals measured were highly intermittent in nature and characterized by the low-frequency high amplitude fluctuations. The effect of the boundary layer thickness variation on the separation length and the frequency of the shock motion was also mentioned and it was found that the boundary layer thickness variation had a direct proportional effect on separation length while it was inversely related to the frequency of the shock motion.

Ardonceau (1984) [47] and Smits and Muck (1987) [8] studied the interaction properties of compression corner flows over a range of inclination angles, varying from attached to separated conditions. Ardonceau (1984) [47] reported the mean flow surveys, the turbulence measurements and the qualitative analysis of the flow-fields deduced from high-speed Schlieren photography. It was observed that a large amount of turbulent energy was contained in the large-scale structures that were not destroyed along the length of the interaction and persisted

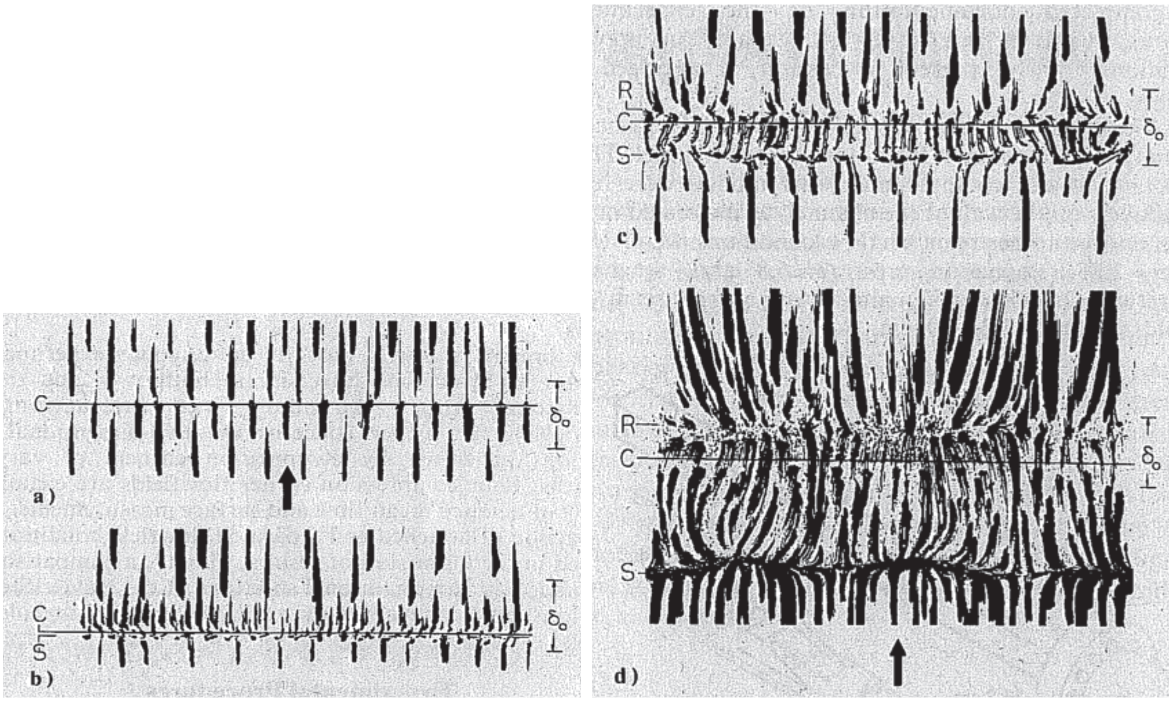

Figure II.6 – (a) to (d) demonstrate the surface streak patters observed for the cases of 8°, 16°, 20° and 24° compression corner interactions. S, C and R denote separation, corner and reattachment locations respectively. From Settles et al. (1979) [6].

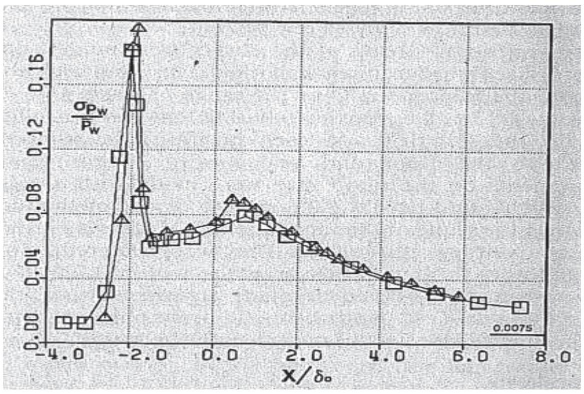

Figure II.7 – Effect of incoming boundary layer thickness variation on wall pressure standard deviation distribution along a 24° compression ramp.$\square, \delta_o = 1.2cm$ and $\triangle, \delta_o = 2.2cm$. From Dolling and Murphy (1983) [7].

downstream of the interaction. A low-frequency unsteadiness associated with the separation bubble was also noticed, however no connective effect with the rest of the flow was detected. In the experiments performed by Smits and Muck (1987) [8], longitudinal mass-flux fluctuations and the mass-weighted shear stress were measured while the Reynolds stresses were deduced from it. As a result of the interaction, an anisotropic amplification of the turbulent stresses and the length scales was noted. Moreover, the maximum amplification of the turbulent quantities was found to be proportional to the overall static pressure rise through the interaction (Fig. II.8). The unsteady behavior of the separated shock and the its wrinkling in the spanwise direction was also discussed.

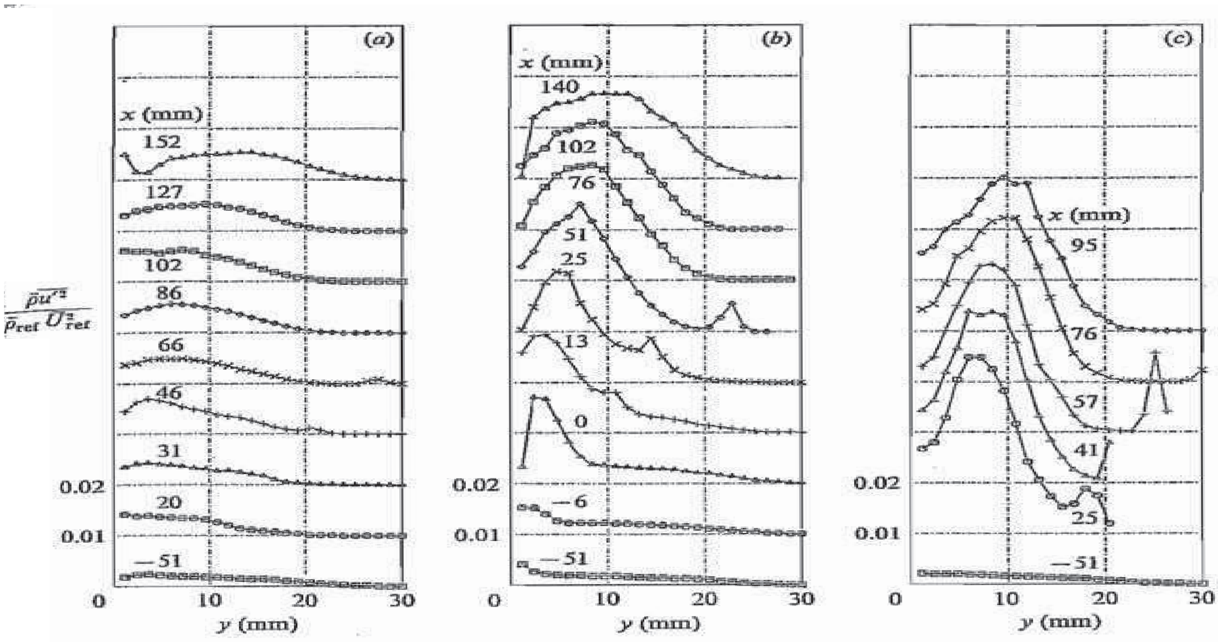

Figure II.8 – (a) to (c) demonstrate the longitudinal Reynolds stress evolution along the interaction region for 8°, 16°, and 20° compression corner interactions. From Smits and Muck (1987) [8].

In the studies performed by Kuntz et al. (1987) [49] two-component coincident velocity measurements were made within the upstream boundary layer and within the downstream redeveloping boundary layer and the effect of an increasing shock strength on various flow-field parameters was analyzed. The significant alteration of the boundary layer was observed as a result of the interaction. They found that the mean velocity profiles downstream of the separated interactions were wake-like in nature. Significant increments in turbulent intensities and Reynolds stresses were considered to be due to the induced interaction and indications of the presence of large-scale turbulent structures were also noticed in the redeveloping boundary layer. Andreopoulos and Muck (1987) [48] measured the pressure fluctuations in the interaction region of the two-dimensional compression corner and deduced that the frequency of the shock unsteadiness is of the same order of magnitude as the bursting frequency of the upstream boundary layer. They used the conditional sampling technique to separate the frequencies related to the turbulence from those of the shock oscillation. No coupling of the shock oscillation with the downstream separated flow was observed.

Selig et al. (1989) [9] showed that the maximum mass-flux turbulence intensity was amplified through the interaction and that the probability density functions (*pdf*'s) of the mass-flux fluctuations changed their distributions from a Gaussian-like undisturbed upstream state to a bimodal state downstream of the interaction (Fig. II.9). The bimodal distribution observed was attributed to the presence of large-scale motions produced by the instability of the inflectional velocity profiles downstream of the interaction. No significant effect of the shock-induced separated region was observed on the shock unsteadiness. Erengil and Dolling (1991) [50] deduced a possible correlation between the pressure fluctuations in the incoming flow and the separation shock motion and the results for two different types of shock motions (shock sweeps and shock turnarounds [2]) were analyzed. It was found that the characteristic pressure variation within the incoming boundary layer was weakly correlated to the large scale downstream shock sweeps, whereas, for the case of upstream shock sweeps no sign of any correlation was observed. However a distinct correlation was determined for motions characterized by shock turnarounds. Moreover, they concluded that the high-frequency jitter component of the shock motion was due to the large scale turbulent structures that were convected into the interaction.

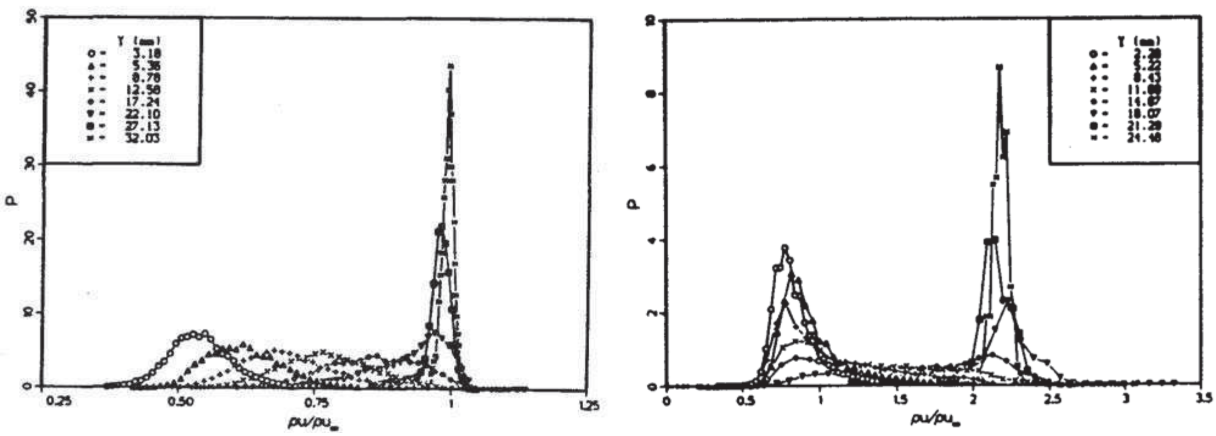

Figure II.9 – Probability density function of mass-flux fluctuations, upstream(left) and downstream(right) of shock. From Selig et al. (1989) [9].

Deleuze (1995) [10] and Laurent (1996) [57] investigated the characteristics of an impinging

[2] shock sweeps: continuous upstream or downstream motion of the shock, shock turnarounds: shock motion changes direction from upstream to downstream or vice versa

oblique shock/turbulent boundary layer interaction by using two component laser Doppler velocimetry (LDV) and hot-wire anemometry (HWA) respectively. Deleuze (1995) [10] presented a detailed analysis of the mean and turbulent velocity fields (e.g. second and higher-order moments, structure parameters etc.) variation within the central interaction region and their evolution downstream of the interaction, and the effect of wall-heating in comparison to the adiabatic wall was also analyzed. It was found that the significant mean field alteration occurred (Fig. II.10, top) with an anisotropic amplification of turbulence (Fig. II.10, bottom left and right) and that the turbulence distribution was similar to that of boundary layers subjected to adverse pressure gradients. The experiments of Laurent (1996) [57] examined the effects of shock strength variation and of wall-heating. The behavior of Van-Driest transformed velocity and temperature profiles downstream of the interaction was studied and it was found that, because of the effect of the interaction and wall heating, the extent of the logarithmic region in the Van-Driest transformed velocity profiles was considerably reduced. It was found that for a specific shock strength the nondimensionalized relaxation distance remained identical for the adiabatic and the heated wall case (the length of interaction was used for nondimensionalization of the relaxation distance). The velocity-temperature correlation coefficient and the Strong Reynold Analogy (SRA) coefficient were not appreciably affected as a result of the interaction, however the effect of wall-heating decreased the value of the SRA coefficient. It was also found that the unsteady motion of the separation bubble was responsible for the low-frequency reflected shock oscillations.

Beresh et al. (2002) [11] examined the relationship between the incoming boundary layer and the unsteady motion of the separation shock foot. A strong correlation was observed between the positive streamwise velocity fluctuations in the lower part of the boundary layer and the downstream sweeps of shock, and vice-versa. The characteristic frequencies representative of these velocity fluctuations were found to be of a lower-order when compared with the frequency of incoming boundary layer ($40K$Hz) and remained in the range of $4-10K$Hz. To explain the mechanism, a simple physical model was proposed. According to this model when positive velocity fluctuations occur in the turbulent boundary layer the velocity profiles have a smaller momentum deficit and become more full. As a result, its resistance against the separation increases and hence the flow experiences a downward motion of the shock and, analogous to this, negative velocity fluctuations result in an upstream motion of the shock (Fig. II.11).

Bookey et al. (2005) [54] performed experiments at DNS and LES accessible Reynolds numbers. Four different flow configurations were studied (24° compression corner and 12° oblique impinging shock case at Mach 2.9, 8° compression corner and sharp fin cases at Mach 8). The experimental results presented comprised velocity profile surveys, surface pressure

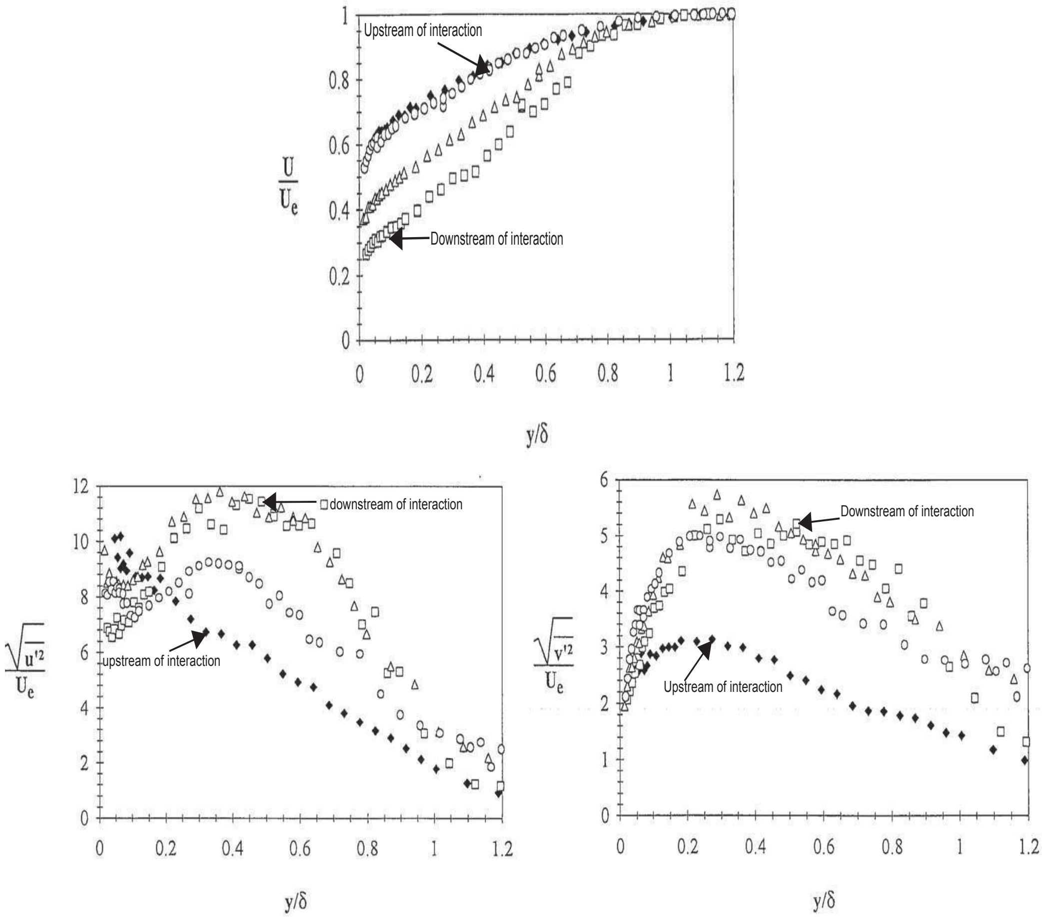

Figure II.10 – Alteration of mean velocity profiles downstream of the interaction induced by an oblique impinging shock (top). Amplification of streamwise and wall-normal components of Reynolds stresses across the shock-system (bottom left and right respectively).From Deleuze (1995) [10].

distributions, surface flow visualizations and two-dimensional flow-field imaging using Filtered Rayleigh Scattering. Large separated regions were observed for flow configurations at Mach 2.9, however, the flow remained attached for the compression corner study at Mach 8. The separated region produced by the sharp fin configuration was three-dimensional in nature.

Haddad (2005) [62] and Dupont et al. (2006) [12] studied the effect of varying shock strength on the unsteadiness of the oblique shock-system. Temporal and spatial scales (reflected shock frequency, length of interaction, shock excursion length) of the interactions were quantified and their variation on several flow deflection angles were also analyzed. The reflected shock was characterized by its low frequency oscillation (ranges between 200 to 600 Hz) and it was

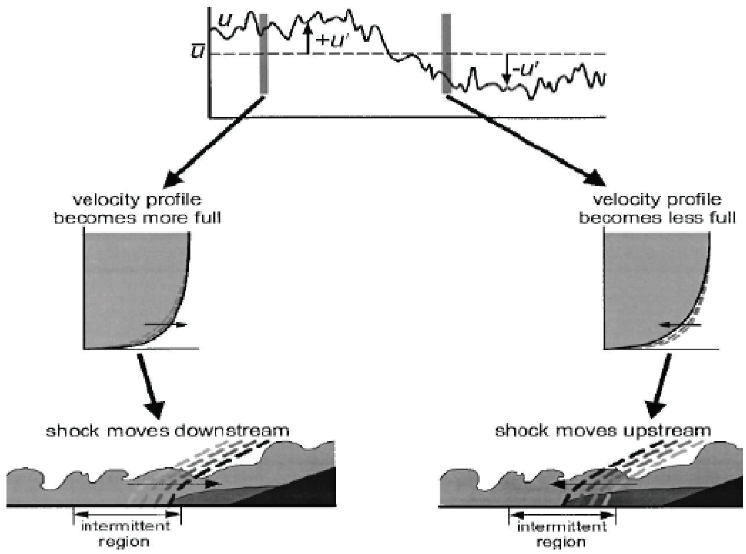

Figure II.11 – Relationship between incoming boundary and separation shock foot unsteadiness. From Beresh et al.(2002) [11]

observed that, depending on the flow deflection angle (7° to 9.5°), it can move over a streamwise extent varying from one to two boundary layer thicknesses. The low frequency unsteadiness of the reflected shock was highlighted in terms of the Strouhal number and it was concluded that for varying shock intensities the Strouhal number corresponding to the reflected shock motion remained in the range of $0.025 - 0.040$ (Fig. II.12). The connection between the unsteady shock motion and the separated region was also observed and it was found that the mean rate of rotation of two counter-rotative spanwise vortices developed inside the recirculation region was of the same order as that of the frequency of the reflected shock oscillation.

In the experiments reported by Ganapathisubramani et al. (2007) [53], the unsteady behavior of SWBLI was investigated. Using planar laser scattering (PLS) and particle image velocimetry (PIV) measurement techniques, they observed in the incoming boundary layer, high and low speed spanwise elongated structures that extended up to streamwise lengths greater than $40\delta_o$. There was conformity between the high- and low-speed elongated structures and the undulation appeared in the instantaneous spanwise separation line. Moreover, similar to Beresh et al. (2002) [11], on the basis of conditional averaging and joint probability distributions, a correlation was observed between the signs of the velocity fluctuations in the upstream boundary layer and the direction of unsteady motion of the separation shock.

Humble (2008) [16] and Humble et al. (2009) [76] investigated the unsteady three-dimensional flow behavior of an incident oblique shock/turbulent boundary layer interaction using tomo-

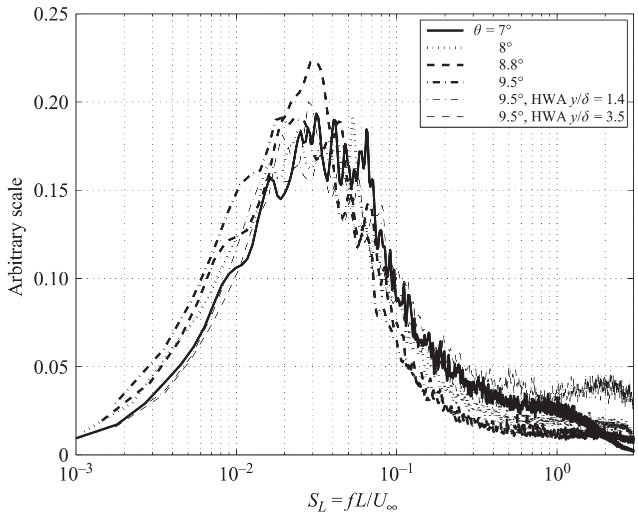

Figure II.12 – Power spectral densities around the reflected shock with varying incident shock strength. From Dupont et al. (2006) [12].

graphic particle image velocimetry and hot wire anemometry. A temporal analysis was made and a considerable change in the global structure of the interaction was observed. A flow connectivity was observed between the incoming boundary layer, the separated flow region and the reflected shock. Dilatation of the separation bubbles was observed to be connected to the deficiency of momentum in the velocity profiles (compared to the mean momentum level the instantaneous velocity profiles were less-full) which forced the reflected shock to move upstream relative to its mean position and vice-versa. Observations in the spanwise direction revealed that large-scale coherent motions in the form of three-dimensional streamwise elongated regions of relatively low- and high-speed fluid were responsible for the streamwise translation and spanwise rippling of the reflected shock. In addition, it was found that the corresponding frequencies in the reflected shock region were observed to be an order of magnitude lower than those within the undisturbed boundary layer.

Piponniau (2009) [63] and Piponniau et al. (2009) [59] studied the interaction between the oblique shock and the fully developed turbulent boundary layer on a flat plate by using particle image velocimetry (PIV). Spatial organization of the instantaneous interaction field was presented for several deflection angles (4° to 9.5°). A strong statistical link between the successive contractions/dilatations (breathing) of the detached bubble and the low frequency unsteadiness of the reflected shock was found. An aerodynamic model to determine the time scale of the unsteady phenomenon, found in shock-induced separated flows, was proposed. The model was also applied to several other previously reported flow configurations, ranging from subsonic to supersonic Mach numbers ($M = 0-5$), and it was found that the estimations provided by the model were in good agreement with the results obtained from measurements.

Souverein (2010) [64] performed a series of experiments at a variety of flow conditions to investigate the interaction characteristics of oblique shock/turbulent boundary layer interaction. Experimental measurement techniques, such as three-component particle image velocimetry and dual-particle image velocimetry, were employed. A Mach 1.7 incipient interaction at a high Reynolds number and a number of Mach 2.3 interactions of varying shock intensity at low Reynolds numbers were studied. It was proposed that the physical mechanism responsible for shock unsteadiness was dependent on the imposed shock intensity. For interactions without instantaneous flow separation, events upstream of the shock were likely to govern the flow unsteadiness completely, with rather high frequencies. While for the cases where the flow remained separated most of the time, the low frequency unsteadiness related to the separation bubble pulsation became predominant. Furthermore, for incipient interactions, the unsteady behavior of the interaction was found to be responsible in a combination of events occurring both upstream and downstream of the interaction and the deviation of interaction properties from the separated cases was found to be dependent on flow separation rate.

II.3.2 Numerical Contributions

Coincident with the numerous experimental investigations, the ongoing development of numerical simulation tools and the advancement in computer technology have reached a level where problems like SWBLI can be attempted with a high degree of accuracy using time dependent techniques such as direct numerical simulation (DNS), large eddy simulation (LES) and hybrid large-eddy simulation/Reynolds-averaged Navier-Stokes (LES-RANS) methods. In addition to the steady aspects of the interaction, such simulations are also quite helpful in enhancing our understanding of the unsteady characteristics of flow dynamics. However, in order to properly resolve the turbulent scales, the direct simulations are still inherently restricted to relatively modest Reynolds number values and limited time spans. The review provided by Knight and Degrez (1998) [77] examined the suitability of Reynolds-averaged Navier-Stokes (RANS) methods for the prediction of shock/turbulent boundary layer interaction and concluded that none of the RANS computations had the ability to successfully capture the large scale unsteadiness of the shock and to predict the fluctuating surface pressure and heat transfer. The more recent reviews compiled by Knight et al. (2003) [43] and Edwards (2008) [45] discussed the capabilities and limitations of DNS, LES and some of the hybrid methods(LES-RANS) for the prediction of the considered phenomenon, and it was found that these methods have the potential to calculate the critical details of SWBLI. The present discussion of numerical contributions regarding SWBLI will remain focused around the studies that employed either DNS or LES as a numerical tool.

According to Edwards (2008) [45], the application of time dependent simulation techniques for the case of SWBLI was first attempted by Hunt and Nixon (1995) [65]. They performed a very coarse mesh "very large eddy simulation" of a Mach 3 compression corner interaction that had been experimentally investigated by Dolling and Murphy (1983) [7]. It is noteworthy that they used some of the simulation techniques, such as the recycling of turbulent fluctuations to sustain turbulent motions and wall-function closures, to perform calculations at high Reynolds numbers, that are still in use, in their modified forms, in the more recent SWBLI simulations (e.g. Garnier et al. (2002) [58], Wu and Martin (2007) [14], Priebe et al. (2009) [15]).

Adams (2000) [51] studied the interaction properties of a 18° compression corner interaction at Mach 3 by direct numerical simulation (DNS). For the generation of inflow conditions, the output from an auxiliary simulation was used. The presented results were averaged over a time span of $385\delta_o/U_\infty$. It was observed that, owing to the shock boundary layer interaction, the mean velocity profiles suggested a wake like representation and the turbulent stresses were significantly amplified. The structure parameter was also found to change as a result of the interaction due to the dissimilar amplification factors of the turbulent normal and shear stresses. The in-depth analysis of the results revealed the fact that, in the interaction region, the compressibility effects were not negligible and the relationship between velocity and temperature fluctuations (strong Reynolds analogy) not hold. It was found that the shock oscillation frequency was similar in magnitude to the bursting frequency of the incoming boundary layer.

Studies conducted by Garnier (2000) [66], Stolz et al. (2001) [67], Rizzetta and Visbal (2002) [68] and Garnier et al. (2002) [58] employed filtered methods for the simulation of SWBLI. Garnier (2000) [66] and Garnier et al. (2002) [58] used the mixed-scale subgrid scale model to close the system of filtered equations, which was found to perform well for wall-bounded flows (Lenormand et al. (2000) [78]). A compressible extension of the rescaling-recycling technique (Urbin and Knight (1999) [79]) was used for the generation of the inflow data. The interaction induced by an 8° oblique impinging shock at Mach 2.3 was considered and the results were compared to the experimental findings of Deleuze (1995) [10] and Laurent (1996) [57]. The results obtained were found to be in good agreement with the experiments. The mean and the root-mean-square distribution of velocity and temperature profiles were well reproduced upstream and downstream of the interaction. Also good predictions of the streamwise evolution of surface skin friction, boundary layer thickness, and displacement thickness were evident. However, the study was limited to short time span and was not able to capture the low frequency oscillation of the shock. Stolz et al. (2001) [67] adapted the approximate deconvolution model (ADM) for the LES of compressible wall-bounded flows and was applied to the case of supersonic compression ramp. The simulation parameters adopted were similar to those of the direct simulation of Adams (2000) [51] and the results of LES were compared with the filtered-DNS data. The analysis of the downstream evolution of the mean and turbulent profiles showed a good agreement with the filtered-DNS results, a maximum difference of 15% was observed for the case of longitudinal Reynolds stress. Moreover, it was found that the mean shock position from the LES was found to be comparable to that of the DNS. Rizzetta and Visbal (2002) [68] investigated compression corner interactions for a range of deflection angles (8°, 16°, 20° and 24°) at Mach 3. LESs were performed using the Smagorinsky dynamic subgrid model and the results were compared to the experiments (Settles et al. (1979) [6], Smits and Muck (1987) [8], Dolling and Murphy (1983) [7]). Significant quantitative discrepancies were observed between numerical simulations and experimental measurements. As, a large difference in Reynolds number existed between the two type of studies.

Dubos (2005) [69], investigated the unsteady mechanism in SWBLI through LES, simulations were performed similar to the experimental conditions of Deleuze (1995) [10] and Laurent (1996) [57]. Mean and turbulent quantities were compared and a fairly good agreement between the experiment and LES was reported, however, certain discrepancies were also mentioned (e.g. the indicated values of the correlation coefficient between the velocity and temperature fluctuations in the simulation were found to be inferior to the ones in the experiments). Spectral analysis of the results demonstrated that all the characteristic frequencies greater than 600 Hz were resolved. It was observed that the oscillation of the reflected shock occurred at low frequencies (less than $1K$Hz) which was in agreement with the experiments. In addition, such low frequency oscillations were also found inside the separated region. On the basis of these observations, an hypothesis was proposed that linked the unsteady motion of the reflected shock with the dynamic properties of the separated region.

Two SWBLI configurations (24° compression corner and 12° impinging shock) were studied by Bookey et al. (2005) [70] at Mach 2.9 using DNS and the results were compared to the experimental data of Bookey et al. (2005) [54] at the same low Reynolds number flow conditions. Based on the two-dimensional density correlation contours, a similarity in the structure angle and shape with experiments was observed. Moreover, the compression corner results were also compared with the high Reynolds number experiments of Selig et al. (1989) [9] and similarities in most of the phenomena were observed. Plotted mass flux turbulence intensities, upstream and downstream of the interaction, within the experimental error, showed a good agreement. It was found that the DNS and the experiment have different surface skin friction values upstream and downstream of the interaction, owing to the different Reynolds numbers, but interestingly the sizes of the separation regions were found to be similar, which indicated that the size of the separation region was Reynolds number independent. In compression corner DNS, due to the surface curvature effects, the turbulence structure downstream of the interaction was determined to be three-dimensional in nature (presence of large spanwise structures). In contrast, no three-dimensional structures were observed in the impinging shock case.

Pirozzoli et al. (2005) [71] and Pirozzoli and Grasso (2006) [13] investigated the dynamic features of an 8° impinging shock/turbulent boundary layer interaction at Mach 2.25 using a fully spatial DNS. In order to understand the flow behavior within the interaction region, instantaneous, mean and turbulent fields were analyzed in detail. The flow properties upstream and farther downstream in the relaxation zone were found to have similarities with the incompressible results when density weighted scaling was employed. It was mentioned that the relaxation length of the order of $\mathcal{O}(10)$ boundary layer thicknesses was required for the complete relaxation of the flow. Shedding of the coherent structures near the average separation point was observed. Moreover, convection of these structures along with the flow and their interaction with the foot of the incident shock was also evidenced. On the basis of these observations, an acoustic resonance mechanism was hypothesized, according to which, the interaction of the coherent structures with the incident shock generates the acoustic waves which propagate in the upstream direction and induce an oscillatory motion of the separation bubble and a flapping motion of the reflected shock. The DNS covered a time span of $25\delta_o/U_\infty$.

Loginov et al. (2006) [80] and Loginov (2006) [72] performed a well-resolved LES of SWBLI by employing the ADM approach of subgrid scale modeling. A detailed study of the instantaneous and the averaged flow structure over a 25° supersonic compression ramp at Mach 2.95 was made and the results were compared with Zheltovodov et al. (1990) [81]. Notably, a good agreement was achieved for the surface-pressure and skin-friction distributions, the mean velocity profiles, the mass-flow, the density and velocity fluctuations and the wall-pressure-fluctuation distributions. The probability density function (*pdf*) analysis of the pressure fluctuations showed a double-peaked *pdf* within the interaction region, attributed to the highly intermittent motion of the shock, and which was in accordance with the experimental observation of Dolling and Murphy (1983) [7]. Along with the direct shock-turbulence amplification, other mechanisms responsible for the turbulence amplification (e.g. downstream traveling shocklets) were also discussed. The existence of streamwise Görtler-type vortices was also evidenced.

A more comprehensive DNS study of the 24° compression corner interaction at Mach 2.9 was performed by Wu and Martin (2007,2008) ([14],[55]) and the results were compared with the experiments of Bookey et al. (2005) [54] at the same flow conditions. The properties of

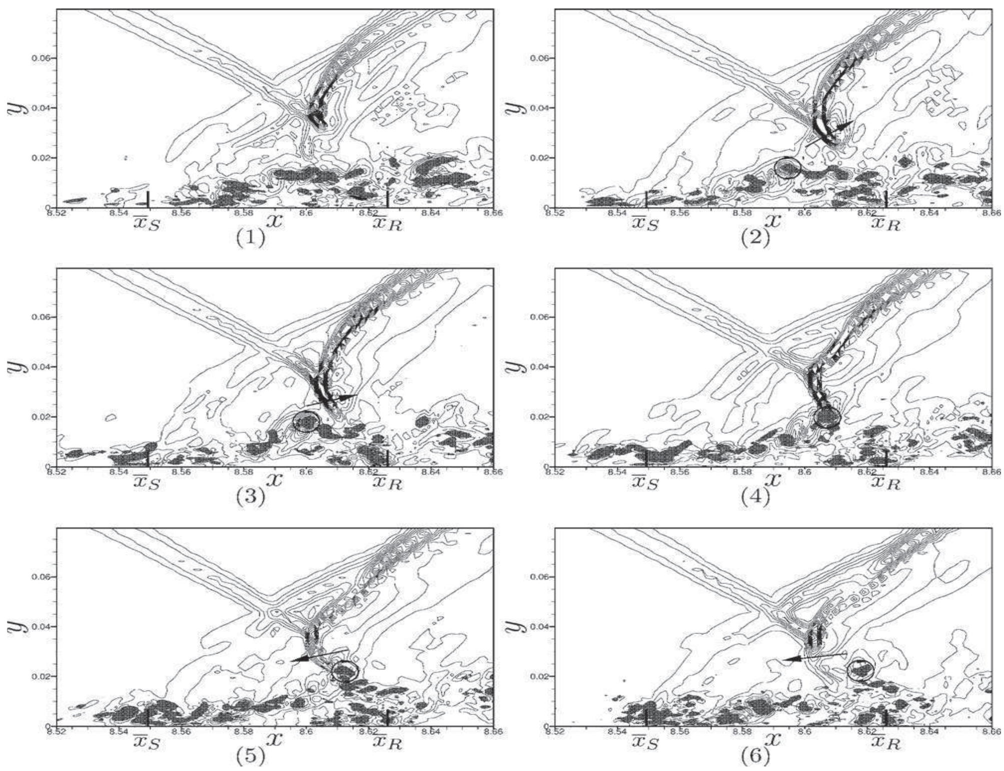

Figure II.13 – From (1) to (6), demonstrate the instantaneous time evolution of the flow, in terms of the isocontours of pressure gradient modulus along with the vortical structures (gray patches) identified on the basis of positive discriminant of velocity gradient tensor. The arrow indicates the instantaneous direction of incident shock foot motion, while the circle tracks the evolution of a specific vortex. From Pirozzoli and Grasso (2006) [13]

the upstream boundary layer, the mean wall-pressure distribution, the size of the separation bubble, the velocity profile downstream of the interaction and the amplification of the mass-flux turbulence intensity were well predicted by DNS within the experimental uncertainty. The Reynolds stress components were greatly amplified due to the interaction with the uneven amplification factors of about $6-24$. The strong Reynolds Analogy was found to be invalid within the neighborhood of the interaction region (Fig. II.14). The three-dimensional structure of the interaction system was also discussed and a spectral analysis of the wall-pressure and the mass-flux signals revealed that the unsteady motion of the shock was of low frequency and had a characteristic frequency scale of about $0.007-0.013U_\infty/\delta_o$, which was in agreement with the experimental findings. Moreover, low-amplitude high frequency spanwise wrinkling of the shock was also observed. The detailed analysis of the correlations between the mean separation point, the reattachment point and the shock location demonstrated that the low-frequency motion of the shock was influenced by the downstream flow. An extension of the present work for the case of a 12° impinging oblique shock interaction was documented in Priebe et al. (2009) [15]. The effect of highly three-dimensional nature of the flow in experiments compared to that of the considered spanwise homogeneity in DNS was also discussed and it was found, in DNS, that the three-dimensional effects were limited to the spanwise wrinkling of the reflected shock (Fig. II.15). The Reynolds stresses were found to be relatively less amplified in the present case compared to the compression corner study and the streamwise curvature in the compression corner case was assumed to be the responsible factor. The unsteady motion of the shock was found to occur in the frequency range of $0.002 - 0.006U_\infty/\delta_o$.

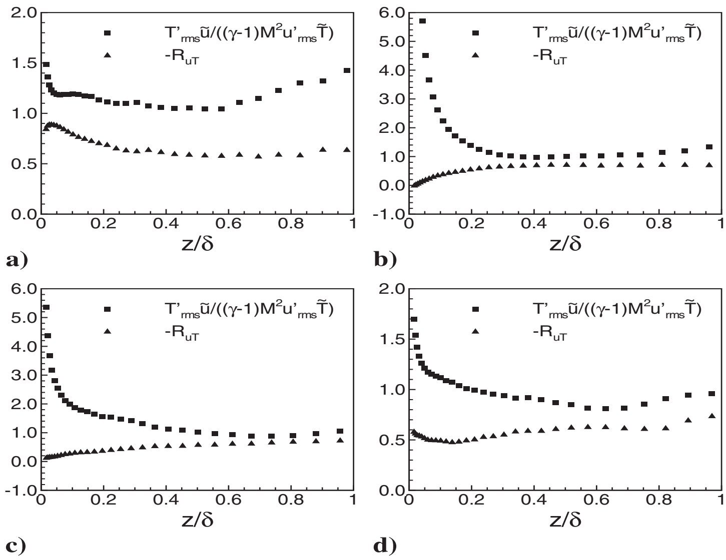

Figure II.14 – Wall-normal variation of two Strong Reynold Analogy(SRA) relations, upstream of the interaction(a), and their variation along the interaction region($b-d$). From Wu and Martin (2007) [14]

Touber and Sandham (2009) [60] performed the large eddy simulation of an 8° oblique impinging shock interaction with a turbulent boundary layer at Mach 2.3, for very long integration times and it was indicated that the low frequency energetic component of the unsteady shock($St = fL_{sep}/U_\infty \approx 0.03$) was found to be in excellent agreement with the experiments. For the generation of inflow turbulent conditions the digital filter approach was used and it was claimed that this didn't introduce any energetically significant low frequencies into the domain which could possibly intervene with the oscillation of the shock system. The behavior of the flow upstream and downstream of the interaction was compared with the PIV measurements of

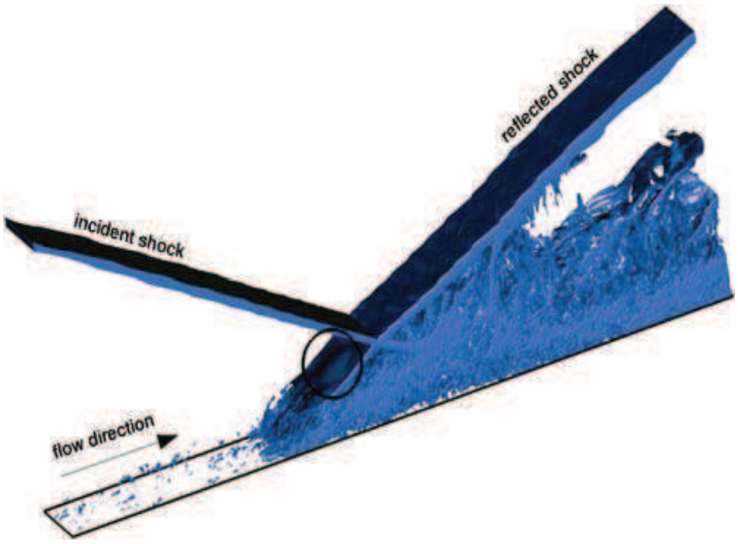

Figure II.15 – Isosurfaces of the magnitude of pressure gradient, showing the three-dimensional structure of SWBLI. From Priebe et al. (2009) [15]

Dupont et al. (2006) [12] and satisfactory agreement was observed. Moreover, a linear stability analysis of the mean flow was made and a 2D most unstable global mode was detected, contrary to the findings of Robinet (2007) [82] where a 3D global mode was found to be most unstable in the case of laminar interaction. A phase link was observed between the wall-pressure fluctuations and the structure of the global mode, that was conjectured to be the driving mechanism for the low-frequency oscillation. Based on the database obtained an analytical model was proposed by Touber and Sandham (2011) [83] that could model the low-frequency motion of the reflected shock.

Large-eddy simulations performed by Hadjadj et al. (2010) [73] and Morgan et al. (2010)[74] investigated the 8° impinging oblique shock interaction case. Hadjadj et al. (2010)[73] used the digital filter approach. Aside from a verification of the mean and turbulent quantities with the experiments (Deleuze (1995) [10], Laurent (1996) [57], Dupont et al. (2003) [84]), the emphasis was placed on the ability of LES to capture the low-frequency motion of the shock. The computed frequencies were found to be in excellent agreement with the experiment and, based on the frequency analysis, a dynamically coupled shock/separation bubble system was hypothesized. For prescribing the turbulent inflow conditions, an improved rescaling-recycling technique, that was termed "Rescaling-Recycling with Reflection" was used by Morgan et al. (2010) [74]. It was mentioned that the non-physical tones, associated with the standard rescaling-recycling technique, were effectively eliminated by the new improved method. The results were compared with the PIV measurements of Humble et al. (2007) [85]. Along with the mean and turbulent flow organization, the instantaneous structure of the shock motion was investigated. A streamwise flapping behavior of the shock was found and was responsible for the spanwise undulant motion of the shock.

II.3.3 Synopsis

In an attempt to briefly summarize the results from the aforementioned studies, some general conclusions about SWBLI can be surmised. The presence of a shock induces significant density and pressure gradients into the flow, and as a consequence the flow properties are altered substantially. It has been found that the characteristics of these interactions are dependent on the factors that include Mach number ([4], [54], [64]), shock strength ([4], [6], [47], [8], [49], [48], [54], [62], [63], [64], [68], [70]), flow geometry ([4], [61], [54], [70], [55], [15]), incoming flow ([4]), thickness of boundary layer ([7]) and the wall thermal boundary conditions ([56], [10], [57]). Depending on these parameters, the resultant interaction fields are either attached, incipiently or fully separated and therefore exhibit different flow dynamics.

Shock/boundary layer interactions generally introduce flow alterations that include:

- Significant alteration of instantaneous and mean flow variables(e.g; see [6], [49], [16], [63]).
- Anisotropic amplification of turbulent statistics across the interaction region(e.g; see [10], [51], [55], [15])
- Generation of three-dimensional structures, even if the flow upstream of the interaction was two-dimensional (in the mean)(e.g; see [6], [63], [15])
- Presence of unsteady pressure and thermal loads due to shock unsteadiness (e.g; [7], [50], [53], [63], [60]).

The shock unsteadiness just noted is an important issue that has been studied extensively. It has been concluded that this unsteady motion of the shock is characterized by relatively low-order frequencies compared to frequencies associated with the incoming boundary layer. However, no general consensus has been reached on the source of the unsteadiness of the shock. Some authors have associated it with the upstream boundary layer ([48], [50], [51], [11], [53]), while others have associated it with the flow characteristics downstream of the interaction (separation region) ([57], [62], [69], [55], [63]).

Chapter III

Numerical Methodology

III.1 Navier-Stokes Equations

The equations solved in the direct numerical simulation are the nondimensional compressible Navier-Stokes equations comprising the density ρ, momentum $\rho u_j = (\rho u, \rho v, \rho w)$, and total energy ρE conservation equations, and coupled with the equation of state for a perfect gas, $p = \rho T$. The conservation equations are given by

$$\frac{\partial \rho}{\partial t} + \frac{\partial}{\partial x_j}(\rho u_j) = 0 \tag{III.1}$$

$$\frac{\partial(\rho u_i)}{\partial t} + \frac{\partial(u_i \rho u_j)}{\partial x_j} = -\frac{\partial p}{\partial x_i} + \frac{M_\infty \sqrt{\gamma}}{Re_\infty}\frac{\partial \sigma_{ij}}{\partial x_j} \tag{III.2}$$

$$\frac{\partial(\rho E)}{\partial t} + \frac{\partial(u_j \rho H)}{\partial x_j} = \frac{M_\infty \sqrt{\gamma}}{Re_\infty}\left\{\frac{\partial}{\partial x_j}\left[u_i \sigma_{ij} - \left(\frac{\gamma}{\gamma - 1}\right) q_j\right]\right\} \ , \tag{III.3}$$

where the viscous stress σ_{ij}, total energy and enthalpy H (total temperature, T_t), and heat flux q_j are given by

$$\sigma_{ij} = 2\mu\left(S_{ij} - \frac{\delta_{ij}}{3}S_{kk}\right), \qquad S_{ij} = \frac{1}{2}\left(\frac{\partial u_i}{\partial x_j} + \frac{\partial u_j}{\partial x_i}\right) \tag{III.4a}$$

$$E = \frac{T}{\gamma - 1} + \frac{u_i u_i}{2}, \qquad H = \frac{\gamma}{\gamma - 1}T_t = \frac{\gamma T}{\gamma - 1} + \frac{u_i u_i}{2} \tag{III.4b}$$

$$q_j = -\frac{\mu}{Pr}\frac{\partial T}{\partial x_j} \ . \tag{III.4c}$$

The nondimensional scaling is based on a characteristic length and velocity scale, where the velocity scale is given by the freestream speed of sound, c_∞, divided by $\sqrt{\gamma}$ ($\gamma = 1.4$ is the constant ratio of specific heats for a perfect gas), and the freestream thermodynamic variables. The Mach number M_∞ and the Reynolds number Re_∞ are based on the freestream values, with $M_\infty = 2.25$, a freestream unit Reynolds number of 25×10^6.

III.2 Spatial Discretization and Time Integration

Numerical algorithms based on finite-difference and finite-volume schemes, utilize interpolation procedures for approximating the solution of differential equations on a discrete set of known data points. Classical finite-difference schemes that adopt fixed stencil interpolations, work well for globally smooth problems; however, these schemes suffer from Gibbs phenomenon (spurious oscillations, often lead to numerical instabilities) near discontinuities. Before the introduction of higher-order non-oscillatory schemes, there were two methods employed for the elimination or diminution of these spurious oscillations. The first was based on the addition of artificial viscosity in the flow regions where significant variations in properties were observed, and the second was the use of limiters that were characterized by the total variation diminishing (TVD) property and were capable of diminishing/suppressing the oscillations by reducing the order of accuracy of the interpolation near discontinuities. The artificial viscosity approach was marred by the fact that one had to adjust the magnitude level of the artificial viscosity for every problem, making this a cumbersome, problem dependent approach. The reduction to the first order accuracy near discontinuities was considered to be the drawback of TVD limiter schemes (Shu [86]). To compensate for these drawbacks, the idea of essentially non-oscillatory (ENO) schemes was proposed by Harten et al. [87]. These schemes are based on the use of a nonlinear adaptive procedure to select the locally smooth stencil from a given set of candidate stencils (the number of candidate stencils being dependent on the required order of accuracy of the scheme), and the selection procedure is designed to avoid any interpolation across the discontinuities and thus limit the generation of spurious numerical oscillations near the discontinuities. Weighted essentially non-oscillatory (WENO) schemes are constructed on the basis of ENO schemes (Liu et al. [88]), where a convex combination of all the candidate stencils of ENO schemes is used to get the optimal order of accuracy in smooth regions while it remains ENO-order accurate near the discontinuities. Based on their ability to efficiently handle the problems containing discontinuities, like shock, these schemes (ENO and WENO) and their variants are widely employed in the numerical simulations of compressible flows.

In the present study, a mixed weighted-ENO compact-difference numerical algorithm is used for the discretization of the three-dimensional Navier-Stokes equations. The inviscid flux function uses a seventh-order weighted-ENO reconstruction of the characteristic inviscid fluxes. The viscous derivative and flux function are determined using a fourth-order compact difference scheme, and the integration in time is performed by means of the four-step fourth-order Runge-Kutta algorithm.

III.2.1 WENO Reconstruction Procedure

The WENO reconstruction procedure for the case of the three dimensional system of Euler equations is explained in this subsection. At the start the details about the standard ENO reconstruction procedure are given and then the extension to the WENO schemes are presented.

One can write the system of Euler equations (the inviscid component of Navier-Stokes equations, Equations (III.1) to (III.3)) in the following form:

$$\frac{\partial \mathbf{U}}{\partial t} + \frac{\partial \mathbf{F_e}}{\partial x} + \frac{\partial \mathbf{G_e}}{\partial y} + \frac{\partial \mathbf{H_e}}{\partial z} = 0 \tag{III.5}$$

Here, $\mathbf{U}$ represents the vector of conservative variables, and $\mathbf{F_e}$, $\mathbf{G_e}$ and $\mathbf{H_e}$ are the vectors of inviscid fluxes in the three-dimensional space and are given as

$$\mathbf{U} = \begin{pmatrix} \rho \\ \rho u \\ \rho v \\ \rho w \\ \rho E \end{pmatrix} \quad \mathbf{F_e} = \begin{pmatrix} \rho u \\ \rho u^2 + P \\ \rho uv \\ \rho uw \\ \rho uH \end{pmatrix} \quad \mathbf{G_e} = \begin{pmatrix} \rho v \\ \rho uv \\ \rho v^2 + P \\ \rho vw \\ \rho vH \end{pmatrix} \quad \mathbf{H_e} = \begin{pmatrix} \rho w \\ \rho uw \\ \rho vw \\ \rho w^2 + P \\ \rho wH \end{pmatrix}$$

The temporal update of conserved variables is dependent on the sum of the discretized spatial derivatives of the fluxes in each space direction (for simplicity here, only the flux reconstruction procedure in the x-direction is described, with the fluxes in the other directions approximated in the same way). This is considered to be the big advantage of employing finite-difference methods since the reconstruction format remains similar for one or several directions. Let $L(\mathbf{U}_i)$ be the higher-order discrete representation of the flux derivative $\partial \mathbf{F_e}/\partial x_i$ at the node coordinates x_i, where i varies from 1 to N, and at these nodes the numerical fluxes are estimated from the difference of flux values $\hat{\mathbf{F}}_{i+1/2}$ and $\hat{\mathbf{F}}_{i-1/2}$ at the cell boundaries $x_{i+1/2}$ and $x_{i-1/2}$ respectively,

$$L(\mathbf{U}_i) = -\frac{1}{\Delta x}(\hat{\mathbf{F}}_{i+\frac{1}{2}} - \hat{\mathbf{F}}_{i-\frac{1}{2}}) \tag{III.6}$$

The hyperbolic nature of the system of Euler equations is implied by the fact that the Jacobian matrices, $\boldsymbol{J}_d$ ($\partial\mathbf{F_e}/\partial\mathbf{U}$, $\partial\mathbf{G_e}/\partial\mathbf{U}$, $\partial\mathbf{H_e}/\partial\mathbf{U}$), are diagonalizable and satisfy the following property

$$\boldsymbol{L}_d\boldsymbol{J}_d\boldsymbol{R}_d = \boldsymbol{\Lambda}_d \tag{III.7}$$

where $\boldsymbol{L}_d$ and $\boldsymbol{R}_d$ ($1 \le d \le 3$ is the space direction index) are the $m \times m$ dimensional basis of left and right eigenvectors respectively, and $\boldsymbol{\Lambda}_d$ is a diagonal matrix containing the real eigenvalues of the Jacobian. The reconstruction algorithm to calculate the numerical fluxes at the cell boundaries using the ENO/WENO scheme is comprised of the following steps:

- Projection to the characteristic space
- Lax-Friedrich type flux splitting
- ENO/WENO interpolation
- Reverse projection

The left eigenvector matrices ($\boldsymbol{L}_d$) are used to transform all the conservative variables and inviscid fluxes in the physical space to the characteristic space. In the present study, the local Lax-Friedrich flux splitting approach has been used and the numerical flux function in terms of projected fluxes in the characteristic space is determined as

$$\mathbf{f}^{+}_{s;i+\frac{1}{2}} = \frac{1}{2}\boldsymbol{L}_{s,i+\frac{1}{2}}(\mathbf{F}_i + \hat{\lambda}_s\mathbf{U}_i) \tag{III.8a}$$

$$\mathbf{f}^{-}_{s;i+\frac{1}{2}} = \frac{1}{2}\boldsymbol{L}_{s,i+\frac{1}{2}}(\mathbf{F}_{i+1} - \hat{\lambda}_s\mathbf{U}_{i+1}), \tag{III.8b}$$

where

$$\hat{\lambda}_s = \max(|\lambda_{s,i}|, |\lambda_{s,i+1}|).$$

Here $\mathbf{f}^{+}_{s;i+1/2}$ and $\mathbf{f}^{-}_{s;i+1/2}$ are the flux components that are evaluated for each characteristic field s. On the basis of these low-order numerical fluxes, the higher-order numerical fluxes are formed by the ENO or WENO interpolation procedure in each characteristic field. It is important to note that the estimated values of the flux components are very much dependent on the form of low-order numerical flux that has been used as a building block for estimating the higher-order ENO or WENO flux, and also on the order of accuracy of the interpolation procedure. The intermediate states to calculate the left and right eigenvectors at the zone boundary $x_{i+1/2}$ are provided by the linearized Riemann solver of Roe, with $\mathbf{V}_i$ and $\mathbf{V}_{i+1}$ as left and right states, respectively (where $\mathbf{V}$ represents the vector of primitive variables, $\mathbf{V} = [\rho, u, v, w, H]$). The details of the Roe averaging formulation to compute the primitive variables at the boundaries, the left and right eigenvectors matrices in all space dimensions and the diagonal matrix for eigenvalues are provided in Appendix A.1. Finally, the flux in physical space is obtained by right multiplying the numerical flux obtained in the local characteristic fields with the matrix of right eigenvectors (reverse projection). The reconstructed higher-order numerical flux at the zone boundary $x_{i+1/2}$ in the physical space is given by

$$\hat{\mathbf{F}}_{i+\frac{1}{2}} = \sum_{s=1}^{m} (\mathbf{f}^{+}_{s;i+\frac{1}{2}} + \mathbf{f}^{-}_{s;i+\frac{1}{2}}) \boldsymbol{R}_{s;i+\frac{1}{2}}. \tag{III.9}$$

The schemes developed on the basis of flux splitting of monotone low-order fluxes are usually more robust than the ones that are constructed based on the Roe scheme. This type of decomposition guarantees that the $\partial \mathbf{f}^{+}/\partial \mathbf{U}$ possess positive eigenvalues and $\partial \mathbf{f}^{-}/\partial \mathbf{U}$ possess the negative eigenvalues. However, this procedure is computationally expensive as the ENO reconstruction procedure is executed twice for estimating the $\mathbf{f}^{+}_{s;i+1/2}$ and $\mathbf{f}^{+}_{s;i-1/2}$, one time for each.

For weighted essentially non-oscillatory schemes r candidate stencils are used to evaluate $\mathbf{f}^{+}_{s;i+1/2}$. Each of these stencils provide an r^{th}-order accurate interpolation function at the boundaries of the zone that has x_i as its zone center. Stencils are denoted by $S_{i;k}$

$$S_{i;k} = (x_{i+k-r+1}, x_{i+k-r+2}, ..., x_{i+k})$$

where k varies from 0 to $r-1$. For the r^{th}-order accurate interpolation of $\mathbf{f}^{+}_{s;i+1/2}$, it is necessary to evaluate the values of the flux components given by

$$\{\mathbf{f}^{+}_{i+k-r+1;i+\frac{1}{2}}, \mathbf{f}^{+}_{i+k-r+2;i+\frac{1}{2}}, ..., \mathbf{f}^{+}_{i+k;i+\frac{1}{2}}\}$$

The r^{th}-order accurate value that can be obtained by the reconstruction using the k^{th} stencil $S_{i;k}$ is given by the linear combination of the flux components.

$$q^{+r}_{s;i;k}(\mathbf{f}^{+}_{i+k-r+1;i+\frac{1}{2}}, \mathbf{f}^{+}_{i+k-r+2;i+\frac{1}{2}}, ..., \mathbf{f}^{+}_{i+k;i+\frac{1}{2}}) = \sum_{j=1}^{r} a^{r}_{k;j} \mathbf{f}^{+}_{i+k-r+1;i+\frac{1}{2}} \tag{III.10}$$

where $a^{r}_{k;j}$ are constant coefficients. Each of the stencils $S_{i;k}$ has a smooth solution of order r, so that by making a convex combination of the interpolated values obtained by each of these r stencils, $(2r-1)^{th}$-order accurate evaluation of interpolated flux components at the boundary

$x_{i+1/2}$ or $x_{i-1/2}$ can be obtained. The convex combination is given by

$$\mathbf{f}^{+}_{s;i+\frac{1}{2}} = \sum_{k=0}^{r-1} C^r_k q^{+r}_{s;i;k}(\mathbf{f}^{+}_{i+k-r+1;i+\frac{1}{2}}, \mathbf{f}^{+}_{i+k-r+2;i+\frac{1}{2}}, \ldots, \mathbf{f}^{+}_{i+k;i+\frac{1}{2}}) \tag{III.11}$$

where C^r_k are the linear optimal weights. As an example, the candidate stencil diagram for the seventh order $(r = 4)$ accurate WENO reconstruction is presented in Fig. III.1.

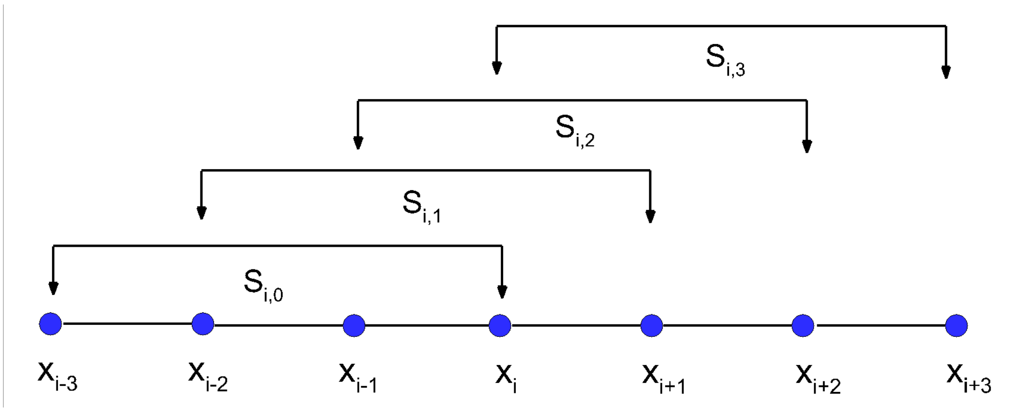

Figure III.1 – Candidate stencil diagram for seventh-order WENO reconstruction

When the solution is adequately smooth, the maximum $(2r-1)^{th}$-order of accuracy is obtained. If this is not the case i.e. the solution has discontinuities, smoothness estimators (IS^r_k) are used, that automatically choose the most smooth stencil out of the r possible ones. Then,

$$\mathbf{f}^{+}_{s;i+\frac{1}{2}} = \sum_{k=0}^{r-1} w^r_k q^{+r}_{s;i;k}(\mathbf{f}^{+}_{i+k-r+1;i+\frac{1}{2}}, \mathbf{f}^{+}_{i+k-r+2;i+\frac{1}{2}}, \ldots, \mathbf{f}^{+}_{i+k;i+\frac{1}{2}}) \tag{III.12}$$

where the coefficients w^r_k depend on the smoothness measures (IS^r_k).
The actual construction of weights is given by

$$w^r_k = \frac{\alpha^r_k}{\alpha^r_0 + \ldots + \alpha^r_{r-1}}, \tag{III.13}$$

where

$$\alpha^r_k = \frac{C^r_k}{(\epsilon + IS^r_k)^p}, \tag{III.14}$$

with $\epsilon = 10^{-15}$ to avoid division by zero and $p = 2$.

The constants $a^r_{k;i}$, the optimal weights C^r_k and the formulations for the estimation of smoothness estimators (IS^r_k) are provided in the table A.1, table A.2 table A.3 (see Appendix VIII) respectively.

III.2.2 Compact Scheme

The classical Padé, or compact finite-difference schemes, are used in the direct numerical simulations for the evaluation of viscous fluxes. An explanation of the higher-order compact schemes and their application to the evaluation of first- and higher-order derivatives, and filtering and interpolation methods is detailed in Lele [89]. In comparison to the traditional finite-difference approximations, these schemes have resolution characteristics similar to that of spectral methods and are also characterized by very low numerical dissipation. As an example fourth-order approximation of the first-order derivative is presented in the following paragraph.

Consider a one-dimensional mesh with node coordinates x_i, where $1 \leq i \leq N$ is again the node index, and a function f with given values f_i at these nodes (here, a compact scheme on the uniform mesh with equal mesh spacing, $h = x_i - x_{i-1}$, is defined while for its extension for non-uniform meshes a Jacobian transformation is used). A fourth-order tridiagonal approximation of the first order derivative ($(df/dx)_{x_i}$ or f_i') at x_i is written as

$$\frac{1}{4}f'_{i-1} + f'_i + \frac{1}{4}f'_{i+1} = \frac{14}{9}\frac{f_{i+1}-f_{i-1}}{2h} + \frac{1}{9}\frac{f_{i+2}-f_{i-2}}{4h}. \tag{III.15}$$

For non-periodic boundary conditions, biased boundary closures are used at the points close to the boundaries, i.e. at nodes 1, 2, $N-1$ and N. Fourth- and third-order compact relations are used at nodes 2 and $N-1$ and at nodes 1 and N, respectively. In practice, the boundary formulation at nodes 1 and 2 for the first-order derivative is given by

$$i = 1, \qquad f'_1 + 2f'_2 = \frac{1}{h}\left(-\frac{5}{2}f_1 + 2f_2 + \frac{1}{2}f_3\right) \tag{III.16a}$$

$$i = 2, \qquad \frac{1}{4}f'_1 + f'_2 + \frac{1}{4}f'_3 = \frac{3}{4h}\left(f_3 - f_1\right), \tag{III.16b}$$

with similar relations at nodes $N-1$ and N.

III.2.3 Temporal Integration

For the advancement of the solution in temporal space, a four-step fourth-order Runge-Kutta Algorithm is used, which is expressed as

$$\begin{aligned}
\mathbf{U}^{(1)} &= \mathbf{U}^{n} + \frac{1}{2}\Delta t L\left(\mathbf{U}^{n}\right) \\
\mathbf{U}^{(2)} &= \mathbf{U}^{n} + \frac{1}{2}\Delta t L\left(\mathbf{U}^{(1)}\right) \\
\mathbf{U}^{(3)} &= \mathbf{U}^{n} + \Delta t L\left(\mathbf{U}^{(2)}\right) \\
\mathbf{U}^{(4)} &= \mathbf{U}^{n} + \Delta t L\left(\mathbf{U}^{(3)}\right) \\
\mathbf{U}^{n+1} &= -\frac{\mathbf{U}^{n}}{2} + \frac{1}{3}\left[\mathbf{U}^{(1)} + 2U^{(2)} + \mathbf{U}^{(3)}\right] + \frac{1}{6}\mathbf{U}^{(4)}
\end{aligned} \tag{III.17}$$

where $\mathbf{U}^{n}$ and $\mathbf{U}^{n+1}$ are solutions at successive time steps and $\mathbf{U}^{(1)}$, $\mathbf{U}^{(2)}$, $\mathbf{U}^{(3)}$ and $\mathbf{U}^{(4)}$ are the intermediate outcomes from four steps of the Runge-Kutta algorithm.

III.2.4 Grid and Computational Domain

The computational domain in the streamwise direction is partitioned into three zones: laminar-transition zone ($N_{x1} = 596$), turbulent zone ($N_{x2} = 1900$), and buffer (sponge) zone ($N_{x3} = 154$). The grid spacing in the laminar-transition zone is relatively coarser than that in developing turbulence regime while in the buffer zone the grid is progressively coarsened to dampen out any numerical oscillations.

The grid spacing in the wall-normal direction through the boundary layer is variable and is based on a geometric stretching algorithm given by $y_j = y_{j-1} + \Delta y_w r^{j-2}$, where $\Delta y_w = y_2 - y_1$ ($y_1 = y_w = 0$ for this study) is set so that $\Delta y_w^+ \simeq 1$ and r is the stretching parameter whose value is slightly greater than 1 ($r \simeq 1.053$, $y_w = 2.675e-06\ m$). For the isothermal case, the grid stretching ratio in the wall-normal direction is greater than the ratio for the adiabatic case ($r \simeq 1.055$, $y_w = 2.032e-06\ m$), since numerical validation tests found that the grid had to be more refined for the isothermal case near the wall. Here it is important to mention that the simulations reported in Chapter IV are simulated using two different grid stretching parameters. In the first place, the results for the no-shock adiabatic and isothermal simulations are compared on the basis of nearly same Δy_w^+ ($\simeq 1$); however, in order to avoid any sort of possible discrepancy due to different stretching parameters, the simulations of turbulent boundary layer with shocks used only one stretching parameter ($r \simeq 1.055$, $y_w = 2.032e-06$

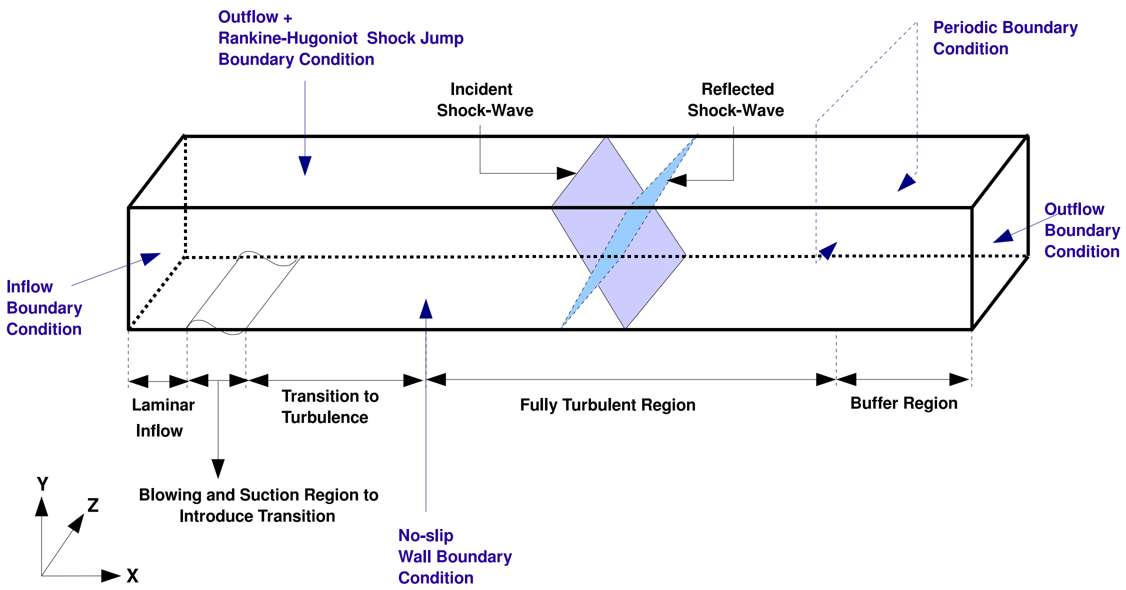

Figure III.2 – The schematic of the computational domain

m). A possible question that can arise either is whether this change can produce any difference in results between two different adiabatic simulations. In a statistical comparison, no change in results was found between the ones obtained upstream of the shock-system (see chapter V, location P01) and the ones obtained for the no-shock adiabatic simulation (see chapter IV). For the spanwise direction, the grid spacing is uniform.

III.2.5 Boundary Conditions

The boundary conditions used in the present set of simulations are indicated in the sketch of the computational domain (Fig. III.2) and are detailed as:

- Inflow boundary (left) : A laminar compressible boundary layer similarity solution (White (1991) [90]) is imposed.

- Outflow boundary (right): A first-order accurate extrapolation condition is imposed on all the primitive variables at the outflow boundary. Along with this, a buffer region (progressively stretch grid) is introduced in the streamwise direction to avoid any reflections of disturbances that may generate during the treatment of outflow boundary conditions.

- Wall boundary (bottom): For the adiabatic case, the simulations were performed with the Neumann boundary condition of no heat flux at the wall, $q_w = 0$, while for the isothermal case, a constant temperature condition is imposed. A boundary layer assumption of $\partial p/\partial y \approx 0$ is used for the pressure, while for the velocity components a no-slip(zero velocity) condition is applied. In order to induce laminar to turbulent transition, a wall-normal velocity blowing and suction function that extended a short (finite) length ($x_a \leq x \leq x_b$) along the wall in the streamwise direction, and spanned the entire length in the spanwise direction, Fig. III.2, is introduced (similar to Rai (1995) [91], Pirozzoli et al. (2004) [92]). Where the normal velocity component is computed as

$$v(x,z,t) = Au_\infty f(x)g(z)h(t) \tag{III.18}$$

with

$$f(x) = 4\sin\theta(1-\cos\theta)/\sqrt{27},$$

$$\theta = 2\pi(x-x_a)/(x_b-x_a),$$

$$g(z) = \sum_{l=1}^{l_{max}} Z_l \sin(2\pi l(z/L_z+\phi_l)),$$

$$\sum_{l=1}^{l_{max}} Z_l = 1, \qquad Z_l = 1.25 Z_{l+1},$$

$$h(t) = \sum_{m=1}^{m_{max}} T_m \sin(m(\beta t + 2\pi\phi_m)),$$

$$\sum_{m=1}^{m_{max}} T_m = 1, \qquad T_m = 1.25 T_{m+1}$$

with $l_{max} = 10$, $m_{max} = 5$, x_a and x_b the streamwise locations of the beginning and end of the blowing/suction strip, respectively, A is the amplitude of the imposed disturbance (0.04), β is the fundamental temporal frequency of disturbance (75000rad/s), ϕ_l and ϕ_m are random numbers ranging between 0.0 and 1.0, and, l_z is the dimension of the computational region in the spanwise direction.

- Outflow and Rankine-Hugoniot shock jump boundary conditions (top): The top boundary contained two types of boundary conditions, over the whole length of the computational domain a outflow boundary condition is employed except in the region where a thin streamwise slot is used to introduce the incident shock from the top boundary of the computational domain. The corresponding shock jump conditions are derived from the Rankine-Hugoniot oblique shock relations.

- Periodic boundaries (front and back): Periodic boundary conditions are employed in the spanwise direction. The size of the computational domain in the spanwise direction is determined based on the analysis of two-point correlations of velocity component and the size has been chosen such that the normalized two-point correlation values are sufficiently small at the tails of the correlation curve (see Fig. IV.3).

Chapter IV

Statistical Characteristics of a Supersonic Turbulent Boundary Layer

IV.1 Introduction

In this chapter, the statistical characteristics of compressible turbulent boundary layers at a freestream Mach number of 2.25 are analyzed. An investigation of this kind is essential to the understanding of fluid dynamic and thermodynamic properties of the turbulent boundary layer and also a prerequisite to establish a foundation for the understanding of the effects of the shock interaction that will be described in later chapters (see chapter V and chapter VI). A thorough analysis and validation of the results is presented and it is shown that the main turbulent statistics of compressible boundary layer at zero pressure gradient exhibit close similarities to incompressible boundary layers when variable density normalization is applied to the compressible results.

Results for two different wall boundary conditions, adiabatic and isothermal cold wall ($T_w/T_{aw} = 0.67$), are reported here and it is discussed that a semi-local type scaling (defined later in the chapter) is quite effective in collapsing the profiles of turbulent stresses for two different wall thermal conditions. A change of wall temperature in a supersonic boundary layer flow can have a significant impact on the behavior of both the velocity and thermal field statistics; however, such boundary layer flow fields have not been extensively investigated through either direct or large eddy simulations. Recent simulation studies involving isothermal wall conditions have focused on channel flow simulations (Tamano and Morinishi [93], Morinishi et al. [94]) and have extended earlier DNS channel flow simulations (Coleman et al. [95], Huang et al. [96]). In addition, previous DNS studies of supersonic boundary layer flows (Guarini et al. [97], Maeder et al. [98], Pirozzoli et al. [92], Pirozzoli et al. [71], Martin [99], Shahab et al. [100]) have focused on adiabatic wall conditions. The study reported here is intended to augment this existing boundary layer database by performing a direct numerical simulation of a developing turbulent boundary layer with an isothermal wall condition of $T_w < T_{aw}$. Results from the simulation studies of Tamano and Morinishi [93] for compressible channel flow and Morinishi et al. [101] for incompressible channel flow suggest that the change of wall temperature conditions can have an effect on the dynamic balance of both the velocity and thermal fields.

IV.2 Problem Definition

For the adiabatic case, the simulations were performed with the (Neumann) condition of no heat flux at the wall $q_w = 0$. The freestream temperature was $T^*_\infty = 170$K (* quantities are dimensional) and the corresponding (recovery) temperature at the wall was $T^*_w = 323$K which varied little along the plate. This corresponded to a recovery factor of $r \approx 0.89$ with is consistent with the value obtained from $r = Pr^{1/3}$ with $Pr = 0.72$. The friction Mach number M_τ ($= u_\tau/c_w$, with $c_w = \sqrt{\gamma T_w}$ and $u_\tau = \sqrt{\tau_w/\rho_w}$) was 0.076. For the isothermal (cold) wall case, the freestream temperature was once again 170K and the wall temperature was set at $T^*_w = 230$K which corresponded to a wall temperature ratio $T^*_w/T^*_{aw} = 0.67$, with $T^*_{aw} = T^*_\infty[1 + (\gamma + 1)M^2_\infty/2]$; whereas, the wall temperature ratio based on the recovery temperature $T^*_r (= T^*_\infty[1 + r(\gamma+1)M^2_\infty/2])$ =323K was 0.71. Finally, for the isothermal case the heat flux parameter, $B_q = q_w/\rho_w u_\tau T_w$, is -0.017 with friction temperature $-B_q T_w = 0.023$, and a friction Mach number of 0.079. A summary of the parameters for each case are given in Table IV.1a.

The details about the grid generation have already been discussed in section III.2.4 (see chapter III); however, the grid spacings, in terms of wall units, in the turbulent zone in the streamwise, wall-normal and spanwise direction for both adiabatic and isothermal simulations are given in Table IV.1b. The location along the plate (x-direction) where the statistics were obtained for the adiabatic case corresponded to $Re_x = 5.4 \times 10^6$ while for the isothermal case it was at $Re_x = 5.34 \times 10^6$. At this station, the momentum thickness Reynolds number, Re_θ (based on freestream values), was 3706 for the adiabatic case and 3798 for the isothermal case. These locations were selected so that nearly equivalent momentum thickness Reynolds numbers (Re_θ) at these locations would provide the basis for comparison between adiabatic and isothermal cases.

The Reynolds averages[1] (and subsequent density-weighted or Favre variables) were obtained through a combination of spatial averaging in the (homogeneous) spanwise direction

[1]The Reynolds averaged quantities are designated by an overbar, $\overline{}$, and the density-weighted, or Favre, averages are designated by $\widetilde{}$, and are defined for a variable f by $\overline{\rho f}/\overline{\rho}$.

Table IV.1 – Parameter specification: (a) Physical parameters; (b) Numerical parameters.

(a) Physical parameters

Wall Condition	M_∞	$Re_\infty/m.$	Re_θ	H	T_∞	B_q	M_τ	T_w
Adiabatic	2.25	25×10^6	3706	3.40	170K	0.0	0.076	323K
Isothermal	2.25	25×10^6	3798	2.65	170K	-0.017	0.079	230K

(b) Numerical parameters

Wall Condition	N_x	N_y	N_z	Δx^+	Δy_w^+	Δz^+	L_x^+	L_y^+	L_z^+
Adiabatic	2650	111	255	13.73	0.98	6.40	2.61×10^4	9.32×10^3	1.63×10^3
Isothermal	2650	111	255	22.05	1.19	10.30	4.19×10^4	1.50×10^4	2.62×10^3

(z-direction) followed by an average in time. A total of 360 instantaneous flow samples have been taken at a constant time interval of $0.1*\delta/U_\infty$ (the boundary layer thickness δ is based on the the wall-normal location where the velocity, $\overline{u}_1$ is 0.99 the freestream velocity). In order to obtain the required number of statistical samples, each simulation has taken $\approx 10^5$hrs. of computation on IBM BLUE GENE cluster (IDRIS HPC resources) using 512 processors.

IV.3 Results Validation

In the following, an attempt has been made to characterize the shape of the velocity distribution using the compressible shape factor H and the results are compared against the values obtained from the analytical relations and the ones obtained from experiments and numerical simulations. In addition, the levels of skin-friction coefficients are quantified against the available skin-friction analytical relations for turbulent flows. While later in this section, two-point correlations and spectral distributions of velocity and thermal fields are plotted to confirm that the width of domain in the spanwise direction is sufficient to not inhibit the turbulence dynamics. And the section closes with the validation of the levels of velocity fluctuations obtained in these direct simulations against the available compressible and the incompressible results found in the literature.

The shape factor H, given by the ratio of displacement thickness to momentum thickness (e.g. White [90] p. 524 for compressible definitions), was 3.40 for the adiabatic case and 2.65

for the isothermal case. It is possible to validate this change with the relationship (see [102])

$$\mathrm{H} = 1.4 + 0.4M_\infty^2 - 1.222\overline{T}_r\left(1 - \frac{\overline{T}_w}{\overline{T}_r}\right) , \tag{IV.1}$$

where the $\overline{T}_r$ and $\overline{T}_w$ are here the nondimensionalized mean recovery and wall temperatures, respectively.

In the adiabatic case, the last term vanishes and it is possible to get an estimate for the change in shape factor given the isothermal wall temperature. Using the freestream Mach number and wall temperature values for these simulations, the change estimated from Eq. (IV.1) is a reduction of 19.5% from the adiabatic value for the isothermal case; whereas, the results obtained from the DNS data using the definitions of displacement and momentum thickness was 22%. This slight deviation is shown in Fig. IV.1 along with shape factor values from other boundary layer simulations. The variation of skin-friction along the plate from the inflow

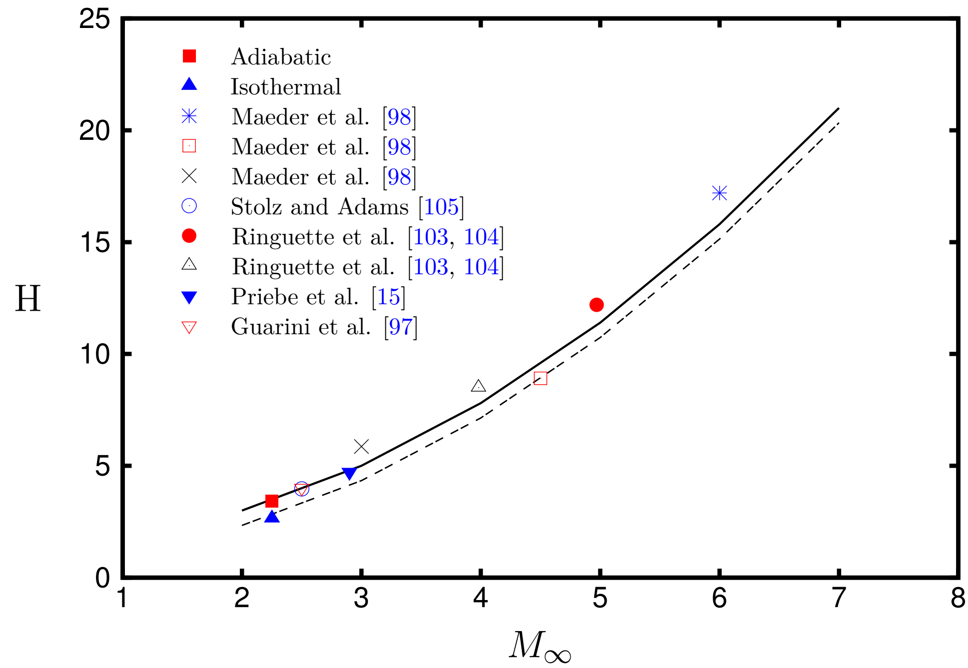

Figure IV.1 – Shape factor distribution as a function of freestream Mach number: ——, Adiabatic; – – –, Isothermal, Eq. (IV.1).

boundary into the fully turbulent region is shown in Fig. IV.2. The results in this figure are consistent with the theoretical estimates obtained from van Driest II [106]. As noted previously, the results to be presented throughout were obtained at the stations $Re_x = 5.4 \times 10^6$

and $Re_x = 5.34 \times 10^6$ for adiabatic and isothermal cases respectively. The simulation results

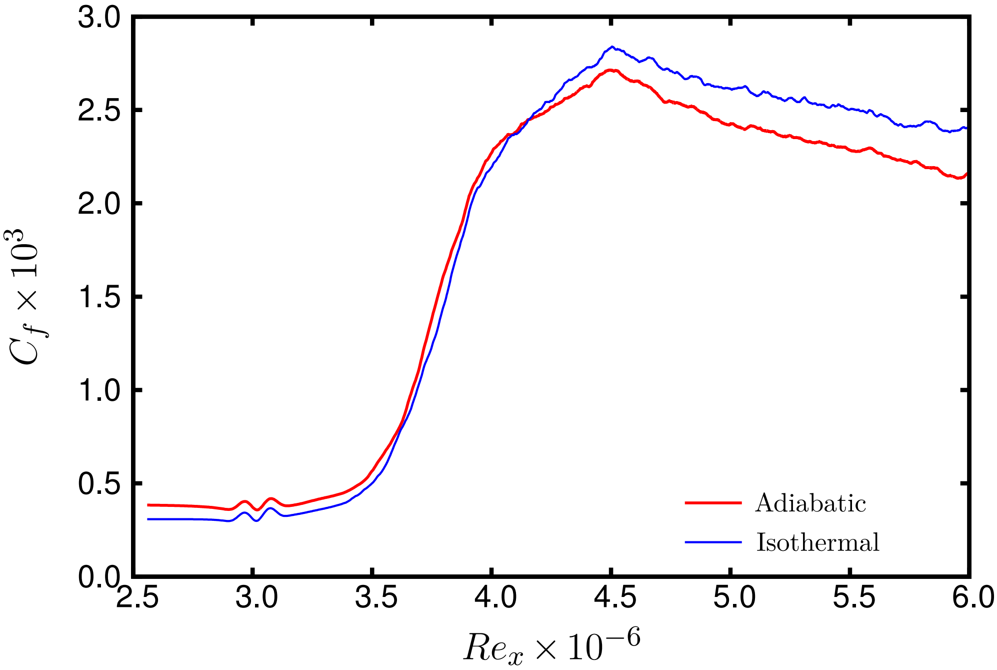

Figure IV.2 – Skin friction variation along flat plate for both adiabatic and isothermal (cold) wall simulations.

in Fig. IV.2 give a difference between the isothermal and adiabatic wall conditions, that is $(C_{fiso}/C_{fadia}) - 1$, of 8.50% at this location. This percentage difference is consistent with the difference obtained from the van Driest II compressible transformation. Both C_{fiso} and C_{fadia} can be obtained from

$$C_f = \frac{C_{f_i}}{F_c} , \tag{IV.2}$$

where C_{f_i} is an incompressible skin-friction value given by the Kármán-Schoenherr relation (see Hopkins and Inouye [107])

$$C_{f_i} = \frac{1}{17.08(\log_{10} Re_{\theta_i})^2 + 25.11 \log_{10} Re_{\theta_i} + 6.012} , \tag{IV.3}$$

and F_c a compressible transformation function given by

$$F_c = \frac{\overline{T}_{aw} - 1}{(\sin^{-1} A + \sin^{-1} B)^2} , \tag{IV.4a}$$

with

$$A = \frac{\overline{T}_{aw} + \overline{T}_w - 2}{[(\overline{T}_{aw} + \overline{T}_w)^2 - 4\overline{T}_w]^{1/2}}, \qquad B = \frac{\overline{T}_{aw} - \overline{T}_w}{[(\overline{T}_{aw} + \overline{T}_w)^2 - 4\overline{T}_w]^{1/2}} \ . \tag{IV.4b}$$

Note that all the formulae presented here are in a nondimensionalized form prescribed earlier in this section. The incompressible momentum thickness Reynolds number required in Eq. (IV.3) is obtained from

$$Re_{\theta_i} = \frac{Re_\theta}{\overline{\mu}_w} = F_{Re_\theta} Re_\theta \ , \tag{IV.5}$$

Substituting the values for the (adiabatic) wall and recovery temperatures into Eq. (IV.4a), then yields $F_c = 1.56$ for the adiabatic case and $F_c = 1.34$ for the isothermal case. Using the respective wall viscosity values yields $F_{R_\theta} = 0.59$ for the adiabatic case and $F_{R_\theta} = 0.77$ for the isothermal case. The resulting analytical estimate for the difference in skin-friction coefficient values, given by $(C_{f iso}/C_{f adia}) - 1$, is 9.88% which compares favorably with the DNS result of 8.50%.

An indication of the adequacy of the domain in the spanwise z-direction can be obtained from the two-point correlation and spectral distributions of the velocity and thermal fields. Figure IV.3 shows the distribution of the two-point correlation function for the three velocity components and the thermodynamic variables density and pressure at a wall-normal location of $y/\delta_c \approx 0.086$ (adiabatic $y^* \approx 87$, isothermal $y^* \approx 108$) which is located approximately in the middle of the log-layer region (see Fig. IV.8) for each case. (Note that in this and subsequent figures where outer scaling is used, the boundary layer thickness δ_c used is based on the wall-normal location where the van Driest velocity, $\overline{u}_c$ (see Eq. (IV.9)) is 0.99 the freestream velocity.) The correlation is defined as

$$R_{\alpha\alpha}(r_z) = \sum_{k=1}^{N_z - 1} \overline{\alpha_k \alpha_{k+k_r}}, \quad k_r = 0, 1, \ldots, k-1, \tag{IV.6}$$

where $r_z = k_r \Delta z$, and α represents one of the variables ρ, u, v, w or p. As the figure shows, the normalized autocorrelations all decay with increase in separation length across the spanwise extent of the domain. For both the adiabatic and isothermal cases, the wall-normal velocity correlation shows the coherence length of the streamwise eddies in the z-direction. This distance is slightly reduced for the isothermal case relative to the adiabatic case which suggests a more compact streamwise eddy structure. The u and w velocity component correlations both show a very weak coherence across most of the span for both the adiabatic and isothermal cases; however, the pressure correlation shows a nonzero spanwise coherence across most of the span - a trend consistent with earlier studies (Coleman et al. [95], Pirozzoli et al. [92]). As a further

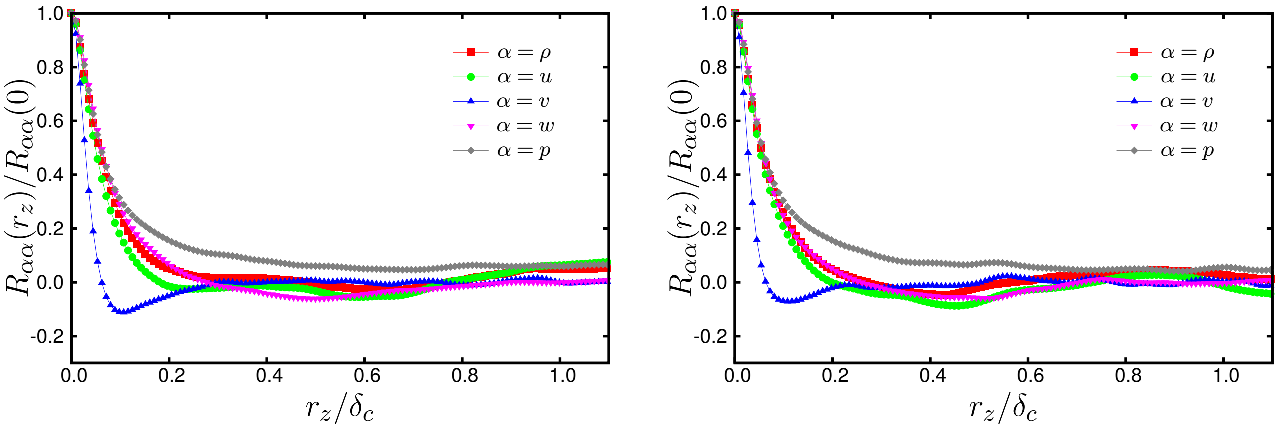

(a) Adiabatic Case   **(b)** Isothermal Case

Figure IV.3 – Two-point correlation as a function of spanwise separation distance: (a) Adiabatic; (b) Isothermal

assessment, the corresponding one-dimensional power spectrum in the spanwise direction for each variable is calculated, and are given here by

$$\Phi_{\alpha\alpha}(k_z\Delta z) = 1 + 2\sum_{k_r=1}^{(N_z-1)/2} R_{\alpha\alpha}(k_r\Delta z)\cos\left(\frac{2\pi n k_r}{N_z-1}\right), \quad n = 0,\ldots,(N_z-1)/2, \tag{IV.7}$$

with $k_z\Delta z = n/(N_z-1)$ and $R_{\alpha\alpha}(k_r\Delta z)$ obtained from the data shown in Fig. IV.3. The spectra in Fig. IV.4 show that all the spectra, except Φ_{vv}, exhibit a monotonic decay of about four decades. The peak in the wall-normal component spectrum at $k_z\delta_c \approx 6$ is associated with the streamwise eddies suggested by under-shoot in the corresponding two-point v-component correlation (see Fig. IV.3). As suggested by Smits and Dussauge [44] (see also Perry et al. [108], the u and w component spectra should behave similarly and distinct from the v-component. This is confirmed in Fig. IV.4 where the u and w component have a similar spectral distribution and as also suggested by the corresponding $-5/3$ behavior seen in any log-layer distribution. In order to substantiate the validity of the direct numerical simulation results, the turbulence properties of the undisturbed boundary layer are characterized in comparison with the experimental measurements and direct simulation data of the compressible and incompressible turbulent boundary layers. Fig. IV.5 and Fig. IV.6 depict the normalized root mean square(RMS) distribution of streamwise and wall-normal velocity components. The comparison of the present adiabatic turbulent boundary layer results with the compressible database includes the laser Doppler anemometry results of Deleuze [10] and Eléna et al. (as reported by [99]), Tomographic

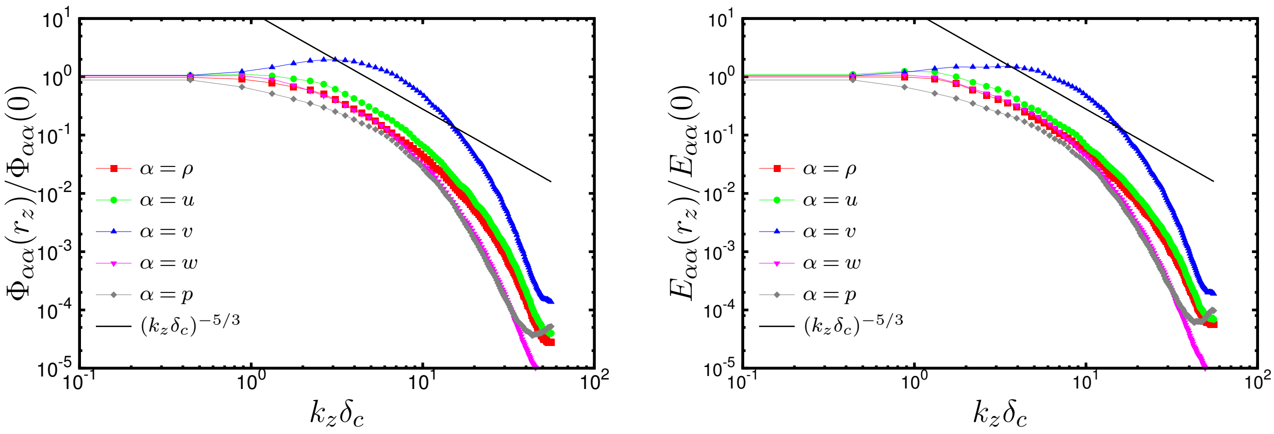

(a) Adiabatic Case

(b) Isothermal Case

Figure IV.4 – Spectral distribution as a function of spanwise wavenumber: (a) Adiabatic; (b) Isothermal

and 2-component PIV measurements of Humble et al. [109] as well as the direct simulation results of Martin [99]. In addition to the compressible results, subsonic turbulent boundary layer hot-wire anemometry measurements of Erm [110] and Klebanoff (as reported by [10]), and incompressible direct simulation results of Spalart [111] and Wu and Moin [112] are also included for comparison.

The results for the present simulation and that of the compressible database are normalized by the friction velocity (u_τ) and the density ratio ($\overline{\rho}/\overline{\rho}_w$) to take into account the effects of density variation as hypothesized by Morkovin [113]. This type of normalization allows us to compare the compressible results with the incompressible ones. The u_1-component of velocity fluctuations $\sqrt{\overline{\rho}\overline{u_1'u_1'}/\overline{\rho}_w u_\tau^2}$ shows a satisfactory agreement with the results found in the compressible boundary layer literature. The results depict a close match with the data of Martin [99], while the slight difference observed in magnitude with the measurements of Deleuze [10] and Eléna et al. [99], Humble et al. [109] is a possible consequence of the uncertainties of measurements as reported by Humble [16]. In addition, the present results collapsed well on the incompressible data; however, in the region where $y/\delta_c > 0.7$ the data from Klebanoff [10] and Spalart [111] represents an underestimation of the velocity fluctuations.

For the u_2-component of velocity fluctuations, $\sqrt{\overline{\rho}\overline{u_2'u_2'}/\overline{\rho}_w u_\tau^2}$, again a good agreement is obtained with the results of Martin [99], while the distributions from all the compressible experiments lie below the present DNS results. Also a good collapse of present DNS values is observed with the incompressible results.

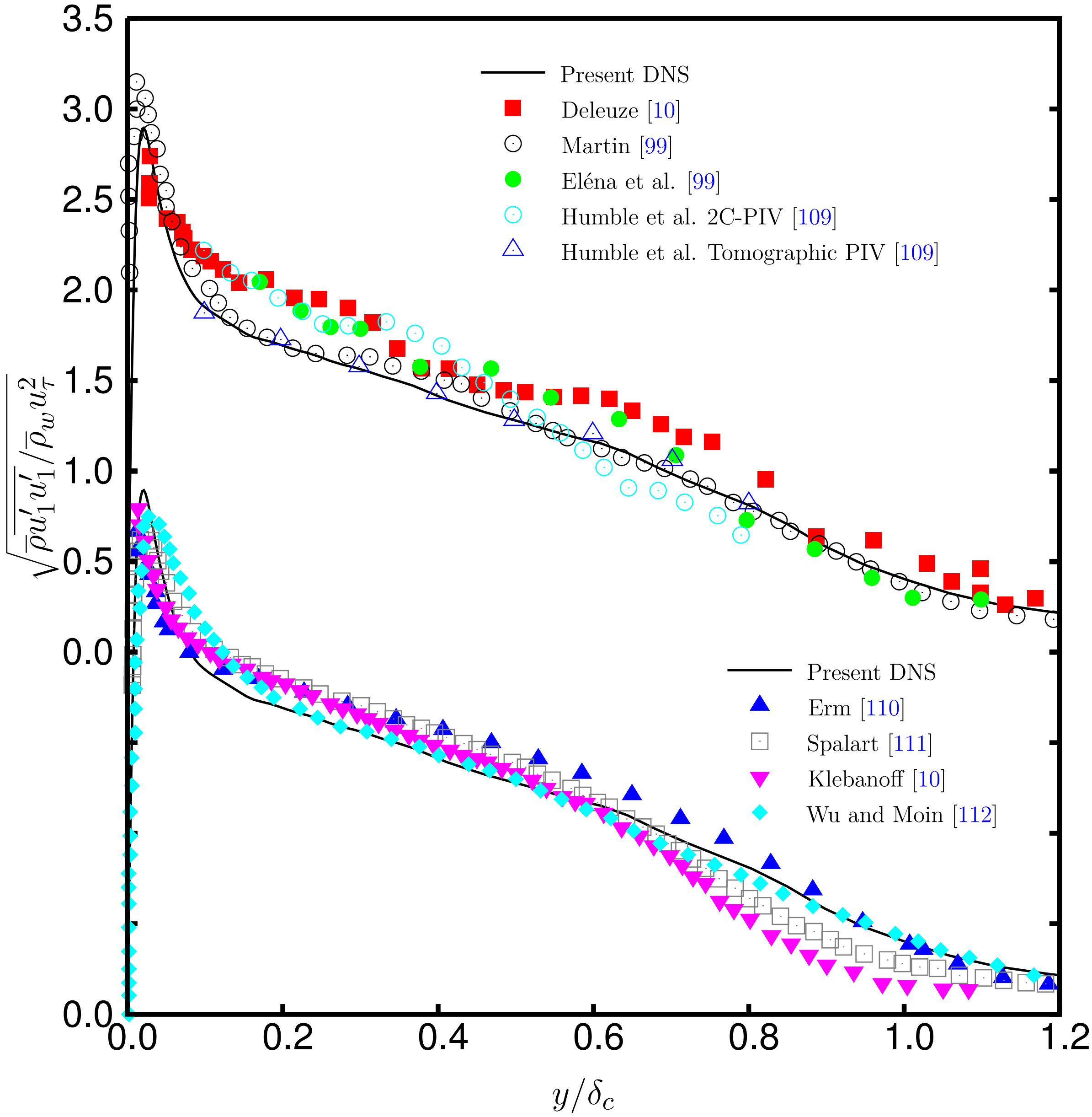

Figure IV.5 – Streamwise RMS velocity component within turbulent boundary layers using Morkovin's scaling, Adiabatic Case.

IV.4 Mean Field Analysis

With an analysis of compressible flows, the question arises whether to analyze Reynolds variables or density-weighted, Favre, variables (where $\widetilde{f} = \overline{\rho f}/\overline{\rho}$, and a Reynolds average is used for both variables). The answer is complicated by the fact that many relations involving velocity and temperature were obtained before the introduction of density-weighted variables but

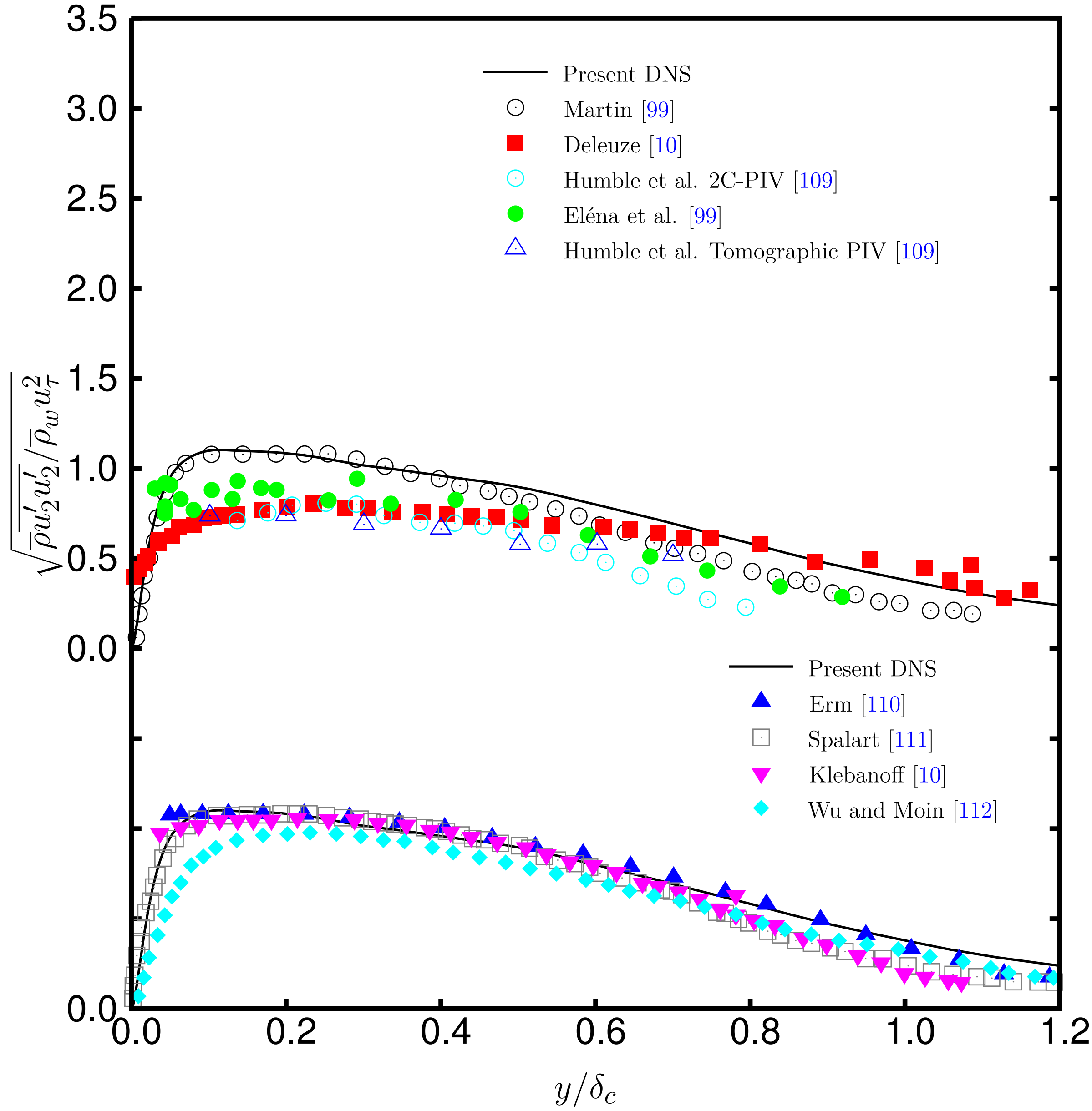

Figure IV.6 – Wall-normal RMS velocity component within turbulent boundary layers using Morkovin's scaling, Adiabatic case.

involved approximations where terms involving mass fluxes were neglected. The consequence of this was that the equations took a form consistent with equations obtained using density-weighted or Favre variables. The situation is further complicated by the fact that equations used for filtered variable simulations (e.g. large eddy simulations) and Reynolds-averaged calculations are expressed in terms of density-weighted, Favre, variables; whereas, of course, physical experiments involve Reynolds variables. Fortunately, with direct numerical simulation, either variable is obtained through a post-processing making each equally available. The difference between the two quantities is easily extracted from the defining relations, which for a variable f is given by

$$\frac{\widetilde{f}}{\overline{f}} - 1 = \frac{\overline{\rho' f'}}{\overline{\rho}\,\overline{f}} \ , \tag{IV.8}$$

where the primed quantity is the Reynolds fluctuation. The maximum difference found for both the streamwise velocity and temperature fields occur in the inner layer. In the adiabatic case, the (absolute) differences are $\approx 1.8\%$ for the streamwise velocity and $\approx 0.7\%$ for the temperature. In the isothermal case, the (absolute) differences are $\approx 0.8\%$ for the streamwise velocity and $\approx 0.2\%$ for the temperature (cf. [98]). These results suggest little need to distinguish between the different variables for the mean field in the adiabatic and isothermal cases considered. Unless otherwise noted, the results presented will apply equally well for the Reynolds or Favre variables.

The mean velocity and thermal fields from the adiabatic and isothermal cases are first compared in outer variable scaling in Fig. IV.7. Outer variable scaling is used initially here to give an overall view of the mean variable trends throughout the boundary layer. More detailed analysis involving inner variable scalings will be introduced and discussed shortly. The figure shows that the velocity field is only slightly affected by the change in thermal wall condition. In the isothermal case, the profile is slightly fuller than the adiabatic case. (Note that in the case of the velocity field, the nondimensionalization is in terms of $c_\infty/\sqrt{\gamma}$ so that in the freestream, $u_\infty = M_\infty\sqrt{\gamma}$.) For the thermodynamic variables, the difference between the density and temperature fields for the two cases is more pronounced. A more in-depth analysis of the difference between the two wall thermal conditions is carried out in terms of inner variable scaling where the usual normalization involving the friction velocity $u_\tau = \sqrt{\tau_w/\rho_w}$ and wall kinematic viscosity $\overline{\nu}_w = \overline{\mu}_w/\overline{\rho}_w$ is used. The starting point is the van Driest transformed velocity given by

$$\overline{u}_c^+ = \int_0^{\overline{u}_1^+} \left(\frac{\overline{\rho}}{\overline{\rho}_w}\right)^{1/2} \mathrm{d}\overline{u}_1^+ \ , \tag{IV.9}$$

where Reynolds variables are used consistent with the original derivation [114]. The corresponding adiabatic and isothermal profiles are compared in Fig. IV.8. Over the range $20 < y^+ < 300$ the cold wall velocity profile lies above the adiabatic one, which is consistent with the trend shown by Huang and Coleman [115]. The slope of the log-law for the adiabatic case is 2.45 ($\kappa = 0.408$) with a corresponding intercept constant of 5.5, and the slope of the log-law for the isothermal case is 2.40 ($\kappa = 0.416$) with a corresponding intercept value of 6.1.The wake pa-

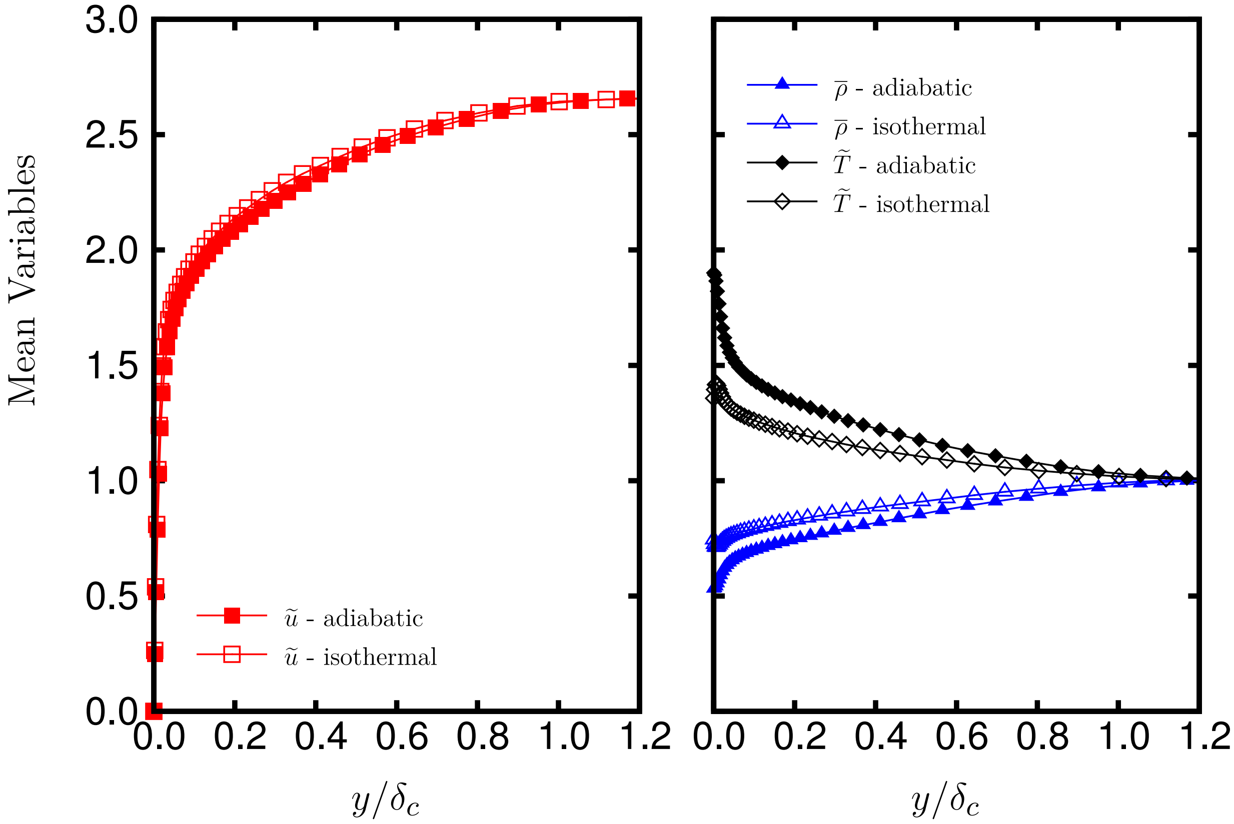

Figure IV.7 – Variation of mean variables across boundary layer.

rameter, which characterizes the outer layer velocity profile, is slightly larger for the isothermal case and is consistent with the fact that this parameter increases with momentum thickness Reynolds number (Cebeci [116], Gatski and Bonnet [46]). The sensitivity of the transformed velocity to changes in the normalized heat flux parameter and the friction Mach number are also highlighted in Fig. IV.8. The overall increase in skin-friction coefficient, shown in Fig. IV.2, for the isothermal case relative to the adiabatic case suggests an increase in the corresponding friction velocity u_τ. In the absence of any other considerations, this would lead to a transformed velocity profile for the isothermal case that should lie below the adiabatic profile. However, as shown by Huang and Coleman [115] (see their Fig. 3), the variation of log-layer slope with B_q has a much greater influence than that for the friction Mach number involving u_τ. Thus, the non-zero value of B_q in the cold wall case has a greater impact on the transformed velocity profile than the change in friction Mach number M_τ from the adiabatic case.

The mean temperature distributions across the boundary layer for the wall normalized temperature, $\overline{T}^+ = \overline{T}/\overline{T}_w$, are shown in Fig. IV.9a for the adiabatic and isothermal cases. The

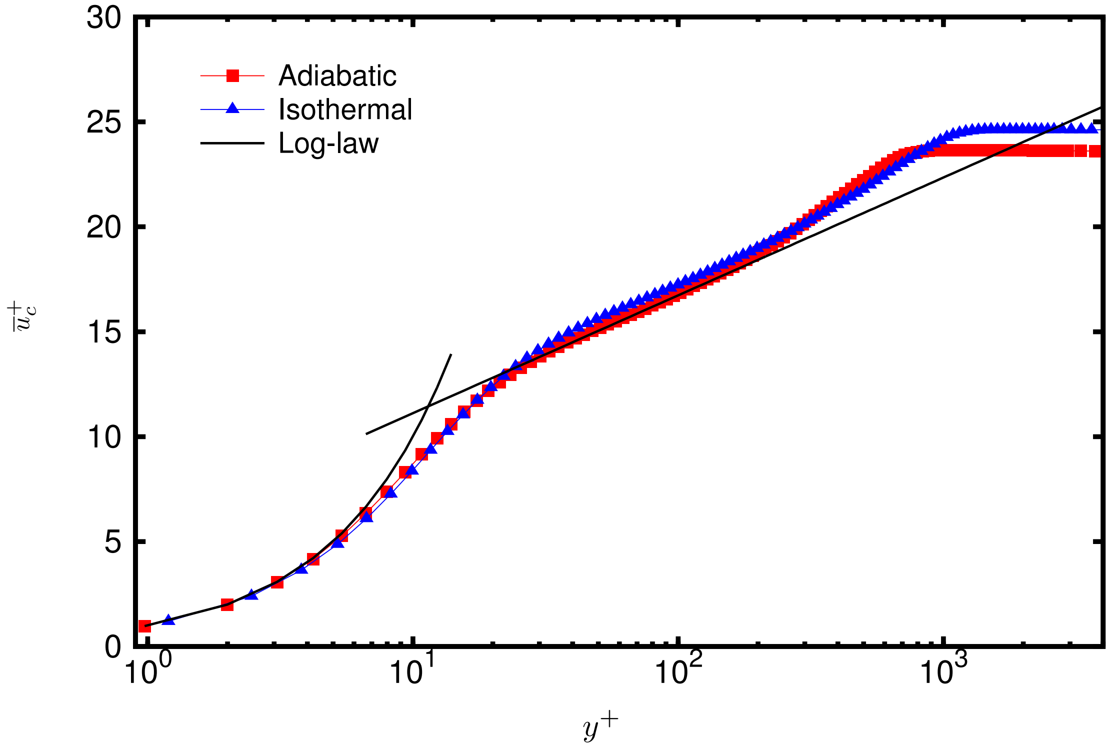

Figure IV.8 – van Driest transformed velocity for adiabatic and cold wall cases.

solid lines in the figure are from an inner layer similarity analysis for the temperature given by,

$$\overline{T}^+ = 1 - Pr_t B_q \overline{u}_1^+ - Pr_t M_\tau^2 \left(\frac{\gamma - 1}{2}\right) \overline{u}_1^{+2} \ . \tag{IV.10}$$

(Once again Reynolds variables are used for consistency with the mean velocity used in determining the van Driest velocity.) The parameter values in the figure are from Table IV.1a with a value of $Pr_t = 0.9$ used for both the adiabatic and isothermal cases. The comparison is for the turbulent inner layer where the turbulent Prandtl number value applies.

For the simulation results, the figure shows a noticeable difference in wall-normal behavior between the adiabatic and isothermal cases. While the adiabatic profile shows a monotonically increasing behavior throughout the layer, the isothermal profile shows a slight decrease up to the start of the buffer layer which is then followed by a monotonic increase. Tamano and Morinishi [93] have attributed this undershoot behavior to the wall-normal gradient of the mean heat flux vector. Near the wall, there is an increase in mean thermal energy diffusion associated with this term for the adiabatic case relative to the isothermal case. This prevents the increase in temperature in this region and results in the monotonic behavior for the adiabatic case and, correspondingly, a local minimum in the isothermal distribution shown in Fig. IV.9a occurs. The consequence of this is a monotonic decrease in temperature for the adiabatic case, but a slight buildup of internal energy (temperature) near the wall for the isothermal case.

Equation (IV.10) can also be rewritten in terms of a total temperature, $\overline{T}^+_{\text{tot}}$, as (cf. [117, 118])

$$\overline{T}^+_{\text{tot}} = \overline{T}^+ - 1 + Pr_t M_\tau^2 \left(\frac{\gamma-1}{2}\right) \overline{u}_1^{+2} = -Pr_t\, B_q\, \overline{u}_1^+ \tag{IV.11a}$$

$$\overline{T}^\dagger_{\text{tot}} = \frac{\overline{T}^+_{\text{tot}}}{-B_q T_w Pr_t} = \overline{u}_1^+ \ , \tag{IV.11b}$$

where a rescaling with the reference temperature, $-B_q T_w$, has been used. Multiplying Eq. (IV.11b) by $\sqrt{\overline{\rho}/\overline{\rho}_w}$ and integrating from the wall yields

$$\mathcal{I}^\dagger_{\text{tot}} = \int_0^{\overline{T}^\dagger_{\text{tot}}} \frac{\mathrm{d}\overline{T}^\dagger_{\text{tot}}}{\sqrt{\overline{T}^+}} = \frac{1}{\kappa} \ln y^+ + C_{\text{tot}} \ . \tag{IV.12}$$

When the isothermal temperature distribution in Fig. IV.9a is recast in terms of $\overline{T}^\dagger_{\text{tot}}$ using Eq. (IV.11), the integrated variable $\mathcal{I}^\dagger_{\text{tot}}$ should then follow the log-law distribution. In Fig. IV.9b the integrated temperature variable $\mathcal{I}^\dagger_{\text{tot}}$ is shown along with a log-law distribution with slope κ^{-1} ($\kappa = 0.41$). Alternative scalings can be developed as well. In the next section, a semi-local scaling will be used which effectively collapses the adiabatic and isothermal turbulent stress results. In addition, Brun et al. [119] have proposed an alternative scaling for the van Driest transformation and (total) temperature similarity scaling. A new spatial variable is introduced dependent on the variation of (dynamic) viscosity through the layer. It has the desirable effect of better collapsing the transformed mean velocity and temperature profiles since it better accounts for wall-normal variations due to temperature effects.

IV.5 Turbulent Field Analysis

In this section, velocity and thermal statistical correlations will be compared. As with the mean flow variables, the question arises about the difference between the Reynolds variable correlations and the Favre variable correlations. Analogous to Eq. (IV.8), the difference between

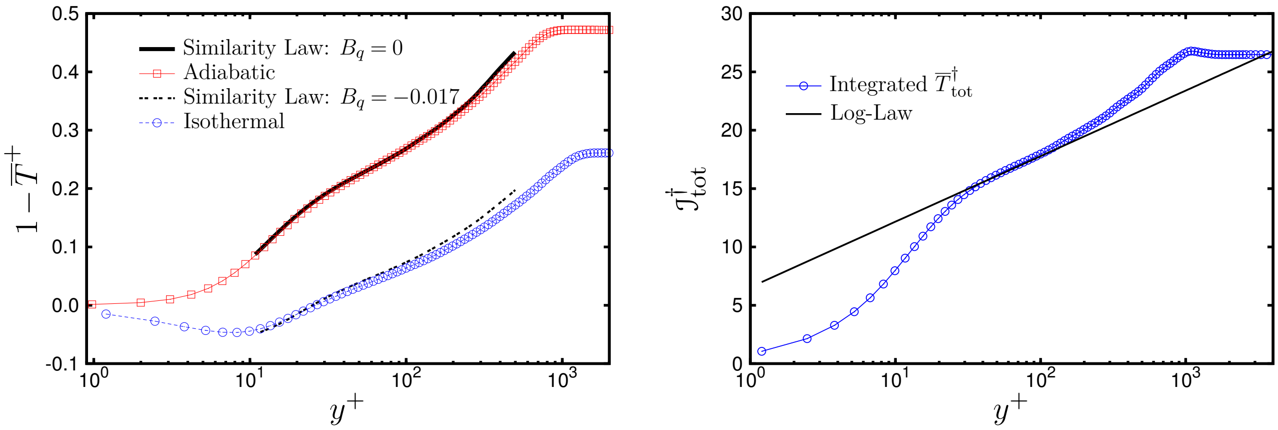

(a) Mean Temperature **(b)** Integrated Mean Total Temperature

Figure IV.9 – Mean thermal variable distribution across boundary layer: (a) mean temperature (solid and dashed lines are temperature similarity law distributions from Eq. (IV.10)); (b) integrated mean total temperature from Eq. (IV.12); Parameter values from Table IV.1a with $Pr_t = 0.90$.

correlations can be written as

$$\frac{\widetilde{u_i''u_j''}}{\overline{u_i'u_j'}} - 1 = \frac{\overline{\rho' u_i' u_j'}}{\overline{\rho}\,\overline{u_i'u_j'}} - \frac{\left(\overline{\rho' u_i'}\right)\left(\overline{\rho' u_j'}\right)}{\overline{\rho}^2\,\overline{u_i'u_j'}} \;, \tag{IV.13}$$

where the Reynolds variable fluctuations are designated with a single $'$, e.g. u_i', and the density-weighted, Favre, variable fluctuations are designated with a double $'$, e.g. u_i''. As shown, the two correlations are related through the appearance of higher-order correlations involving the density and velocity fluctuating quantities. In order to quantify the difference here, a comparison is made in Fig. IV.10 between the adiabatic and isothermal cases. The figure shows that the (absolute) maximum difference that occurs is $\approx 6\%$ for the adiabatic case, and this is associated with the streamwise normal stress component and the shear stress component. For the isothermal case, similar qualitative and quantitative results are obtained, but with less variation with increasing distance from the wall. Note that for the mean variables, it sufficed to examine the inner layer behavior using the wall variable normalization, and for the adiabatic case this wall variable scaling of the turbulent correlations also applies; however, for the isothermal case, a semi-local scaling has been shown by Morinishi et al. [94] and Huang et al. [96] to collapse the correlation data better than the wall scaling. This semi-local scaling involves a friction velocity given by $u_{\tau^*} = \sqrt{\tau_w/\overline{\rho}}$ and local viscosity $\overline{\nu} = \overline{\mu}/\overline{\rho}$ ($y^* = y u_{\tau^*}/\overline{\nu}$). As

Fig. IV.10 shows, the semi-local scaling is used in the inner region; nevertheless, in the analyses to follow, both scalings will be used where necessary to further emphasize the effects of the cross-stream density variation.

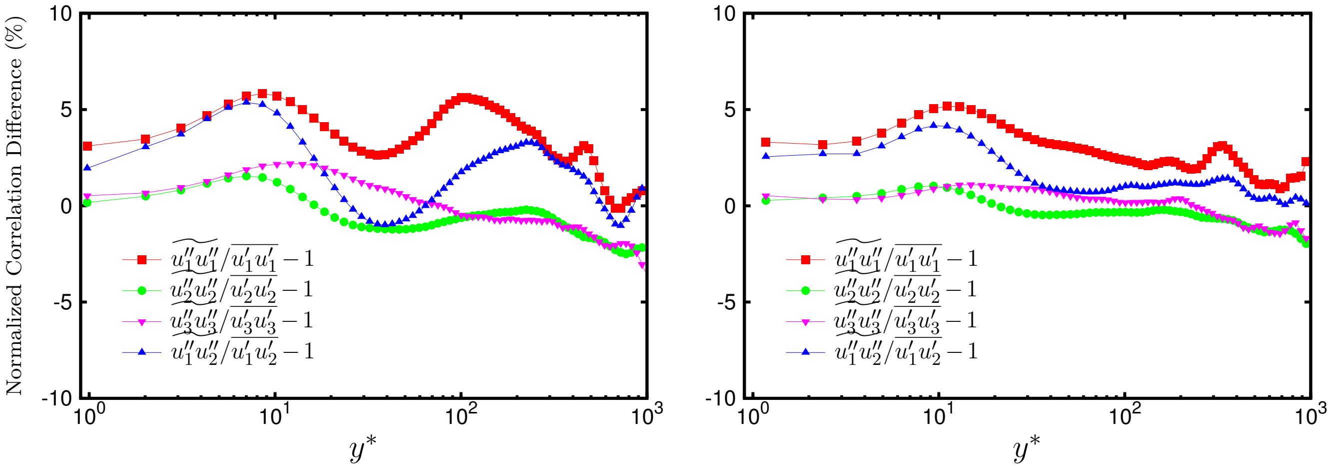

(a) Adiabatic Case **(b)** Isothermal Case

Figure IV.10 – Percentage differences between Favre- and Reynolds-averaged stresses across boundary layer: (a) Adiabatic; (b) Isothermal

IV.5.1 Turbulent Velocity Field

For the turbulent velocity second-moments, the turbulent stresses, there is no inherent scaling so the proper choice of normalization is dictated by the collapse of the correlation data. In addition, the question of which turbulent second moment variables are relevant arises as well. Since LES simulations and RANS computations are expressed in terms of Favre variables with closure required of the associated stressed, it is the Favre or density-weighted stresses defined by $\overline{\rho}\tau_{ij} = \overline{\rho}\,\widetilde{u_i''u_j''}$ that are more relevant. Figure IV.11 shows the distribution of the turbulent shear stress across the boundary layer. The scaling by semi-local variables aligns the two curves through most of the boundary layer.

For the turbulent normal stresses shown in Fig. IV.12, the change in scaling affects the location of the peak values by shifting the isothermal distributions toward the adiabatic results as in the shear stress case. As in the case of Morinishi et al. [94], the maximum value of the streamwise component in the adiabatic case lies below that of the isothermal case even with the semi-local scaling. The wall-normal and spanwise components show only a small variation in both peak amplitude and peak location from their corresponding adiabatic values. The shift

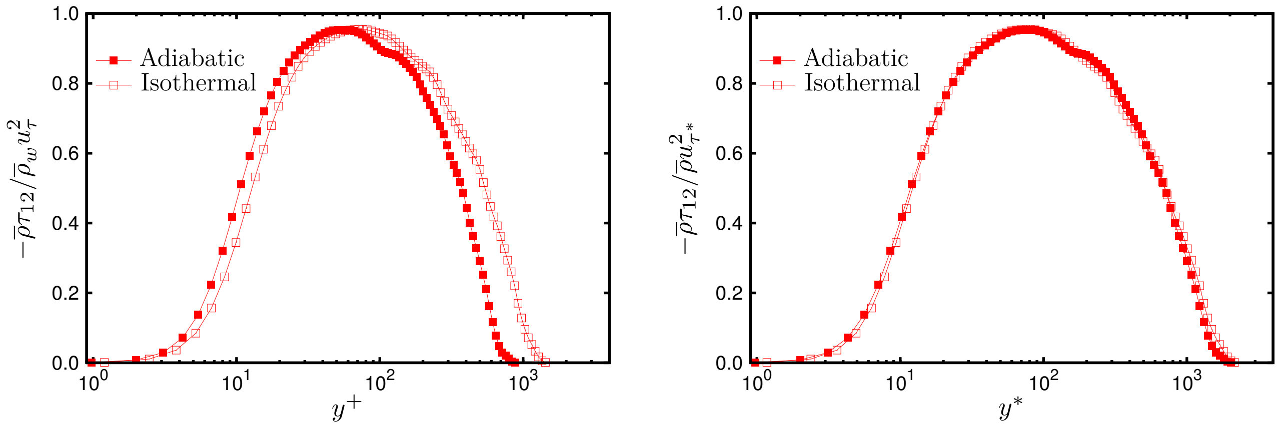

(a) wall unit scaling

(b) semi-local scaling

Figure IV.11 – Distribution of turbulent shear stress: (a) wall unit scaling; (b) semi-local scaling

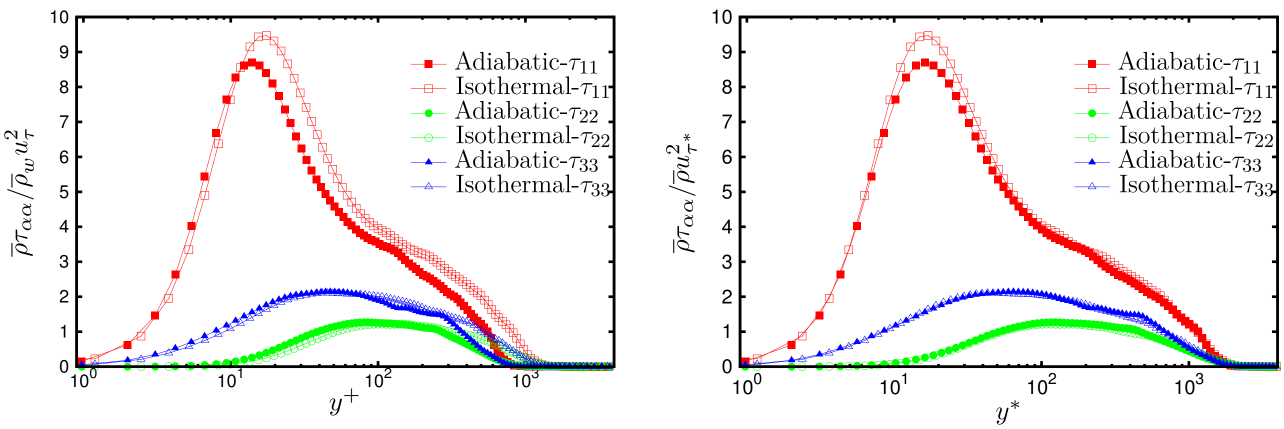

(a) wall unit scaling

(b) semi-local scaling

Figure IV.12 – Distribution of turbulent normal stresses ($\tau_{\alpha\alpha}$, no sum): (a) wall unit scaling; (b) semi-local scaling

in peak amplitude location for both the shear and normal stresses is consistent with the van Driest transformed velocity result. In that case, the shift in intercept indicated a thickening of the inner layer region which would correspond to the peak of the normal stress occurring at large value of y^+.

These results for the velocity second-moments suggest that the turbulence anisotropy may be altered from the adiabatic case. This can be investigated by considering the turbulent stress tensor anisotropy, $b_{ij} = \tau_{ij}/\tau_{ii} - \delta_{ij}/3$.

Figure IV.13a shows the distribution of the shear stress anisotropy component (structure parameter) across the boundary layer. There is an increase in the length of the region where b_{12} is relatively constant compared to the adiabatic case; although, in the isothermal case, the maximum level reached by the b_{12} component is relatively close to the adiabatic case. Assessing the influence of the other anisotropy components on the flow is best shown through the behavior of the associated second and third invariants. Figure IV.13b shows the turbulent stress anisotropy invariant map, with the second and third invariants given by II_b $(=-b_{ij}b_{ji}/2= -b_{ii}^2/2)$ and III_b $(=b_{ij}b_{jk}b_{ki}/3= b_{ii}^3/3)$, respectively. The distribution shown for both cases in the invariant map figure is typical of two-dimensional boundary layer flows (Krogstad and Torbergsen [120]). However, for the isothermal case, there is a shift along the two-component boundary away from the two-component axisymmetric limit. This implies a strengthening of the streamwise fluctuating velocity component as shown in Fig. IV.12 relative to the wall-normal component. While the qualitative trend for both the adiabatic and isothermal cases are the same, the relative location of the various invariant values through the boundary layer have shifted. Once again, this is also consistent with the alteration of the boundary layer as indicated in Fig. IV.8.

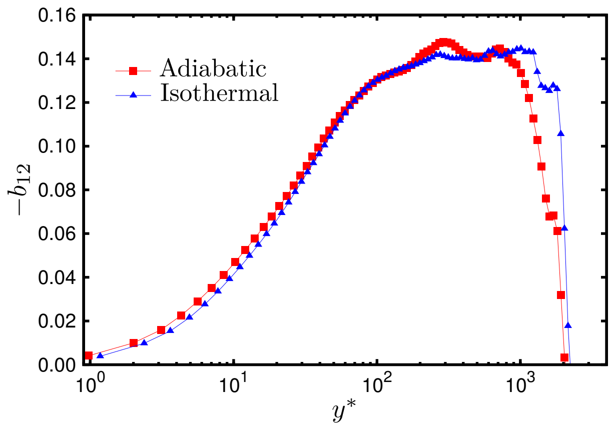

(a) Structure parameter

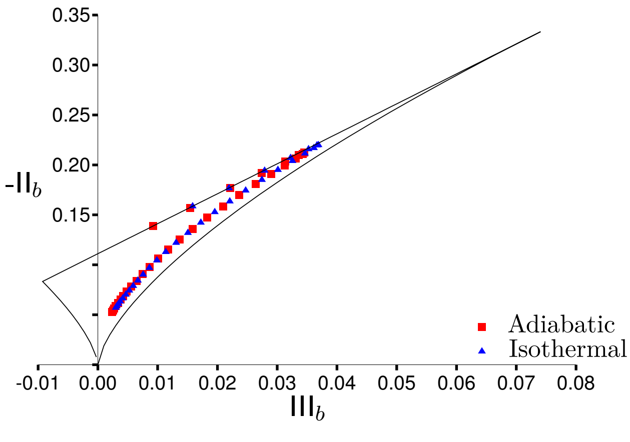

(b) Anisotropy Invariant Map

Figure IV.13 – Thermal influence on turbulent stress anisotropy: (a) structure parameter; (b) Invariant map

Further analysis of the turbulent dynamics can be made through an assessment of the transport equation for the turbulent kinetic energy, $\overline{\rho}K = \overline{\rho}\tau_{kk}/2$ ($\tau_{ij} = \widetilde{u_i''u_j''}$ which can be written as

$$-A_K + P_K + \mathit{\Pi}_K + T_K + D_K - \epsilon + M_K = 0 \ , \tag{IV.14}$$

where $A_K = \overline{\rho}\ \widetilde{u}_j(\partial K/\partial x_j)$ is the advection term, and the remaining terms are the kinetic energy production,

$$P_K = -\overline{\rho}\tau_{ik}\widetilde{S}_{ki}\ , \tag{IV.15a}$$

the pressure-dilatation,

$$\Pi_K = \overline{p' s'_{kk}}\ , \tag{IV.15b}$$

the turbulent diffusion by velocity and pressure fluctuations,

$$T_K = -\frac{\partial}{\partial x_k}\left[\frac{\overline{\rho}\widetilde{u''_i u''_i u''_k}}{2} + \overline{p' u'_i}\delta_{ik}\right]\ , \tag{IV.15c}$$

the viscous diffusion,

$$D_K = -\frac{\partial}{\partial x_k}\left[\overline{\sigma'_{ik} u'_i}\right]\ , \tag{IV.15d}$$

the turbulent kinetic energy dissipation rate

$$\epsilon_K = \overline{\sigma'_{ik} s'_{ki}}\ , \tag{IV.15e}$$

with σ_{ij} the viscous stress tensor, and the compressible mass flux contribution,

$$M_K = \overline{\rho' u'_i}\left(\frac{\partial \overline{p}}{\partial x_i} - \frac{\partial \overline{\sigma}_{ik}}{\partial x_k}\right)\ . \tag{IV.15f}$$

The turbulent kinetic energy dissipation rate ϵ can be decomposed into terms involving correlation between fluctuations of the deformation tensor $s'_{ij} = [(\partial u'_i/\partial x_j) + (\partial u'_j/\partial x_i)]/2$ and terms involving correlations between fluctuations of viscosity and s'_{ij}. It will be assumed here that the contributions involving the fluctuating viscosity are negligible relative to those involving the mean viscosity $\overline{\mu}$ (see Kreuzinger et al. [121]). Of course, as a practical matter, any balance equations formed from the fluctuating viscosity correlations would yield even higher-order correlations of (probably) even smaller magnitude. The terms involving the mean viscosity can be expressed as the sum of three parts consisting of solenoidal, ε, and dilatational, ε_d, dissipation rates, and an inhomogeneous contribution, ε_I. This dissipation rate partitioning can be written as

$$\varepsilon = \overline{\mu}\overline{w'_{ij}w'_{ij}} = \overline{\mu}\overline{\omega'_i\omega'_i} \tag{IV.16a}$$

$$\varepsilon_d = \frac{4}{3}\overline{\mu}\overline{s'_{kk}s'_{ll}} \tag{IV.16b}$$

$$\varepsilon_I = 2\overline{\mu}\left[\frac{\partial^2(\overline{u'_iu'_j})}{\partial x_i\partial x_j} - 2\frac{\partial}{\partial x_k}\left(\overline{u'_k\frac{\partial u'_j}{\partial x_j}}\right)\right]. \tag{IV.16c}$$

where $w'_{ij} = [(\partial u'_i/\partial x_j) - (\partial u'_j/\partial x_i)]/2$ is the rate of rotation tensor and $\omega'_i = e_{ikj}w'_{jk}$ is the vorticity vector. In the analysis here, of the kinetic energy budget, it will be assumed that $\epsilon_K \approx \varepsilon$ throughout.

A comparison of the K-budgets for the adiabatic and isothermal cases are shown in Fig. IV.14. Only at the wall, does the pressure-dilatation make a small positive contribution. Nevertheless,

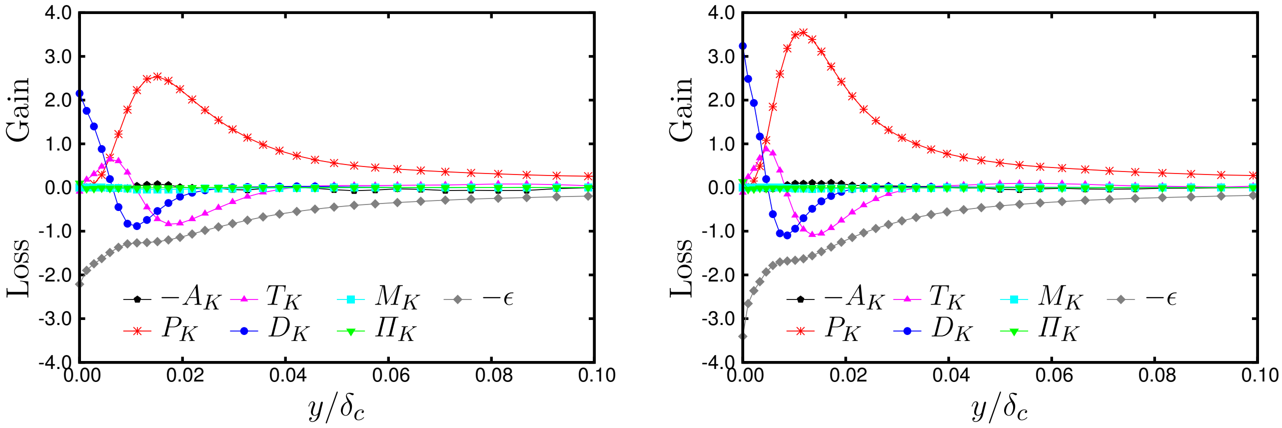

(a) Adiabatic

(b) Isothermal

Figure IV.14 – Turbulent kinetic energy budgets: (a) adiabatic wall, (b) isothermal wall.

one can neglect the effects of compressibility in the overall dynamic balance of K. The main contributors to the dynamic balance, as expected, are the production and destruction terms. As the distance from the wall decreases, the production of energy is first balanced by a combination of dissipation, transport and diffusion. Then, as the distance from the wall decreases further, the production is first augmented by a contribution from the turbulent transport, and then by a contribution from the turbulent diffusion. Throughout, the destruction term ϵ acts as a sink of energy to the system. In both cases, the pressure-dilatation and mass flux terms contribute negligibly to the overall balance throughout the layer. These results agree with the trends found by Morinishi et al. [94] in their channel flow simulations with adiabatic and isothermal (cold) walls.

While this qualitative description of the spatial distribution of terms holds for both the adiabatic and isothermal cases, there are two primary quantitative differences. First, in the isothermal case, the distribution of terms described in the last paragraph is confined to a region in closer proximity to the wall. This suggests a smaller sublayer region than in the adiabatic case. The second difference, is the slightly larger peak values in all the non-negligible contributors to the dynamic balance. It should be noted that the first difference necessitated a finer grid spacing in the wall proximity region and a subsequent decrease in computational time step.

The total temperature variation across the boundary layer comprises both the mean field velocity and temperature as well as the turbulent kinetic energy, and is given by

$$\tilde{T}_t = \tilde{T} + \left(\frac{\gamma - 1}{2\gamma}\right)\left[\tilde{u}_i\tilde{u}_i + \widetilde{u_i''u_i''}\right] \ . \tag{IV.17}$$

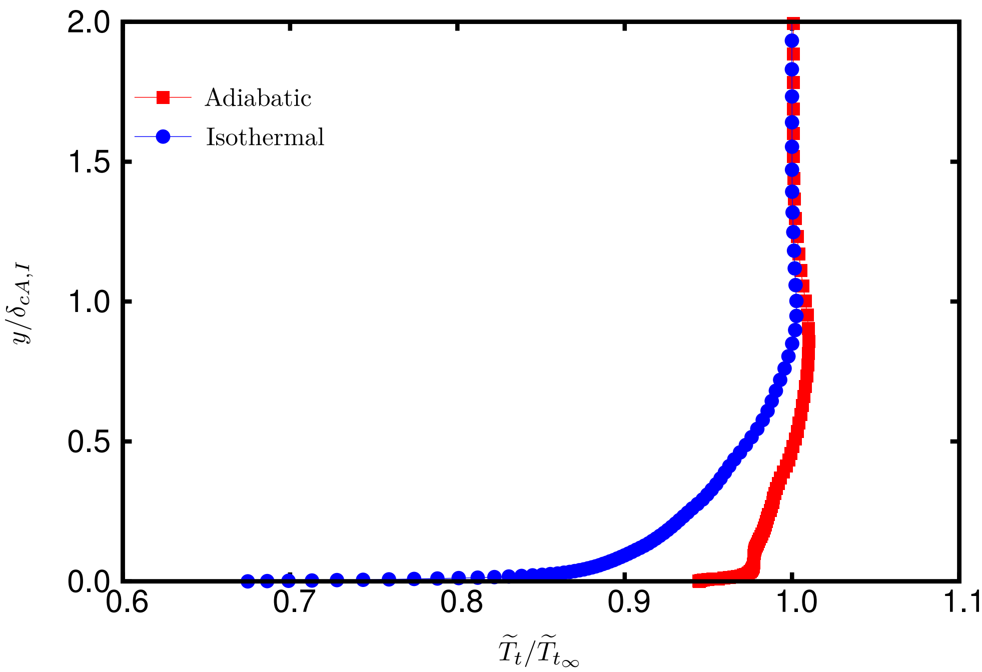

Figure IV.15 – Mean total temperature distribution across boundary layer.

Figure IV.15 shows the variation of the total energy, across the boundary layer for the adiabatic and cold wall cases. For the adiabatic case, the overall trend is for an increase in total temperature with distance from the wall; although, this case is also characterized by a slight overshoot in the distribution in the outer layer of the boundary layer. This overshoot is explained by the fact that the total energy thickness defined by,

$$\Delta = \int_0^\infty \frac{\overline{\rho}\widetilde{u_1}}{\sqrt{\gamma}M_\infty}\left(\frac{\widetilde{T}_t}{\widetilde{T}_{t\infty}} - 1\right) \mathrm{d}y \ , \tag{IV.18}$$

must be independent of the streamwise location in the adiabatic case which, when coupled with the conservation of total energy, leads to the result that the integral in Eq. (IV.18) should vanish. However, since the total temperature ratio $\widetilde{T}_t/\widetilde{T}_{t\infty} < 1$ in the inner layer, there must be a region where it exceeds unity in order for total energy thickness to vanish. In contrast, for the isothermal case, the variation of heat flux along the wall in the streamwise direction removes the restriction that the total energy thickness be constant which leads to a monotonic growth of total energy with distance from the wall.

Beyond the velocity second moments, two other higher-order velocity, statistical moments are of interest. These are the skewness and flatness (kurtosis) factors defined, respectively, as

$$S(u_i') = \frac{\overline{u_i'^3}}{(\overline{u_i'^2})^{3/2}}, \qquad F(u_i') = \frac{\overline{u_i'^4}}{(\overline{u_i'^2})^2} \ . \tag{IV.19}$$

These factors are closely connected to the shape of the probability density function (*pdf*) of the argument random variables (see Lumley [122]). Figure IV.16a and Figure IV.16b respectively compares the skewness and flatness factors for the streamwise fluctuating velocity between the adiabatic and isothermal cases. (Semi-local scaling is used here for consistency with the second-moment results discussed previously, and best aligns the inner layer adiabatic and isothermal results.) The change in wall condition has essentially no impact on these factors throughout the inner layer. Nevertheless, the peak values for the skewness (≈ 1) and the flatness (≈ 4.3) factors in proximity of the wall are consistent with recent channel flow simulation results (Tamano and Morinishi [93]). The skewness plot shows that strong positive streamwise fluctuations exist close to the wall and subsequently diminish as distance from the wall increases ($y^* \lesssim 18$). Beyond this point, the less intense negative skewness values reach a minimum at $y^* \approx 30$ and then relax to a value of ≈ -0.2 through the remainder of the inner layer. The flatness factor shown in Fig. IV.16b is also consistent with the previous simulation results (Tamano and Morinishi [93]). It shows that for $y^* \approx 8$, the u_1' fluctuations become more intermittent, but above this value effects of intermittency appears to vanish.

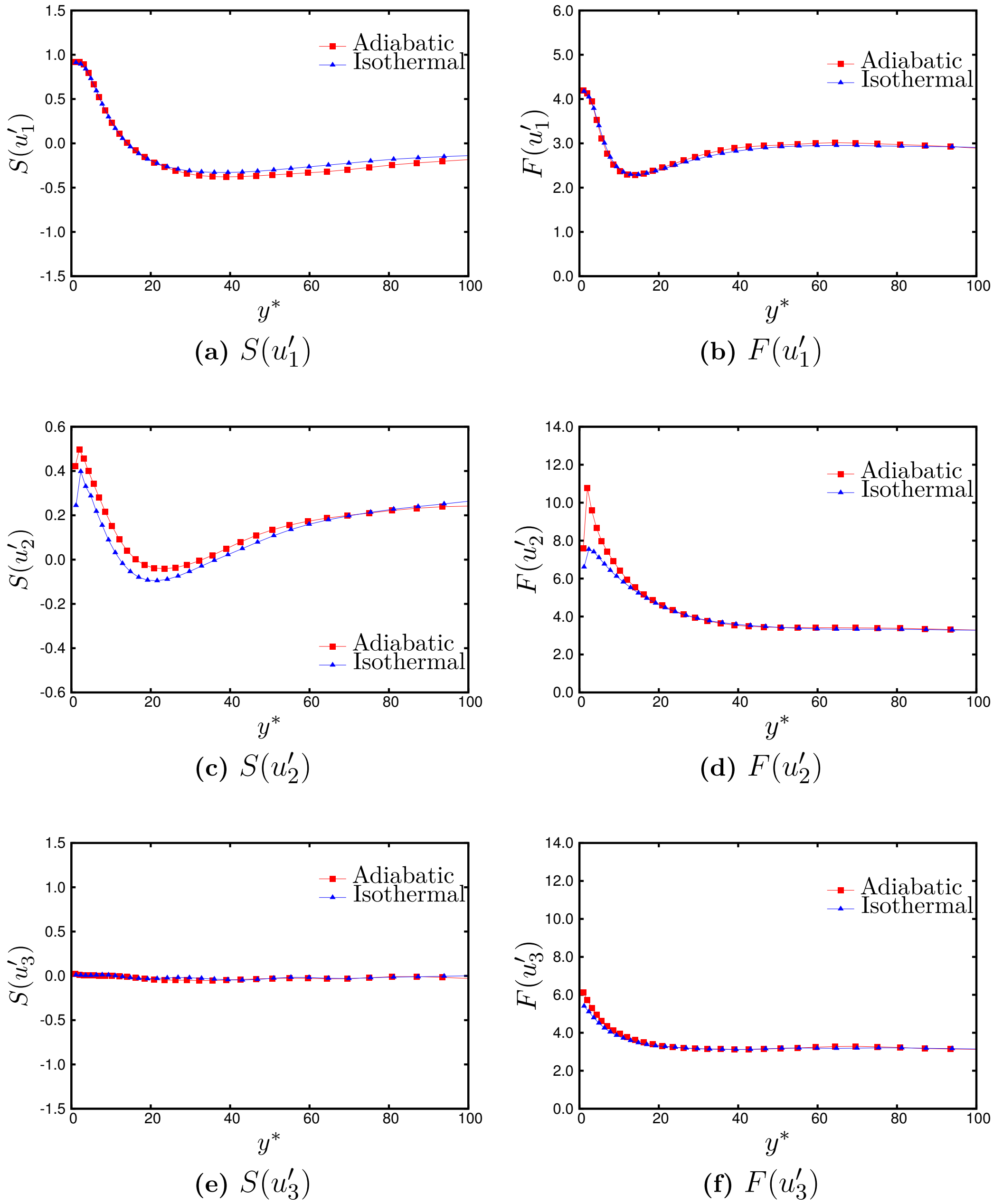

Figure IV.16 – Variation of skewness and flatness factors across boundary layer: (a) and (b), Streamwise fluctuating velocity component; (c) and (d), Wall-normal fluctuating velocity component; (e) and (f), Spanwise fluctuating velocity component.

For the wall-normal velocity skewness $S(u_2')$ shown in Fig. IV.16c, the isothermal case has lower values than the adiabatic case from the wall through the buffer layer region, and through the remainder of the inner layer ($y^* > 30$) the two cases show little difference. This indicates that the thermal wall condition dampens the positive wall-normal fluctuations and appears to slightly enhance the negative wall-normal fluctuations. The regions where $u_1' > 0$ and $u_2' > 0$ suggest strong outward motion of fluid; although, in the isothermal case the outward motion is reduced relative to the adiabatic case. In the relatively narrow region where $u_1' > 0$ and $u_2' < 0$, fluid is swept toward the wall albeit with a slightly greater intensity in the isothermal case than in the adiabatic case. The flatness factor for the wall-normal fluctuating velocity is significantly affected by the presence of the isothermal wall showing a significant reduction in the flatness factor suggesting a much more intermittent character to the u_2' fluctuations. Although the qualitative trends are the same as the Tamano and Morinishi channel flow $S(u_2')$ and $F(u_2')$ results, the magnitude differ slightly probably owing to the inherent difference between the channel flow and developing boundary layer.

In Fig. IV.16e and Fig. IV.16f respectively the skewness and flatness factors for the spanwise fluctuating velocity are shown. The skewness levels in both the adiabatic and isothermal cases are near their Gaussian values of zero, and significant trends away from this are difficult to assess quantitatively. The flatness does show the increase in intermittent character characteristic of the near-wall region and shown in the skewness and flatness factors for the other component velocities. The levels here are consistent with incompressible channel flow simulation data (Kim et al. [123]). Although the influence of the isothermal boundary condition had an impact on the fluctuating velocity field, this effect can largely be accounted for by considering the density variation across the boundary layer through the introduction of semi-local scaling.

IV.5.2 Turbulent Thermal Field

Both the temperature variance and total temperature variance play different but relevant roles in the assessment of the turbulent thermal field. The temperature variance enters into RANS-type closure models that attempt to account for variable turbulent Prandtl number effects through the introduction of a temperature variance scale equation. For the total temperature fluctuations, it is well-known that in the initial formulation of the Strong Reynolds Analogy (SRA) one of the underlying assumptions was that the total temperature fluctuations were negligible. Figure IV.17a shows the distribution of temperature variance across the boundary layer in semi-local wall units. As the figure shows, the temperature fluctuations are significantly damped in the isothermal case relative to the adiabatic case. However, in contrast to the adiabatic case where there is a continuous decline from the peak at $y^* \approx 30$, the isothermal case shows a relatively constant value throughout the log-layer and a gradual decline farther out in the outer layer.

In Fig. IV.17b for the total temperature distribution, there is less of an effect on the relative magnitudes of the total temperature variance between the two wall conditions. As for the variation across the boundary layer, however, the isothermal case now exhibits a peak at $y^* \approx 20$ but then attains a relatively constant value in a part of the log-layer and outer layer. Correspondingly, in the same part of the log-layer and outer layer, the adiabatic case also reached a relatively constant (higher) value. In addition, note that the relative levels between the temperature variance and total temperature variance for the adiabatic case are approximately the same; whereas, for the isothermal case the total temperature variance is uniformly higher than the temperature variance. This strong influence on the fluctuating temperature field suggests

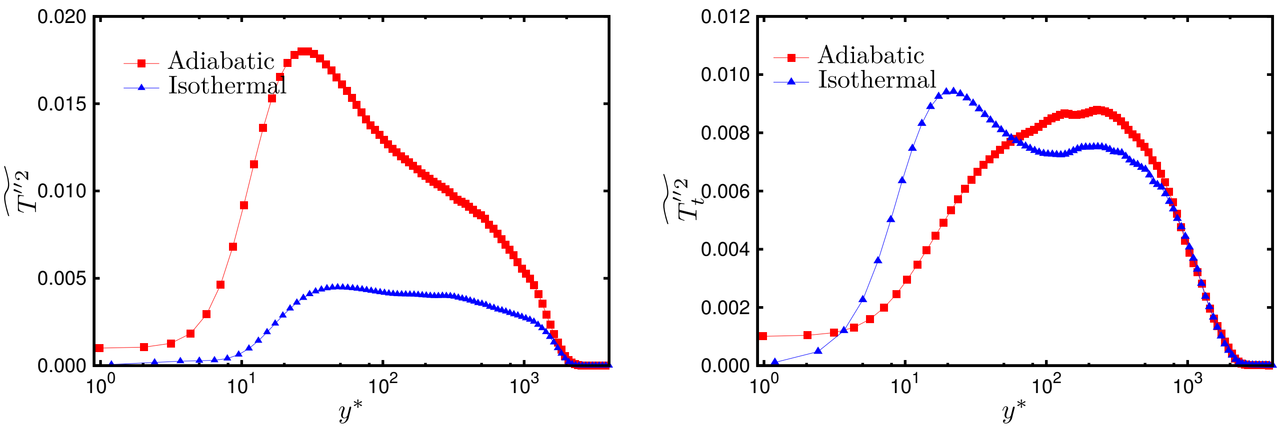

(a) Temperature Variance

(b) Total Temperature Variance

Figure IV.17 – Mean square fluctuating thermal field distributions across boundary layer: (a) temperature variance; (b) total temperature variance.

that development of closure models for the respective transport equations (e.g. temperature variance) will require careful study in order to properly sensitize them to a range of isothermal conditions.

It remains now to examine the effect of the isothermal conditions on the heat fluxes. As in the case of the second-moments of velocity, the filtered simulation methods and RANS-type methods all require density-weighted, Favre, variables; whereas, physical experiments yield correlations involving Reynolds variables. Analogous to Eq. (IV.13), the difference between the Favre and Reynolds variable fluxes is given by

$$\frac{\widetilde{u_i''T''}}{\overline{u_i'T'}} - 1 = \frac{\overline{\rho' u_i' T'}}{\overline{\rho}\,\overline{u_i'T'}} - \frac{\left(\overline{\rho' u_i'}\right)\left(\overline{\rho' T'}\right)}{\overline{\rho}^2\,\overline{u_i'T'}} \,, \qquad \text{(IV.20)}$$

As was found for the turbulent stresses (see Fig. IV.10), the difference between Favre and Reynolds variables reached a maximum value approaching 6%. The results shown in Fig. IV.18 for the variation across the boundary layer show a slightly larger variation with a maximum value approaching 8%. Such differences between Favre and Reynolds heat flux correlations are relevant to any type of model development and comparison between numerical and experimental results. In addition, the suggested importance of the various mass flux correlations implies these terms may have to be included in any transport equation closure model.

The significance of these differences is that they occur in wall-layer regions that are the most difficult regions in which to develop widely applicable models. Since the models to be developed are, as pointed out, necessarily developed for density-weighted variables, their validation becomes problematic and limited to direct simulations rather than physical experiments where Reynolds variable fluxes are obtained. The variation of the heat flux correlations across

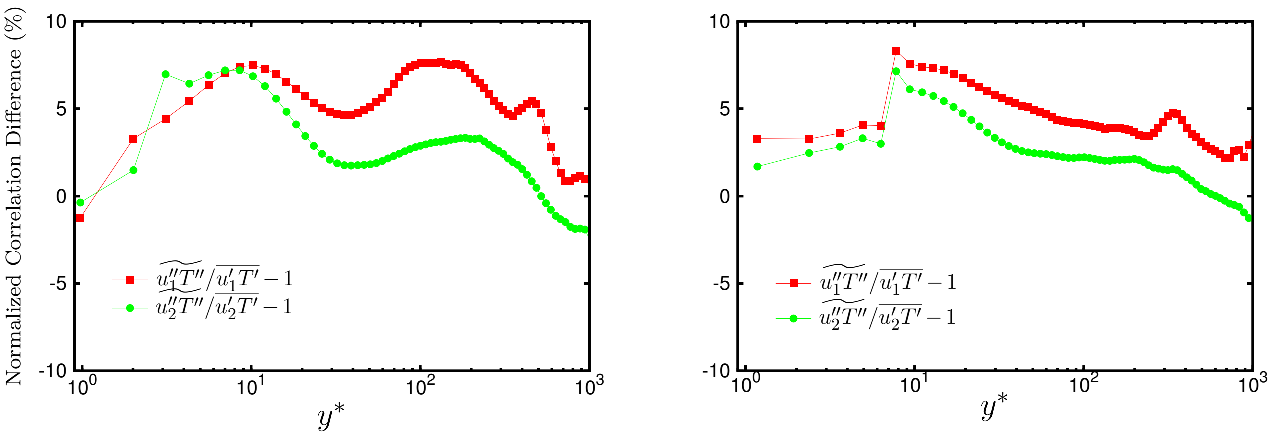

(a) Adiabatic Case

(b) Isothermal Case

Figure IV.18 – Percentage differences between Favre- and Reynolds-averaged heat flux variables across boundary layer: (a) Adiabatic; (b) Isothermal.

the boundary layer is shown in Fig. IV.19a. The streamwise component dominates in both the adiabatic and isothermal case, but there is a significant reduction in the streamwise heat flux levels for the isothermal case consistent with the results for the temperature variance. In addition, the location of the peak amplitude is shifted away from the location of the adiabatic peak to $y^* \approx 30$ even with the semi-local y^* scaling. An interesting feature of the boundary layer distribution is the region in the isothermal distribution where $-\widetilde{u_1''T''} < 0$. In the mean transport equation for the total energy $\overline{\rho}\widetilde{E}$ (Gatski and Bonnet [46]), the turbulent heat flux contribution $-\widetilde{u_1''T''}$ appears as a source term in the equation. As Fig. IV.19a shows, in the vicinity of the wall ($0 < y^* \lesssim 10$), the turbulent heat flux now acts as a sink term in the total energy equation. For the wall-normal heat flux component there is a slight reduction in the amplitude between the adiabatic and isothermal cases, but the qualitative distribution across the boundary layer between the two remains the same. Although small in amplitude, there is a rather large region across the log-layer where $-\widetilde{u_2''T''} < 0$, and where this term acts as a sink in the total energy equation. From the heat flux distribution shown, it does appear that turbulent heat flux effects in close proximity to the wall are essentially removed from the dynamic balance.

The equation of state for a perfect gas that is used here applies to the fluctuating pressure, density, and temperature fields, and it can be rearranged to give a relationship between the different scalar fluxes. The heat flux correlation can then be related to the mass flux and pressure-velocity correlation through

$$-\frac{\widetilde{u_i''T''}}{\widetilde{T}} = \frac{\overline{\rho' u_i'}}{\overline{\rho}} - \frac{\overline{p' u_i'}}{\overline{p}} \ . \tag{IV.21}$$

In the absence of any mean pressure gradients or shocks, the type of boundary layer flow considered here has minimal pressure fluctuations (absence of the acoustic mode). This suggests little or no effect of the pressure-velocity correlation in the balance of Eq. (IV.21) and that the behavior of the heat flux correlation is related to that of the mass flux, which is shown in Fig. IV.19b. The reduction in magnitude for the streamwise mass flux component, shown for the heat flux in Fig. IV.19a, is also shown here with the corresponding peak amplitude shift to $y^* \approx 30$ as in the heat flux distribution. However, unlike the heat flux case, the streamwise mass flux component for both the adiabatic and wall thermal cases essentially coincide starting in the outer part of the log-layer. As in the heat flux case, the wall-normal component is reduced in this isothermal case which further reduces its influence on the flow field dynamics. Although the turbulent mass flux vector does not appear in any of the averaged transport equations in Favre variables, it does provide, as has been shown, a measure of difference between Reynolds-averaged and density-weighted variables.

The dynamics of the heat flux vector can be further assessed by examining the transport equations for the streamwise and wall-normal components of the heat flux vector $\widetilde{u_i''T''}$. These transport equations can be extracted from the mass conservation, fluctuating velocity and fluctuating temperature equations. The resulting form is then given by

$$-A_i + P^1_{Ti} + P^2_{Ti} + \Phi_{Ti} - \varepsilon_{Ti} + D_{Ti} + C_{Ti} = 0 \ , \tag{IV.22}$$

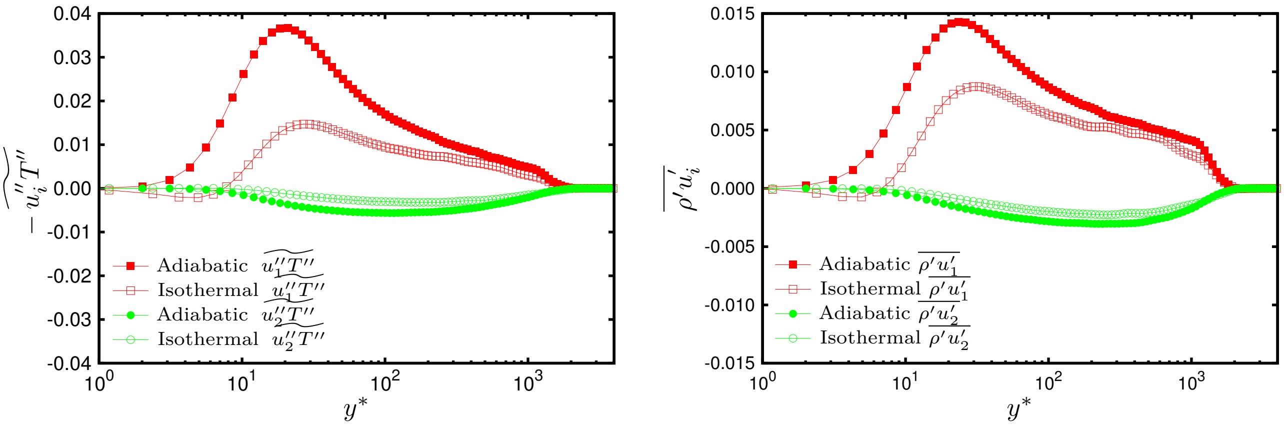

(a) Heat Flux **(b)** Mass Flux

Figure IV.19 – Scalar flux distribution across boundary layer: (a) heat flux; (b) mass flux.

where $A_{Ti} = \overline{\rho}\ \widetilde{u}_j(\partial \widetilde{u_i''T''}/\partial x_j)$ is the advection term, and the remaining terms in the dynamic balance are the production due to the mean temperature and velocity gradients,

$$P^1_{Ti} = -\overline{\rho}\tau_{ik}\frac{\partial \widetilde{T}}{\partial x_k} - \overline{\rho}\widetilde{u_k''T''}\frac{\partial \widetilde{u}_i}{\partial x_k} - \overline{\rho}\,(\gamma-1)\,\widetilde{u_i''T''}\widetilde{S}_{kk} + \left(\frac{\gamma}{c_p}\right)\overline{u_i''\sigma'_{jk}}\widetilde{S}_{kj} \tag{IV.23a}$$

the production due to the fluctuating strain rate field,

$$P^2_{Ti} = \left(\frac{\gamma}{c_p}\right)\left[\overline{u_i''\sigma'_{jk}s''_{kj}} - \overline{u_i''p's''_{kk}}\right] , \tag{IV.23b}$$

the "pressure-scrambling" term,

$$\Phi_{Ti} = -\left[\overline{T''\frac{\partial p}{\partial x_i}}\right] , \tag{IV.23c}$$

the turbulent viscous-thermal dissipation term,

$$\varepsilon_{Ti} = \left(\frac{\gamma}{c_p}\right)\left[\overline{k}_T\overline{\frac{\partial u_i''}{\partial x_k}\frac{\partial T'}{\partial x_k}} + \overline{k'_T\frac{\partial u_i''}{\partial x_k}}\frac{\partial \overline{T}}{\partial x_k} + \overline{k'_T\frac{\partial u_i''}{\partial x_k}\frac{\partial T'}{\partial x_k}}\right] + \left[\overline{\sigma'_{ik}\frac{\partial T''}{\partial x_k}}\right] , \tag{IV.23d}$$

the turbulent and viscous-thermal transport contribution,

$$D_{Ti} = \left(\frac{\gamma}{c_p}\right)\frac{\partial}{\partial x_k}\left[\overline{k}_T\overline{u_i''\frac{\partial T'}{\partial x_k}} + \overline{k'_T u_i''}\frac{\partial \overline{T}}{\partial x_k} + \overline{k'_T u_i''\frac{\partial T'}{\partial x_k}}\right] - \frac{\partial}{\partial x_k}\left[\overline{\rho u_i''T''u_k''} - \overline{\sigma'_{ik}T''}\right] \tag{IV.23e}$$

and terms associated with compressibility,

$$C_{Ti} \; = \; \overline{T''}\frac{\partial \overline{\sigma}_{ik}}{\partial x_k} + \left(\frac{\gamma}{c_p}\right)\left[\overline{u_i''}\overline{\sigma}_{jk}\widetilde{S}_{kj} + \overline{u_i'' s_{kj}''}\left(\overline{\sigma}_{kj} - \overline{p}\delta_{kj}\right)\right] \; . \tag{IV.23f}$$

As the terms in Eq. (IV.23) show, the dynamic balance associated with the transport equation for the heat flux vector is complex owing to the fact that it is a composite of fluctuating momentum and temperature equations. Nevertheless, the various terms listed can be examined across the layer and providing some additional insight into the dynamic balance.

Figure IV.20 shows the distribution of terms appearing in Eqs. (IV.23a) to (IV.23f) for the streamwise heat flux component $-\widetilde{u_1''T''}$. Throughout the inner layer, it is clear that the production due to the fluctuating strain rate field has little impact on the dynamics. On the positive (gain) side, the dynamics are dominated by the production term $\overline{\rho}P_{T1}$ and compressibility term $\overline{\rho}C_{T1}$ in the log-layer and in the outer layer region shown $y \gtrsim 0.02$. Nearer the wall, in the inner layer region, the turbulent and viscous-thermal transport term $\overline{\rho}D_{T1}$ dominates. Note that as the wall is approached, the mean production term $\overline{\rho}P_{T1}$ changes sign and acts as a sink term in the dynamic balance in this region. In the log-layer and outer layer region shown, the destruction terms are composed of the viscous-thermal dissipation, the pressure scrambling term, and the turbulent turbulent and viscous-thermal transport term. In the regions shown, farthest away from the wall, the viscous-thermal dissipation and pressure scrambling terms dominate. Nearer the wall in the inner layer, the viscous-thermal dissipation term dominates the destruction effect.

For the isothermal wall case shown in Fig. IV.20b, the same qualitative description generally holds throughout the layer. However, in the inner layer as the wall is approached, the dynamic balance is altered relative to the adiabatic case. The dynamic roles of the transport, destruction terms, $\overline{\rho}\varepsilon_{Ti}$ are reversed, and $\overline{\rho}\varepsilon_{Ti}$ now acts as a source term and $\overline{\rho}D_{Ti}$ as a sink term. In addition, the production term $\overline{\rho}P^1_{Ti}$, which became slightly negative in the adiabatic case, now has larger negative values in the isothermal case. These changes in the dynamic roles of the various terms would suggest a change in the inner layer behavior of the streamwise heat flux component. From Fig. IV.19a it is seen that as the wall is approached in the adiabatic case, the streamwise heat flux component is positive and monotonically decreasing as the wall is approached. In the isothermal case, Fig. IV.19a shows that the streamwise heat flux becomes slightly negative at $y^* \approx 10$ and monotonically increases to its vanishing wall value.

These results for the streamwise heat flux highlight the difficulty in extracting a RANS-type model that can accurately represent the physical characteristics of the flow. While the behavior of the streamwise heat flux itself is represented by a monotonic decrease (adiabatic) or increase (isothermal) as the wall is approached, the underlying dynamics as represented by the streamwise heat flux transport equation shows a complex interplay between the production, transport and destruction terms. This suggests that usual damping function wall-proximity modifications to any (streamwise) heat flux component model, that is applicable to a range of isothermal wall conditions may not suffice.

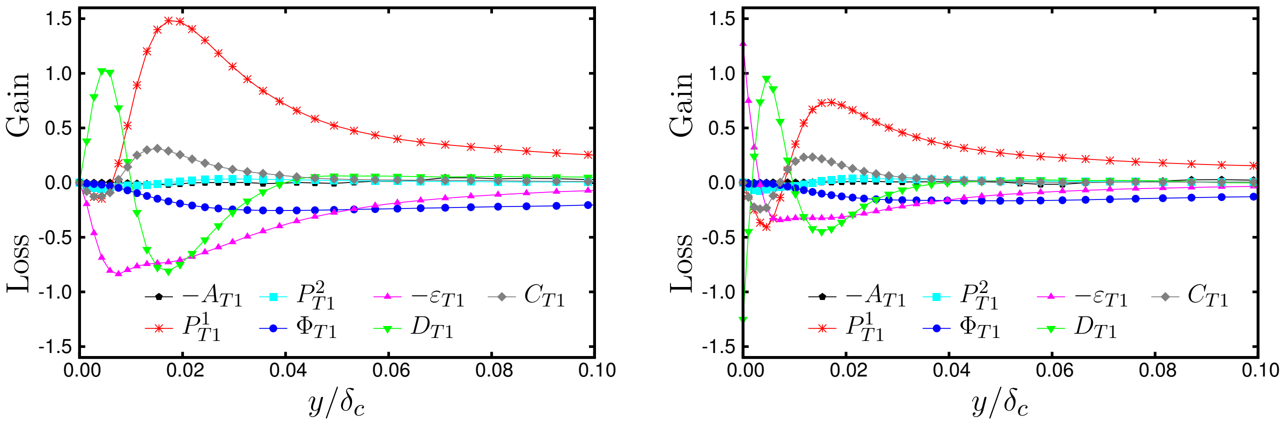

(a) Adiabatic **(b)** Isothermal

Figure IV.20 – Streamwise heat flux component budgets: (a) adiabatic wall, (b) isothermal wall.

The distribution across the inner layer of the terms appearing in Eqs. (IV.23a) to (IV.23f) for the wall-normal heat flux component, $\widetilde{u_2''T''}$ are shown in Fig. IV.21. Once again, throughout the inner layer it is clear that the production due to the fluctuating strain rate field P^2_{T2} has little impact on the dynamics, and in addition, the compressibility term, C_{T2}, now contributes little to the overall dynamics. For the adiabatic case shown in Fig. IV.21a, the net increase in $\widetilde{u_2''T''}$ is dominated by the production due to the mean temperature and velocity gradients, P^1_{T2}, over most of the inner layer. As the wall is approached, the role of the turbulent and viscous-thermal transport term, $D_{T2,}$ is reversed, and it now acts as source term in the transport equation. The net decrease in $\widetilde{u_2''T''}$ is dominated by the pressure-scrambling term, Φ_{T2}, over almost all of the inner layer. It is supplemented by the the transport term, $D_{T2,}$, over a short distance in the lower part of the log-layer, and then by the dissipation term, ε_{T2} in close proximity to the wall. For the isothermal case shown in Fig. IV.21b, the overall role of the various terms just discussed in the adiabatic case remains the same; although, at a reduced magnitude level as would be expected. In close proximity to the wall, a very weak reversal between source and sink contributions between the transport and dissipation terms.

From a modeling perspective, the dynamic balance exhibited by the wall-normal heat flux transport equation is simpler than the corresponding streamwise component. This disparity in behavior, nevertheless, further complicates any modeling behavior. If a vector-tensor representation for the heat flux vector is used rather than the solution of the corresponding transport equations, it will have to be sufficiently general to accommodate this change in dynamic behavior between vector components. Clearly, low-order models have insufficient degrees of freedom to be able to do this generally, and higher-order models will have to be calibrated carefully to properly represent the observed behavior. Fortunately, from Fig. IV.19a, the wall-normal component of the heat-flux vector is negligible when compared to the streamwise component and in absolute terms, as a low-order approximation, it can be neglected in the equation for the mean temperature field.

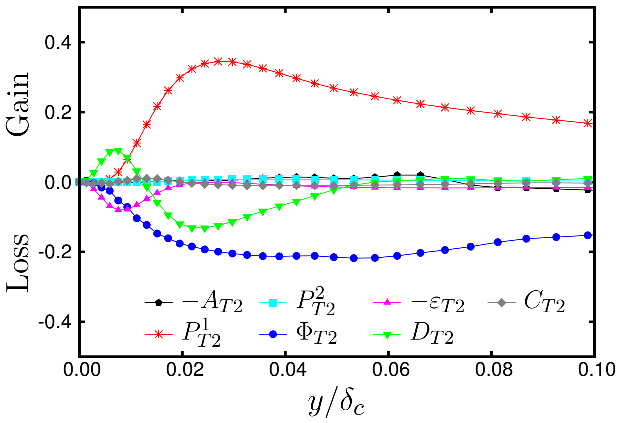

(a) Adiabatic

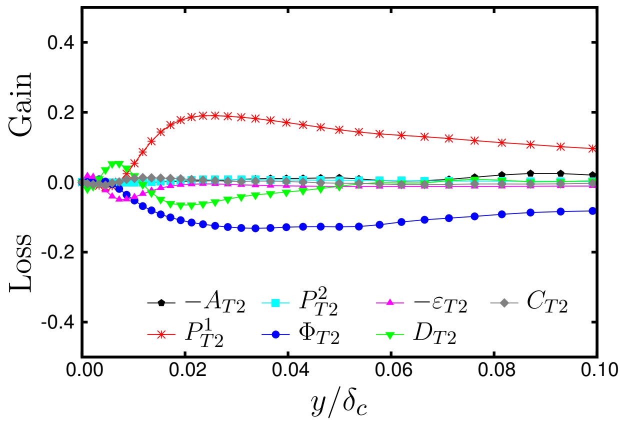

(b) Isothermal

Figure IV.21 – Wall-normal heat flux component budgets: (a) adiabatic wall, (b) isothermal wall.

With the analysis of the mean variables and turbulent velocity and thermal correlations introduced so far, it is possible to construct other parameters relevant to compressible dynamics. Of primary importance are the various relations connected to the forms of the Strong Reynolds Analogy (SRA). One such relation is that associated with turbulent Prandtl number. In general, the various forms that have been assumed can be written as

$$\frac{1}{(\gamma-1)\,M^2}\left(\frac{\tilde{u}}{\tilde{T}}\right)\sqrt{\frac{\widetilde{T''^2}}{\widetilde{u_1''^2}}} = \begin{cases} 1 \quad \text{SRA} \\ \left[Pr_t\left(1-\dfrac{\partial \tilde{T}_t}{\partial \tilde{T}}\right)\right]^{-1} \end{cases} \tag{IV.24}$$

where the value of unity on the right is the original SRA value (Morkovin [113]) and the term extended SRA relation involving the total temperature and Prandtl number fields was proposed by Huang et al. [96] to account for isothermal wall effects. Since the simulations provide all the mean and turbulent variables, Eq. (IV.24) can be inverted and used to obtain the turbulent Prandtl number Pr_t. This value can be compared with the Pr_t definition of the ratio of the turbulent eddy viscosity $\overline{\nu}_t$ to the thermal diffusivity $\overline{\kappa}_t$, $Pr_t = \overline{\nu}_t/\overline{\kappa}_t$, where both diffusivities are obtained from the usual gradient diffusion relations; $\overline{\nu}_t = \widetilde{u_1''u_2''}/\partial\tilde{u}/\partial y$ and $\overline{\kappa}_t = \widetilde{u_2''T''}/\partial\tilde{T}/\partial y$. Figure IV.22 shows the comparison of these two Pr_t estimates in the log-layer region (where the SRA applies). In contrast to the original Prandtl number estimate of unity as first proposed in the SRA, a variation exists across the log-layer. In addition, Fig. IV.22(a) for the adiabatic case shows a qualitatively similar decay behavior for both the Pr_t from the diffusivity ratio and Pr_t from the ESRA Eq. (IV.24). As distance from the wall increases in the log-layer, both Pr_t values tend to vary around $Pr_t \approx 0.9$. A similar decay behavior occurs for the isothermal case shown in Fig. IV.22(b), but with a slightly higher value of Pr_t in the upper part of the log-layer. A Prandtl number variation across the entire boundary layer is best described by the

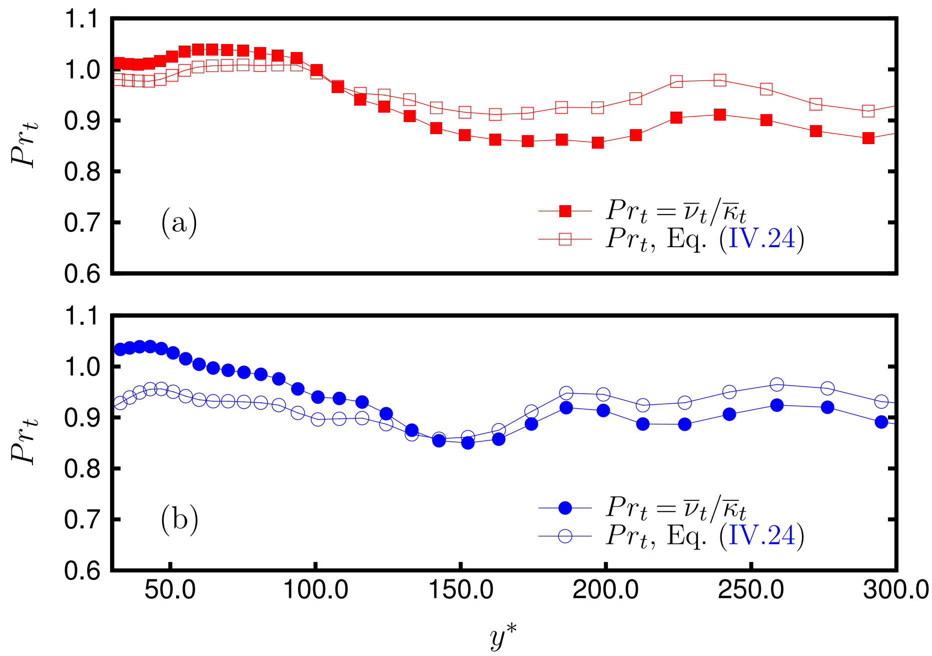

Figure IV.22 – Comparison of Prandtl number Pr_t variation in log-layer region for: (a) adiabatic, and (b) isothermal cases.

mixed Prandtl number given by

$$Pr_m = (\mu + \mu_t)\left[\frac{\mu}{Pr} + \frac{\mu_t}{Pr_t}\right]^{-1} . \tag{IV.25}$$

This composite parameter behaves as the molecular Prandtl number Pr near the wall and as the turbulent Pr_t away from the wall. This is exemplified in Fig. IV.23 which shows that near the wall $Pr_m \approx 0.72$ and away from the wall in the log-layer region, a value of $Pr_m \approx 0.9$ is obtained and with a further decay in the outer layer as the edge of the boundary layer is approached. For values of $y/\delta_c > 0.8$, the turbulent shear stress and heat flux values are extremely small and the accuracy of Pr_t deteriorates.

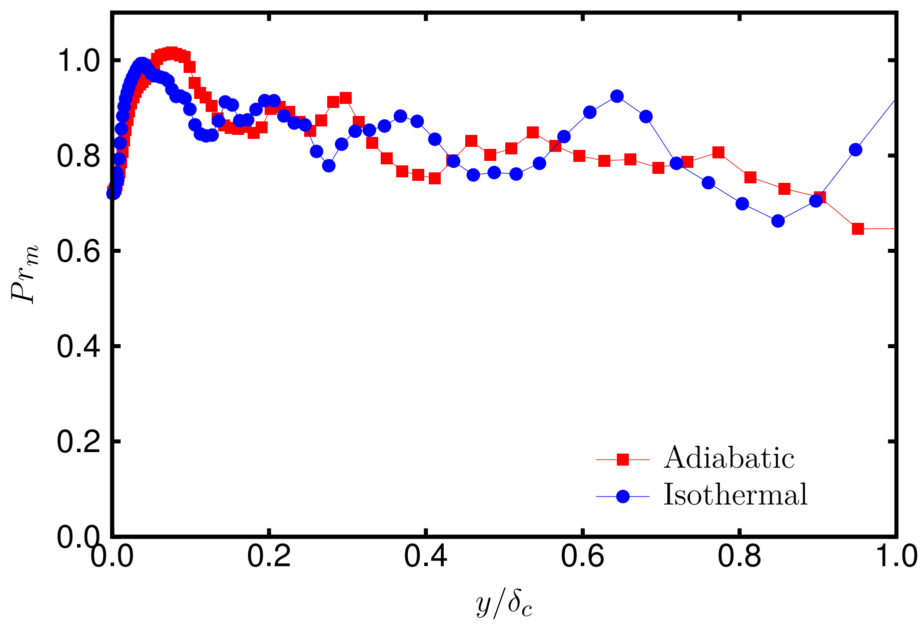

Figure IV.23 – Mixed Prandtl number Pr_m variation across boundary layer.

In addition to a parameter such as Pr_t, which plays an important role in the formulation of gradient diffusion models in heat transfer calculations, the turbulent time scale ratio between the thermal and velocity fields is often introduced (Abe et al. [124], Nagano and Shimada [125], Nagano [126]), and provides a further quantification of the coupling between these fields. This ratio is defined here as

$$R = \frac{K_{th}/\varepsilon_{th}}{K/\varepsilon} \ , \tag{IV.26a}$$

where

$$K_{th} = \frac{\widetilde{T''^2}}{2}, \qquad K = \frac{\widetilde{u_i''^2}}{2}$$

$$\varepsilon_{th} = \frac{\gamma}{Pr}\left[\overline{\overline{\mu}\frac{\partial T''}{\partial x_j}\frac{\partial T'}{\partial x_j}} + \overline{\mu'\frac{\partial T''}{\partial x_j}}\frac{\partial \overline{T}}{\partial x_j} + \overline{\mu'\frac{\partial T''}{\partial x_j}\frac{\partial T'}{\partial x_j}}\right], \quad \varepsilon = \overline{\sigma'_{ij}s'_{ji}}, \tag{IV.26b}$$

with $\overline{\rho}K_{th}$ the thermal potential energy, $\overline{\rho}K$ the turbulent kinetic energy, ε_{th} the dissipation rate of temperature variance, and ε the turbulent kinetic energy dissipation rate. The form of the thermal and velocity dissipation rates differs slightly from the simpler forms usually encountered in incompressible flows. The qualitative and quantitative difference is minor and for consistency with the compressible formulation these complete forms are used here.

As Fig. IV.24 shows, throughout the outer layer R attains a relatively constant value of ≈ 0.49 which is consistent with the commonly accepted value (Béguier et al. [127], Abe et al. [128], Nagano [126]). For homogeneous flows, R also reaches an equilibrium value (e.g. Jin et al. [129]), and can be used for model evaluation and development. For example, the specification of a dissipation rate of temperature variance can be problematic since its associated transport equation contains higher-order correlations that can be difficult to model even for regions away from solid boundaries. With the time scale ratio constant in a region of the flow, the dissipation rate of temperature variance ε_{th} can be extracted with a knowledge of the turbulent kinetic energy, dissipation rate and temperature variance. As has been shown in the budget plots, the behavior near the wall becomes more complex and would require some inclusion, for example, of damping functions to properly account for wall-proximity effects.

IV.6 Summarizing Comments

The results from two direct numerical simulations at similar flow field conditions, but differing in the wall thermal boundary condition, adiabatic and isothermal (cold) wall, have been comparatively analyzed. Mean and turbulent, velocity and thermal variables have been compared both to validate the results relative to theory, where possible, and to isolate the effect of cold thermal wall condition on the flow variables. It was found that mean variable quantities such as shape factor and skin-friction coefficient were consistent with theoretical estimates of isothermal effects. The velocity and temperature law of the wall were found for both the adiabatic and isothermal cases.

An analysis of the turbulent kinetic energy transport equation was performed for the adiabatic and isothermal cases. It was found that the cold wall condition enhanced both the

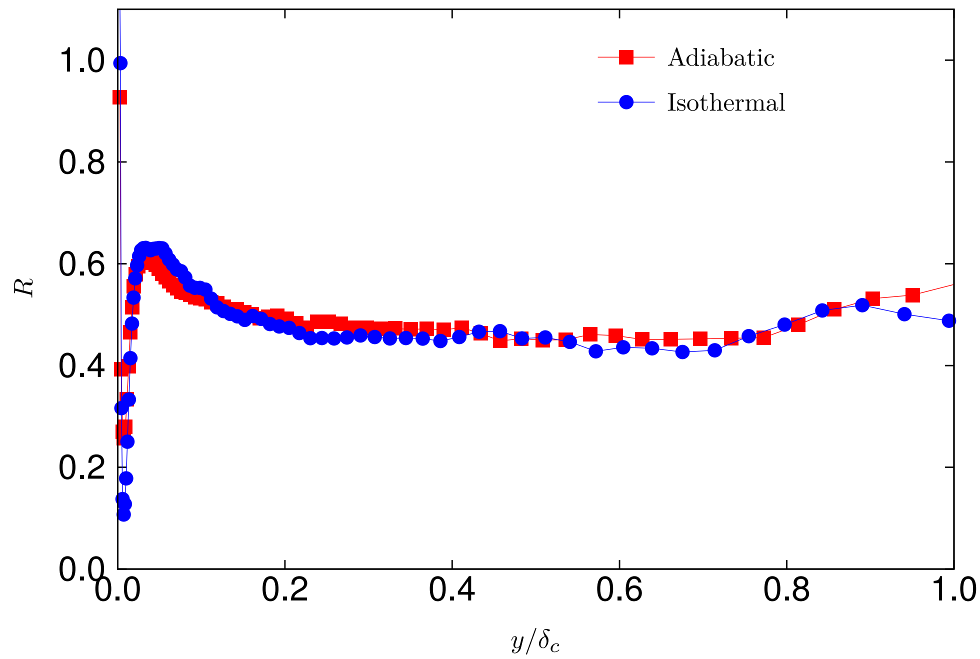

Figure IV.24 – Time scale ratio parameter R variation across boundary layer.

production and destruction terms in the energy balance relative to the adiabatic case. In addition, it was shown that a kinetic energy formed from density-weighted variables differed from the corresponding Reynolds variable kinetic energy by about 6% across the inner and log-layer regions. Two higher-order correlations, the skewness and flatness factors (Reynolds variables) were compared between the adiabatic and isothermal cases. The skewness factor showed the ejections of fluid from the wall is slightly diminished relative to the adiabatic case, however, farther away from the wall there is a slight increase in fluid swept toward the wall in the isothermal case relative to the adiabatic case.

The change in wall thermal conditions had a significant impact on the turbulent thermal fluctuation correlations. The temperature variance distribution across the boundary layer was significantly reduced relative to the adiabatic case; however, a slightly opposite trend occurred for the total temperature variance where, relative to the adiabatic case, the isothermal case showed higher values in the wall layer and only slightly diminished values in the log-layer. An essential quantity in the formulation of closure models for flows with thermal effects is the heat flux vector. It was shown that the difference between heat flux correlations defined using density-weighted and Reynolds variables differed across a significant portion of the boundary layer. The results suggest that any modeling proposals, or at least model calibrations, could be dependent on whether Favre or Reynolds correlations are being considered. Not surprisingly, an analysis of the density-weighted heat flux correlation transport equations, showed a complex balance of production, destruction and redistribution terms in the equation. It was found that the qualitative balance of terms between the adiabatic and isothermal cases was the same for each heat flux component; however, the balance did differ between the streamwise and wall-normal components.

The turbulent Prandtl number variation across the boundary layer was determined from the definition of diffusivities ratio, and from the extended SRA. It was shown that qualitatively similar results in the log-layer were obtained using the two approaches. As distance from the wall increased, the variation in Pr_t diminished and values ~ 0.9 reasonably approximated the Pr_t levels. The mixed Prandtl number Pr_m was used to show the composite variation across the boundary layer. For both Pr_t and Pr_m little qualitative difference existed between the adiabatic and isothermal cases. The turbulent velocity and thermal time scale ratio showed a large variation across the inner part of the boundary layer. Although relatively constant in the outer layer, very near the commonly accepted value of 0.5, such variations show strong wall influences that may complicate its role as a modeling parameter.

Chapter V

Post-Shock Downstream Evolution of Turbulent Boundary Layer

V.1 Introduction

In engineering applications, the interaction of a shock with a turbulent flow is of great practical importance. During the last decade, numerous publications have appeared that contribute significantly to the understanding of the physics involved in the interaction. Due to the complex nature of the phenomenon, the problem is not completely resolved non completely understood. The interaction between a shock and turbulence is mutual. A shock exhibits substantial unsteadiness and deformation as a result of the interaction; whereas, the characteristic velocity, time and length scales of turbulence change considerably. The result of the interaction depends on the strength, orientation, location, and shape of the shock, as well as the flow geometry and boundary conditions. The state of turbulence and compressibility of the incoming flow are additional parameters that also affect the interaction.

V.2 Problem Definition

Similar to no-shock simulations, the effects of shock interaction on the turbulent boundary layer for two different thermal wall boundary conditions, adiabatic and isothermal cold wall, are investigated. The details about the flow conditions, boundary conditions and grid generation have already described in the previous chapters (see sections III.2.4, III.2.5 and IV.2) are not repeated here. The oblique incident shock with a flow deflection angle of 8° is impinged on the boundary layer.

Statistics are obtained at six different streamwise planes, with one plane upstream of the shock-system and the remaining in the relaxation region downstream of the incident shock

	$x_{pos} = (x - x_{imp})/\delta^o_\omega$
Plane	Adiabatic/Isothermal
$P01$	-2.9
$P02$	0.4
$P03$	3.0
$P04$	5.6
$P05$	8.2
$P06$	16.7

Table V.1 – Diagnostic plane positions (x_{imp} is the impingement position of incident shock-wave, and δ^o_ω is the boundary layer thickness at reference station $P01$).

impingement point (see table V.1). At plane $P01$, $Re_x = 5.2 \times 10^6$ with a momentum thickness Reynolds number, Re_θ (based on freestream values), of 3390 for the adiabatic case and 3775 for the isothermal case. Due to the significant distortion of the mean streamwise velocity field, a vorticity measure is chosen for the boundary layer thickness, δ_ω. The vorticity measure is based on the invariant $\sqrt{2\mathsf{II}_W}$ ($2\mathsf{II}_W = -W_{ij}W_{ji}$, and W_{ij} is the skew-symmetric part of the velocity gradient tensor). This allows for a consistent boundary layer measure at all the streamwise positions examined. The threshold vorticity level (2.5) was chosen so that the vorticity thickness ($\delta^o_\omega = 7.66 \times 10^{-2}$) at plane $P01$ coincided with the boundary layer thickness based on 0.99 of the freestream velocity. In the literature, other boundary layer thickness measures have also been suggested. For example, Garnier et al. [58] used a combination dilatation-rotation measure (Ducros sensor, Ducros et al. [130]) and Pirozzoli et al. [131] have recently used a measure based on the spanwise vorticity. At plane $P01$, the Reynolds number based on δ_ω is $Re_{\delta_\omega} = 4.86 \times 10^4$. At each streamwise position, statistics are gathered using 2500 flow-field sets extending over a total time period of $65\delta^o_\omega/U_\infty$. Similar to the no-shock simulations the averages are obtained through a combination of spatial averaging in the (homogeneous) spanwise, z, direction followed by an average in time. A numerical schlieren snapshot of the flow-field for the adiabatic case is presented in figure V.1 in order to illustrate the enhancement of turbulent structures and the change of flow dynamics that occur as a consequence of interaction with the shock-system, and also to indicate the positions of the diagnostic planes used in the present analysis.

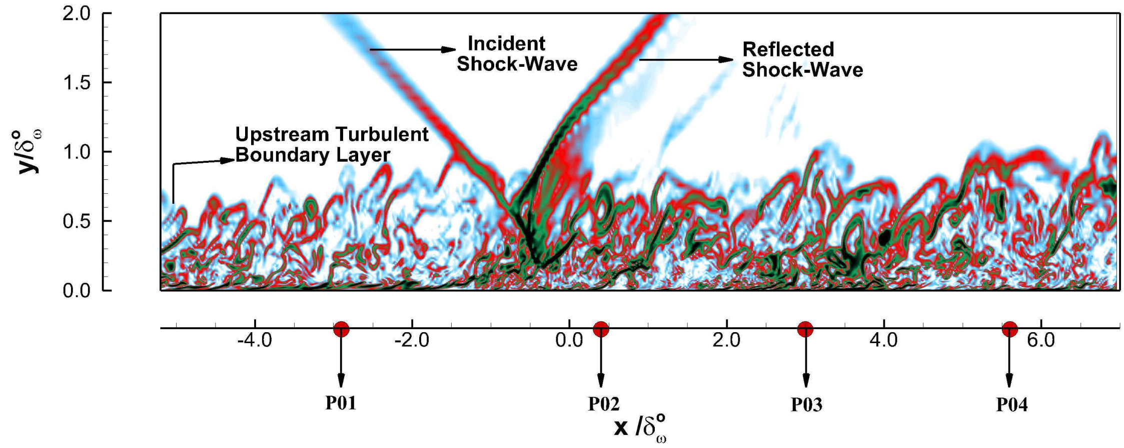

Figure V.1 – Instantaneous numerical schlieren plot for the present direct numerical simulation along with the relative location of the diagnostic planes. Location of stations $P05$ and $P06$ that are not shown are given in table V.1. Contours represent instantaneous density gradient.

V.3 Velocity Field Analysis

The effects induced by the shock on the properties of mean and turbulent velocity fields will be investigated in this section.

V.3.1 Mean Flow Evolution

The characteristics of the turbulent boundary layer downstream of the shock-system (in the immediate vicinity downstream of the incident shock and in the relaxation zone) are studied and a comparison is made with the characteristics of the undisturbed boundary layer to determine whether the distance of around 17 δ_ω^o downwards from the point of impingement of the incident shock is adequate for the flow to relax back to the characteristics observed before the interaction. In numerical simulations, information about the relaxation lengths is useful for closure model development as it can provide an additional means of validation in assessing model performance. As an accurate prediction of the relaxation distances from these models can provide an accurate estimation of the mean and turbulent field evolution.

In order to better understand the dynamics of the evolution within the relaxation zone (dynamic range) the mean primitive variable trends are first presented in outer variable scaling and followed by inner variable scaling. An evolution of mean streamwise velocity profiles downstream of the interaction is presented in Fig. V.2. The velocity scale is normalized by the velocity at the edge of the boundary layer U_e while the length scale with the vorticity based boundary layer thickness δ_ω^l is computed at each streamwise station.

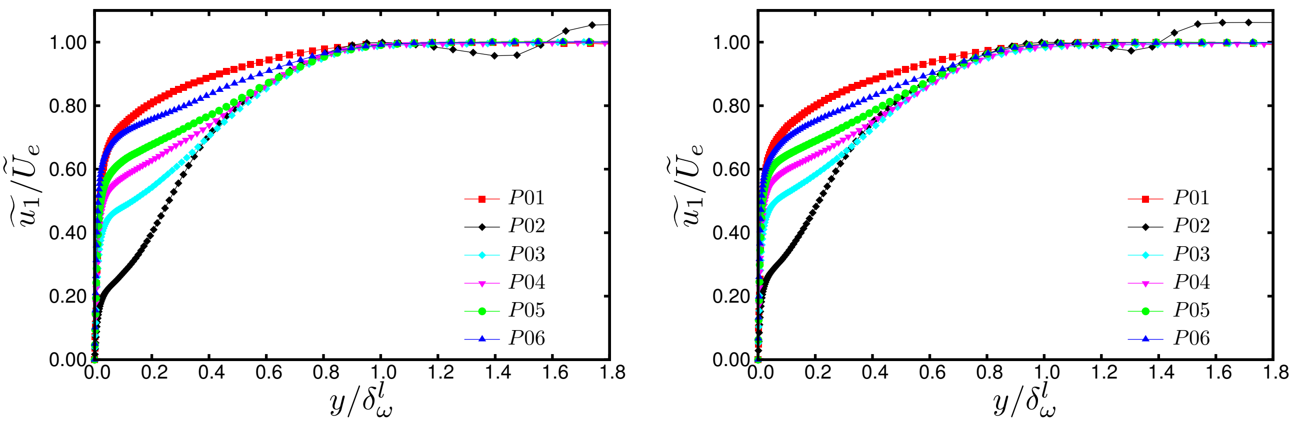

(a) Adiabatic **(b)** Isothermal

Figure V.2 – Post-shock downstream evolution of mean streamwise velocity, $\widetilde{U}/\widetilde{U}_e$: (a) Adiabatic; (b) Isothermal

In comparison to the undisturbed boundary layer profile upstream of the interaction, which represents a fully developed turbulent boundary layer with a negligible transverse component, the redeveloping profiles within the initial stage of relaxation (notably plane $P02$) have a significant velocity deficit in most across of the boundary layer . Note the presence of reflected shock wave at this plane, slightly above the edge of the boundary layer. Further downstream, in the recovery zone, the mean flow gains back its energy from the fluctuating flow field and relaxes towards its undisturbed state. After an inspection of these profiles it can be deduced that the boundary layer is not able to completely relax to a mean equilibrium state within the distance of around 17 δ_ω^o downstream of the extrapolated wall impact point of the incident shock wave, hence the distance is not enough to exactly get back its initial undisturbed state. The length of the recovery zones observed in different experimental and numerical simulations studies are summarized in Table V.2. Only the results presented in [10] shows a well-recovered mean flow field while the other studies either demonstrate a partial recovery of the flow field or primarily focused on the interaction region.

The van Driest transformed streamwise velocity profiles are shown in Fig. V.3a and Fig. V.3b for the adiabatic and isothermal cases respectively as a function of the distance from the wall y^+. In contrast to the mean velocity profiles in Fig. V.2, the transformed velocity profiles provide a clearer quantification of the downstream boundary layer recovery. Upstream of the interaction, the flow is identical to the no-shock case, and the results from DNS follows the expected

Table V.2 – Length of recovery zone studied

Study Type	Reference	Length of recovery zone examined in δ_c^o
Experimental	Deleuze [10]	12
Experimental	Laurent [57]	8
Experimental	Humble [16]	2
Numerical(DNS)	Priebe et al. [15]	5
Numerical(DNS)	Pirozzoli et al. [13]	11
Numerical(LES)	Morgan et al. [74]	2
Numerical(LES)	Garnier [66]	8

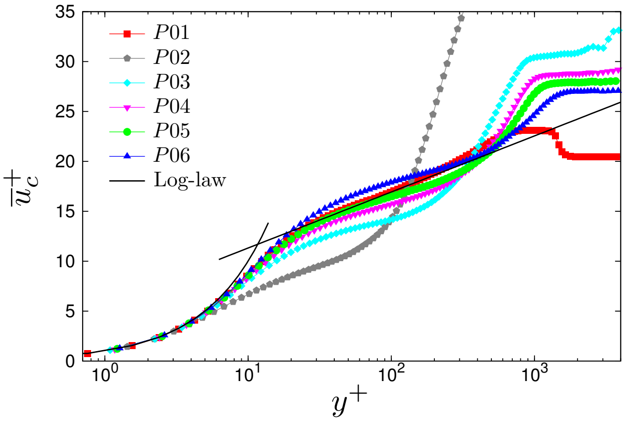

(a) Adiabatic Case

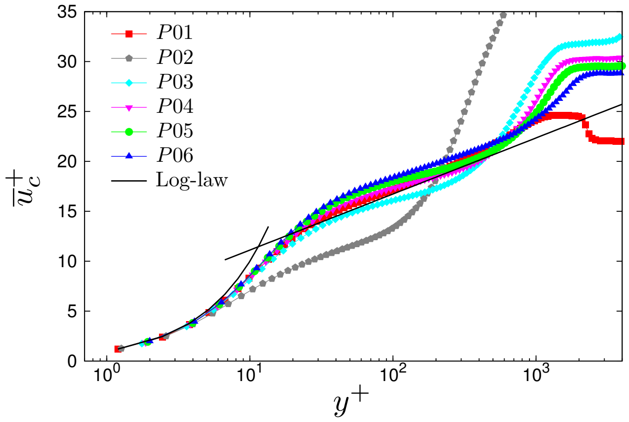

(b) Isothermal Case

Figure V.3 – Post-shock downstream evolution of van Driest transformed mean streamwise velocity, $\overline{u}_c^+$: (a) Adiabatic; (b) Isothermal

logarithmic law in the region $15 > y^+ < 300$. As the flow experiences a strong perturbation in the interaction region caused by the induced adverse pressure gradient, the planes ($P02$-$P05$) downstream of the incident shock display a characteristic 'dip' below the log-law, indicating the non-equilibrium state of the boundary layer. A similar behavior was found by Priebe et al. [15] in their impinging shock simulation as well as in the compression corner experiments of Smits and Muck [8]. These dips suggest that in this region the length scale increases with the distance from the wall at a rate greater than κy where κ is the von Kármán constant and y is the distance from the wall. The results presented at the very downstream plane ($P06$) show that the profiles are almost relaxed back to an undistorted state, and well-defined, sublayer, log and wake regions are observed as in the incoming turbulent boundary layer.

For the isothermal case, the results exhibit the same qualitative trends as the adiabatic case. However there are some differences that need to be discussed. The transformed velocity profile for the incoming boundary layer (plane $P01$) lies above the log-law, with a value of κ nearly equivalent to that of the law-of-the-wall but with a slight variation in value of C. This deviation from the log-law is caused by the non-zero value of normalized heat flux parameter $B_q = -0.017$, which has already been discussed in detail (see chapter IV, section IV.2). In addition, the flow regains an undistorted state more rapidly than the adiabatic case.

V.3.2 Turbulence Properties Evolution

V.3.2.1 Reynolds Stress Tensor Amplification and Evolution

One of the most significant effects of the shock-turbulence interaction is the fact that the turbulent fluctuations increase and the turbulent length scales decrease when passing through sufficiently strong shocks. For a detailed review about this subject see Andreopoulos [132]. In order to give an estimate of the amplification of turbulent stresses across the shock, some results are summarized in Table V.3. The amplification factors presented in Table V.3 represent the ratio of the maximum value of a particular Reynolds stress component after the interaction with the peak value of the corresponding stress component in the incoming boundary layer. These studies show that the Reynolds stress tensor undergoes an anisotropic amplification as the flow passes through the shock system. The level of amplification depends upon the strength, orientation and shape of the shock, the state of turbulence and compressibility of the incoming flow, as well as the flow geometry and the boundary conditions.

The behavior of various components of the Reynolds stress tensor at different streamwise locations is shown in (Fig. V.4a, V.5a, V.6b, V.7b) and (Fig. V.4b, V.5b, V.6b, V.7b) for the adiabatic and the isothermal cases, respectively. The Reynolds stresses are normalized by the velocity scale at the edge of the boundary layer (U_e). The simulation parameters of the present DNS are closely related to the experimental conditions of Deleuze [10]. The results confirm that the interactions produce a large increase in turbulence activity. The maximum amplification is found in wall-normal component ($\overline{u_2'u_2'}$) while the streamwise component ($\overline{u_1'u_1'}$) amplified the least. The Reynolds stress distributions obtained as a result of interaction in the present direct simulation are qualitatively quite similar to the ones obtained by Deleuze [10] for the impinging shock case, and in addition the amplification factors estimated in these two studies are also comparable. The evolution of the streamwise component ($\overline{u_1'u_1'}$,Fig. V.4a) demonstrates that the effect of the interaction shifts the maximum of the stress from the very near wall region to a level of $y/\delta_\omega^l \approx 0.26$ (Plane,$P02$) in the boundary layer, and as also reported by, Garnier

Table V.3 – Amplification factors for fluctuating components

Case	Reference	Mach number	Scaling type	Amplification factor			
				u_1u_1	u_2u_2	u_3u_3	u_1u_2
Compression ramp,18°	Adams [51]	3.0	$\overline{\rho u_i'' u_j''}$	4.0	$n.a$	$n.a$	13.0
Compression ramp,24°	Wu and Martin [14]	2.9	$\overline{\rho u_i' u_j'}/\overline{\rho} U_\infty^2$	6.0	12.0	6.0	24.0
Compression ramp,16°	Smits and Muck [8]	2.9	$\overline{\rho}\overline{u_i' u_j'}/\rho_\infty U_\infty^2$	5.0	$n.a$	$n.a$	6.0
Compression ramp,20°	Smits and Muck [8]	2.9	$\overline{\rho}\overline{u_i' u_j'}/\rho_\infty U_\infty^2$	7.0	$n.a$	$n.a$	12.0
Impinging shock ,12°	Priebe et al. [15]	2.9	$\overline{\rho u_i' u_j'}/\overline{\rho} U_\infty^2$	10.0	18.0	10.0	21.0
Impinging shock ,8°	Deleuze [10]	2.28	$\overline{u_i' u_j'}/U_e^2$	1.4	3.4	$n.a$	2.3
Impinging shock ,8°	Present DNS,Adiabatic	2.25	$\overline{u_i' u_j'}/U_e^2$	1.2	4.6	3.2	3.7
Impinging shock ,8°	Present DNS,Isothermal	2.25	$\overline{u_i' u_j'}/U_e^2$	1.2	4.1	2.9	3.7

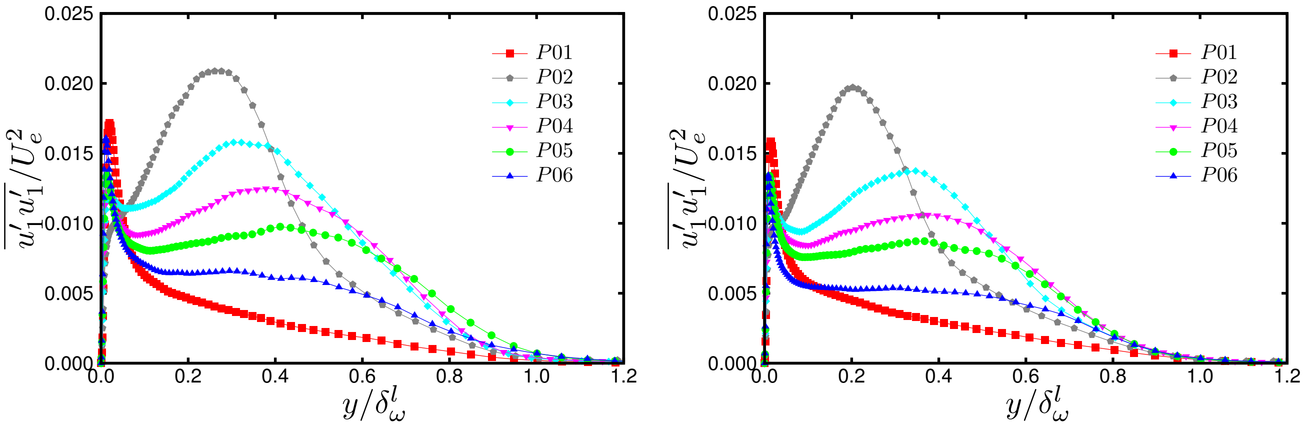

(a) Adiabatic Case **(b)** Isothermal Case

Figure V.4 – Post-shock downstream evolution of streamwise component of turbulent normal stress, $\overline{u_1' u_1'}/U_e^2$: (a) Adiabatic; (b) Isothermal

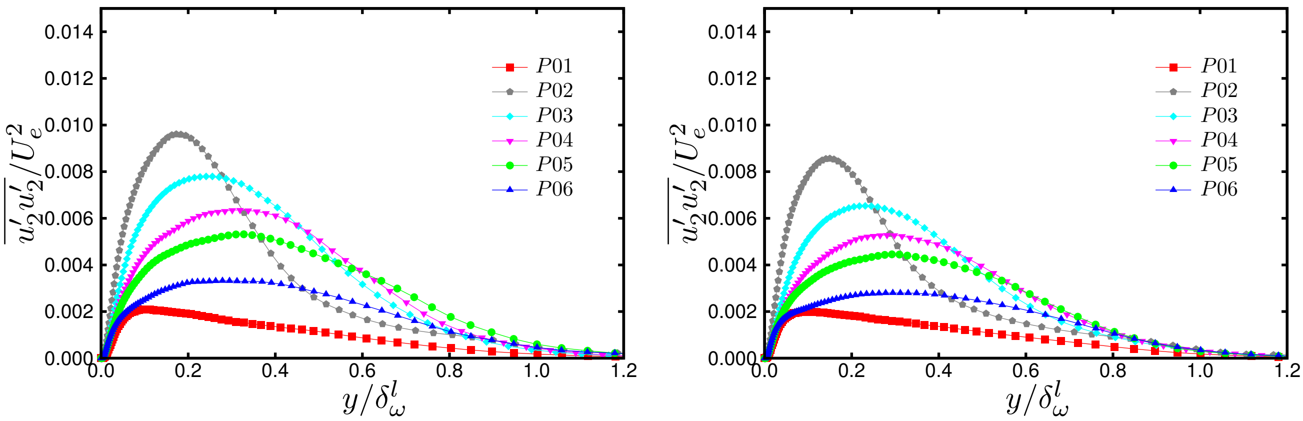

(a) Adiabatic Case **(b)** Isothermal Case

Figure V.5 – Post-shock downstream evolution of wall-normal component of turbulent normal stress, $\overline{u_2'u_2'}/U_e^2$: (a) Adiabatic; (b) Isothermal

[66], Laurent [57], Deleuze [10] and Selig et al. [9]. Further downstream in the recovery zone (Planes,$P03$-$P06$), the presence of a second peak in the stress distribution very near to the wall is observed, as well as the diminution of stress levels in the outer part of the boundary layer, which correlates with the progressive return of the boundary layer toward an energetic equilibrium state.

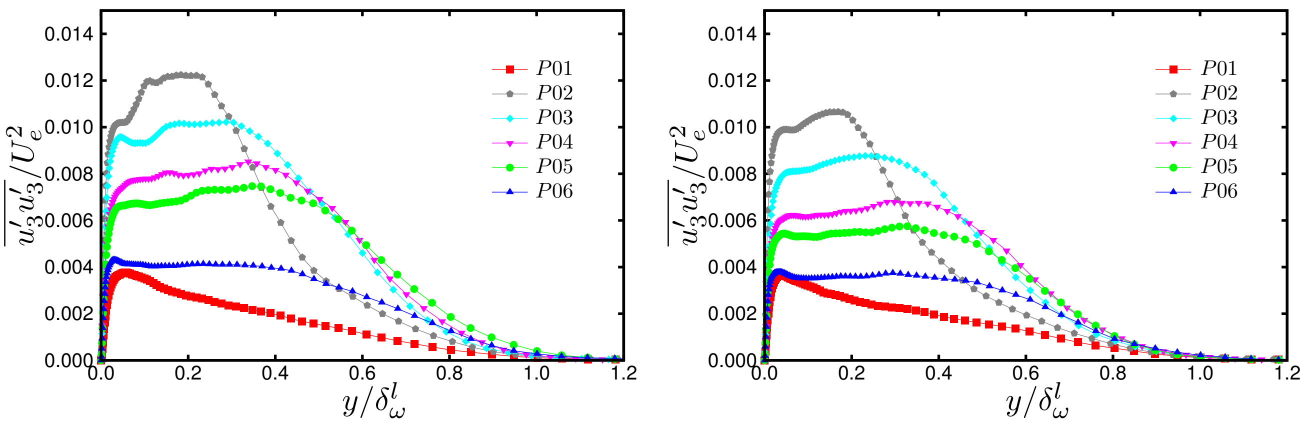

(a) Adiabatic Case **(b)** Isothermal Case

Figure V.6 – Post-shock downstream evolution of spanwise component of turbulent normal stress, $\overline{u_3'u_3'}/U_e^2$: (a) Adiabatic; (b) Isothermal

The qualitative trends of the rest of the components are almost similar(Fig. V.5a, V.6a,

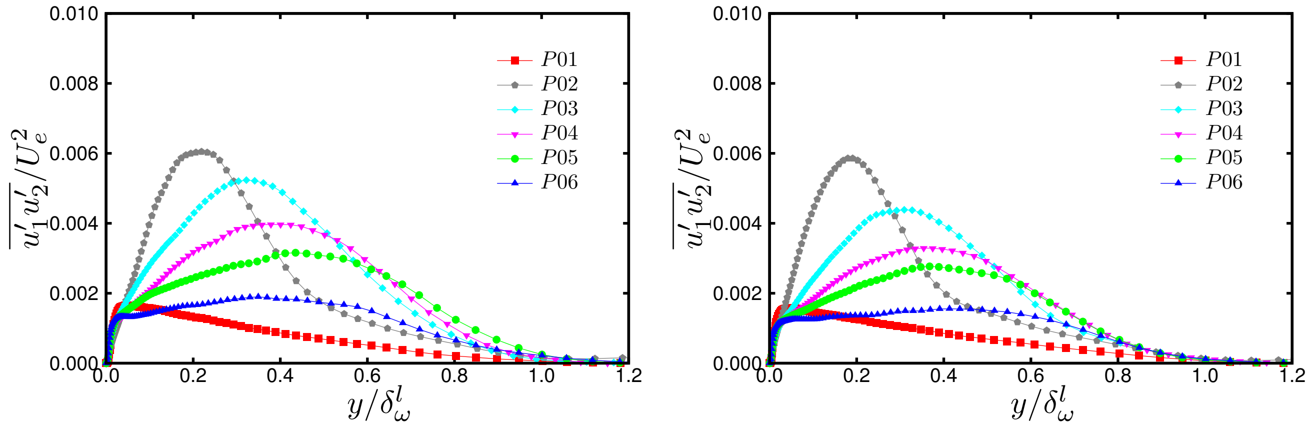

(a) Adiabatic Case

(b) Isothermal Case

Figure V.7 – Post-shock downstream evolution of turbulent shear stress, $\overline{u_1'u_2'}/U_e^2$: (a) Adiabatic; (b) Isothermal

V.7a). Just after the interaction, there is a characteristic rise of the turbulence level away from the wall and then a subsequent drop-off in values downstream in the recovery zone.

The observations are similar for the isothermal case, except for the slight diminution in the amplification factors of the wall-normal and spanwise Reynolds stress components with respect to the adiabatic case (Table V.3), and the results presented at the very downstream station are closer to those in the undistorted state than from the adiabatic simulation, and which is consistent with the observation in Fig. V.3.

In Fig. V.8–V.11, the Reynolds stress tensor is presented in the form of Morkovin scaling as a function of the wall-normal distance in wall units (y^+). Morkovin's [113] hypothesis asserts that the compressibility or Mach number only affects the turbulence (at least the velocity correlations) through variations in mean density, and that fluctuations in density ρ' have little effect on the turbulence. The type of scaling ($\overline{\rho}\overline{u_i'u_j'}/\overline{\rho}_w u_\tau^2$) allows the collapse of results obtained from supersonic and subsonic flows, i.e. it takes into account the variation of density and also the flows with and without heat transfer. For the best representation of the near wall region, the results are plotted on a logarithmic scale. Once again, the level of amplification is close to the one presented by Deleuze [10]. It is evident from the results that, similar to the previous representation the wall-normal component of the Reynolds stress is amplified the most. The amplification factor is about 5.2 for the streamwise component as compared to 6.2 in Deleuze experiments , 15.6 as compared to 12.5 for the wall-normal component, 11.9 for the spanwise component, and 12.9 as compared to 11.0 for the shear component. The near wall relaxation

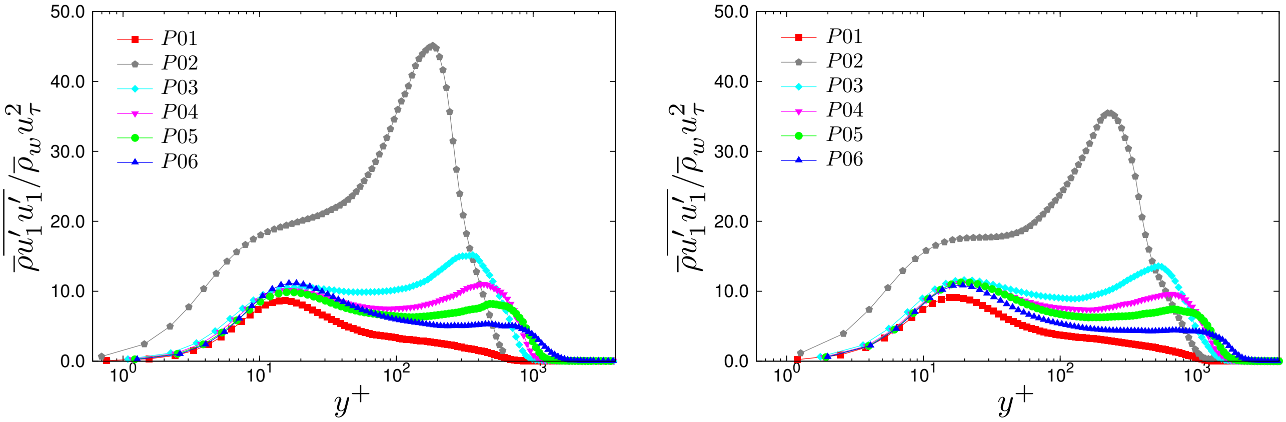

(a) Adiabatic Case

(b) Isothermal Case

Figure V.8 – Post-shock downstream evolution of streamwise component of turbulent normal stress in terms of wall unit scaling, $\overline{\rho u_1' u_1'}/\overline{\rho}_w u_\tau^2$: (a) Adiabatic; (b) Isothermal

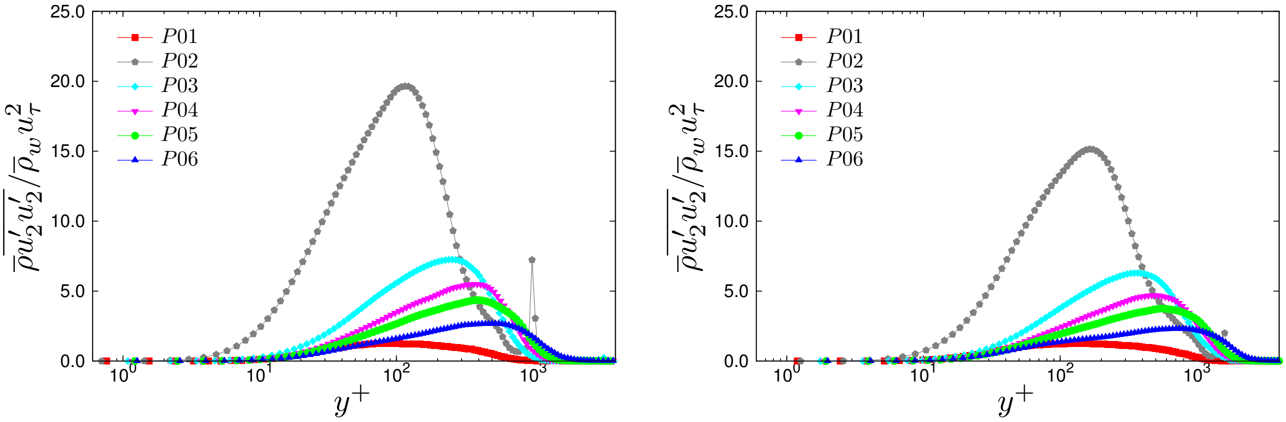

(a) Adiabatic Case

(b) Isothermal Case

Figure V.9 – Post-shock downstream evolution of wall-normal component of turbulent normal stress in terms of wall unit scaling, $\overline{\rho u_2' u_2'}/\overline{\rho}_w u_\tau^2$: (a) Adiabatic; (b) Isothermal

of stresses is clearly more visible in the present scaling. It is observed from the results that the streamwise component relaxes up to a larger wall-normal extent in the boundary layer around ($y^+ \approx 200$) as compared to the other components of the Reynolds stress tensor. As suggested by Smits and Muck [8], the unsteady shock motion smears the region over which the amplification occurs, and it may produce a local peak in the turbulence intensity profiles. At the streamwise plane $P02$, this behavior is also observed in the distributions of wall-normal ($\overline{\bar{\rho} u_2' u_2'}/\bar{\rho}_w u_\tau^2$) and shear ($\overline{\bar{\rho} u_1' u_2'}/\bar{\rho}_w u_\tau^2$) stresses outside the edge of the boundary layer.

For the isothermal case, the amplification factors are comparatively less than the adiabatic case. The streamwise component is amplified by a factor of 3.9, the wall-normal by 12.1, the spanwise by 8.6 and the shear component by 10.9.

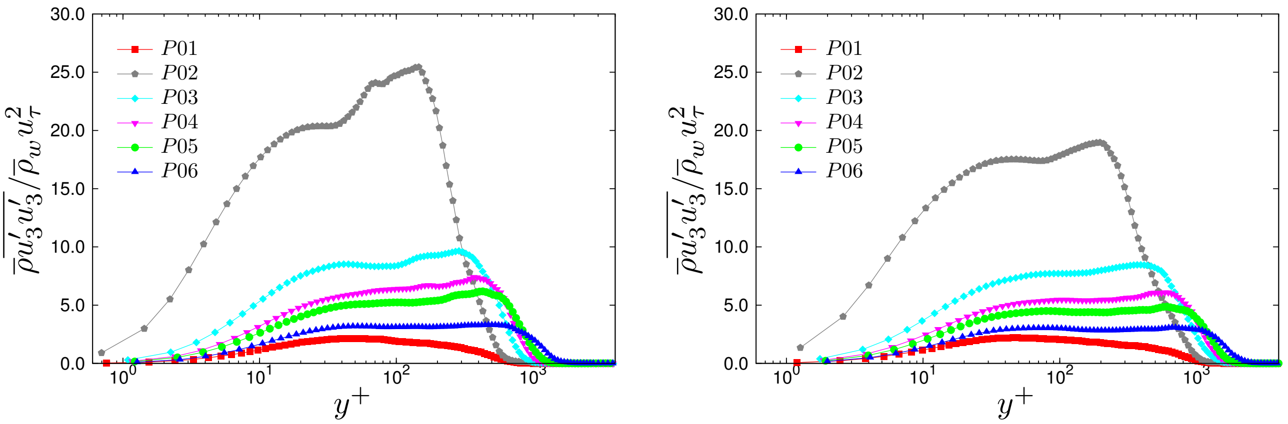

(a) Adiabatic Case **(b)** Isothermal Case

Figure V.10 – Post-shock downstream evolution of spanwise component of turbulent normal stress in terms of wall unit scaling, $\overline{\bar{\rho} u_3' u_3'}/\bar{\rho}_w u_\tau^2$: (a) Adiabatic; (b) Isothermal

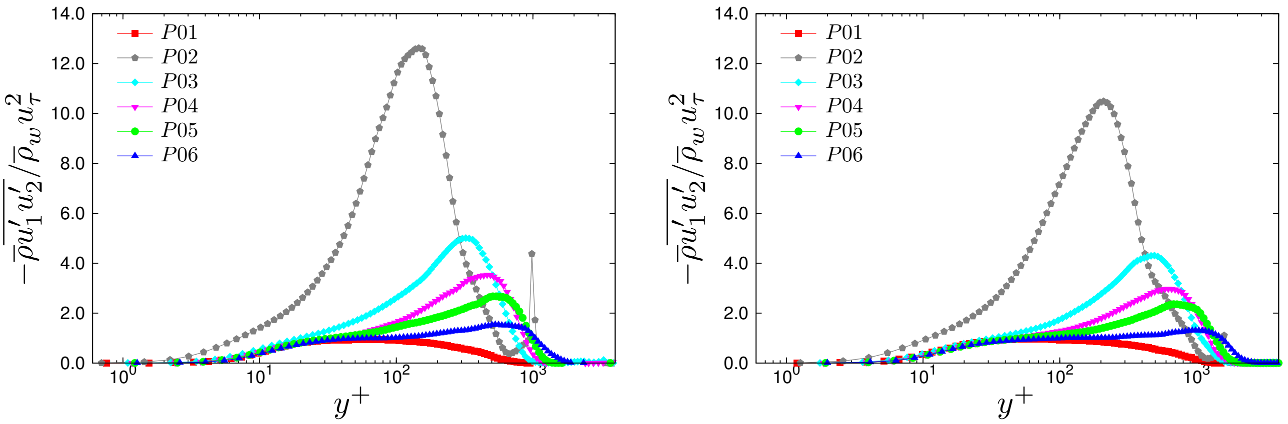

(a) Adiabatic Case **(b)** Isothermal Case

Figure V.11 – Post-shock downstream evolution of turbulent shear stress in terms of wall unit scaling, $\overline{\bar{\rho} u_1' u_2'}/\bar{\rho}_w u_\tau^2$: (a) Adiabatic; (b) Isothermal

V.3.2.2 Structure Parameters Evolution

In order to characterize the turbulence structure of the interaction, independent of the magnitude of the velocity fluctuations, the results are presented in terms of the correlation coefficient and turbulent stress ratios. The evolution of the correlation coefficient between u_1 and u_2 ($R_{u_1u_2}$) is shown in Fig. V.12 and defined by

$$R_{u_1u_2} = \frac{\overline{u_1'u_2'}}{\sqrt{\overline{u_1'}^2}\sqrt{\overline{u_2'}^2}}, \tag{V.1}$$

Upstream of the interaction (plane $P01$), the correlation coefficient $-R_{u_1u_2}$ varies from a value of about 0.25 very near the wall region to around 0.45 in the outer part of the boundary layer. Farther from the wall, it deviates a little throughout a large portion of the boundary layer ($0.15 < y/\delta_c^l < 0.6$) and then starts decreasing near the edge of the boundary layer. The behavior is in accordance with the earlier results obtained in subsonic (Klebanoff [133], Skåre and Krogstad [134]) and supersonic (Elena and Lacharme [135], Deleuze [10], Pirozzoli and Grasso [13], Humble [16]) flows studies.

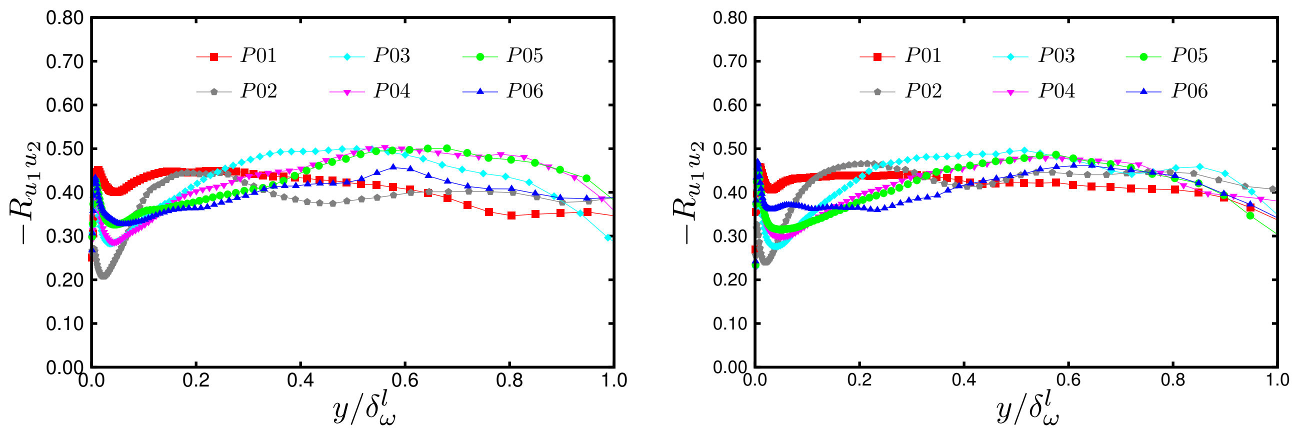

(a) Adiabatic Case **(b)** Isothermal Case

Figure V.12 – Post-shock downstream evolution of correlation coefficient, $-R_{u_1u_2}$: (a) Adiabatic; (b) Isothermal

A common finding in the previous studies is the presence of a constant $-R_{u_1u_2}$ region in the outer part of the boundary layer. The constant values observed in these moderate Reynolds number studies closely resemble the subsonic flow value ($-R_{u_1u_2} \approx 0.5$). Contrary to this, Fernando and Smits [136] indicated that $-R_{u_1u_2}$ decreases significantly with the distance from the wall, and suggested a compressibility effect as a possible cause; Although, alternatively it has been suggested that such a decreasing trend may be due to a high Reynolds number effect (see Smits and Dussauge [44]) for further discussion).

Downstream of the interaction, the correlation coefficient $-R_{u_1u_2}$ varies significantly very near the wall and decreases to 0.2. The effect of the interaction augments the level of correlation in the outer part of the boundary layer to a value ≈ 0.5 (Planes $P03$-$P05$). This increase in correlation in the outer part of boundary layer has been also reported by Deleuze [10] and Fernando and Smits [136]. The strong correlation between u_1' and u_2' implies the existence of large scale eddies downstream of the interaction (Kuntz et al. [49]). As a result of gradual dissipation and diffusion of turbulence through the boundary layer, a somewhat relaxed correlation distribution is obtained at the far downstream station ($P06$). Analogous conclusions are reached for the isothermal case.

Turbulent stress ratios are often investigated in order to quantify the relative contribution of each component of the turbulent stress tensor with respect to the others. Here these ratios are defined as

$$a_1 = \frac{\overline{u_2'u_2'}}{\overline{u_1'u_1'}}, \qquad a_2 = \frac{\overline{u_3'u_3'}}{\overline{u_1'u_1'}}, \qquad a_3 = \frac{\overline{u_2'u_2'}}{\overline{u_3'u_3'}}$$
$$a_4 = \frac{\overline{u_3'u_3'}}{\overline{u_1'u_1'}+\overline{u_2'u_2'}}, \qquad a_5 = \frac{-\overline{u_1'u_2'}}{2k_t} \tag{V.2}$$

where k_t is the turbulent kinetic energy, $k_t = (\overline{u_1'u_1'}+\overline{u_2'u_2'}+\overline{u_3'u_3'})/2$.

In the literature, the ratios a_1 and a_5 are referred to as the anisotropy parameter and the structure parameter, respectively. Fig. V.13 shows the variation of the anisotropy parameter a_1 across the boundary layer downstream of the interaction in comparison to the upstream undisturbed state. Upstream of the interaction the anisotropy parameter varies considerably near the wall; however, in most of the boundary layer ($0.15 < y/\delta_\omega^l < 0.8$) it remains almost constant at a level ≈ 0.45. Close to the wall, low values of a_1 imply that the impact of the wall forces the turbulence to become dominant in the streamwise direction and thus causes a deviation from its isotropic state. The observed value of $a_1 \approx 0.45$ lies within the range of values (0.25–0.45) found in different supersonic flow experiments (Deleuze [10], Humble [16], Fernando and Smits [136], Elena and Lacharme [135]), and it was suggested by Smits and Dussauge [44] that the differences are possibly due to the Reynolds number effect. For the incompressible flows, the a_1 parameter varies around $0.40-0.45$ (Klebanoff [133], Skåre and Krogstad [134], Spalart [111]).

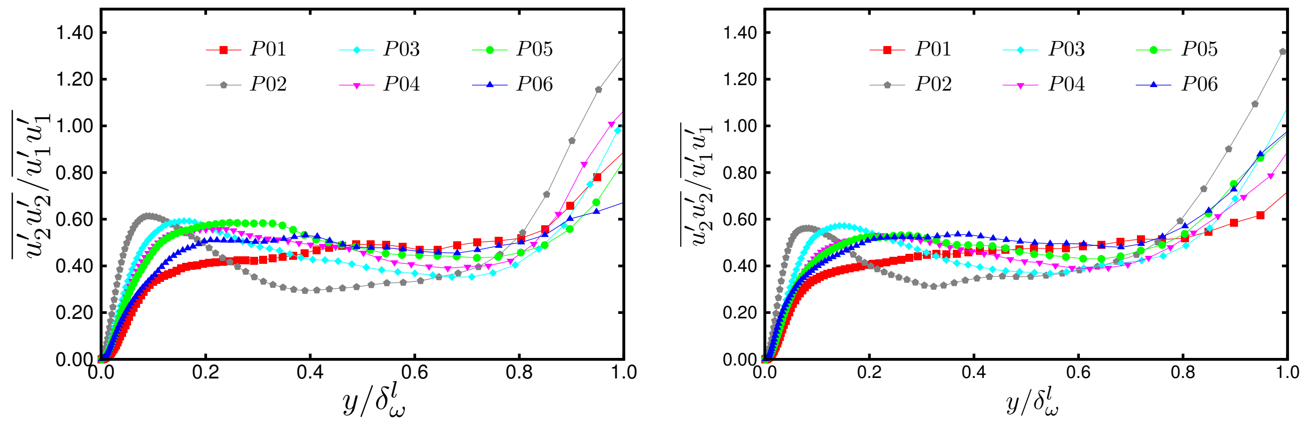

(a) Adiabatic Case **(b)** Isothermal Case

Figure V.13 – Post-shock downstream evolution of turbulent stress ratio, $a_1 = \overline{u_2'u_2'}/\overline{u_1'u_1'}$: (a) Adiabatic; (b) Isothermal

Downstream of the interaction, the anisotropy parameter changes noticeably in the inner part of the boundary layer. The effect of the interaction augments the level of wall-normal fluctuations with respect to the streamwise fluctuations in the inner part of the boundary layer while in the outer layer the effect is the opposite. Similar observations have also been made by Deleuze [10], Humble [16]. Near the edge of the boundary layer the values of the anisotropy parameter systematically rise above unity (plane $P02$), this behavior is attributed to wall-normal fluctuations occurring in the outer intermittent part of the boundary layer, which do not affect the streamwise velocity fluctuations since the mean velocity defect is considered small. The trends are similar for the isothermal case.

For the main part of the undisturbed boundary layer ($0.15 < y/\delta_\omega^l < 0.90$), the turbulent stress ratios a_2 and a_3 are roughly constant at ≈ 0.6 and ≈ 0.7 respectively. Similar to a_1, these values are nearly equal to the observed values in incompressible flows (Skåre and Krogstad [134]). As expected $\overline{u_2'u_2'}$ is seen to vanish faster than $\overline{u_1'u_1'}$ and $\overline{u_3'u_3'}$ near the wall (Fig. V.13, Fig. V.14) owing to the stronger damping of fluctuations normal to the wall than in the planes parallel to it. Near the boundary layer edge, the ratios grow, primarily because $\overline{u_2'u_2'}$ decays at a slower rate than $\overline{u_1'u_1'}$ and $\overline{u_3'u_3'}$. Therefore, in the outer boundary layer the ratio $\overline{u_3'u_3'}/\overline{u_1'u_1'}$ is virtually independent of y/δ_ω^l.

As a consequence of the interaction, the ratio a_2 increases sharply very near the wall ($y/\delta_\omega^l < 0.15$), showing a large increase in the turbulence activity in the spanwise direction. In contrast,

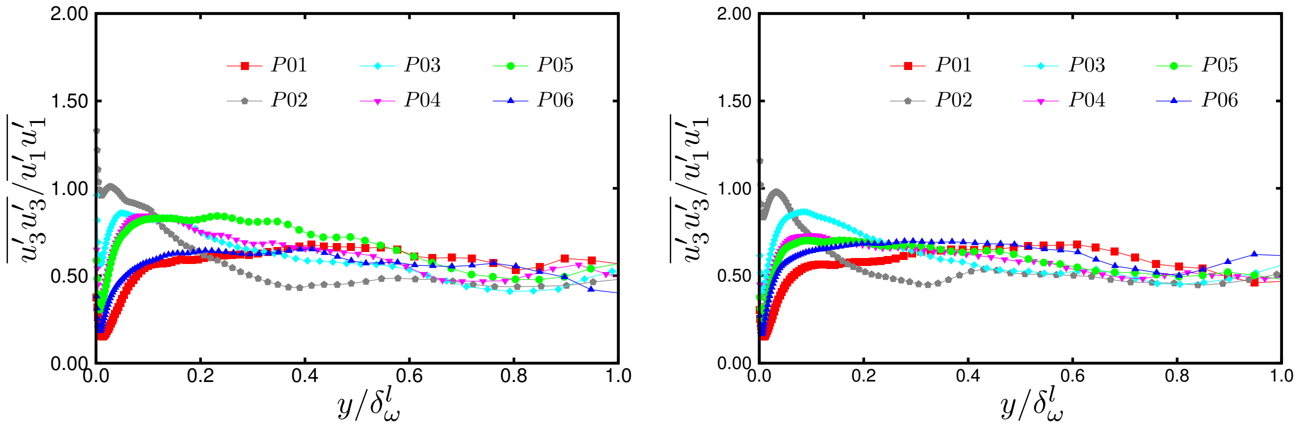

(a) Adiabatic Case   **(b)** Isothermal Case

Figure V.14 – Post-shock downstream evolution of turbulent stress ratio, $a_2 = \overline{u_3'u_3'}/\overline{u_1'u_1'}$: (a) Adiabatic; (b) Isothermal

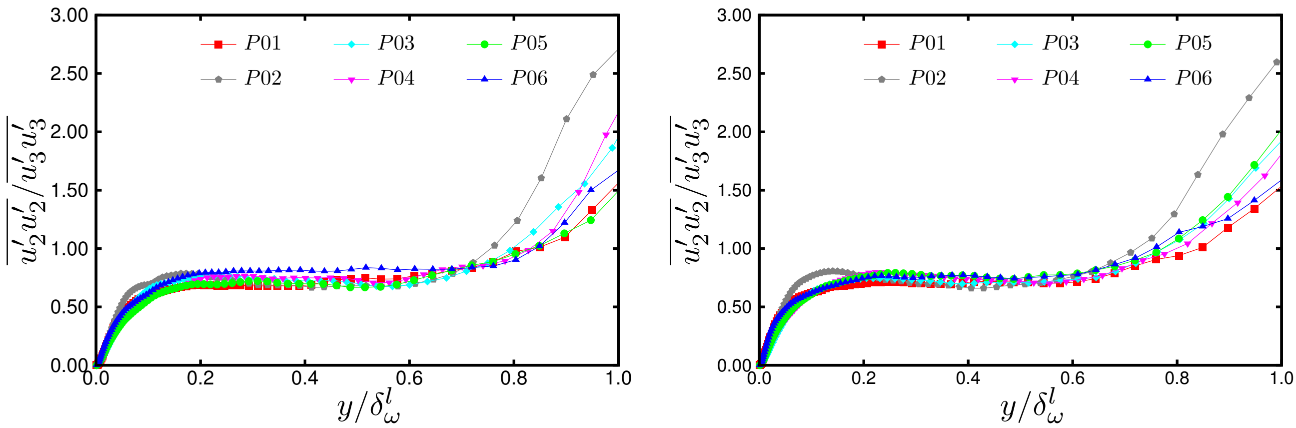

(a) Adiabatic Case   **(b)** Isothermal Case

Figure V.15 – Post-shock downstream evolution of turbulent stress ratio, $a_3 = \overline{u_2'u_2'}/\overline{u_3'u_3'}$: (a) Adiabatic; (b) Isothermal

the turbulent stress ratio a_3 is only slightly affected by the perturbation and recovers its initial distribution very quickly.

In the experiments where fluctuations in the transverse or spanwise direction are not measured, the spanwise component has often been estimated by making the assumption $\overline{u_3'u_3'} = a_4(\overline{u_1'u_1'} + \overline{u_2'u_2'})$, where a_4 is kept constant and the commonly used value is 0.5 (Bradshaw [137], Cutler and Johnston [138], Deleuze [10], Fernando and Smits [136]). However, the results in

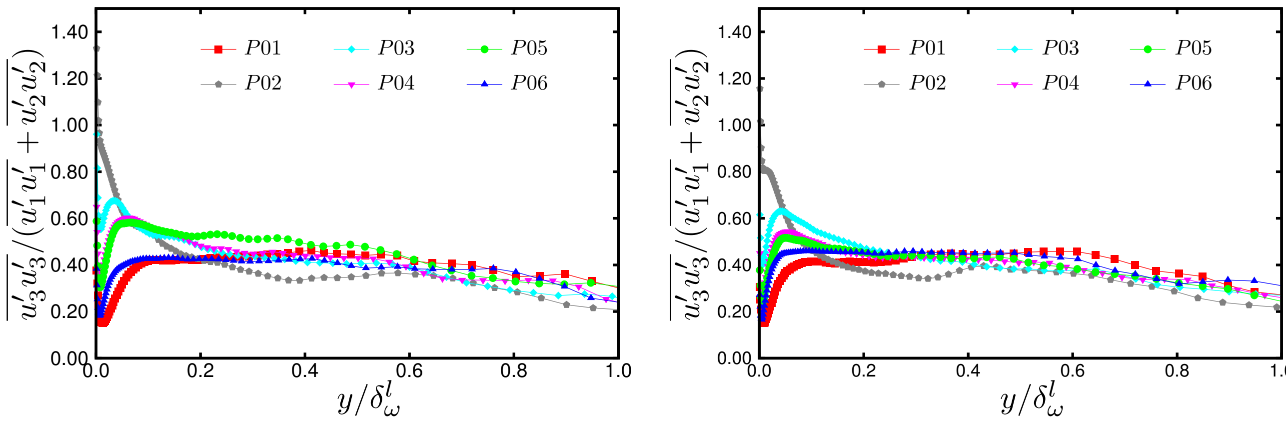

(a) Adiabatic Case **(b)** Isothermal Case

Figure V.16 – Post-shock downstream evolution of turbulent stress ratio, $a_4 = \overline{u_3'u_3'}/(\overline{u_1'u_1'}+\overline{u_2'u_2'})$: (a) Adiabatic; (b) Isothermal

the subsonic experiments of Skåre and Krogstad [134], the direct simulation of Spalart [111] and the present data (Fig. V.16) suggest that $a_4 \approx 0.4$ would be a better choice as the above expression seems to overestimate $\overline{u_3'u_3'}$ slightly in most of the layer. The behavior of a_4 near the wall is also noticeable and shows a strong dependence on y/δ_ω^l. Close to the wall, the effect of the interaction makes a considerable change in the distribution of the turbulent kinetic energy among its different components, and the change is particularly visible in Fig. V.16.

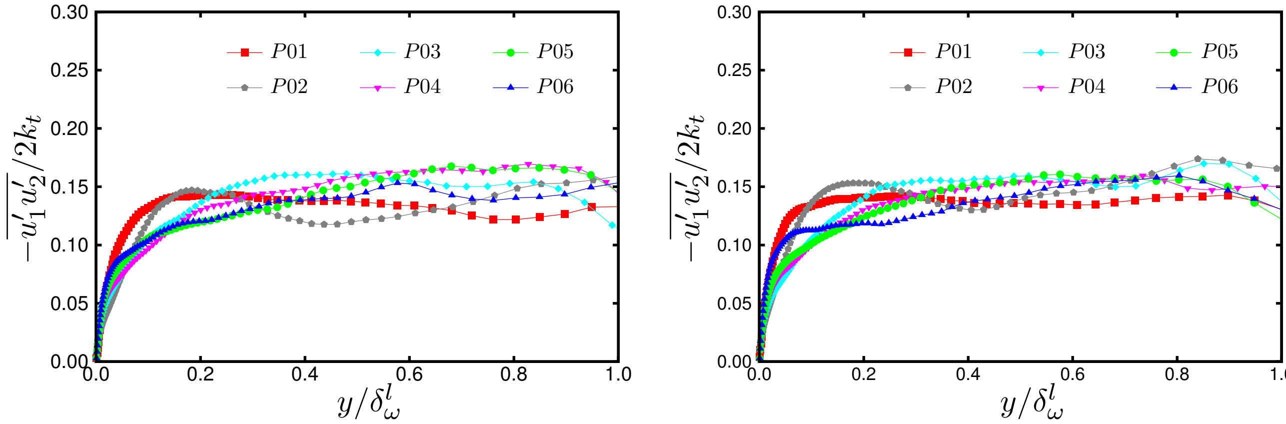

(a) Adiabatic Case **(b)** Isothermal Case

Figure V.17 – Post-shock downstream evolution of turbulent stress ratio, $a_5 = -\overline{u_1'u_2'}/2k_t$: (a) Adiabatic; (b) Isothermal

The downstream development of a_2, a_3 and a_4 for the isothermal case is not significantly different than the adiabatic case, except that the near-wall relaxation of the distribution is more rapid in the isothermal case, which is consistent with the previous observations in the mean flow section.

The streamwise evolution of the structure parameter a_5, which is defined by the ratio of the Reynolds shear stress $(\overline{u_1' u_2'})$ to the turbulent kinetic energy (k_t), is shown in Fig. V.17. In general, for moderate Reynolds number flows, this parameter remains constant along a considerable part of the boundary layer and has values between $0.13-0.17$ (Klebanoff [133], Erm [110], Skåre and Krogstad [134], Shiloh et al. [139], Deleuze [10], Adams [51]). In the present DNS, this parameter has taken a roughly constant value of around 0.14 and only shows a y/δ_ω^l dependency in the inner layer of the boundary layer. The interaction caused the distribution to deviate from its undisturbed state. In the inner part of the boundary layer $(y/\delta_\omega^l < 0.2)$, the level of a_5 slightly decreases at plane $P02$ and significant attenuation in the levels is observed farther downstream (planes $P03$-$P06$). While in outer part of the boundary layer, the ratio exhibits an augmentation in its level (also observed by Deleuze [10]) for all the streamwise planes downstream of the incident shock impingement point, an exception is observed for the case of plane $P02$ where the a_5 values first drop in the region $0.2 < y/\delta_\omega^l < 0.7$ and then increases in the later part of the boundary layer.

The anisotropy tensor $\bar{b}_{ij}$ (here, $\bar{b}_{ij}$ is formed from Reynolds variables i.e; $\bar{b}_{ij} = \overline{u_i' u_j'}/\overline{u_i' u_i'} - \delta_{ij}/3$) provides a rational measure that can be used to objectively and quantitatively measure the degree of anisotropy. The turbulent stress anisotropy invariant map (see Lumley [140]) plays an important role in illustrating the inherent complex flow dynamics associated with the shock, boundary layer interaction. The borders of this domain describe different states of the turbulent stress tensor. Fig. V.18 and Fig. V.19 shows the streamwise evolution of the turbulent stress anisotropy invariant map downstream of the interaction for adiabatic and isothermal cases, respectively. The second and third invariants given by II_b $(= -\bar{b}_{ij}\bar{b}_{ji}/2 = -\bar{b}_{ij}^2/2)$ and III_b $(= -\bar{b}_{ij}\bar{b}_{jk}\bar{b}_{ki}/3 = -\bar{b}_{ii}^3/3)$ respectively. For clarity of presentation the invariant values lying below $y/\delta_\omega^l < 0.6$ are only shown. For each case, two locations are marked: **P** marks the location on the invariant curve where -II_b is maximum and **Q** marks the location on the invariant curve where -II_b is minimum.

For both the adiabatic and isothermal cases, the upstream invariant map (plane $P01$) is similar to the distribution usually found for a boundary layer flow. The point **P** is located at $y^+ \approx 8$ $(y = 0.012\delta_\omega)$ and the point **Q** is located at $y^+ \approx 300$ $(y = 0.41\delta_\omega)$ for the adiabatic case. In the isothermal case, the corresponding locations are for point **P** $y^+ \approx 10$ $(y = 0.009\delta_\omega)$ and the point **Q** is located at $y^+ \approx 650$ $(y = 0.54\delta_\omega)$. At this upstream plane $P01$, a comparison

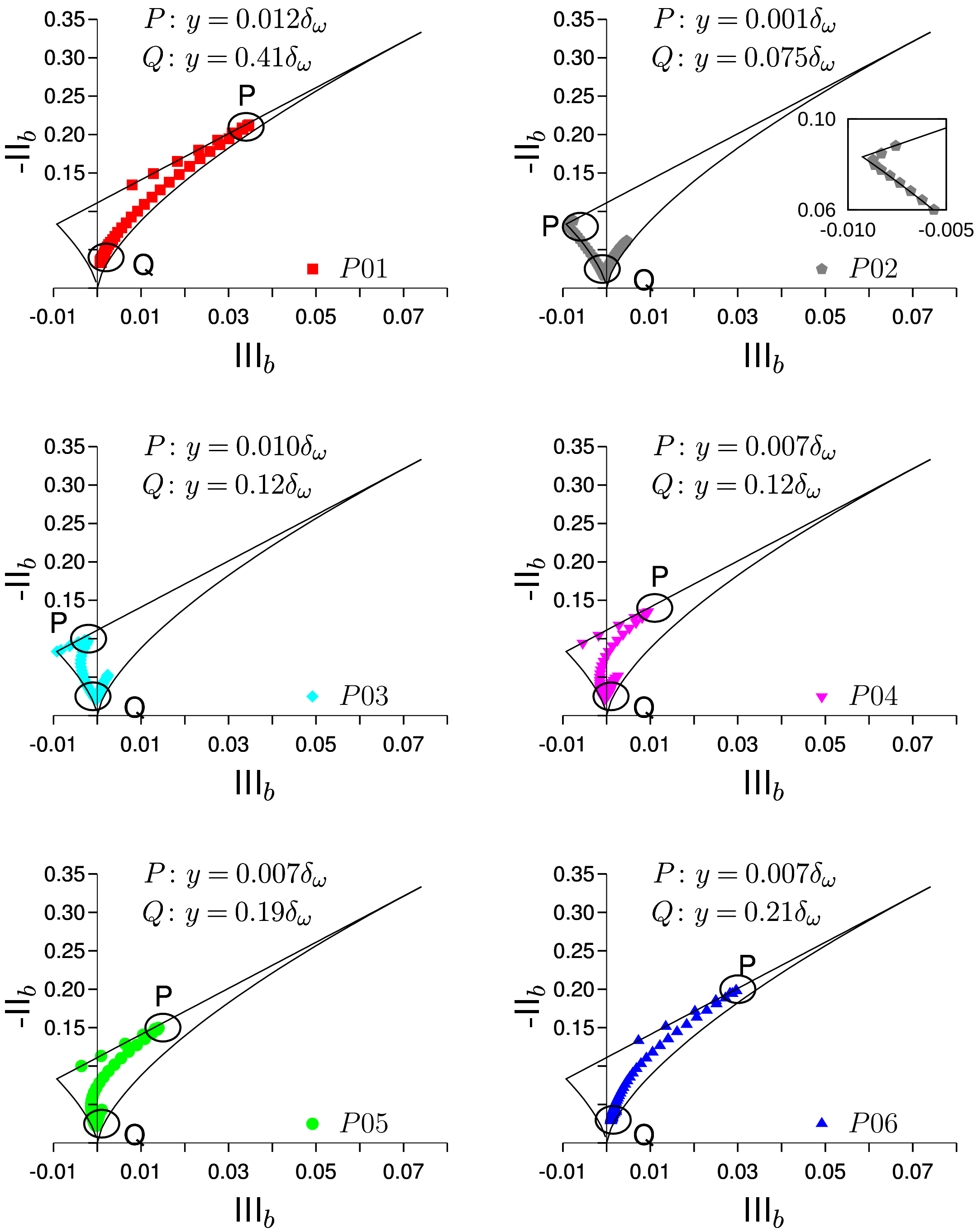

Figure V.18 – Reynolds stress anisotropy map for adiabatic case

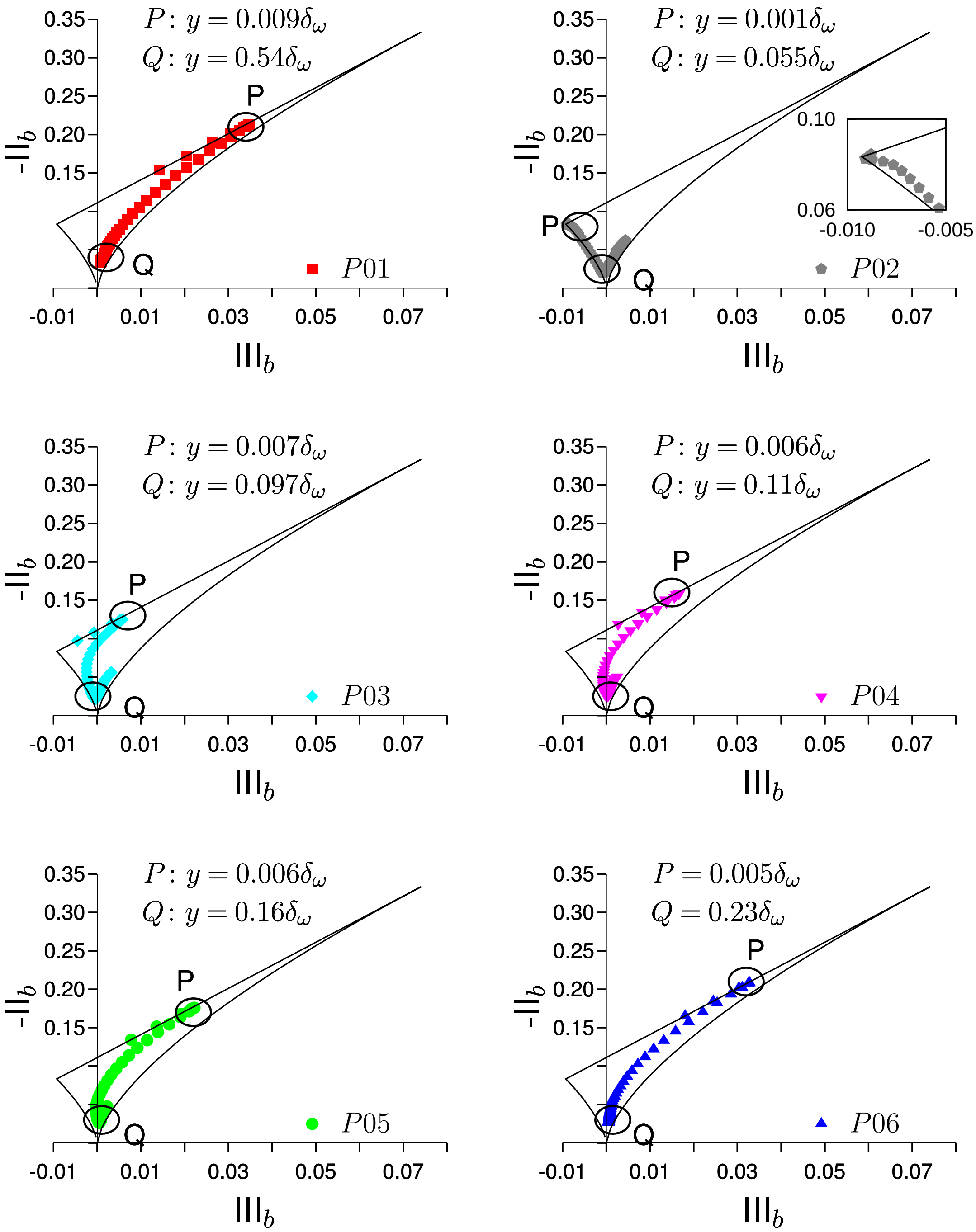

Figure V.19 – Reynolds stress anisotropy map for isothermal case with Fig. V.3a and Fig. V.3b, show that the locations **P** and **Q** delimit the length between the buffer layer and the end of the log-layer region for both the adiabatic and isothermal cases. In this region, Fig. V.4a, Fig. V.5a and Fig. V.6a, show the well-known behavior where the streamwise Reynolds normal stress dominates over the other two normal stress components with $\overline{u_3'u_3'} > \overline{u_2'u_2'}$. For the isothermal case (Fig. V.19), the wall point clearly moves along the two-component limit line away from the axisymmetric limit towards the one-component limit. Consistent with the observation made by Frohnapfel et al. [141] where an increase in the mean flow Mach number shifts the wall points more toward the one-component limit, here a decrement in wall temperature increases the local Mach number in the near wall region and generates the same behavior.

At plane $P02$, immediately downstream of the incident shock impingement location, a significant deviation of the invariant curve from that at plane $P01$ occurs. For the adiabatic case (see figure V.18), point **P** at $y^+ \approx 0.8$ $(y = 0.001\delta_\omega)$ lies in very close proximity of the two-component limit boundary (see insert at plane $P02$ in Fig. V.18). As the distance from the wall increases, the invariant curve migrates to the adjacent axisymmetric boundary. The influence of the shock is clearly felt on the distribution within the invariant triangle since mapping from the data closest to the shock is heavily biased near one of the axisymmetric boundaries of the triangle. This boundary represents a compressive effect on the turbulence structure consistent with the influence of the shock (Simonsen and Krogstad [142]). This axisymmetric limit represents the action of two dominant normal-stress components ($\overline{u_1'u_1'}$ and $\overline{u_3'u_3'}$) and a weaker third normal stress component ($\overline{u_2'u_2'}$). For the isothermal case (see Fig. V.19), the qualitative trend is similar to the adiabatic case for plane $P02$; however, there is a slight change in the quantitative values. In this case, the invariant curve migrates away from the axisymmetric boundary as a consequence of a more rapid increase in the $\overline{u_2'u_2'}$ Reynolds stress component relative to the adiabatic case. This enhanced suppression of the wall-normal Reynolds stress immediately downstream of the shock impingement location appears to be the dominant influence on the turbulence. In contrast to plane $P01$, point **Q** at plane $P02$ is located at $y^+ \approx 55$ $(y = 0.075\delta_\omega)$ for the adiabatic case, and at $y^+ \approx 70$ $(y = 0.055\delta_\omega)$ for the isothermal case. In both thermal cases, the point **Q** now lies in close proximity to the isotropic limit point and the axisymmetric boundary intersection. As distance from the wall increases, the invariant curves for the adiabatic and isothermal cases assume a form consistent with the outer limits of the undistorted invariant curve of plane $P01$. Recall that at plane $P01$, a large part of the boundary layer thickness was delimited by points **P** and **Q**. The shock impingement has significantly altered the distance within the boundary layer delimited by **P** and **Q**; although, this has also provided a quantitative estimate of the region where the turbulence is most susceptible to the effects of the impinging shock.

The remaining streamwise planes in Fig. V.18 and Fig. V.19 exhibit a slow streamwise reconstruction of the turbulent stress anisotropy field that originates near the wall and spreads away from the wall with increasing streamwise distance. Once again, a comparison with the invariant maps at position $P06$ and those at position $P01$ suggest that the isothermal case more rapidly recovered from the shock perturbation. Although Fig. V.4b, Fig. V.5b and Fig. V.6b showed that the increase of all the normal Reynolds stress components was less in the isothermal case than the adiabatic, the reason for this inhibited response is not clear at this point and what connection it has with augmented downstream recovery is, as yet, unanswered.

V.3.2.3 Higher-Order Moments Evolution

In an analysis of the statistical moments, it is useful to examine some higher-order moments that can provide some insight into the flow structure as well as into the probability density function (*pdf*) associated with the turbulence. Similar to the no-shock case, the higher-order moments investigated are the skewness and flatness factors. The skewness is associated with the asymmetry of the tails of the *pdf* function and the flatness is a relative measure of the weight in the tails of distribution. As discussed for the no-shock case , the qualitative trends for the skewness and flatness factors obtained here are quite similar to the distributions found in the other wall-bounded experiments and simulations (Kim et al. [123], Tamano and Morinishi [93], Gupta and Kaplan [143], Kreplin and Eckelmann [144], Ueda and Hinze [145], Deleuze [10], Elena and Lacharme [135], Erm [110], Skåre and Krogstad [134], Simpson et al. [146]). The downstream evolution of the third-order moments of velocity fluctuations (skewness factors) are presented in Fig. V.20, Fig. V.21, Fig. V.22 for the streamwise, the wall-normal and the spanwise components respectively. In the inner part of the boundary layer the skewness factor of the u_1-component of velocity ($S(u_1')$, Fig. V.20) shows a change of sign from negative to positive that implies that positive values of u_1' are more frequent than the negative values as compared to the trend observed before the interaction. In contrast to the evolution of the u_1-component, the skewness factor of the u_2-component of velocity ($S(u_2')$, Fig. V.21) changes sign from positive to negative. Simpson et al. [146], have also observed the same sign reversal behavior for the case of the subsonic boundary layer with an adverse pressure gradient, while Deleuze [10] found it for the case of the supersonic boundary layer with an impinging shock.

As suggested by Simpson et al. [146] and Skåre and Krogstad [134], in a turbulent boundary layer the streamwise skewness factor changes sign at a location in a boundary layer where the Reynolds shear stress and the turbulent intensities reach their maximum values. The region

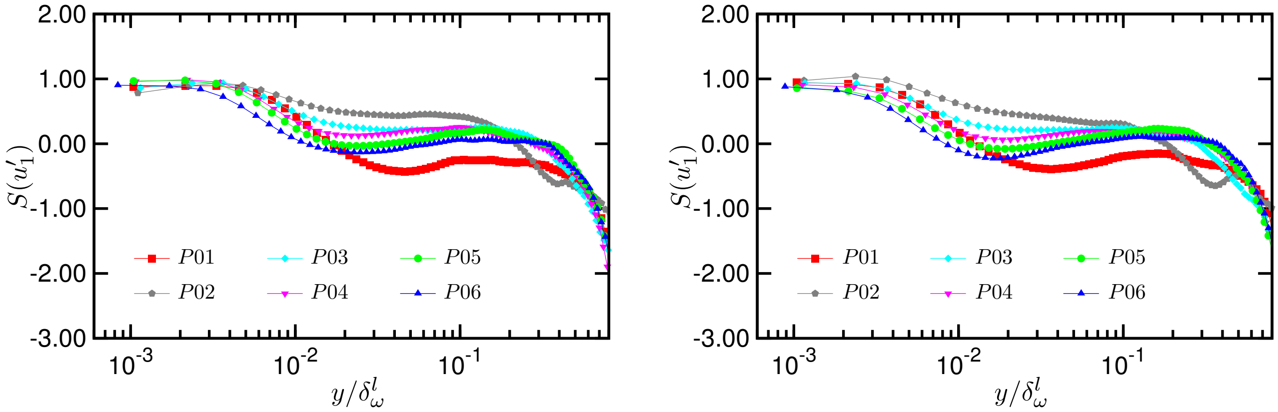

(a) Adiabatic Case

(b) Isothermal Case

Figure V.20 – Post-shock downstream evolution of skewness factor of streamwise velocity fluctuations, $S(u'_1)$: (a) Adiabatic; (b) Isothermal

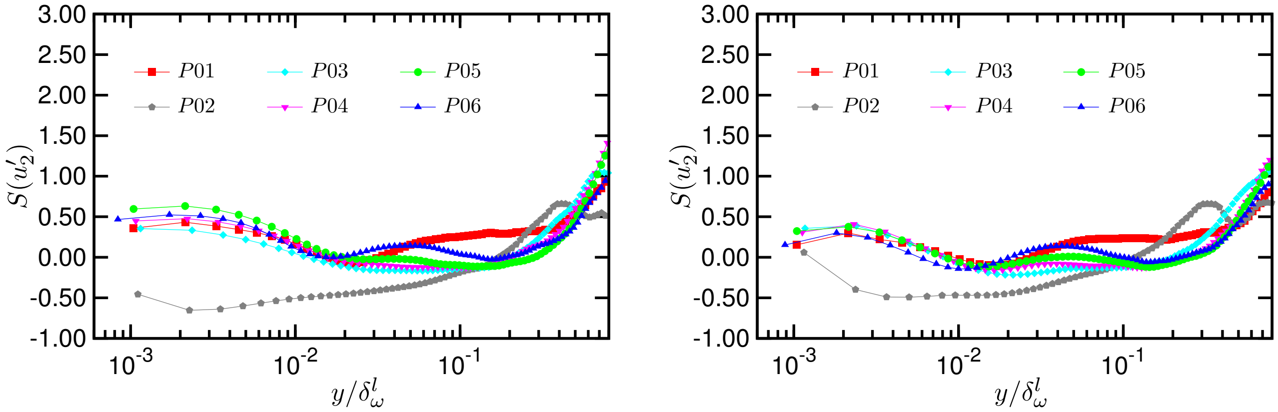

(a) Adiabatic Case

(b) Isothermal Case

Figure V.21 – Post-shock downstream evolution of skewness factor of wall-normal velocity fluctuations, $S(u'_2)$: (a) Adiabatic; (b) Isothermal

corresponding to the maximum stresses involves an intense momentum exchange and lacks the possibility of occasionally occurring very-high and very-low fluctuations and as a consequence of this the probability distribution is nearly symmetric (Gaussian). As shown in Fig. V.4–V.7 after the interaction, the peak of the stresses shifts away from the wall which causes the skewness factors ($S(u'_1)$ and $S(u'_2)$) to reverse their signs higher in the boundary layer ($y/\delta^l_\omega \approx 0.26$). The second notable feature is the fact that the skewness distribution shows a rapid drop-off in its level as distance from the wall increases similar to the standard distribution of the turbulent

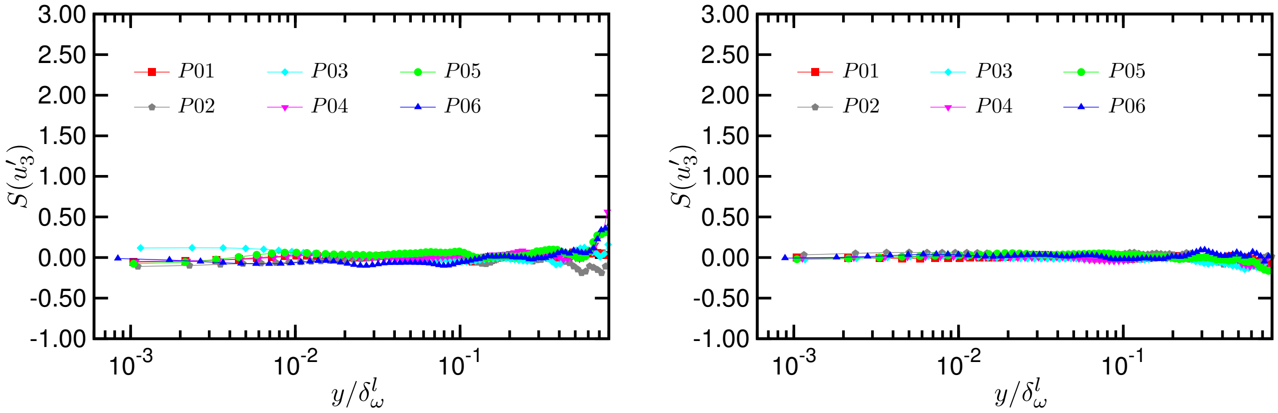

(a) Adiabatic Case **(b)** Isothermal Case

Figure V.22 – Post-shock downstream evolution of skewness factor of spanwise velocity fluctuations, $S(u_3')$: (a) Adiabatic; (b) Isothermal

boundary layer.

The skewness factor for the spanwise velocity component ($S(u_3')$,Fig. V.22) remains nearly equal to its Gaussian value ($S(u_3') \approx 0$) even after the interaction except near the outer edge of the boundary layer where some abrupt fluctuations are observed. The post-interaction behavior of the skewness factors ($S(u_1')$, $S(u_2')$ and $S(u_3')$) for the isothermal case are similar to that of their adiabatic counterpart.

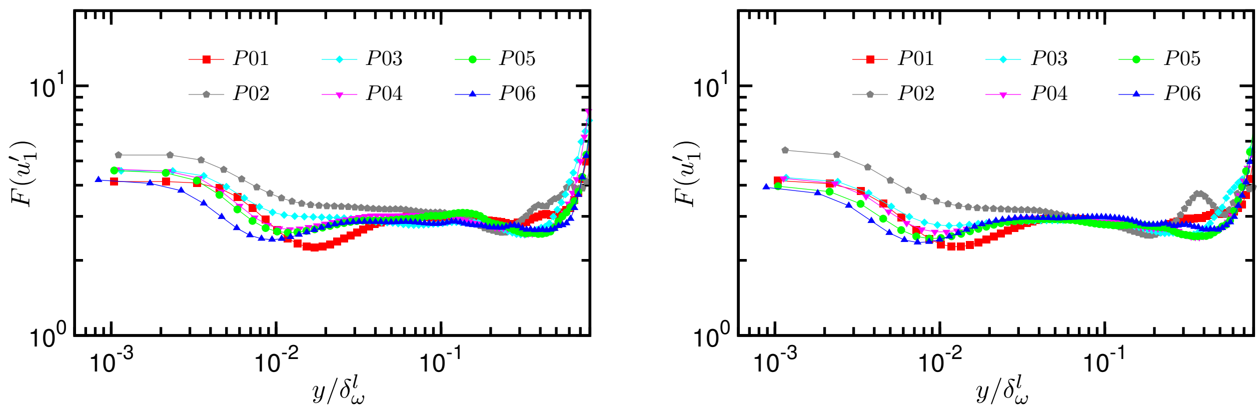

(a) Adiabatic Case **(b)** Isothermal Case

Figure V.23 – Post-shock downstream evolution of flatness factor of streamwise velocity fluctuations, $F(u_1')$: (a) Adiabatic; (b) Isothermal

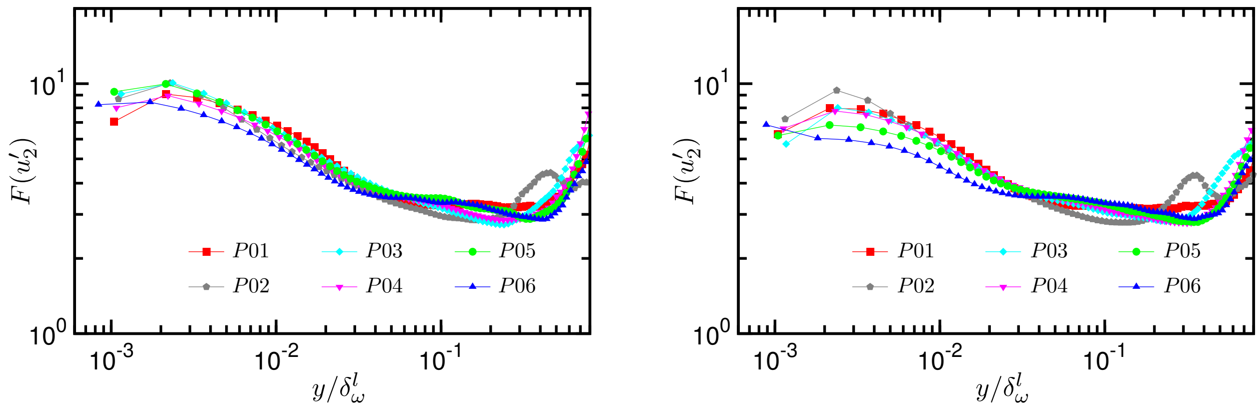

(a) Adiabatic Case

(b) Isothermal Case

Figure V.24 – Post-shock downstream evolution of flatness factor of wall-normal velocity fluctuations, $F(u_2')$: (a) Adiabatic; (b) Isothermal

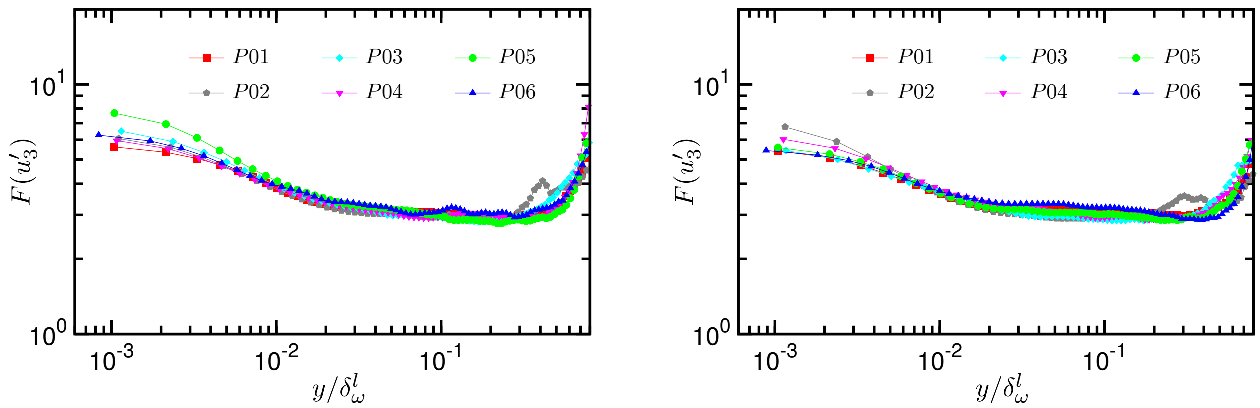

(a) Adiabatic Case

(b) Isothermal Case

Figure V.25 – Post-shock downstream evolution of flatness factor of spanwise velocity fluctuations, $F(u_3')$: (a) Adiabatic; (b) Isothermal

The flatness factors for all three components of the fluctuating velocity are shown in Fig. V.23–V.25. Fig. V.23 depicts that at plane $P01$, that corresponds to the undisturbed turbulent boundary layer, relative to the Gaussian value of 3 the flatness factor $F(u_1')$ attains values much higher than in the sublayer region while a slight dip is observed in the buffer layer of the boundary layer. These observations are consistent with turbulent boundary layer distributions reported by Gupta and Kaplan [143], Ueda and Hinze [145], Kreplin and Ecklemann [144] and Tamano and Mornishi [93]. Simpson et al. [146] have indicated that the high values of

$F(u_1')$ within the viscous sublayer occur because the influx phase of bursting cycle which brings in high velocity fluid from the outer region results in large amplitude positive u-fluctuations and consequently produces a very narrow width bell-shape like velocity probability distribution. Similarly near the outer edge of the boundary layer, the intermittent large-amplitude negative u-fluctuations occurs as a result of the large eddies driving the fluid from the low velocity regions outwards, which tends to increase the flatness factor $F(u_1')$.

At plane $P02$ downstream in the shock impingement interaction zone, the flatness factor $F(u_1')$ is significantly affected in both the adiabatic and isothermal cases. The increase in the $F(u_1')$ factor over a large portion of the boundary layer suggests a reduction of streamwise fluctuation levels relative to the undistorted state at $P01$. This is consistent with the general thickening of the boundary layer downstream of the shock impingement that results in lower streamwise velocity values over a portion of the boundary layer relative to the upstream, undistorted values. For the adiabatic case, the $F(u_2')$ and $F(u_3')$ factors are only minimally influenced; however, the $F(u_2')$ and $F(u_3')$ factors in the isothermal case are increased relative to their adiabatic counterparts. Although the increase is not significant, it does suggest an attenuation of these components relative to the adiabatic case.

With increasing distance downstream, planes $P03$ to $P06$, a relaxation process ensues; although, as in the previous results that have been analyzed, the relaxation process and flow structure reconstruction have not been fully completed even at the far downstream position $P06$.

V.3.2.4 Evolution Based on Quadrant Analysis

Quadrant analysis is one of technique that is commonly used to detect and to quantify the composition of the occurrence of different turbulent events (e.g. ejections and sweeps) in a turbulent boundary layer. As proposed by Lu and Willmarth [147], the technique involves the splitting of the u_1'-u_2' velocity plane into four quadrants according to the signs of the velocity fluctuations (u_1' and u_2'). The associated events with the instantaneous Reynolds shear stresses, $(u_1'u_2')_i$, can then be detected by attributing the stresses to their corresponding quadrant based on the signs of fluctuations. On the basis of this conditional sampling, the averages in each quadrant are estimated by using the following expression

$$(\overline{u_1'u_2'})_i = \frac{1}{N}\sum_{j=1}^{N} S_i \times (u_1'u_2')_j, \tag{V.3}$$

where $S_i = 1$ if the point $(u'_1 u'_2)_j$ is in the ith quadrant, $S_i = 0$ otherwise, and N is the number of data samples at each point of consideration. The turbulent events relative to each u'_1-u'_2 quadrant are defined as follows: the first quadrant where $u'_1 > 0$ and $u'_2 > 0$ contains the events associated with the outward motion of the high-speed fluid; the second quadrant, where $u'_1 < 0$ and $u'_2 > 0$ contains the events that are associated with the ejections (or bursts) of the low-speed fluid away from the wall; the third quadrant, where $u'_1 < 0$ and $u'_2 < 0$ carries the events corresponding to the inward motion of the low-speed fluid; and the fourth quadrant, where $u'_1 > 0$ and $u'_2 < 0$ determines the events that define the sweeping of the high-speed fluid towards the wall. The sketch presented in Fig. V.26 summarizes the above discussion about the turbulent events.

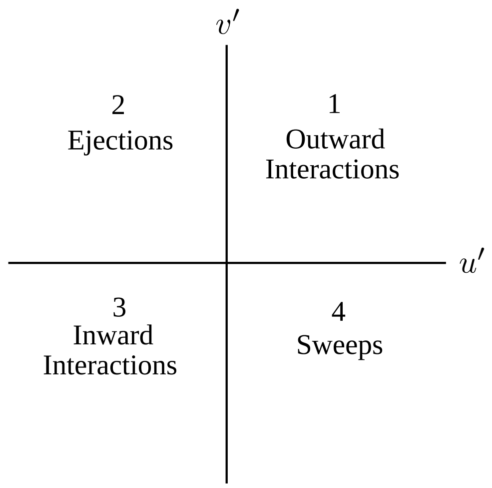

Figure V.26 – The four quadrants of $u' - v'$ plane

Fig. V.27 shows the downstream evolution of the contributions of conditionally averaged Reynolds shear stresses $(\overline{u'_1 u'_2})_i$ across the boundary layer for the adiabatic case, in comparison to their values upstream of the interaction (Plane $P01$). The results presented are normalized with respect to total turbulent shear stress $(\overline{u'_1 u'_2})$ in order to determine the relative contribution of each quadrant.

Upstream of the interaction (plane $P01$) the trends obtained here are in qualitative agreement with the observations made in incompressible and compressible wall-bounded flows (Kim et al. [123], Deleuze [148], Wallace et al. [149]). The dominant contributions to the Reynolds shear stress $(\overline{u'_1 u'_2})$ are from the second and fourth quadrants i.e. the ejections and sweeps. Note also that in a large part of the boundary layer $(0.1 < y/\delta^l_\omega < 0.5)$ upstream of the interaction, the conditional averages haven't shown a large variation, and that away from the wall, ejection events show their dominance over all the other contributors. However very near

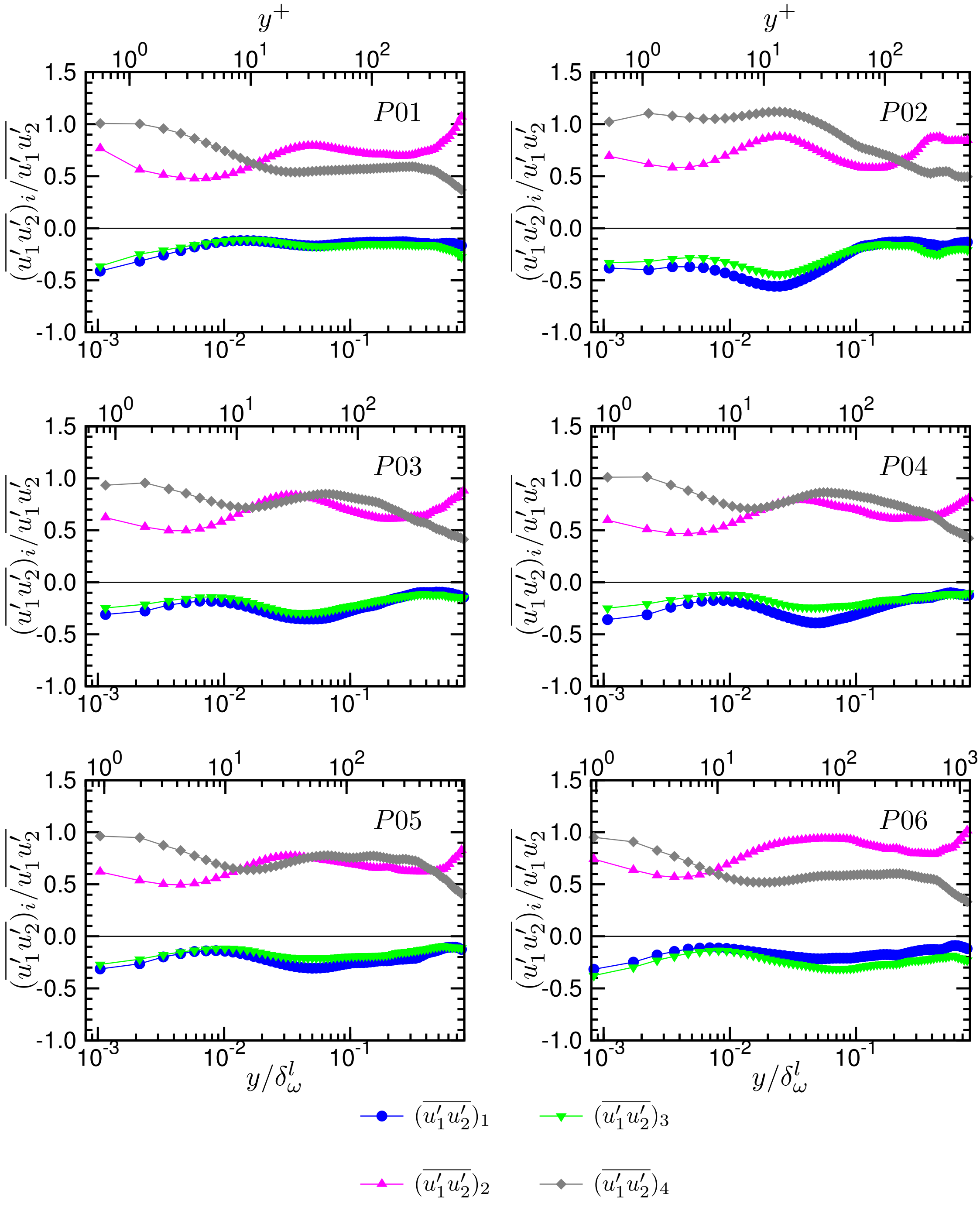

Figure V.27 – Post-shock downstream evolution of conditionally averaged turbulent shear stress, $(\overline{u_1'u_2'})_i/\overline{u_1'u_2'}$: Adiabatic Case

the wall ($y/\delta_\omega^l < 0.02$), the sweeps are the highest contributor. On average, the ejections add a $\approx 73\%$ share to the Reynolds shear stress ($\overline{u_1'u_2'}$), sweeps account for the $\approx 57\%$, while the remaining $\approx 30\%$ negative contributions are from the first and third quadrants (the average being based on the region $0.1 < y/\delta_\omega^l < 0.5$ at the plane upstream of the interaction, $P01$). The percentage decomposition of the total turbulent shear stress $(\overline{u_1'u_2'})$ in terms of the conditional Reynolds stress components described above show reasonable agreement with the results found in the literature. For example, Lu and Willmarth [147] indicated the following composition: -15% in the first quadrant, 77% in the second quadrant, 17% in the third quadrant, and 55% in the fourth quadrant, while Deleuze et al. [148] reported the undermentioned composition: -5% in the first quadrant, 60% in the second quadrant, -5% in the third quadrant, and 50% in the fourth quadrant.

Downstream of the interaction (planes $P02$-$P06$), a notable change in the ejections and sweeps contribution is observed and the cross-over point between the second (ejections) and fourth (sweeps) quadrant distributions move away from the wall. This observation has also been reported by Deleuze [10] in his impinging shock study with a turbulent boundary layer. In addition, the sign reversal behavior found in the skewness factor (Fig. V.20,Fig. V.21) evolution, downstream of the interaction, is also consistent with the present observation. The disturbance produced by the shock relaxes with downstream distance in the recovery zone and the results obtained at the station $P06$ display a set of undisturbed conditional Reynolds stress distributions similar to that of an undisturbed boundary layer.

For the isothermal case (Fig. V.28), the average percentage composition of each quadrant is similar to that of the adiabatic case. Moreover, downstream of the interaction, the region where sweeps remain dominant over the ejections is comparatively less in the isothermal case as compared to the adiabatic counterpart. Also, the relaxation process is relatively fast in the isothermal case, which is again consistent with the conclusions made earlier in this chapter.

In order to further clarify the changes which occurred downstream of the interaction from the contributions by the ejection and sweep events, the ratios of second (ejections) and fourth (sweeps) quadrant events are plotted in Fig. V.29 along with the distribution in the undisturbed boundary layer. The ratio of $(\overline{u_1'u_2'})_2/(\overline{u_1'u_2'})_4$ in the undisturbed boundary layer (Plane $P01$) shows a qualitative and somewhat quantitative agreement with the results obtained by Deleuze [10] and Lu and Willmarth [147]. It is clear that upstream of the interaction in most part of the boundary layer the ejections contributed the most; however, very near the wall the sweep events show their dominance. This drop-off in the values of $(\overline{u_1'u_2'})_2/(\overline{u_1'u_2'})_4$ in the very near wall region ($y/\delta_\omega^l < 0.02$) is not observed by Deleuze [10] and Lu and Willmarth [147] due to the unavailability of data in this region. However, the phenomenon is considered to be characteristic of turbulent boundary layers as Kim et al. [123] and Wallace et al. [149] indicated that sweeps are more predominant in the near wall region than the ejections. In the region, $y/\delta_\omega^l > 0.6$, the

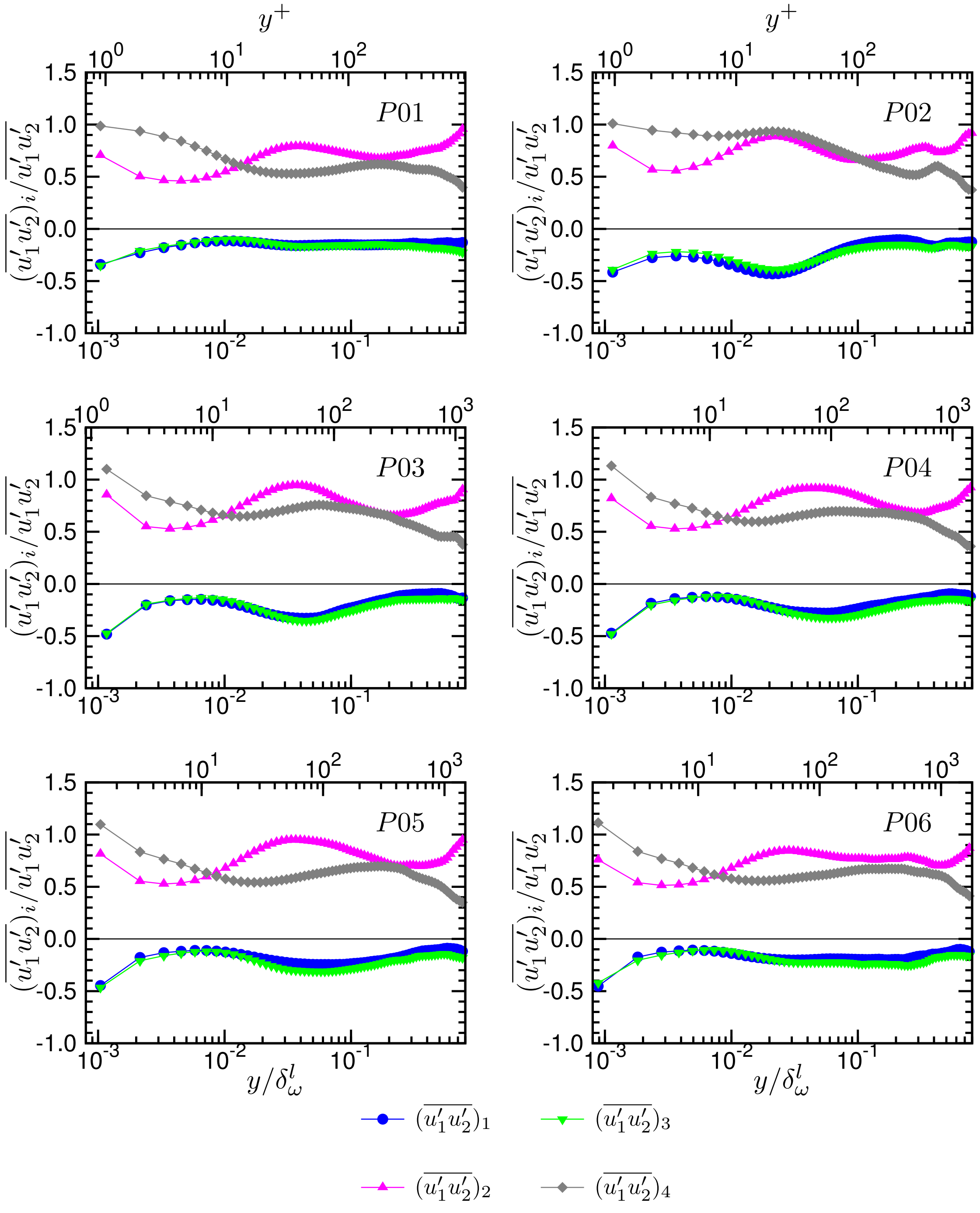

Figure V.28 – Post-shock downstream evolution of conditionally averaged turbulent shear stress, $(\overline{u_1'u_2'})_i/\overline{u_1'u_2'}$: Isothermal Case

ratio $(\overline{u_1'u_2'})_2/(\overline{u_1'u_2'})_4$ increases rapidly due to the prevailing rise of the ejection events and the pronounced decrease in the sweep contributions.

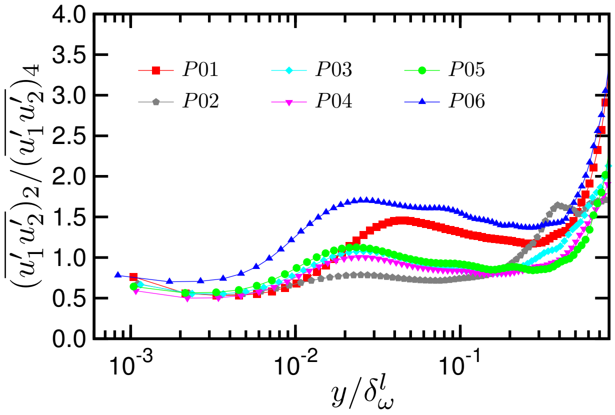

(a) Adiabatic Case

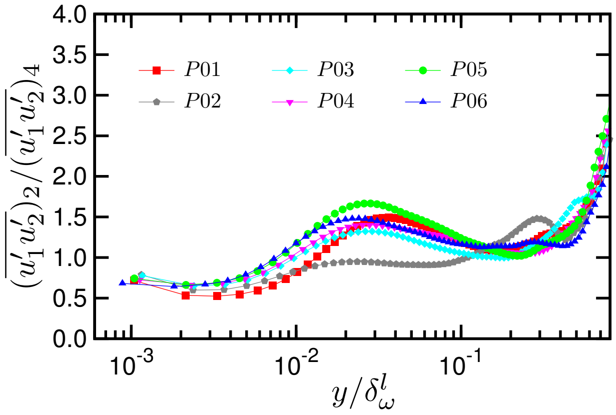

(b) Isothermal Case

Figure V.29 – Post-shock downstream evolution of the ratio of ejections and sweeps contributions, $(\overline{u_1'u_2'})_2/(\overline{u_1'u_2'})_4$: (a) Adiabatic; (b) Isothermal

The effect of the interaction on the ratio of $(\overline{u_1'u_2'})_2/(\overline{u_1'u_2'})_4$ is clear from the distribution of the profiles $P02-P06$. The shifting of the cross-over point between the second and fourth quadrant distributions away from the wall (Fig. V.27 and Fig. V.28) causes the ratio to drop slightly less than one, and is consistent with the conclusion of Deleuze [10] for the case of turbulent boundary layer interaction with an impinging shock. For the isothermal case, it appears that the effect of interaction is limited in the recovery zone and the relaxation process is more rapid than in the adiabatic case.

V.4 Thermal Field Analysis

The effects induced by the shock on the properties of mean and turbulent thermal fields will be investigated in this section.

V.4.1 Mean Flow Evolution

Having analyzed the effects of the shock interaction on the velocity field, the effects on the thermal field will now be discussed. The evolutions of thermodynamic variables (T, ρ, T_t) downstream of the incident shock impingement position (X_{imp}) are compared against the undisturbed distributions obtained upstream of the interaction. The normalization based on the freestream values upstream of the interaction ($\widetilde{T}_{\infty,bi}$, $\overline{\rho}_{\infty,bi}$, $\widetilde{Tt}_{\infty,bi}$) will be used for the data representation. This is considered to be more appropriate in the present context than the one based on the quantities at the edge of the boundary layer ($\widetilde{T}_e$, $\overline{\rho}_e$, $\widetilde{Tt}_e$). Because normalization in terms of edge values display a shift in the wall values that was not desired for a better presentation.

The downstream evolution (after the interaction) of the mean static temperature variation across the turbulent boundary layer at various streamwise stations is presented in Fig. V.30a and Fig. V.30b for the adiabatic and isothermal cases respectively. The significant effect produced by the impinging shock perturbation on the boundary layer distribution is clearly visible. For the adiabatic case the mean static temperature profiles at all the planes ($P01$-$P06$) display a monotonic decay of the mean static temperature from the wall toward the end of the boundary layer, except for the discontinuous change visible in the profile $P02$ which is the effect of reflected shock passing just above the edge of the boundary layer (see also Fig. V.2). It is to be noted that the recovery temperature at the wall doesn't vary much after the interaction as compared to the value upstream of the interaction. This observation is consistent with Pirozzoli and Grasso [13], Adams [51], Garnier [66] and Laurent [57].

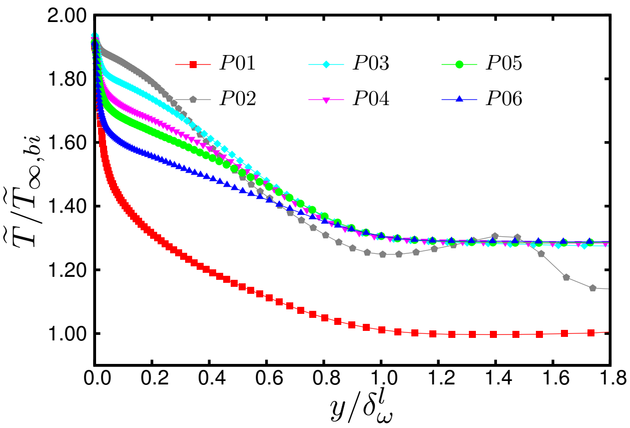

(a) Adiabatic Case

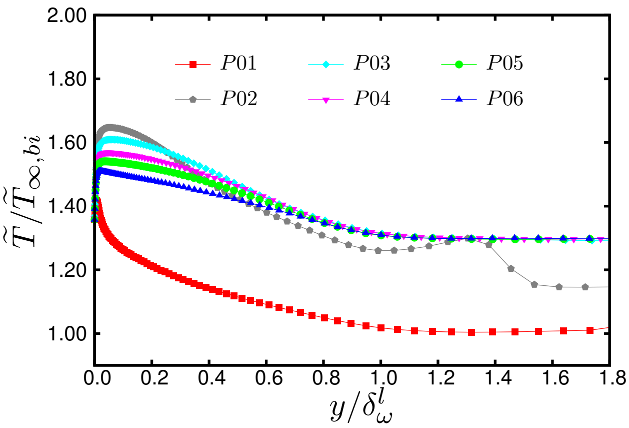

(b) Isothermal Case

Figure V.30 – Post-shock downstream evolution of mean static temperature, $\widetilde{T}/\widetilde{T}_{\infty,bi}$: (a) Adiabatic; (b) Isothermal

The profiles shown for the isothermal case (Fig. V.30b) demonstrate an interesting behavior of the mean static temperature rise in the inner layer of the boundary layer that reaches a peak value and then follows a smooth decay toward its local freestream value. This behavior of the temperature augmentation can be explained by considering the temperature-velocity Crocco relation for compressible flows known as modified Crocco relation or Walz's equation (given for

$P_{rm} \neq 1$, see Smits and Dussauge [44] for further discussion) which is given as:

$$\widetilde{T} = \widetilde{T}_w + \left(\widetilde{T}_r - \widetilde{T}_w\right)\frac{\widetilde{U}}{\widetilde{U}_e} - \left(\widetilde{T}_r - \widetilde{T}_e\right)\left(\frac{\widetilde{U}}{\widetilde{U}_e}\right)^2, \tag{V.4}$$

Problems involving heat transfer through the wall have a non-zero heat flux, i.e. $\partial\widetilde{T}/\partial y \neq 0$, that can be computed by taking the derivative of the above equation (Eq. (V.4)) with respect to y (distance from the wall).

$$\frac{\partial \widetilde{T}}{\partial y} = \frac{\partial \widetilde{U}}{\partial y}\left[\frac{\left(\widetilde{T}_r - \widetilde{T}_w\right)}{\widetilde{U}_e} - \frac{2\widetilde{U}\left(\widetilde{T}_{0e} - \widetilde{T}_e\right)}{\widetilde{U}_e^2}\right], \tag{V.5}$$

For the present isothermal cold wall condition simulation where $T_w < \widetilde{T}_r$, the derivative of the temperature $\partial\widetilde{T}/\partial y$ at the wall $(y = 0, \widetilde{U} = 0)$ is positive, which forces the mean static temperature to rise in the boundary layer until the temperature reaches its extremum ($\partial\widetilde{T}/\partial y = 0$) where the temperature derivative changes sign and allows the mean static temperature profiles to continue with a general decreasing trend. Eq. (V.6) can be used to estimate the mean velocity at the point of the temperature extremum,

$$\widetilde{U}_{tmax} = \frac{\widetilde{U}_e\left(\widetilde{T}_r - \widetilde{T}_w\right)}{2\left(\widetilde{T}_r - \widetilde{T}_e\right)} = \frac{\gamma}{r\,(\gamma - 1)}\frac{\left(\widetilde{T}_r - \widetilde{T}_w\right)}{\widetilde{U}_e}. \tag{V.6}$$

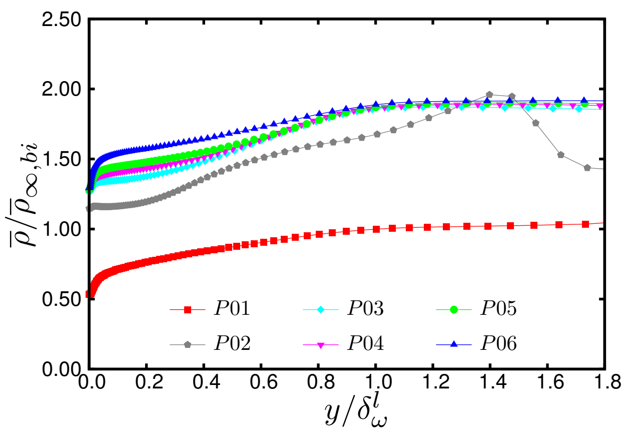

(a) Adiabatic Case

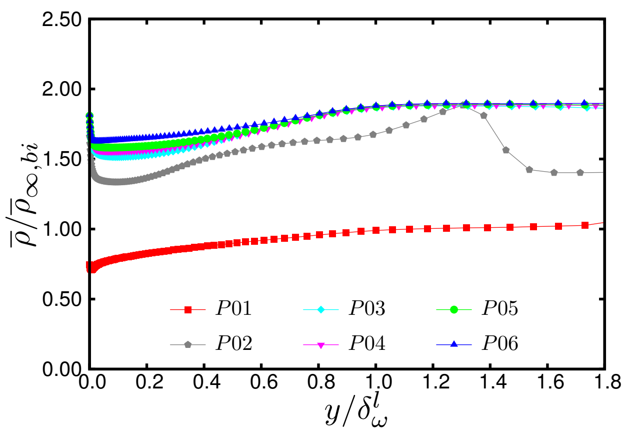

(b) Isothermal Case

Figure V.31 – Post-shock downstream evolution of mean density, $\overline{\rho}/\overline{\rho}_{\infty,bi}$: (a) Adiabatic; (b) Isothermal

Downstream of the interaction, the extremum point shifts away from the wall (see profile at plane $P02$), with respect to its position upstream of the interaction and the magnitude of the difference $(\widetilde{T}_{infl} - \widetilde{T}_w)$ also increases, although the difference level drops off with increasing distance into the recovery zone. For a clear representation of the near wall behavior of the mean static temperature profiles, Fig. V.32a shows a magnified view of the profiles in the near-wall region $y/\delta_\omega^l < 0.15$.

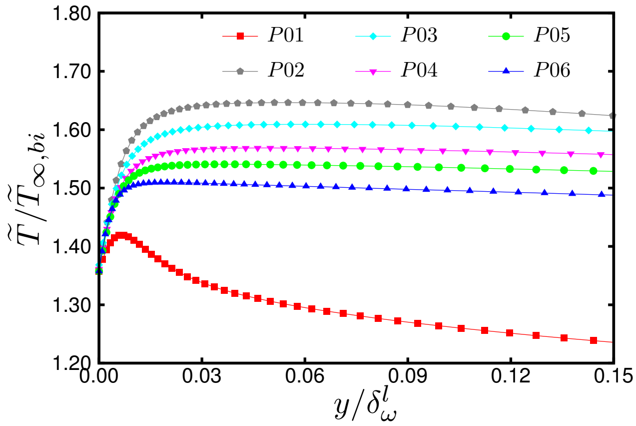

(a) Mean temperature

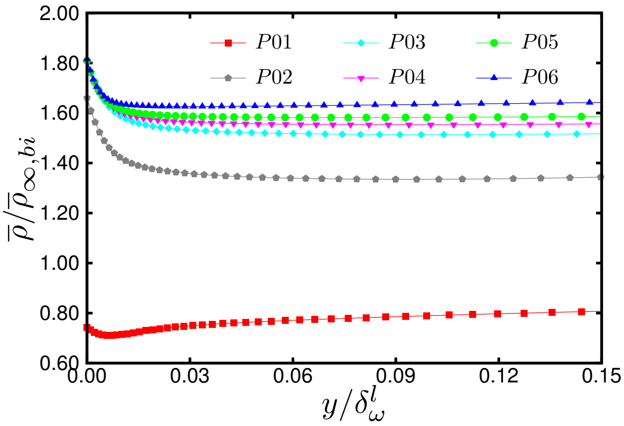

(b) Mean Density

Figure V.32 – Post-shock downstream near-wall evolution of mean static temperature $(\widetilde{T}/\widetilde{T}_{\infty,bi})$ and density $(\overline{\rho}/\overline{\rho}_{\infty,bi})$, Isothermal Case: (a) Mean Temperature; (b) Mean Density

Fig. V.31 shows the post-interaction evolution of the mean density profiles for the adiabatic and isothermal cases. Similar to the mean velocity and mean static temperature, the mean density profiles are significantly affected by the interaction, but which relax in the recovery zone. As an effect of the interaction, for the adiabatic case (zero heat flux wall boundary condition) the wall-values of mean static temperature slightly vary at different streamwise stations while for isothermal case (constant temperature wall boundary condition) it remains constant. However, this is not the case with the mean density which displays a noticeable jump in wall-values after the interaction. For both cases, regardless of the magnitude, the mean density distribution for all the profiles show a behavior inverse to that of the mean static temperature distribution. In the inner layer region, as in the mean static temperature profiles, the mean density profiles for the isothermal case also indicate a different behavior compared to the trends seen in the adiabatic case. The minimum of the density profiles appears at the same position where the extremum is found in the mean static temperature distribution. A magnified representation of the mean density profiles in the near-wall region is presented in

Fig. V.32b.

The post-shock evolution of the mean total temperature at different streamwise stations is shown in figure Fig. V.33 for both the adiabatic and isothermal cases. In the no-shock simulation with adiabatic wall-conditions, a characteristic overshoot of the mean total temperature in the outer part of the boundary layer has been observed and discussed (see Fig. IV.15). This phenomenon is also reported by Smits and Dussauge [44] and Pirozzoli et al. [92]). Moreover, this characteristic of the adiabatic turbulent boundary layer remains even after the interaction with the shock system (Pirozzoli and Grasso [13]). The overshoot in the mean total temperature distribution, that appears in the outer region ($0.6 < y/\delta^l_\omega < 0.9$) of the boundary layer is highlighted in Fig. V.33a. In contrast, in the isothermal case, the heat transfer to the wall avoids any accumulation of energy within the boundary layer.

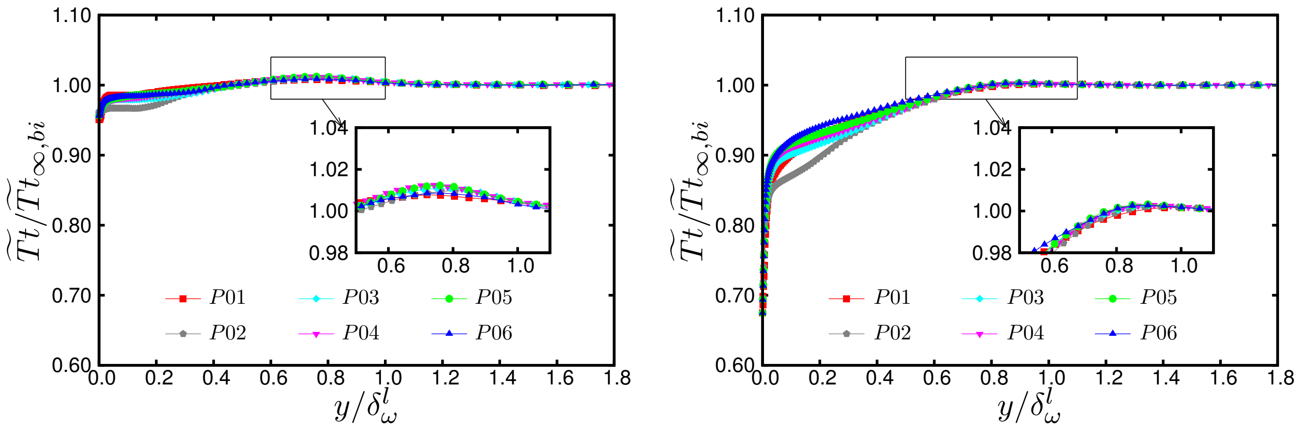

(a) Adiabatic Case

(b) Isothermal Case

Figure V.33 – Post-shock downstream evolution of mean total temperature, $\widetilde{Tt}/\widetilde{Tt}_{\infty,bi}$: (a) Adiabatic; (b) Isothermal

V.4.2 Turbulence Properties Evolution

Analogous to the fluctuating velocity second-order moments, the post-shock evolution of relevant quantities of interest concerning the thermodynamic field (e.g. the static temperature variance, total temperature variance and density variance) are also presented. Fig. V.34 shows the evolution of the static temperature variance ($\widetilde{T''^2}$) downstream of the interaction. For the adiabatic case, the static temperature variance distribution upstream of the interaction (plane $P01$) depicts a peak of the temperature fluctuations in the inner layer of the boundary layer ($y/\delta^l_\omega \approx 0.034$) that smoothly decays towards its almost zero value near the freestream edge of the boundary layer. The existence of the peak of the temperature variance in the near wall region is consistent with the results reported by Garnier [66], Laurent [57] and Adams [51], but the observations of Garnier and Laurent do not indicate a continuous drop of temperature fluctuation in the outer part of the boundary layer. However, the results are in agreement with the observations of Adams for the case of a turbulent boundary layer at $M = 3$. Downstream of the shock system (planes $P02$-$P05$), the effect of the interaction displaces the large temperature fluctuation region from very near to the wall to some height in the boundary layer. With the passage of the recovery zone the high-level temperature fluctuations diffuse within the body of the boundary layer which helps the boundary layer return to its undisturbed state. For the isothermal case, the overall magnitude of the static temperature fluctuations, before and after the interaction, is relatively small when compared with the results of the adiabatic wall condition. Upstream of the interaction (plane $P01$), the static temperature variance distribution reaches its maximum from zero at the wall and then remains almost constant in a large part of the boundary layer, while after the interaction (planes $P02$-$P05$) the notable feature in the distribution is the appearance of the secondary peak in the very near wall region which is highlighted in the Fig. V.34b.

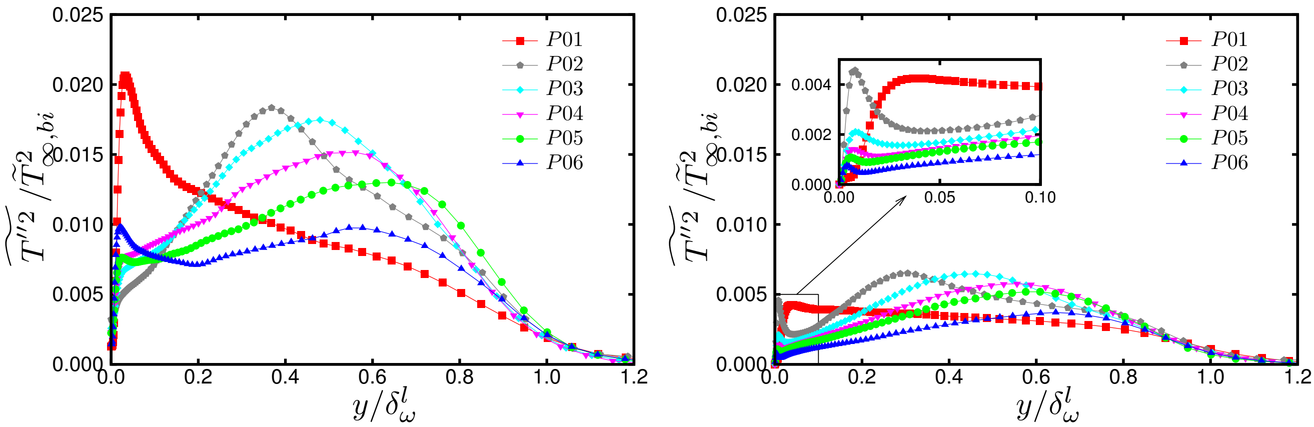

(a) Adiabatic Case　　**(b)** Isothermal Case

Figure V.34 – Post-shock downstream evolution of static temperature variance, $\widetilde{T''^2}/\widetilde{T}^2_{\infty,bi}$: (a) Adiabatic; (b) Isothermal

The comparison of total temperature variance upstream of the shock system with that downstream of it, is presented in Fig. V.35. It is evident from the results that the total temperature fluctuations are non-negligible in a greater part of the boundary layer, which is in agreement with Morkovin [113] for compressible turbulent boundary layers. The conclusion of non-negligible fluctuations remains valid for both cases. However, for the isothermal case the relative magnitude is smaller than the total temperature fluctuations level in the adiabatic case, which is consistent with the fact that the turbulence intensity of the total temperature fluctuations were seen to increase in the heated wall experiments of Debiève et al. [118]. For the adiabatic case, downstream of the shock system, the total temperature fluctuations level increased and its maximum was displaced to a position farther from the wall in the boundary layer. For the isothermal case, the scenario is slightly different. The total temperature fluctuation peak observed in the near wall region, before the interaction, remains even after the interaction; nevertheless, as a consequence of the interaction a second maximum appeared in the outer part of the boundary layer.

For the case of an adiabatic supersonic turbulent boundary layer, Guarini et al. [97] has observed that the maximum turbulence intensity of the static temperature fluctuations $(\overline{T'^2}/\overline{T}_{yl})$[1] is around 11% and in the present DNS it is approximately 9%, while the maximum turbulence intensity of total temperature fluctuations $(\overline{Tt'^2}/\overline{Tt}_{yl})$[2] indicated by Guarini et al. [97] is around 6%, Debiève et al. [118] found it be 4% and in present DNS the outcome is 5%.

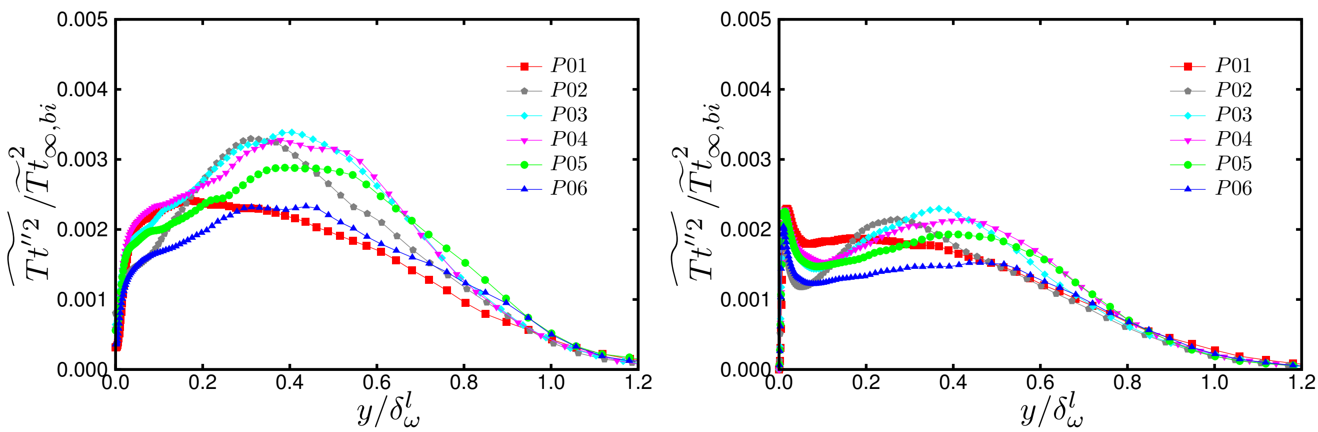

(a) Adiabatic Case **(b)** Isothermal Case

Figure V.35 – Post-shock downstream evolution of total temperature variance, $\widetilde{Tt''^2}/\widetilde{Tt}^2_{\infty,bi}$: (a) Adiabatic; (b) Isothermal

At supersonic speeds the effects induced by compressibility are important. Density fluctuations are considered to be an important element that accounts for the compressibility effects in turbulent flows. The post-shock evolution of the density variance is shown in Fig. V.36 for

[1] $\overline{T}_{yl}$, local values of mean static temperature at each y position
[2] $\overline{Tt}_{yl}$, local values of mean total temperature at each y position

both cases, along with the distribution upstream of the interaction for comparison. Likewise for the static temperature variance and total temperature variance, the magnitude of the density variance in the isothermal simulation is relatively smaller than the adiabatic case. In both cases, before the interaction the density variance remains almost constant in a larger part of the boundary layer ($0.05 < y/\delta_\omega^l < 0.8$), however, after the interaction, the density variance level increases and the maximum lies in the outer part of the boundary layer. For the isothermal case, the density variance distribution varies in a different manner than in the adiabatic case and is illustrated in Fig. V.36b.

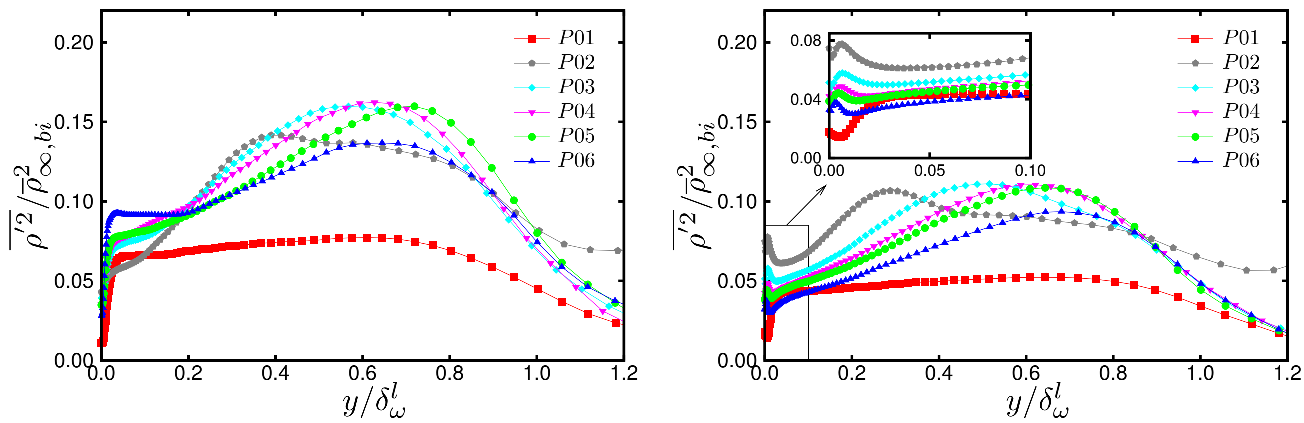

(a) Adiabatic Case **(b)** Isothermal Case

Figure V.36 – Post-shock downstream evolution of density variance, $\overline{\rho'^2}/\overline{\rho}^2_{\infty,bi}$: (a) Adiabatic; (b) Isothermal

Similar to the static temperature variance $\widetilde{T''^2}$, the effect on the turbulent heat flux $\widetilde{u_i''T''}$ distribution after the interaction with shock system is analyzed, since the accurate information of these quantities can provide useful information in the development of turbulence models for scalar fluxes. The post-shock evolution of the streamwise heat flux and the wall-normal heat flux distributions across the boundary layer are shown in Fig. V.37 and Fig. V.38 respectively. For the adiabatic case, the interaction causes the maximum to shift in the outer part of the boundary layer and the qualitative trends of the distribution in the relaxation zone are similar to that of the temperature variance distribution . For the isothermal case, the positive contribution of $\widetilde{u_1''T''}$ in the near wall region increases as the result of the interaction and similar to the adiabatic case, the region of high turbulent heat flux activity is observed in the outer region of the boundary layer.

In general the wall-normal component of turbulent heat flux $-\widetilde{u_2''T''}$, has a lesser magnitude

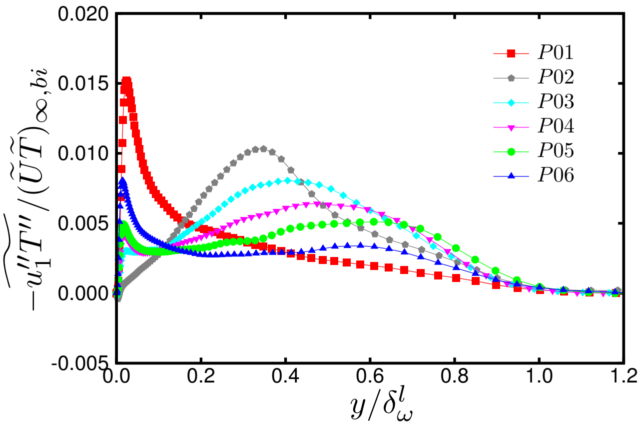

(a) Adiabatic Case

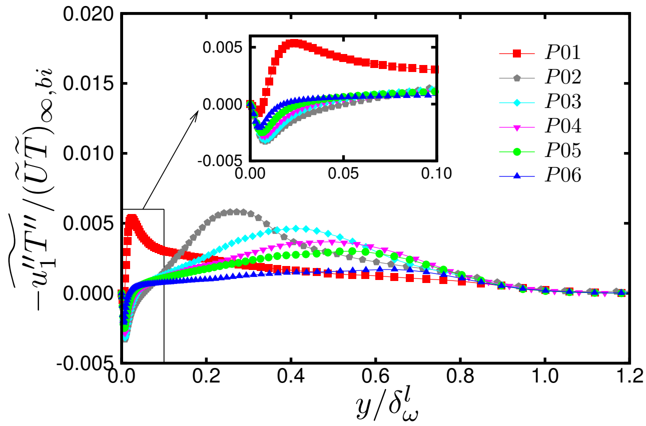

(b) Isothermal Case

Figure V.37 – Post-shock downstream evolution of streamwise component of turbulent heat flux, $\widetilde{u_1''T''}$: (a) Adiabatic; (b) Isothermal

compared with the streamwise flux component $-\widetilde{u_1''T''}$. Again, the interaction of the boundary layer with the shock system produces significant changes in the wall-normal turbulent heat flux distribution, along with an effect on its magnitude. For the isothermal case, the appearance of the negative component of $-\widetilde{u_2''T''}$ in the near wall region produced as a result of the interaction is also marked in the highlighted region of Fig. V.38b.

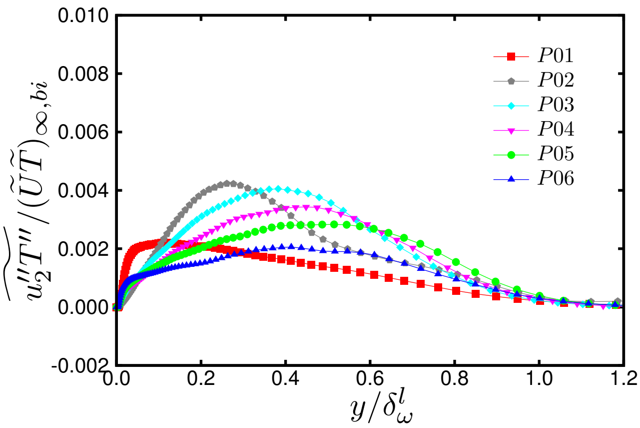

(a) Adiabatic Case

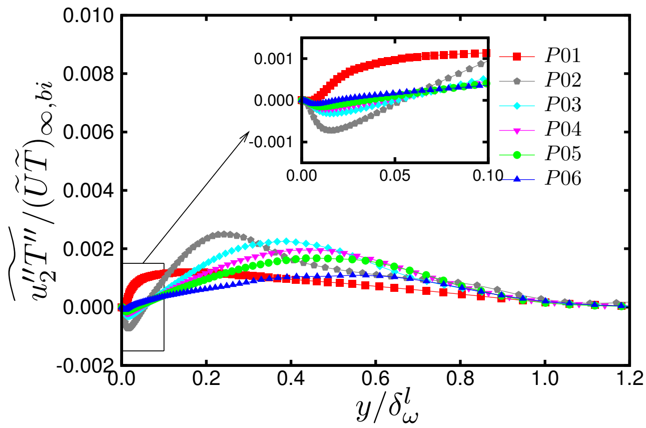

(b) Isothermal Case

Figure V.38 – Post-shock downstream evolution of wall-normal component of turbulent heat flux, $\widetilde{u_2''T''}$: (a) Adiabatic; (b) Isothermal

Since the Strong Reynolds Analogies (SRA), relate the quantities relevant to heat transfer

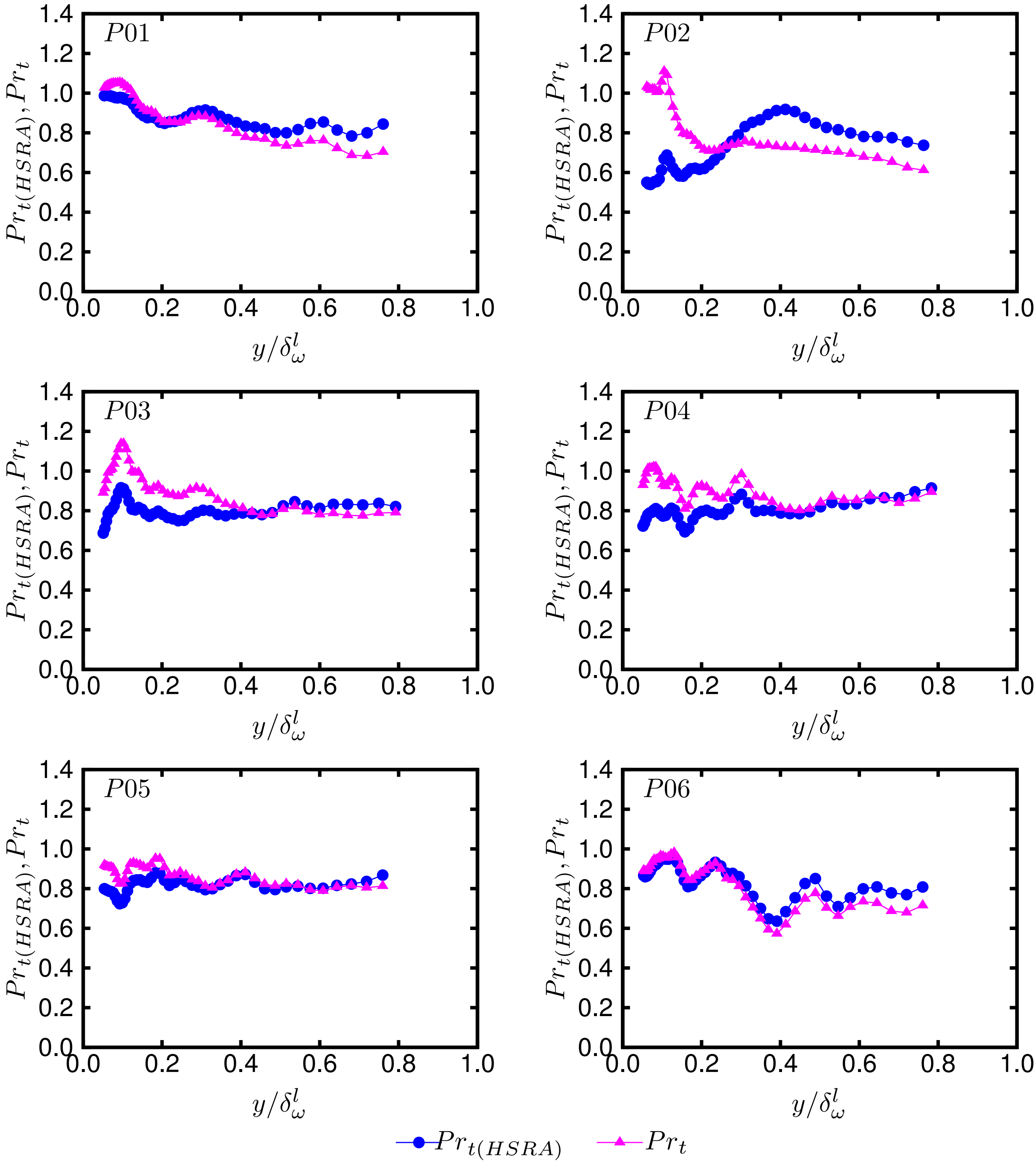

Figure V.39 – Post-shock downstream evolution turbulent Prandtl number, $Pr_{t(HSRA)}, Pr_t$: Adiabatic Case

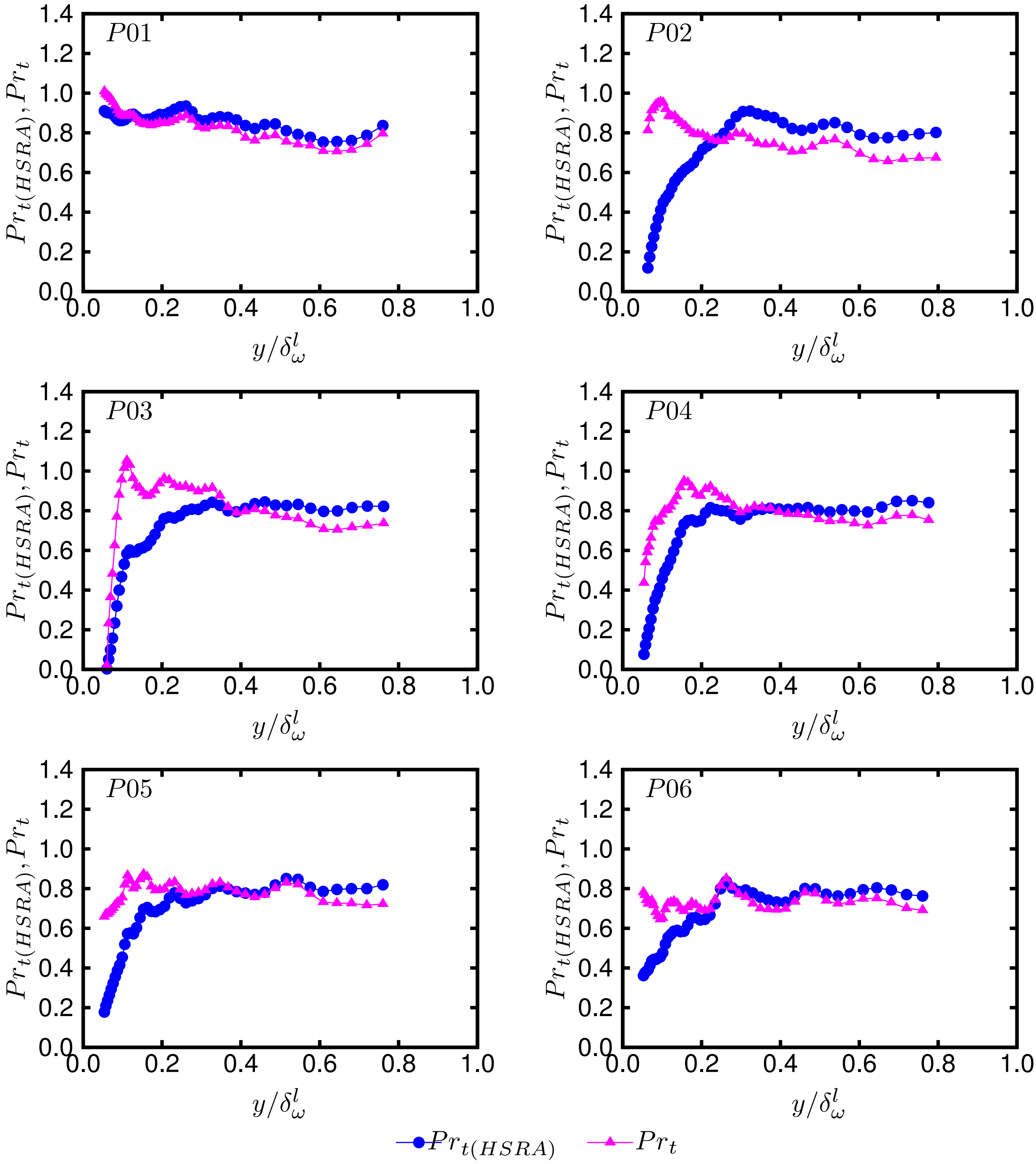

Figure V.40 – Post-shock downstream evolution turbulent Prandtl number, $Pr_{t(HSRA)}, Pr_t$: Isothermal Case with quantities relevant to momentum transfer in a turbulent boundary layer, so an investigation of the relation in the post-shock region can bring additional insight to the issues pertaining to flow dynamics modeling. In addition to the adiabatic wall conditions the effects of cold wall boundary conditions are also examined. The Extended Reynolds Analogy relation proposed by Huang et al. [96] (here on referred as HSRA) is most relevant in problems involving heat transfer and has already been discussed in Chapter IV (see Eq. (IV.24)). As in the no-shock case, a comparison of the turbulent Prandtl number extracted from the HSRA ($Pr_{t(HSRA)}$) and the turbulent Prandtl number (Pr_t) based on the ratio of momentum eddy diffusivity and heat transfer eddy diffusivity is presented in Fig. V.39 and Fig. V.40 for the adiabatic and isothermal cases, respectively. The data is intentionally displayed in the region $0.05 < y/\delta_\omega^l < 0.8$ of the turbulent boundary layer, as the SRA is not applicable in the very near wall ($y/\delta_\omega^l \approx 0.05$ is equivalent to $y^+ \approx 30$, at the plane upstream of the interaction (plane $P01$)) and in the very outer part of the boundary layer. In the excluded regions the standard deviations of velocity and static temperature fluctuations are very small, which cause the HSRA relation to deviate strongly in these regions.

For the adiabatic case, except for the plane $P02$ which is positioned just after the shock system and shows an enormous distortion in the displayed distributions, the qualitative trends generated by HSRA are in agreement with the distribution of Pr_t obtained from diffusivity ratios, and the estimation of magnitude is also comparable. For the isothermal case, in the post-interaction region , it is evident from the results presented that the estimated magnitude of $Pr_{t(HSRA)}$ deviates considerably when compared to the values of Pr_t, the prominent deviation can be marked in the region $y/\delta_\omega^l < 0.2$.

Based on the baseline assumption of negligible total temperature fluctuations in the turbulent boundary layer in the original Strong Reynolds analogy (SRA), the formulation suggested by Morkovin [113], eventually brings the relationship $R_{u_1 t} \approx -1$, which indicates that the streamwise velocity fluctuations and static temperature fluctuations should have a strong anti-correlation. However, this is not exactly true under the conditions where the Prandtl numbers are not one and the total temperature fluctuations are not zero. According to the observations in the experiments of compressible turbulent boundary layers (adiabatic), in the large part of the boundary layer, away from the wall, the correlation coefficient $R_{u_1 t}$ remains almost constant and lies in the range of -0.80 to -0.90 (Dussauge & Gaviglio [150], Laurent [57], Debiève [151]), while direct numerical simulations of supersonic boundary layers (adiabatic) yield a comparatively weak anti-correlation and show $R_{u_1 t}$ lies in the range of -0.55 to -0.7 (Pirozzoli & Grasso [13], Guarini et al. [97], Adams [51], Priebe et al. [15]). The discrepancy between the experimental and numerical assessment of correlation coefficient is not clear and no rational argument is available in the literature. The post-shock evolution of the correlation coefficient R_{u_1t}, defined in Eq. (V.7), across the boundary layer is presented in Fig. V.41 for the adiabatic and isothermal simulations. In present direct numerical simulations the values observed for R_{u_1t} upstream of the interaction, for both cases, lie in the range of -0.65 to -0.55 noticed in the region $0.2 < y/\delta_\omega^l < 0.8$.

$$R_{u_it} = \frac{\widetilde{u_i''t''}}{\sqrt{\widetilde{u_i''^2}}\sqrt{\widetilde{t''^2}}}, \tag{V.7}$$

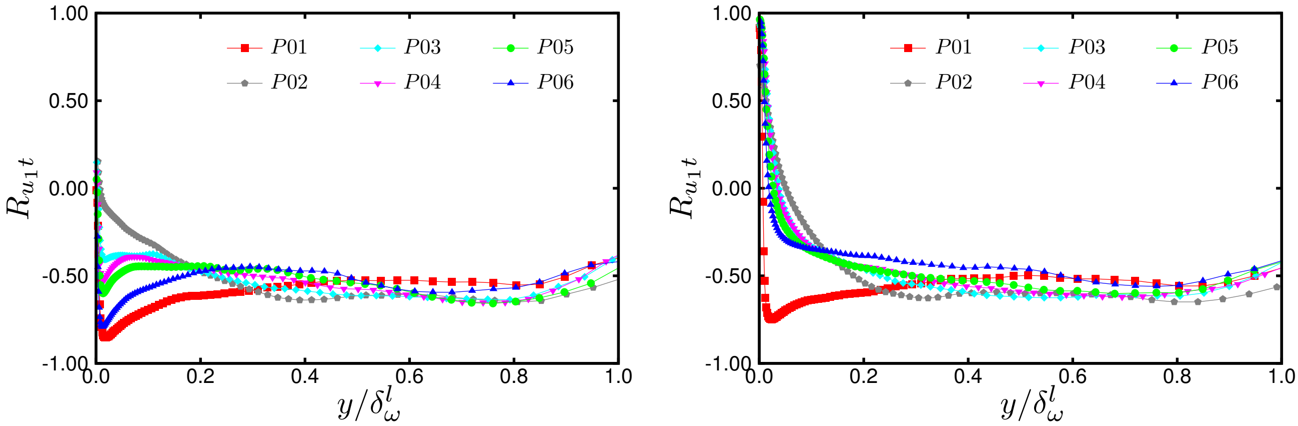

(a) Adiabatic Case **(b)** Isothermal Case

Figure V.41 – Post-shock downstream evolution of correlation coefficient R_{u_1t}: (a) Adiabatic; (b) Isothermal

For the adiabatic case, Fig. V.41a, the effect of the interaction significantly dampens the correlation, R_{u_1t}, in the inner region of the boundary layer ($y/\delta_\omega^l < 0.2$), while the behavior of the correlation coefficient in the outer part of the boundary layer persists in the same manner as was observed before the interaction with the shock system. The present observations are consistent with the results of Priebe et al. [15] for the case of an impinging shock interaction with a supersonic turbulent boundary layer. Farther downstream in the recovery zone the correlation coefficient profile (plane $P06$) almost returns back to undisturbed distribution. For the isothermal case, Fig. V.41b, the interesting feature is the presence of a very strong positive correlation in the near wall region that remains even after the interaction. This is due to the fact that, for the isothermal case, the turbulent heat flux $(-\widetilde{u_1''T''})$ changes sign in the near wall region (see Fig. V.37b). A second noticeable element is the indication that profiles in the relaxation region are remarkably less relaxed than the adiabatic counterpart, which suggests that contrary to the velocity field, the thermal field in the isothermal case takes much longer to relax completely back to its undisturbed state.

The post-shock evolution of the correlation coefficient of the wall-normal velocity fluctuations and static temperature fluctuations R_{u_2t} across the boundary layer for adiabatic and isothermal cases are presented in Fig. V.42a and Fig. V.42b respectively. For both cases, up-

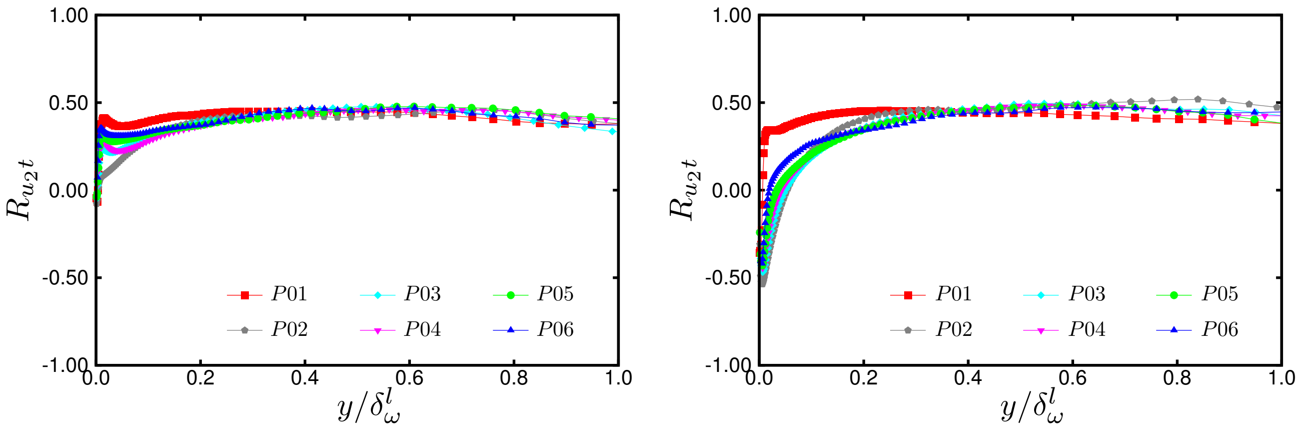

(a) Adiabatic Case

(b) Isothermal Case

Figure V.42 – Post-shock downstream evolution of correlation coefficient R_{u_2t}: (a) Adiabatic; (b) Isothermal

stream of the interaction the coefficient R_{u_2t} remain almost constant at a value ≈ 0.45, over a large extent in the boundary layer $0.2 < y/\delta_\omega^l < 1.0$. This suggests that in the outer part of the boundary layer the correlation coefficients R_{u_2t} and $R_{u_1u_2}$ are strongly correlated (see Fig. V.12) and display a close agreement with the relationship $R_{u_1u_2} \approx -R_{u_2t}$ found in the classical SRA. Downstream of the interaction, for both cases, the values of R_{u_2t} do not change too much in the outer part of the boundary layer; however, in the inner layer the R_{u_2t} correlation coefficient follows the same development trends as that observed for R_{u_1t}.

V.5 Summarizing Comments

The effects induced by an incident and reflected shock-system at two different wall thermal boundary conditions on the statistical characteristics of a turbulent boundary layer have been discussed. Just downstream of the shock-system (plane $P02$) significant effects of the interaction have been observed on the characteristics of the turbulent boundary layer which is progressively relaxed farther downstream. However, within the limits of the computational domain, for both adiabatic and isothermal simulations, the perturbed fields are not able to recover back their undistorted states observed upstream of the interaction. In addition, for the isothermal case a relatively faster recovery process is observed with reference to its adiabatic counterpart.

In the post-shock region, due to retardation effects induced by the adverse pressure gradient, significant deficit of momentum has been observed in the velocity profiles. All the components of the Reynolds stress tensor are anisotropically amplified across the shock-system and their maximum values shift away from the wall due to the upward motion experienced by the flow in the interaction region. The structure of the turbulence has been analyzed through an evolution of the correlation coefficient ($R_{u_1 u_2}$) and various structure parameters. A strong correlation between u_1' and u_2' in the outer part of the boundary layer has been identified that is associated with the presence of large scale eddies. Moreover, relatively high levels of the wall-normal and spanwise velocity fluctuations with respect to the streamwise velocity fluctuations are observed. An interesting feature is identified in the analysis of the Reynolds stress anisotropy invariant map. Upstream of the interaction, the distribution is similar to the ones usually found for the turbulent boundary layers, while due to compressive effects induced by the shocks a heavily biased distribution lying along the one of the axisymmetric boundary of the invariant triangle is obtained downstream of the shock-system.

The effects of the shock-system on the higher-order moments of the velocity fluctuations are also investigated. It is found that the skewness factor for the streamwise fluctuations changes sign from negative to positive in the inner part of the boundary layer with reference to the trends observed upstream of the interaction, suggesting a higher frequency of positive u_1-fluctuations then negative ones, while for the skewness factor of the wall-normal component an opposite effect is observed. The effect of the interaction is also exhibited through the distribution of the streamwise flatness factor which increases in the near wall region.

The distributions of the conditionally averaged shear stresses reveals that in most of the boundary layer upstream of the interaction, ejection events are more prevalent over the other contributions, except very near to the wall where sweep events shows their dominance. The effect of the shock interaction increases the extent in the boundary layer over which the sweep contributions dominate over the ejections.

The major effects of the isothermal wall boundary condition on the developing turbulent boundary evolution are identified through the analysis of the thermal field. With reference to the adiabatic case, significantly different distributions of the mean and the turbulent thermal fields are observed for the isothermal case. Downstream of the shock-system, similar to the velocity field, the maximums of the turbulent quantities are shifted away from the wall with reference to the wall proximity positions observed upstream of the interaction. In addition, for the isothermal case in the near wall region, a secondary peak in the distributions of the static temperature variance, total temperature variance and density variances is also observed and a sign reversal is identified for the streamwise and wall-normal turbulent heat flux components.

Turbulent Prandtl number variation across the boundary layer based on the ratio of diffusivities in comparison of the turbulent Prandtl number extracted from HSRA is examined. In the post-shock region, a significant deviation between the two is observed in the inner part of the boundary layer and suggests that the HSRA does not hold in the perturbed regions up to a quite significant height in the boundary layer. It has been found that a negative correlation exists between the streamwise velocity and temperature fluctuations and downstream of the shock-system its value significantly decreases in the near-wall region. On the contrary, for the isothermal case, strong positive correlations between streamwise velocity and temperature fluctuations are observed downstream of the shock-system. For the isothermal case, an overall observation of the results shows that contrary to the velocity field, the thermal field takes much longer to relax completely back to its undisturbed state.

Chapter VI

Characteristics of Turbulent Boundary Layer in the Central Interaction Region

This chapter is focused on the analysis of turbulent boundary layer properties in the central interaction region (i.e. the region bounded by the legs of the incident and reflected shocks and its immediate vicinity, see Fig. V.1). The effects of the interaction are more pronounced in this region and the turbulent boundary layer is more perturbed, suggesting a much more complex flow dynamics of the mean and turbulent field with respect to flow regimes upstream and downstream of the shock-system.

VI.1 Evolution of Mean Flow along the Interaction Region

In this section, the evolutions of the mean velocity and thermal fields along the interaction region will be discussed. The effects of the shock interaction and different wall thermal boundary conditions on the evolutions of primitive variables, skin-friction coefficient, wall-pressure and integral parameters (shape factor, displacement thickness and momentum thickness) will be investigated.

VI.1.1 Evolution of Wall-Pressure and Skin-Friction Coefficient

As explained in Chapter II, the upstream influence of the shock-system is most commonly determined from the inspection of the wall-pressure distribution while the skin-friction coefficient is widely employed to measure the separation characteristics of the flow. In the following, two different length scales (upstream influence length and separation lengths) are utilized to provide an estimate of the upstream influence of the shock and the streamwise extent of the separation region. As reported by Délery and Marvin [41], the upstream influence length (L_{ui}) is defined as the distance between inviscid origin of the shock (X_{imp}) and the position where the existence of the shock is first felt in the viscous flow (e.g. for the case of wall-pressure, the position where its value start to rise with reference to the level upstream of the interaction). The separation length (L_{sep}) is defined as the streamwise distance between the mean separation (X_{sep}) and the reattachment points (X_{re}). In Fig. VI.1b, the skin-friction coefficient and the wall-pressure distributions for the adiabatic and isothermal cases are plotted as a function of nondimensional streamwise coordinate $X^* = (X - X_{imp})/\delta^o_\omega$, where X_{imp} corresponds to the inviscid origin of the incident shock. This shows an upstream influence length (L_{ui}) of $\approx 2.3\delta^o_\omega$ for adiabatic case and $\approx 1.7\delta^o_\omega$ for isothermal case, while the estimated separation lengths (L_{sep}) are $\approx 1.1\delta^o_\omega$ and $\approx 0.8\delta^o_\omega$ for the adiabatic and isothermal cases, respectively. In comparison with the adiabatic wall conditions, the results show that the effect of wall cooling reduces the separation and upstream influence lengths. As for the cold wall case, the speed of sound across the boundary layer decreases so that the local Mach number rises in the boundary layer. This results in the thinning of the subsonic region of the boundary layer which consequently reduces the upstream influence length. Due to the difference in flow conditions, no direct quantitative comparison with the available literature can be made. However, a qualitative comparison can be made with the experiments performed by Back and Cuffel [56] and Spaid and Frishette [152] who studied the effects of wall cooling ($T_w/T_t = 0.44$ [56] and $T_w/T_t = 0.47$ [152]) on shock/boundary layer interaction and arrived at the same conclusion that separation and upstream influence lengths were reduced for the cold-wall experiment. In Fig. VI.2, the wall-pressure and skin-friction distributions are also shown as a function of nondimensionalization based on the separation length (L_{sep}), $X^{**} = (X - X_{re})/(X_{re} - X_{sep})$. An interesting observation from this is that, for both configurations, the resulting pressure rise and friction coefficient evolution collapse on the same curve as long as the nondimensionalization based on the separation length is taken into account.

VI.1.2 Evolution of Integral Parameters of Developing Boundary Layer

In order to analyze the mean flow organization along the interaction region, the longitudinal evolution of incompressible and compressible integral parameters of the developing turbulent boundary layer (displacement thickness, momentum thickness and shape factor) are plotted in Fig. VI.3 and Fig. VI.4, respectively. The results for both adiabatic and isothermal wall conditions are presented. The incompressible and compressible definitions of these integral

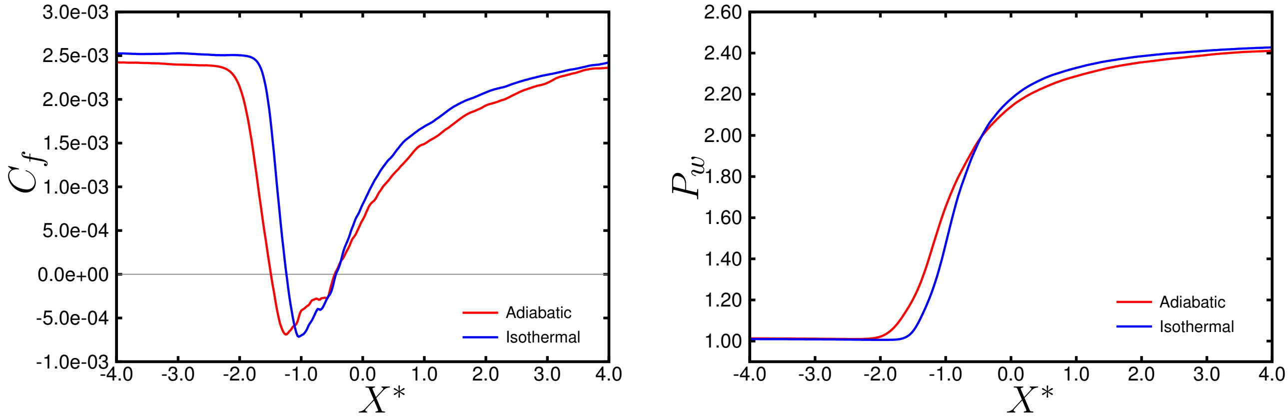

(a) Skin-Friction Coefficient **(b)** Wall-Pressure

Figure VI.1 – Longitudinal evolution of mean wall-pressure and skin-friction distributions as a function of nondimensional streamwise distance $X^* = (X - X_{imp})/\delta^o_\omega$: (a) Wall-Pressure; (b) Skin-Friction Coefficient

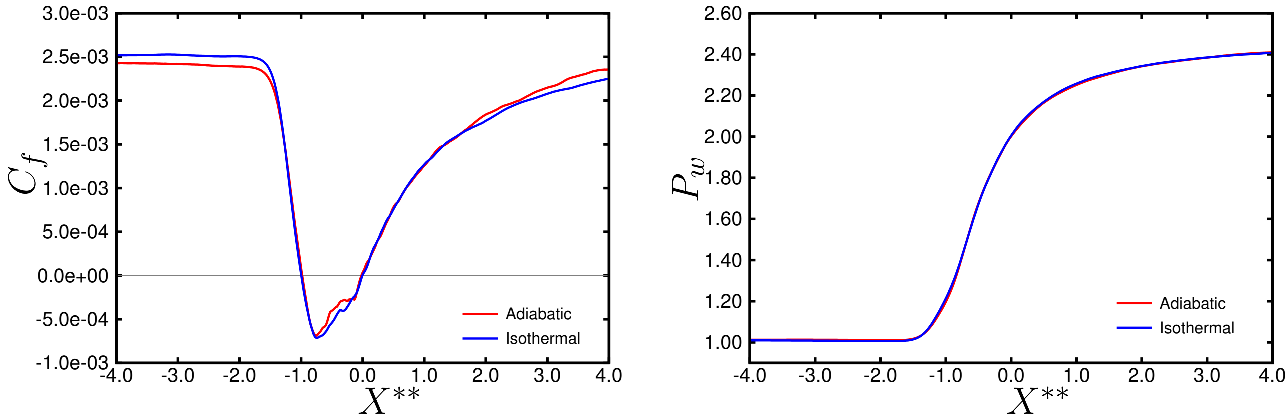

(a) Skin-Friction Coefficient **(b)** Wall-Pressure

Figure VI.2 – Longitudinal evolution of mean wall-pressure and skin-friction distributions as a function of nondimensional streamwise distance $X^{**} = (X - X_{re})/(X_{re} - X_{sep})$: (a) Wall-Pressure; (b) Skin-Friction Coefficient

parameters are given in Eq. (VI.1) and Eq. (VI.2), respectively.,

$$\delta_i^* = \int_0^{\delta_\omega^l} \left(1 - \frac{u_1}{U_e}\right) \mathrm{d}y, \qquad \theta_i = \int_0^{\delta_\omega^l} \frac{u_1}{U_e}\left(1 - \frac{u_1}{U_e}\right) \mathrm{d}y, \qquad H_i = \frac{\delta_i^*}{\theta_i} \tag{VI.1}$$

$$\delta^* = \int_0^{\delta_\omega^l} \left(1 - \frac{\rho u_1}{\rho_e U_e}\right) \mathrm{d}y, \qquad \theta = \int_0^{\delta_\omega^l} \frac{\rho u_1}{\rho_e U_e} \left(1 - \frac{\rho u_1}{\rho_e U_e}\right) \mathrm{d}y, \qquad H = \frac{\delta^*}{\theta} \tag{VI.2}$$

It can be seen that the integral parameters remain almost constant in the region that corresponds to the undisturbed boundary layer ($X^* < -2$), but undergo different evolutions as the flow crosses the shock-system. In general, the incompressible shape factor (H_i) is weakly dependent on the Mach number and decreases with the increase of the Reynolds number (Délery and Marvin [41]). As the Reynolds number increases, the boundary layers represent velocity profiles with less velocity deficit, while in contrast, the less filled velocity profiles suggest thicker subsonic layers and correspondingly higher values of H_i. As a result of interaction, due to the adverse pressure gradient, the flow is retarded in the streamwise direction. The corresponding velocity fields have thick subsonic layers and highly decelerated velocity distributions (see Fig. VI.5) that reflects higher values of H_i in this region. For adiabatic case, H_i attains a maximum value of ≈ 2.5 which is found to be in agreement with the commonly accepted values (≈ 2.5, see Délery and Marvin [41]) associated with the turbulent separations. Further downstream of the location of maximum shape factor ($X^* > -0.2$), the retardation effect ceases in the region close to the wall; whereas, it still continues at the boundary layer outer edge since the pressure is still rising in this region. This reversal is due to the action of the turbulent viscous forces which are greatly enhanced by the retardation effect. As a consequence of this change in the evolution of the profile shape, the shape parameter starts to decrease and the progressive relaxation of the boundary layer towards the mean equilibrium state is identified. For the isothermal case, the overall scenario remains the same; however, slight modifications observed are marked here. Unlike the very steep rise in values of H_i found in the adiabatic case, a more progressive increase for the isothermal case is found and the maximum value obtained for H_i is ≈ 2.3, which is slightly less than its adiabatic counterpart. It can be noted that the compressible shape factors H decreases significantly in the separation region which is due to the combined effect of increasing density and extremely retarded velocity distributions in this region. In addition, the maximum value of H obtained for the isothermal case (≈ 15) is substantially higher than its adiabatic counterpart (≈ 9).

The shock interaction with the boundary layer causes the incompressible displacement thickness δ_i^* to increase rapidly in the interaction region, while only a moderate increase in the value of the incompressible momentum thickness θ_i is observed. In the first part of the interaction, a small dip in the distribution of δ^* is observed in the region $-1.5 < X^* < -1.2$, and following that it steeply increases and attains a maximum value of $\approx 38\%$ of the undistubed boundary layer thickness. A progressive drop in values is observed downstream of the shock impingiment point ($X^* = 0$) that suggests the flow recovery towards the mean equilibrium state. The momentum thickness essentially follows the same trends as that of δ_i^* and obtains a maximum value of around $\approx 15\%$ of the undistubed boundary layer thickness, while the corresponding maximum values for the isothermal case are $\approx 32\%$ of the undisturbed boundary layer thickness for δ_i^* and $\approx 15\%$ of the undisturbed boundary layer thickness for θ_i. As suggested by Délery

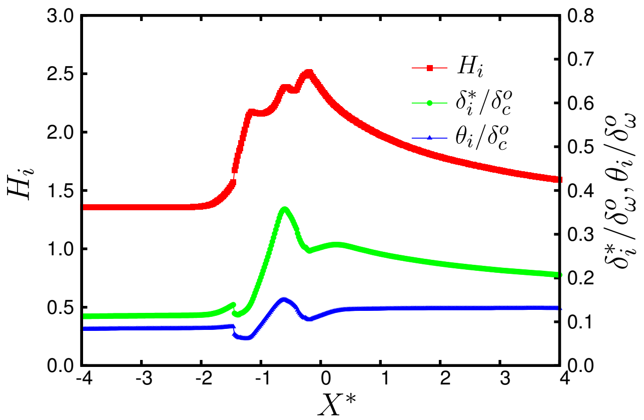

(a) Adiabatic Case

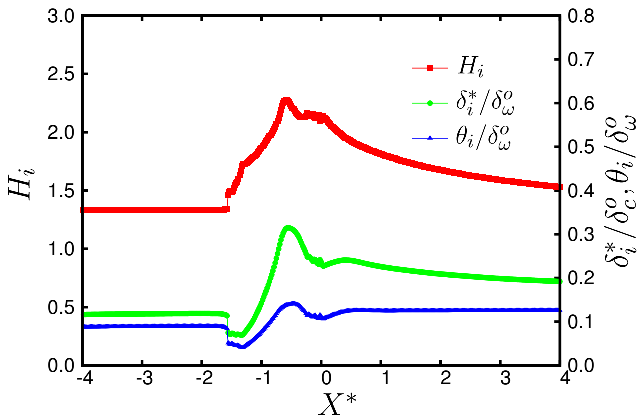

(b) Isothermal Case

Figure VI.3 – Incompressible shape factor, incompressible displacement thickness and incompressible momentum thickness evolution along the interaction region: (a) Adiabatic Case; (b) Isothermal Case

and Marvin [41], the momentum thickness development along the interaction region can be explained by considering the von Kàrmàn integral momentum equation for an incompressible flow,

$$\frac{\partial \theta}{\partial x} = \frac{C_f}{2} - (2 + H)\frac{1}{U_e}\frac{\partial U_e}{\partial x_j}\theta \tag{VI.3}$$

Since the pressure gradient remains positive throughout the first part of the interaction (i.e. $\partial U_e/\partial x < 0$), and the skin-friction coefficient C_f remains a small but positive quantity (except in the separation region), then $\partial\theta/\partial x$ must also remains necessarily positive. This explains the increase in the momentum thickness throughout most of the interaction zone. Note that for the compressible case, the integral momentum equation has an additional term $-(\theta/\rho_e)\partial\rho_e/\partial x$ on the right-hand side, which does not significantly affect the results for the case of compressible momentum thickness evolution(Fig. VI.4). These results suggest that the behavior of both compressible and incompressible evolutions of shape factor are primarily dependent on the variation of the displacement thickness along the interaction region and are consistent with the observations of Délery and Marvin(1986)[41] in their studies involving transonic flow

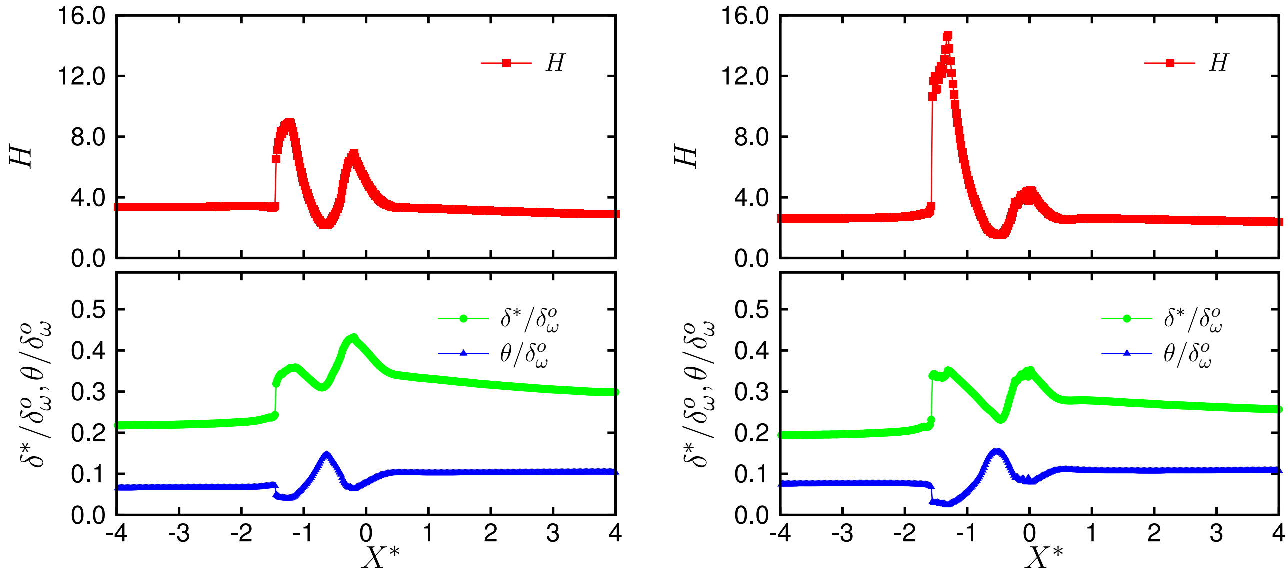

(a) Adiabatic Case

(b) Isothermal Case

Figure VI.4 – Compressible shape factor, compressible displacement thickness and compressible momentum thickness evolution along the interaction region: (a) Adiabatic Case; (b) Isothermal Case

interactions.

VI.1.3 Evolution of Primitive Variables

This section, provides a qualitative and quantitative description of the interaction field, in terms of mean primitive variable values (velocity and thermodynamic variables). The evolution of mean streamwise velocities along the interaction region for the adiabatic and isothermal cases are presented in Fig. VI.5a and Fig. VI.5b respectively. Mean velocity vectors are also shown (with a sampling of 1 in 15 in streamwise direction and 1 in 2 in wall-normal direction) that provide a sketch of velocity profile development under the influence of the external perturbation induced by the shock-system. The change in velocity field due to the presence of flow discontinuities (like incident shock, reflected shock and expansion fans) can be clearly identified. One can observe the deficit in streamwise velocity component in the region downstream of $X^* = -2\delta^o_\omega$ and a corresponding increase in the subsonic part of the boundary layer. In support of the earlier argument, the contours of Mach number variation along the interaction region are plotted in Fig. VI.6, and the corresponding evolution of sonic line is marked with dashes. The flow retardation due to the adverse pressure gradient induced by the shock can be identified through the evolution of the velocity vectors. Significantly, no flow reversal of the velocity vectors are detected within the interaction region; however, the negative magnitude of the velocity contours establish the fact that there is a reversed flow region but on average the size of the separation bubble is very small. Similar observations have also been made by Pirozzoli and Grasso [13] and Humble [16] that the height of the separation bubble can be very small. Downstream of the shock-system ($X^* > 0$), the flow starts to regain its energy from the turbulent field and a progressive relaxation toward a mean equilibrium state is depicted. Due to the negligibly small height of the separation region (see Fig. VI.5), the mean flow interaction mechanism closely resembles the sketch for the case of an attached impinging oblique shock boundary layer interaction problem (see section II.2.2, Fig. II.3a). For the isothermal case, the general features of the interaction remains the same; however, a slightly thinner subsonic layer (downstream of interaction onset) can be observed in comparison to its adiabatic counterpart, and a faster recovery of the redeveloping flow field can also be noticed.

Fig. VI.7 and Fig. VI.8 describe the variation of mean wall-normal and spanwise component of the velocity field along the interaction region. The results show that, as a result of the reflected shock interaction with the boundary layer, the flow experiences a lift from the wall (region between $X^* = -2\delta^o_\omega$ and $X^* = -0.5\delta^o_\omega$) with a maximal wall-normal velocity of about $0.12U_{\infty,bi}$ (marked with blue levels). These results are in close agreement with the ones reported by Humble [16] who observed an upward movement of flow in the region $X^* = -2\delta^o_\omega$ and $X^* = -0.6\delta^o_\omega$ with a maximum wall-normal velocity of $0.15U_{\infty,bi}$. Downstream of the shock-system $X^* > 0$, in the redeveloping boundary layer, a large region is observed where the fluid is moving towards the wall with a velocity magnitude within the range of $0 - 0.05U_{\infty,bi}$, which is again consistent with the values found by Humble [16]. For the isothermal case, Fig. VI.7b, the cross-over point between the two shocks is found to be at a relatively lower position in the boundary layer when compared with the adiabatic case and the shock is reflected with a relatively less acute angle than the adiabatic one. Moreover, the region in which the flow moves away from the wall is limited to $X^* = -1.6\delta^o_\omega$ and $X^* = -0.6\delta^o_\omega$.

For both the adiabatic and isothermal simulations, downstream of the reflected shock, the non-zero values of spanwise velocity are observed in comparison negligible values upstream of the interaction. This can be caused by the effect of the interaction which can introduce inhomogeneity in the spanwise direction. However, it is important to note that its magnitude is very small compared to the freestream velocity upstream of the interaction (such as having a maximum value of $0.005U_{\infty,bi}$ for the adiabatic case). The contours of mean static pressure evolution within the interaction region for the adiabatic and isothermal cases are presented in

Fig. VI.9a and Fig. VI.9b, respectively. It can be seen that as the impinging oblique shock propagates through the inviscid rotational part of the boundary layer, its intensity is being affected due to the decrease in the local Mach number (see Fig. VI.6), and hence the resulting shape of the incident shock is being curved. As the strength of the shock decreases, it starts to disperse in the form of compression waves, which on reaching the sonic line, reflect back in the form of expansion waves. Influenced by the pressure gradient induced by the incident shock, the subsonic portion of the boundary layer thickens and generates the compression waves that combine at some height within the boundary layer and results in the formation of the reflected shock. Similar to the wall-pressure distribution presented in Fig. VI.1b, the pressure distribution pattern shown also helps in determining the extent to which the upstream influence of the shock-system can be sensed over the whole height of the boundary layer. The effects of the wall cooling on the pressure field shifts the position of the shocks cross-over point to a relatively lower position in the boundary layer with respect to adiabatic case and the impinging shock reflects with a less acute angle in comparison with its adiabatic counterpart. These observations are in qualitative agreement with the findings of Back and Cuffel [56]. Fig. VI.10a and Fig. VI.10b demonstrate the variation of static temperature field within the interaction region for both adiabatic and isothermal cases, respectively. Unlike the velocity fields, as a result of differently imposed wall thermal boundary conditions, a clear difference in the mean static temperature interaction fields for the adiabatic and isothermal cases can be identified. The main difference between the two cases in the near-wall region can be remarked . For adiabatic wall condition, $\overline{T}/T_{\infty,bi}$ reaches its maximum value at the wall which is equivalent to the adiabatic wall temperature; moreover, there is a sublayer within the boundary layer ($y/\delta^o_\omega < 0.2$), in the region $-1 < X^* < 1$ in which the the mean static temperature varies in the range of $\overline{T} = 1.83 - 1.95 T_{\infty,bi}$. In contrast, for an isothermal wall boundary condition, the above argument does not hold. For the isothermal case, the maximum of static temperature is not found at wall, but is found at some height in the inner layer of the boundary layer (located very close to the wall and not identified in the present contour plot). However, in the region downstream of $X^* > 1$ at a height $y/\delta^o_\omega > 0.2$ the overall temperature distribution remains qualitatively quite similar for both cases.

The evolution of mean density along the interaction region are presented in Fig. VI.11 for both the adiabatic and isothermal cases. For the adiabatic case, relatively lower magnitudes of density are found in the region $-1 < X^* < 1$ in comparison with isothermal counterpart. Again, similar to the temperature field, the relative near-wall evolution is different for the two cases (adiabatic and isothermal) and details can be identified through the magnified views of the profiles presented in Chapter V (see Fig. V.32) .

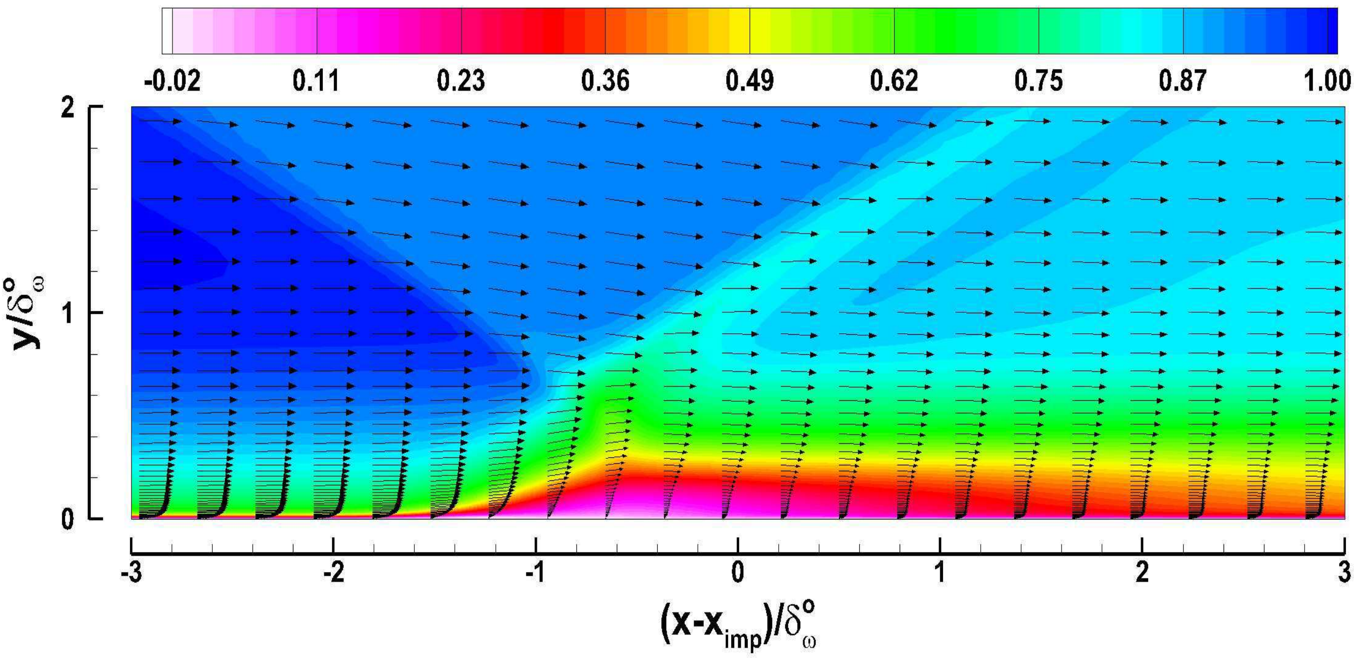

(a) Adiabatic Case

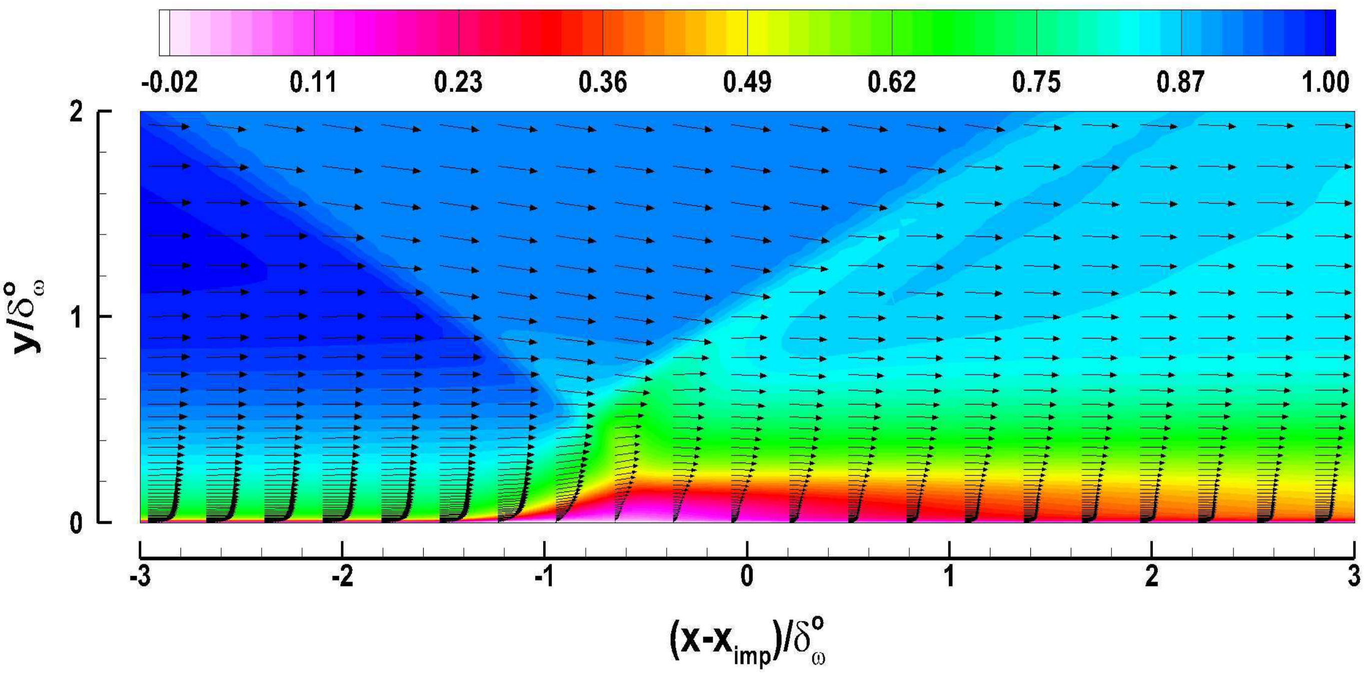

(b) Isothermal Case

Figure VI.5 – Evolution of mean streamwise velocity, $\overline{u_1}/U_{\infty,bi}$, along the interaction region:(a) Adiabatic Case; (b) Isothermal Case

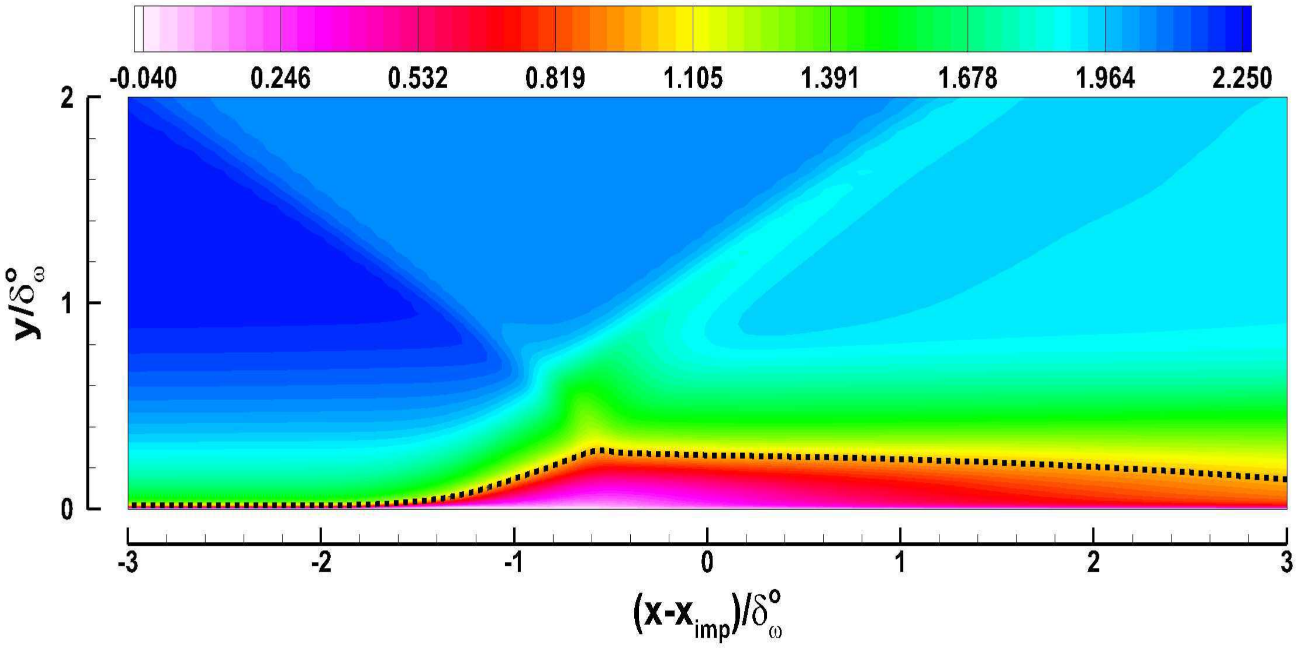

(a) Adiabatic Case

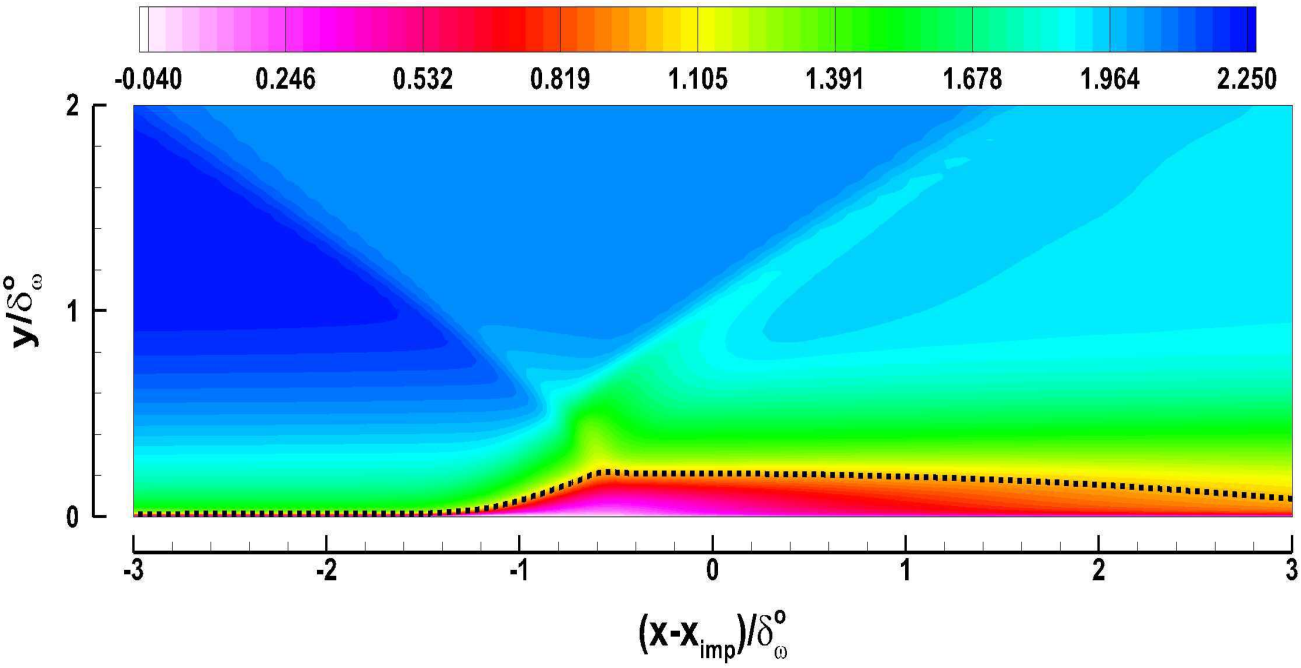

(b) Isothermal Case

Figure VI.6 – Evolution of Mach number, M, along the interaction region:(a) Adiabatic Case; (b) Isothermal Case

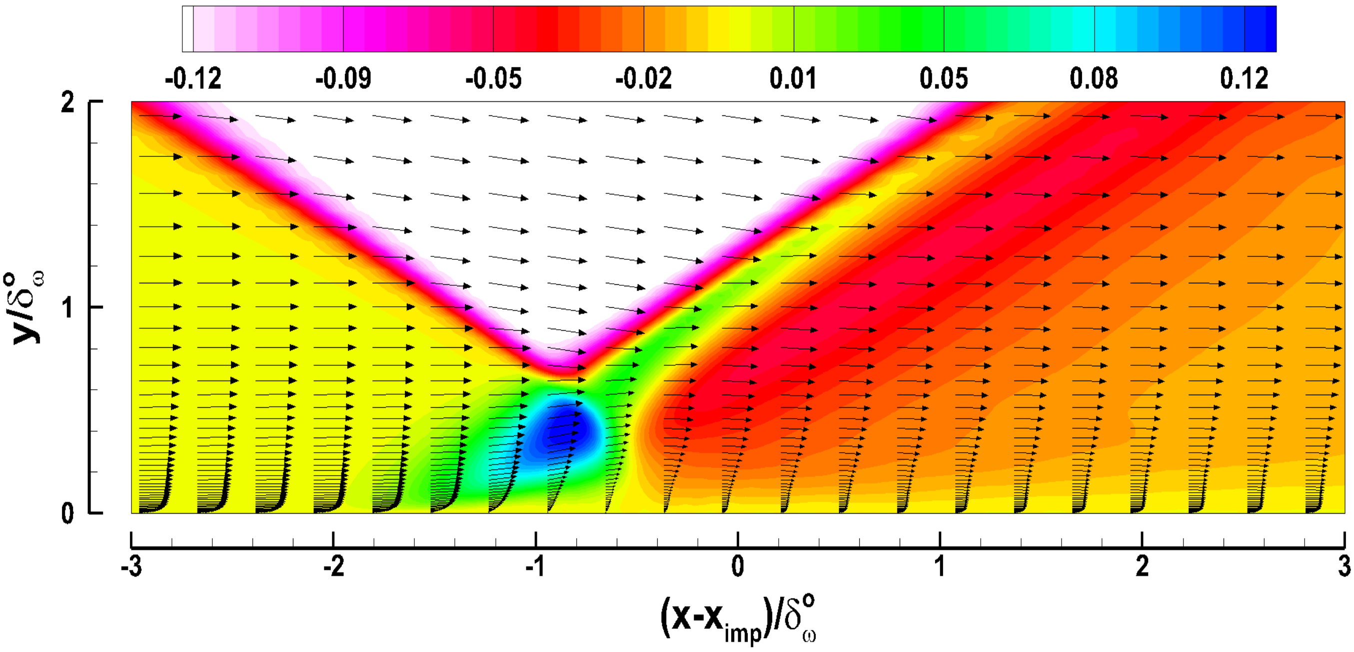

(a) Adiabatic Case

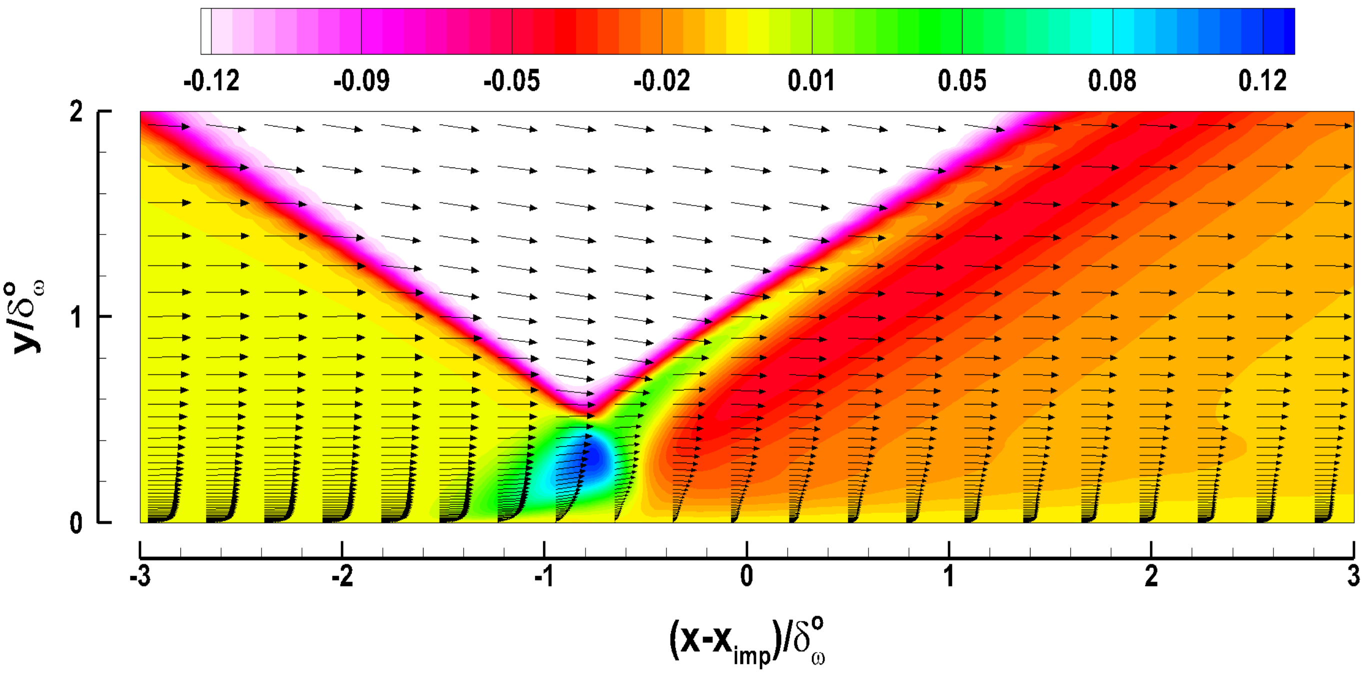

(b) Isothermal Case

Figure VI.7 – Evolution of mean wall-normal velocity, $\overline{u_2}/U_{\infty,bi}$, along the interaction region:(a) Adiabatic Case; (b) Isothermal Case

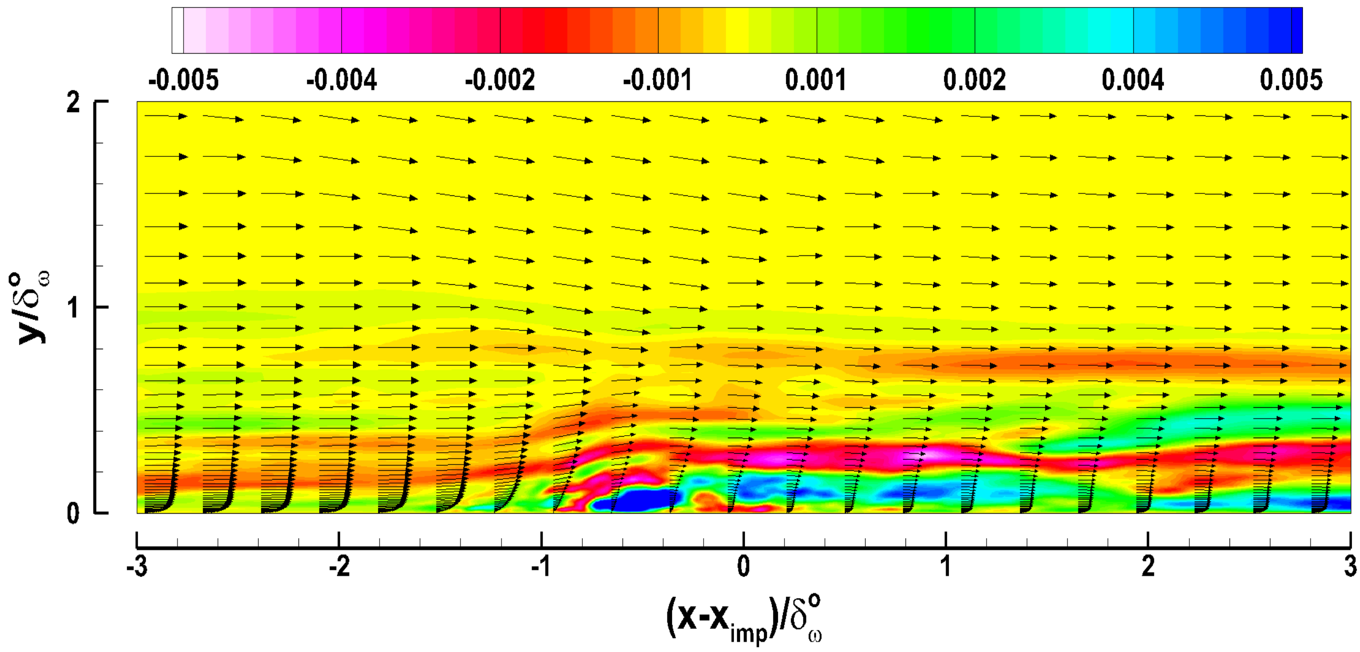

(a) Adiabatic Case

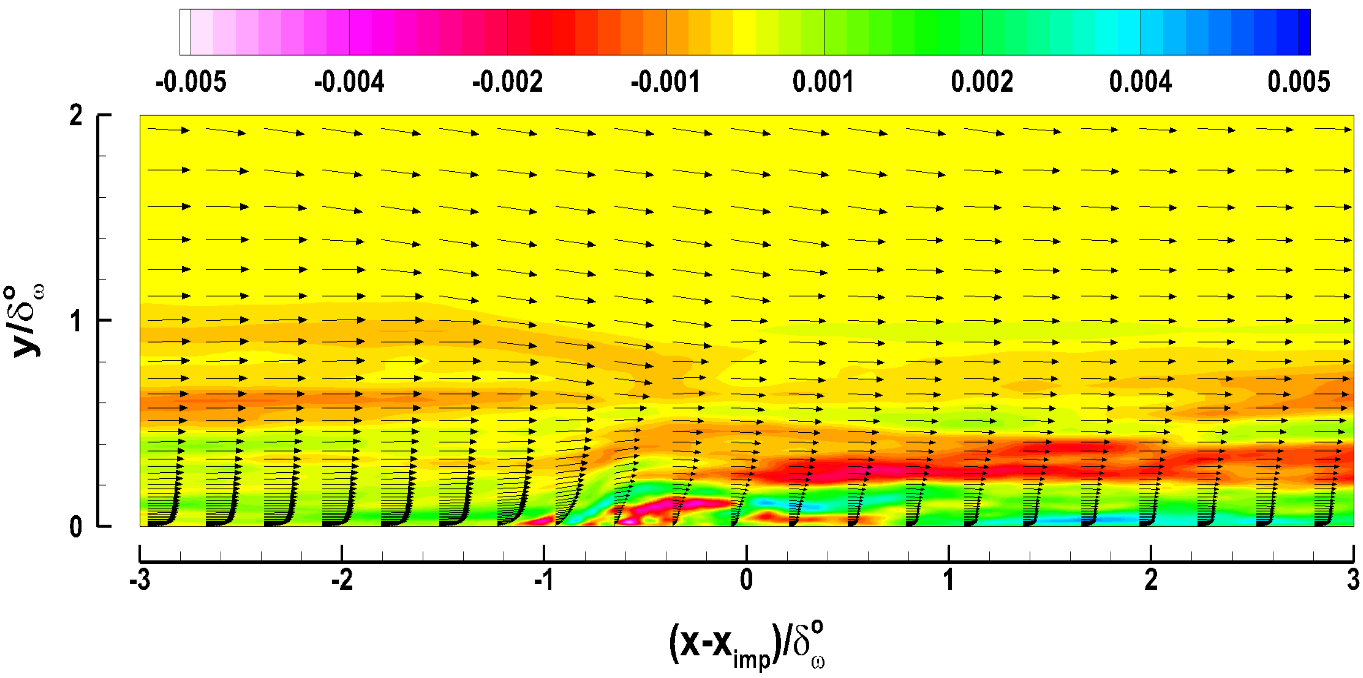

(b) Isothermal Case

Figure VI.8 – Evolution of mean spanwise velocity, $\overline{u_3}/U_{\infty,bi}$, along the interaction region:(a) Adiabatic Case; (b) Isothermal Case

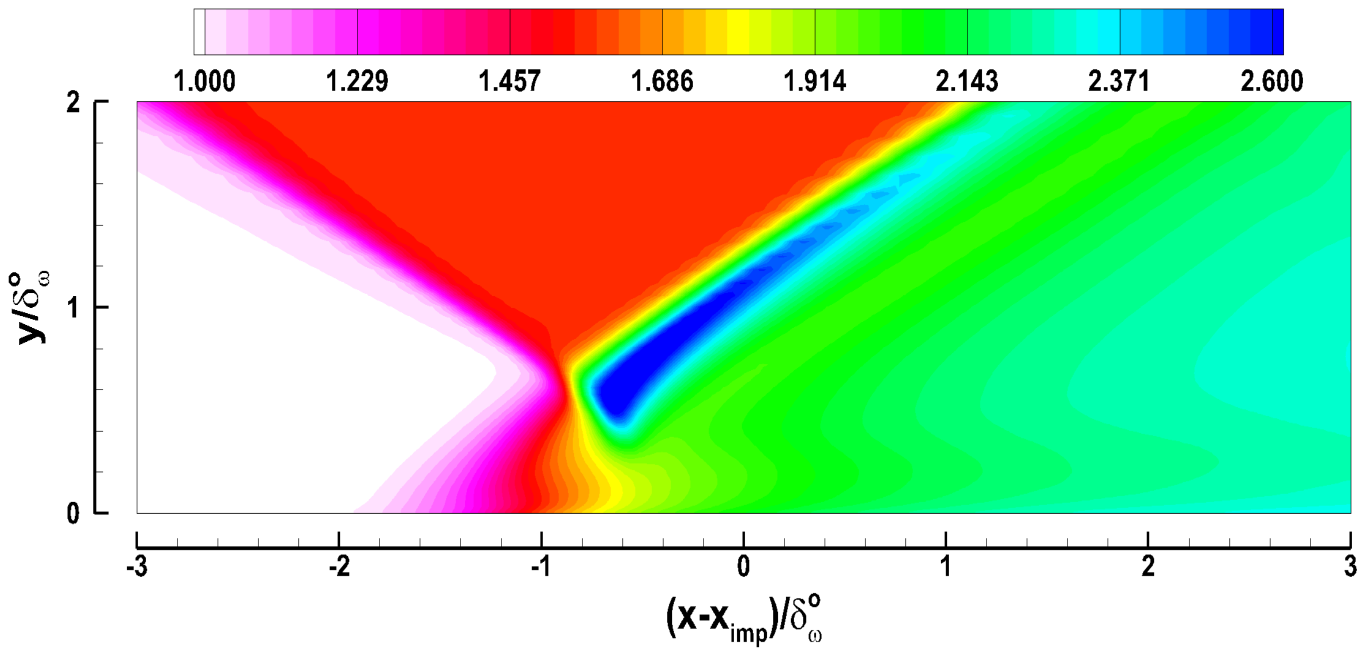

(a) Adiabatic Case

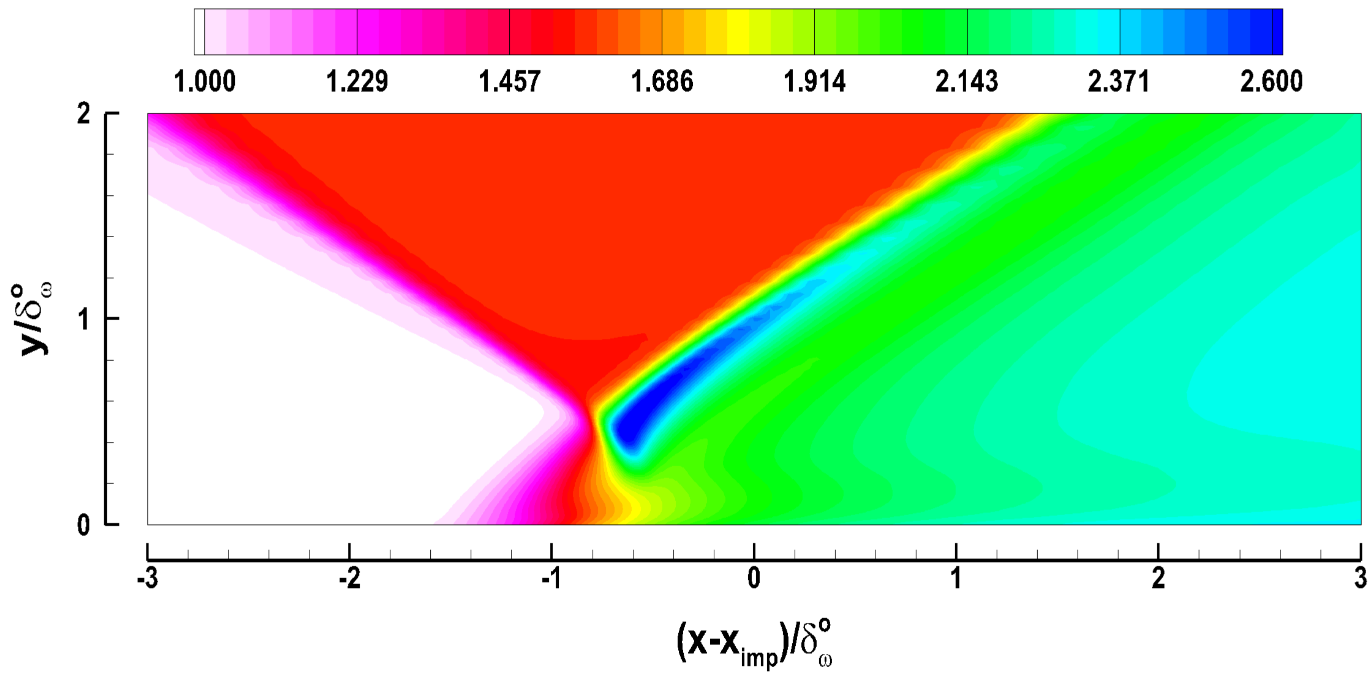

(b) Isothermal Case

Figure VI.9 – Evolution of mean static pressure, $\overline{P}/P_{\infty,bi}$, along the interaction region:(a) Adiabatic Case; (b) Isothermal Case

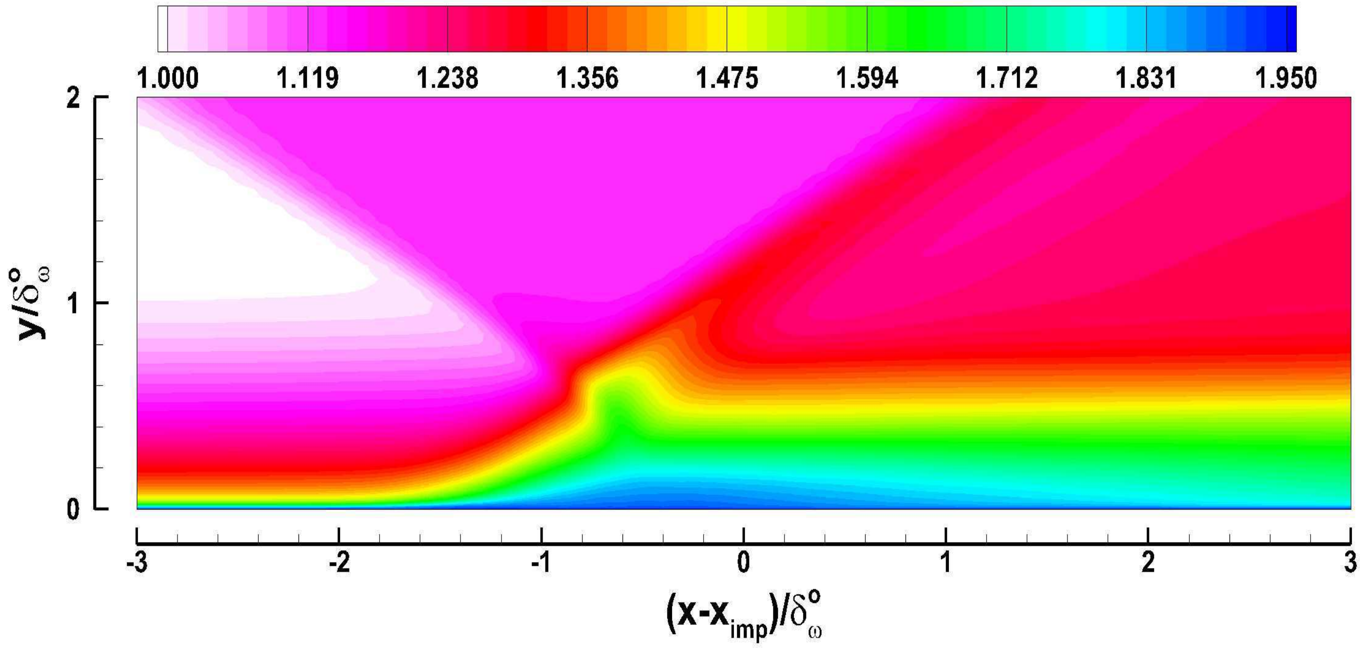

(a) Adiabatic Case

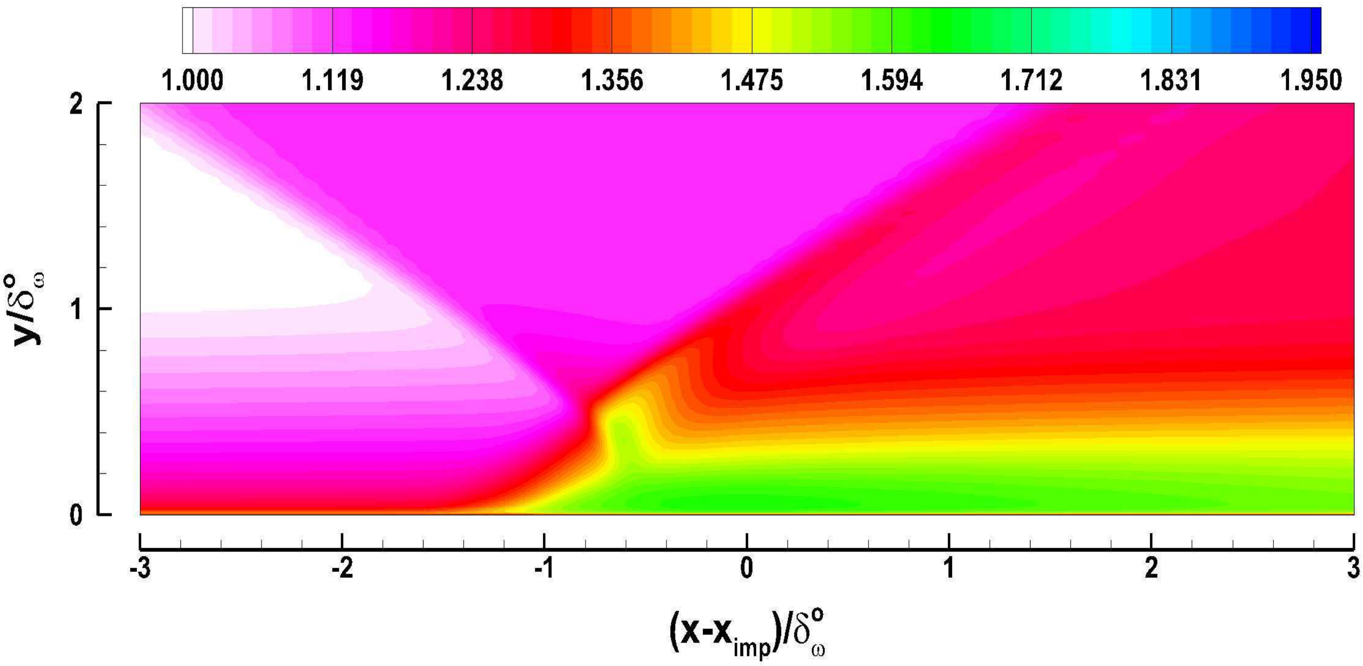

(b) Isothermal Case

Figure VI.10 – Evolution of mean static temperature, $\overline{T}/T_{\infty,bi}$, along the interaction region:(a) Adiabatic Case; (b) Isothermal Case

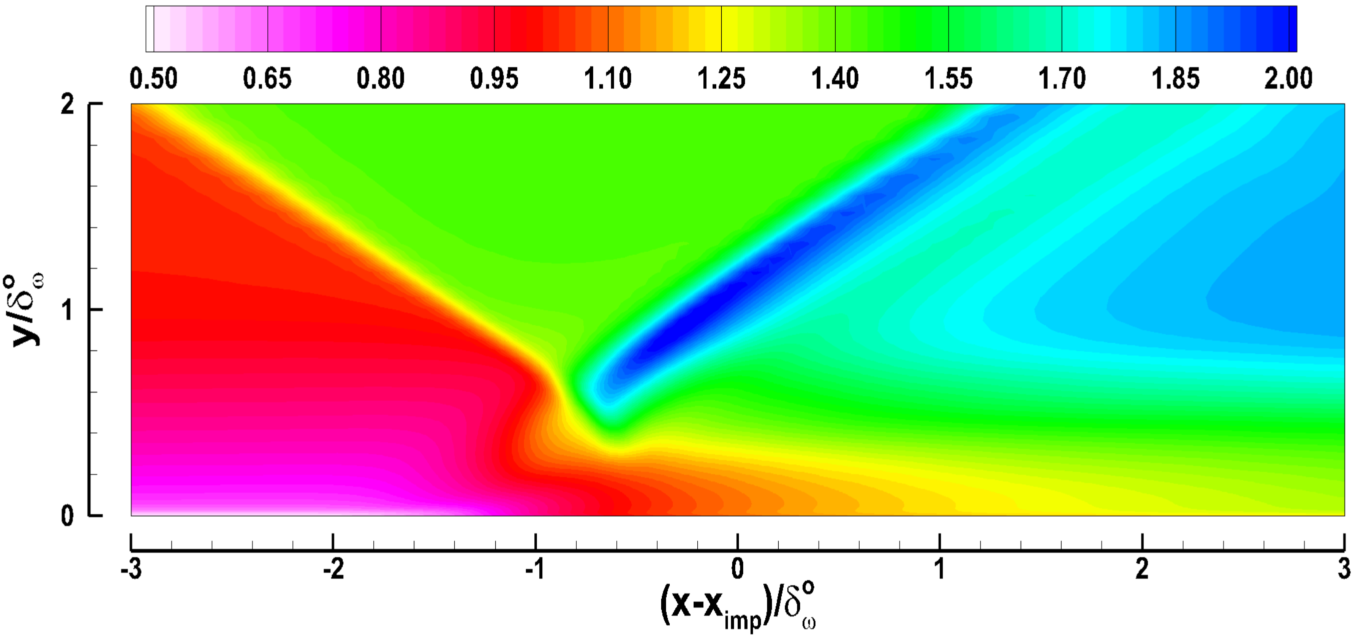

(a) Adiabatic Case

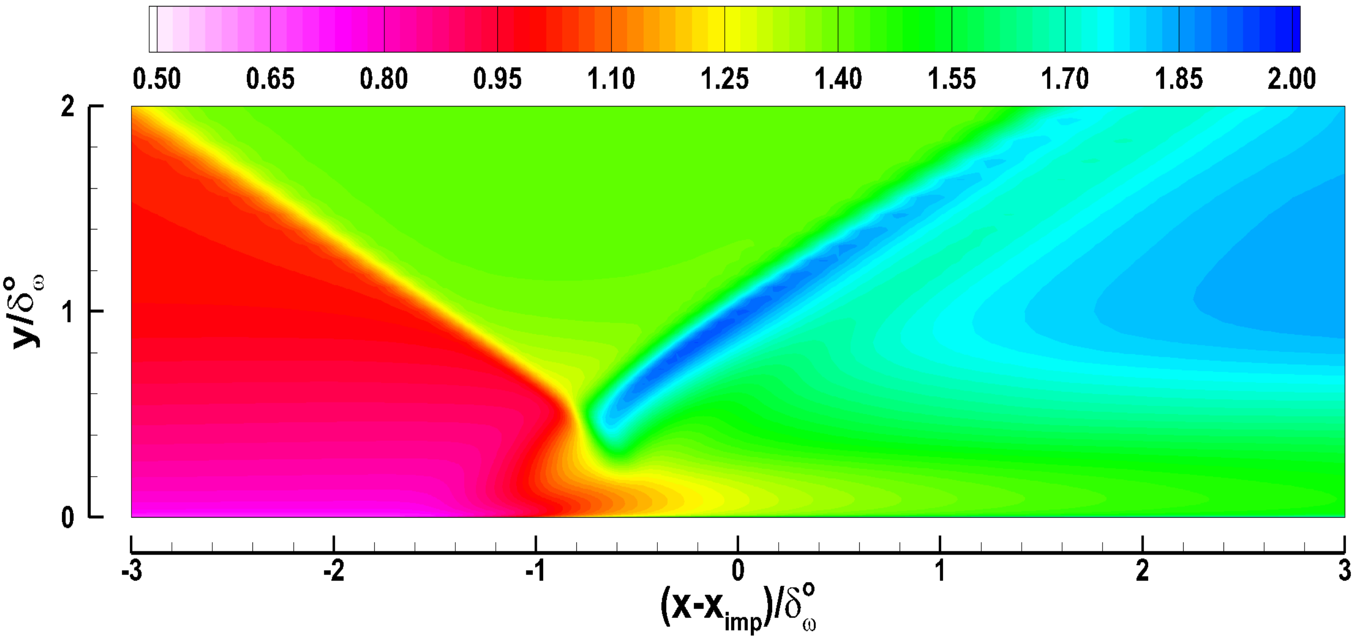

(b) Isothermal Case

Figure VI.11 – Evolution of mean density, $\overline{\rho}/\rho_{\infty,bi}$, along the interaction region:(a) Adiabatic Case; (b) Isothermal Case

VI.2 Evolution of Turbulence Properties along the Interaction Region

In this section, the evolutions of the turbulent velocity and thermal fields along the interaction region will be discussed. In addition, the extent to which the perturbed turbulent boundary layer deviate from its equilibrium state will be identified by plotting the evolution of the normalized shear stress against the equilibrium shape parameter.

VI.2.1 Equilibrium Phase Portraits

Following East and Sawyer [153] and Délery and Marvin [41], the entire history of interacting boundary layer, starting from the upstream of the interaction to far downstream state in the relaxation region can be depicted by plotting the streamwise evolution in 'phase plane' of the square-root of the maximum shear-stress coefficient (C_τ) versus the equilibrium shape parameter (J), where C_τ and J are defined as

$$C_\tau = \frac{-\left(\bar{\rho}\overline{u_1' u_2'}\right)_{max}}{\frac{1}{2}\bar{\rho}_e \overline{U}_e^2}, \qquad J = 1 - \frac{1}{H_i} \tag{VI.4}$$

East and Sawyer [153] have introduced a function G, given by Eq. (VI.5), which has the unique characteristic that its value remains constant for "equilibrium" boundary layer flows, with the value of the constant (6.55) corresponding to a zero pressure gradient boundary layer and indicated by the straight line in Fig. VI.12. As reported by Délery and Marvin [41], an equilibrium boundary layer is the one that undergoes a specific transformation in which an instantaneous adjustment occurs between the distributions of mean velocity and shear stress. Generally, this can only be possibly true for very progressive and slow evolving boundary layers.

$$G = \frac{J}{\sqrt{0.5 C_\tau}} = 6.55 \tag{VI.5}$$

The trajectories of interaction in the phase plane ($\sqrt{C_\tau}$, J) for both adiabatic and isothermal cases are plotted in Fig. VI.12a and Fig. VI.12b, respectively. It is important to mention that the time and spanwise averaged results obtained over a computational volume that covers a longitudinal range of $-6.1\delta_\omega^o$ to $6.9\delta_\omega^o$ are plotted in the present section, along with it the corresponding results for six diagnostic planes ($P01$ to $P06$, presented in Chapter V) are also plotted to describe their relative position along the trajectory and because these data points will help in determining the extrapolated end of the trajectory (represented by the dashed lines Fig. VI.12) at the farthest downstream location in the computational domain ($P06 = 16.7\delta_\omega^o$, see chapter V). The function G for equilibrium boundary layers, represented by the straight line is also shown in order to compare the deviation of the perturbed boundary layer from its equilibrium state. The results reveal that the trajectory starts from a point "A" which is close to the equilibrium line and represents the state of undisturbed incoming boundary layer. As the boundary layer is subjected to shock interaction, the data points start showing a divergence from the initial equilibrium locus and follow the classic non-equilibrium trajectory below the equilibrium line (similar to the one observed by Délery and Marvin [41], for the case of transonic shock boundary layer interaction). This characterized by the rapid increase in J (see shape factor evolution, Fig. VI.3a), and followed by a lag of turbulent shear stress as the turbulence response to the perturbation. Contrary to Délery and Marvin [41] and Délery [154], who

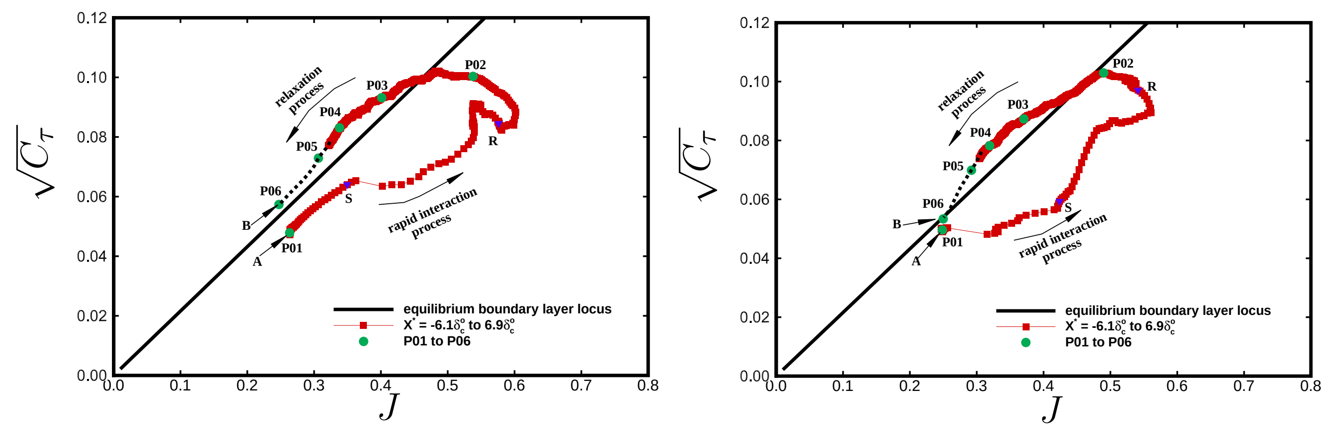

(a) Adiabatic Case **(b)** Isothermal Case

Figure VI.12 – Variation of normalized maximum shear stress in the phase plane(J,$\sqrt{C_\tau}$): (a) Adiabatic Case; (b) Isothermal Case

observed a single global maximum of Reynolds-averaged shear stress magnitude, two global maximums of Reynolds-averaged shear stress magnitude (see Fig. VI.17) are observed here. The first is observed in the separation region (which is indicated as the region bounded by the separation "S" and reattachment "R" points), and is represented by a bump in the trajectory. This reflects the amplification of the Reynolds shear stress magnitude due to the interaction of the boundary layer with the reflected shock. A second global maximum in the distribution of Reynolds shear stress, results in due to amplification of shear stress by the convection of the large scale eddies downstream of the incident shock. In both, adiabatic and isothermal cases, the equilibrium shape parameter (J) attains its maximum value around the reattachment point

"R" and then starts to decrease (following the distribution of incompressible shape factor, see Fig. VI.3), resulting in the bending of trajectory towards the equilibrium line. During this phase of interaction, the value of Reynolds shear stress is still increasing until it reaches the maximum at a streamwise station that coincides with the point where the trajectory crosses the equilibrium line. Downstream of this station, in the absence of any external perturbation, the flow starts recovering towards its undisturbed state similar to that upstream of the interaction. The final position obtained within the limits of the present computational domain is marked with point "B". For the isothermal case (Fig. VI.12b), the bump observed in the trajectory of C_τ is not that prominent, however one can still observe the rise in C_τ due to the first global maximum in the shear stress distribution.

In a similar manner, the longitudinal evolutions of maximum streamwise Reynolds stress component against the equilibrium shape parameter, for the adiabatic and isothermal cases, are plotted in Fig. VI.13a and Fig. VI.13b, respectively. Both $(\sqrt{\overline{u_1'u_1'}})_{max}/U_e$ and J increase rapidly in the region in close proximity to the foot of the reflected shock. For both adiabatic and isothermal cases, $(\sqrt{\overline{u_1'u_1'}})_{max}/U_e$ reaches its peak value in the separation region, and the region designated as the "maximum turbulent activity region" represents the interaction phase in which $(\sqrt{\overline{u_1'u_1'}})_{max}/U_e$ varies slower than the value of J. Farther downstream, in proximity of reattachment point "R", the shape factor attains its maximum value and begins to decrease. Simultaneously, $(\sqrt{\overline{u_1'u_1'}})_{max}/U_e$ also decreases indicating that the boundary layer profile is adjusting itself to the disturbance induced as a result of the interaction. Further on (downstream of the shock-system), in the absence of any external perturbation, the turbulent field transfer energy back to mean field, and the flow starts relaxing back towards its undisturbed conditions. A similar trend for supersonic boundary layer interaction has been observed by Humble [16]. However, the maximum value of $(\sqrt{\overline{u_1'u_1'}})_{max}/U_e$ observed by Humble [16] is around 0.2 while in the simulations here it is around 0.23. This is due to the fact that the edge velocity U_e was used at each corresponding streamwise location for normalization while Humble [16] used a normalization based on the freestream velocity upstream of the interaction ($U_{\infty,bi}$). For the isothermal case, $(\sqrt{\overline{u_1'u_1'}})_{max}/U_e$ rises more rapidly in the first part of the interaction in comparison with the adiabatic case where the rise in $(\sqrt{\overline{u_1'u_1'}})_{max}/U_e$ is more uniform and gradual.

VI.2.2 Evolution of Turbulent Velocity Field

Similar to the mean flow evolutions, a qualitative and quantitative evolutions of the turbulent properties of the developing boundary layer along the interaction region are presented. The

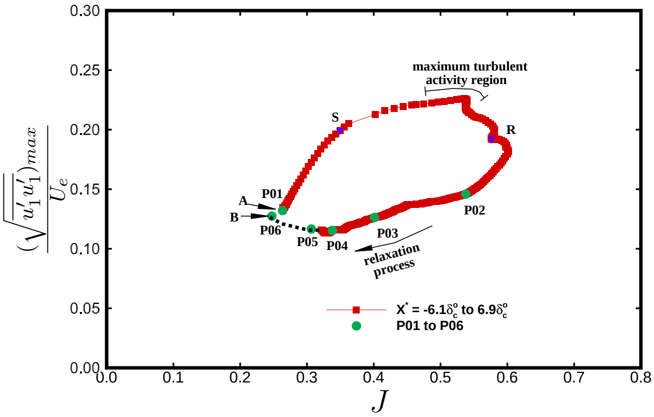

(a) Adiabatic Case

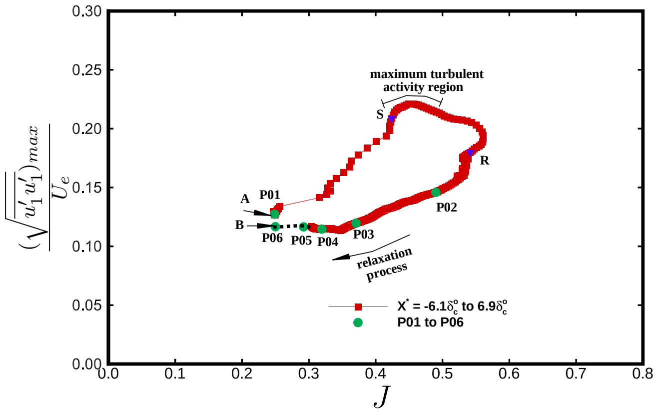

(b) Isothermal Case

Figure VI.13 – Longitudinal variation of maximum streamwise Reynolds stress component in the phase plane$(J, \frac{(\sqrt{\overline{u_1'u_1'}})_{max}}{U_e})$: (a) Adiabatic Case; (b) Isothermal Case

variations of Reynolds averaged normal stresses along the interaction regions are presented in Fig. VI.14, Fig. VI.15 and Fig. VI.16, and the results for both adiabatic and isothermal cases are shown. Qualitative trends obtained for the present adiabatic wall simulation are consistent with the simulation results reported by Garnier [66] as well as with experiments of Humble [16] and Piponniau [63]. Upstream of the interaction, the larger fluctuations of velocity are observed in the near-wall region; however, in the interaction region, the velocity fluctuations get amplified, and the location of the peak amplitude of velocity fluctuations (Reynolds stresses) shifts away from the wall. The maximum amplification of streamwise component of normal Reynolds stresses $\overline{u_1'u_1'}/U_{\infty,bi}^2$ is found to be in this region, $-1.6 < X^* < -0.8$, and is amplified by a factor of 2.4. Downstream of the global maximum stress location, the local maximums of $\overline{u_1'u_1'}/U_{\infty,bi}^2$ continue to lie at a comparatively higher position in the boundary layer; however, the magnitude decreases as the flow starts relaxing farther downstream of the shock-system.

For the wall-normal component of Reynolds normal stresses, $\overline{u_2'u_2'}/U_{\infty,bi}^2$, a significant increase in value occurs along the reflected shock, away from the wall $0.6 < y/\delta_\omega^o < 1.2$, that characterize the rippling motion of the reflected shock. Moreover, the amplification across the refracted part of the reflected shock (region $y/\delta_\omega^o < 0.6$) is quite less, suggesting a non-coupled motion between two parts of the reflected shock. In comparison with the local maximum values observed upstream of the interaction, the wall-normal component is amplified by a factor of 4.0 $(-1.0 < X^* < 0.8)$. Downstream of the incident shock tip $(X^* > -0.5)$, elevated levels of the v-component velocity fluctuations remain persist and spread over the most part of the boundary layer. As suggested by Humble [16] and Piponniau [63], these elevated levels of $\overline{u_2' u_2'}/U_{\infty,bi}^2$ correspond to a statistical footprint of the vortex shedding process that is initiated as a result of the interaction and convect with the flow in the downstream region. In support of the previous argument, an instantaneous snapshot of the interaction field is presented for the adiabatic simulation in Fig. VI.18. The iso-surfaces of the Q-criterion, $(W_{ij}W_{ij} - S_{ij}S_{ij})/2$, are plotted and the relative position of the shock-system is indicated in terms of the magnitude of the pressure gradient $|\nabla P|$ (Threshold values are selected such that a better representation of the vortex structures upstream of the shock-system and following that the corresponding influence of shock-system on the boundary layer can be identified). Upstream of the interaction, elongated and intermittent structures are observed. As an effect of interaction, one can easily identify the presence of large scale coherent structures in the interaction zone, which are inclined at an acute angle with the flow direction and resemble hair-pin type structures.

For the spanwise component of Reynolds normal stresses, $\overline{u_3' u_3'}/U_{\infty,bi}^2$, the maximum fluctuation level of (levels in blue) are observed in the region $-1.2 < X^* < -0.4$ and amplified by a factor of 3.7 with respect to the local maximum values obtained upstream of the interaction; however, similar to the v-component fluctuations, the elevated levels continue to exist downstream of the interaction over a significant height within the boundary layer.

The contours of the shear stress $\overline{u_1' u_2'}/U_{\infty,bi}^2$ component are presented in Fig. VI.17. The local peaks in shear stress magnitude are observed along the shock structure which is consistent with the experiments of Humble [16] and Piponniau [63], and in agreement with the suggestion of Smits and Muck [8] that the unsteady motion of the shock may produce local peaks in turbulence intensity profiles. Another notable feature is the change of sign of shear stress in the region identified by the tip of the incident shock. This was also observed by Deleuze [10] who related this change of sign of shear stress with the region where one observes a positive wall-normal component of velocity in combination with negative values of longitudinal direction derivative (for further discussion see Deleuze [10]). Similar to the normal stresses, amplified magnitude levels, of the shear stresses are observed in the interaction region. It is important to note that two regions of global maximum amplified shear stress are observed. The first maximum is identified in the region bounded by the incident and reflected shocks and the second maximum is in the region downstream of the tip of the incident shock. The region downstream of the incident shock is characterized by the large magnitude of shear stress in the lower half of the boundary layer ($y/\delta_\omega^o < 0.4$) and its negative magnitude suggests high contributions to the turbulent events by ejections and sweeps (see section V.3.2.4). Furthermore, Ardonceau [47], Kuntz [49] and Humble [16] explained that the elevated levels of shear stress downstream of the incident shock correspond to the turbulent motions characterized by the large-scale eddies. For the isothermal case, one can identify the comparatively shorter influenced lengths and relatively faster relaxation process.

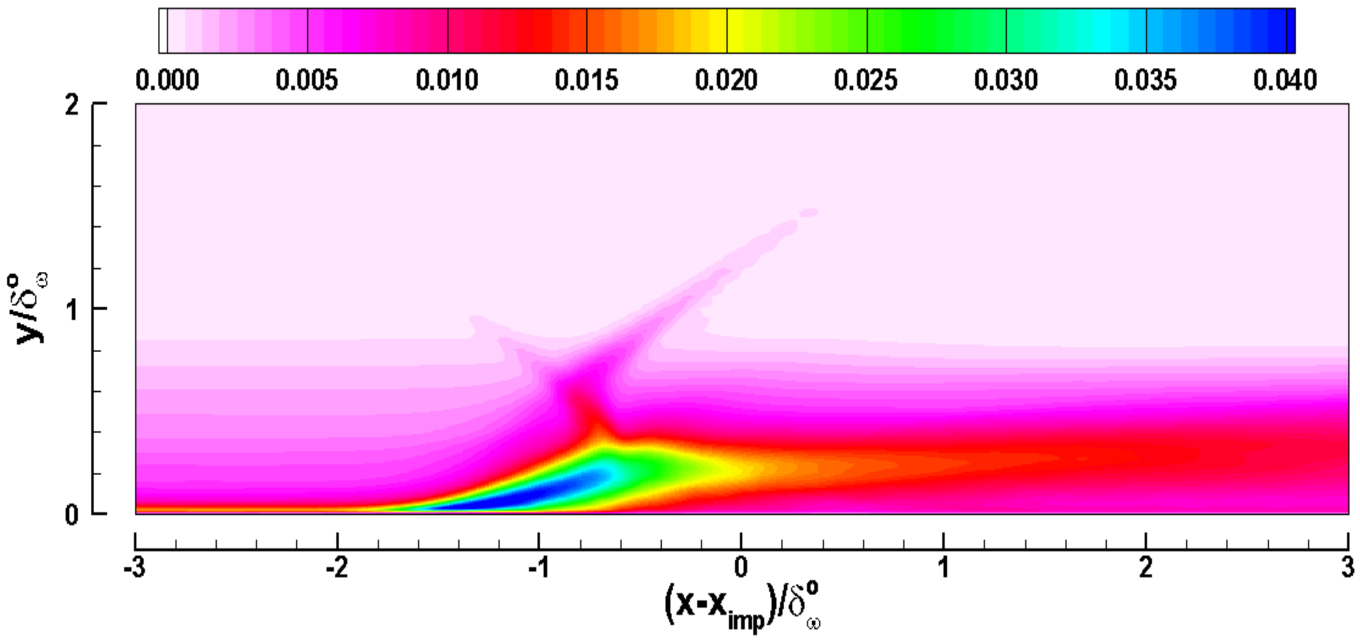

(a) Adiabatic Case

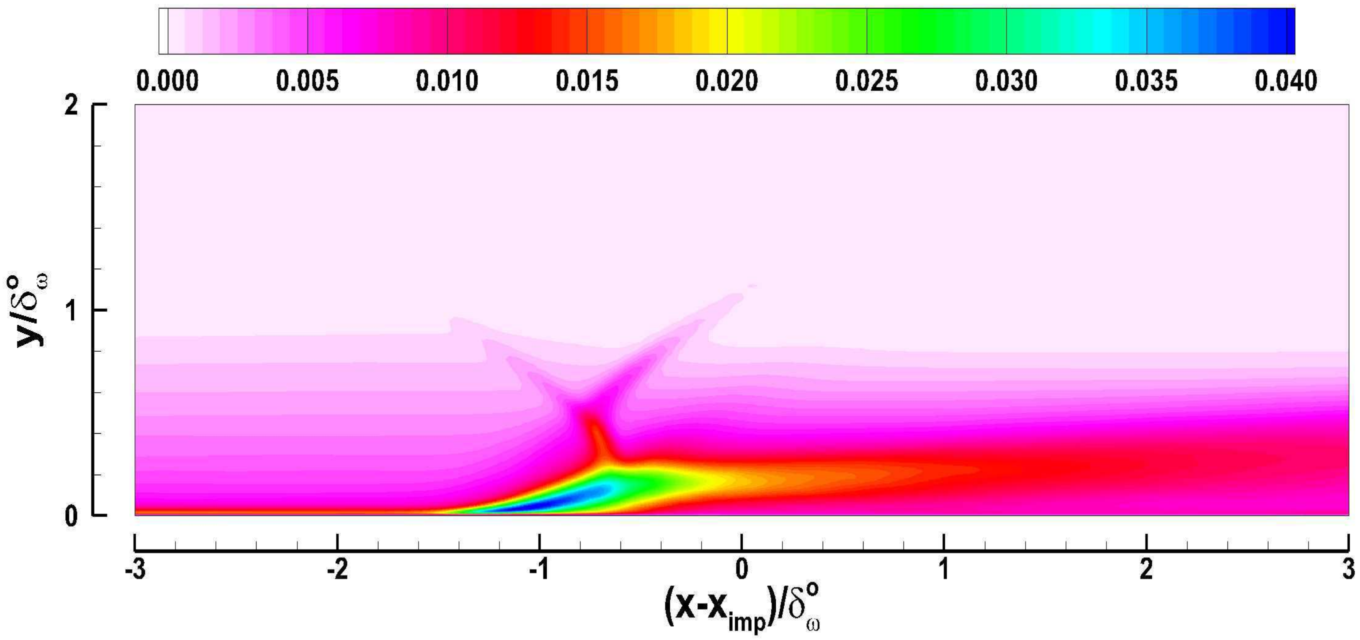

(b) Isothermal Case

Figure VI.14 – Evolution of streamwise component of Reynolds normal stress, $\overline{u_1'u_1'}/U_{\infty,bi}^2$ along the interaction region:(a) Adiabatic Case; (b) Isothermal Case

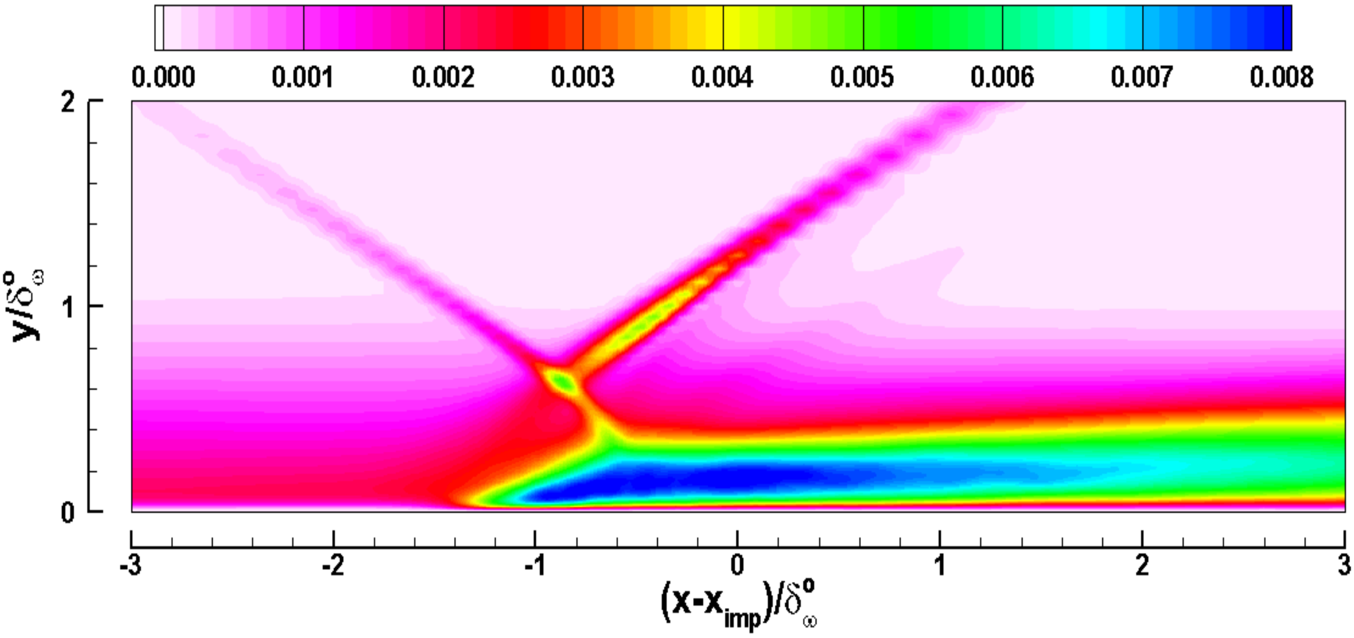

(a) Adiabatic Case

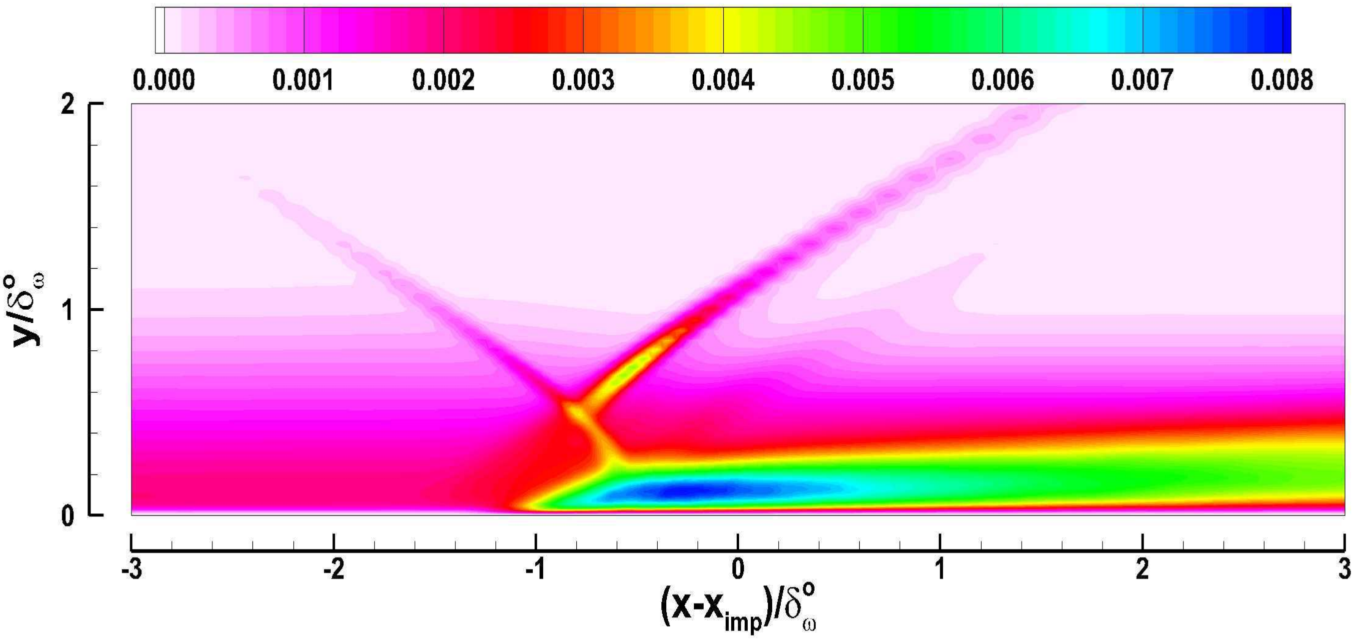

(b) Isothermal Case

Figure VI.15 – Evolution of wall-normal component of Reynolds normal stress, $\overline{u_2'u_2'}/U^2_{\infty,bi}$, along the interaction region:(a) Adiabatic Case; (b) Isothermal Case

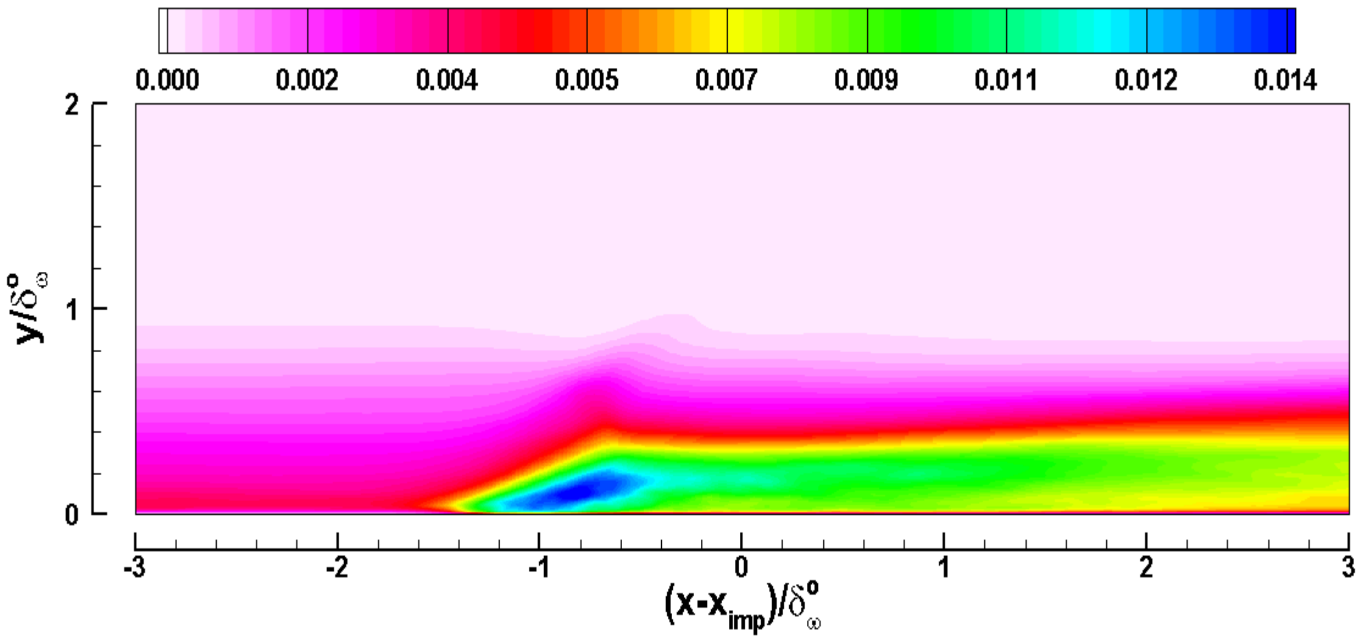

(a) Adiabatic Case

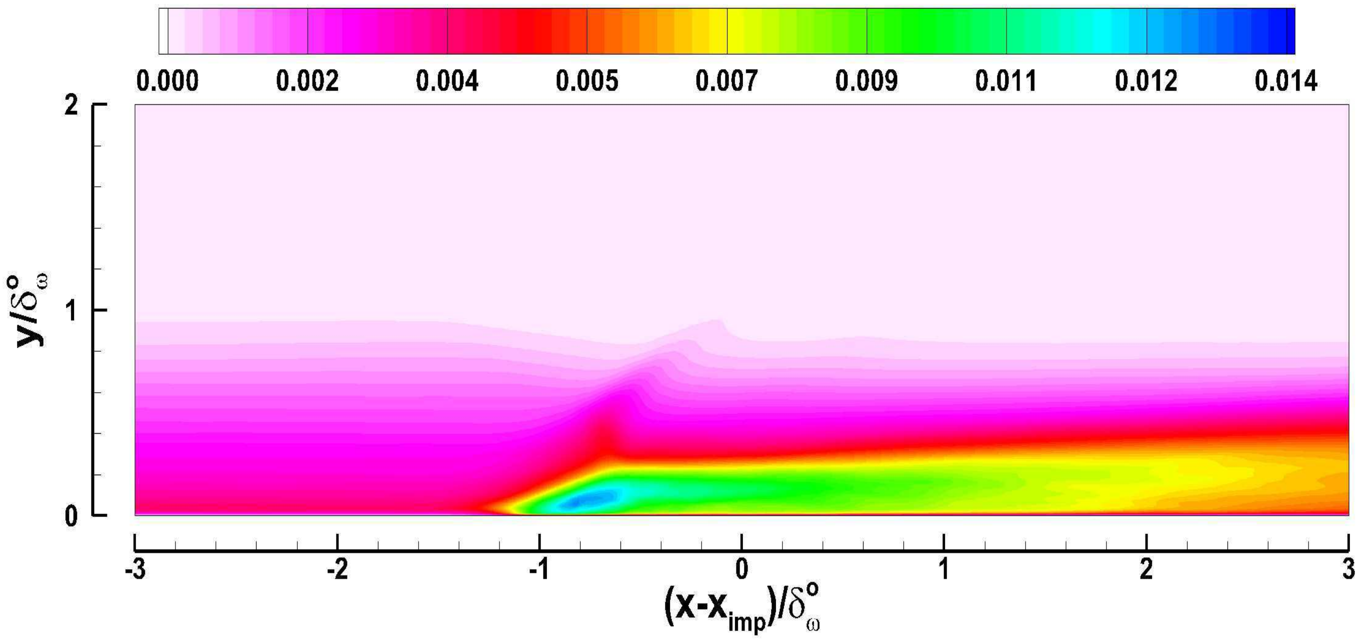

(b) Isothermal Case

Figure VI.16 – Evolution of spanwise component of Reynolds normal stress, $\overline{u'_3 u'_3}/U^2_{\infty,bi}$, along the interaction region:(a) Adiabatic Case; (b) Isothermal Case

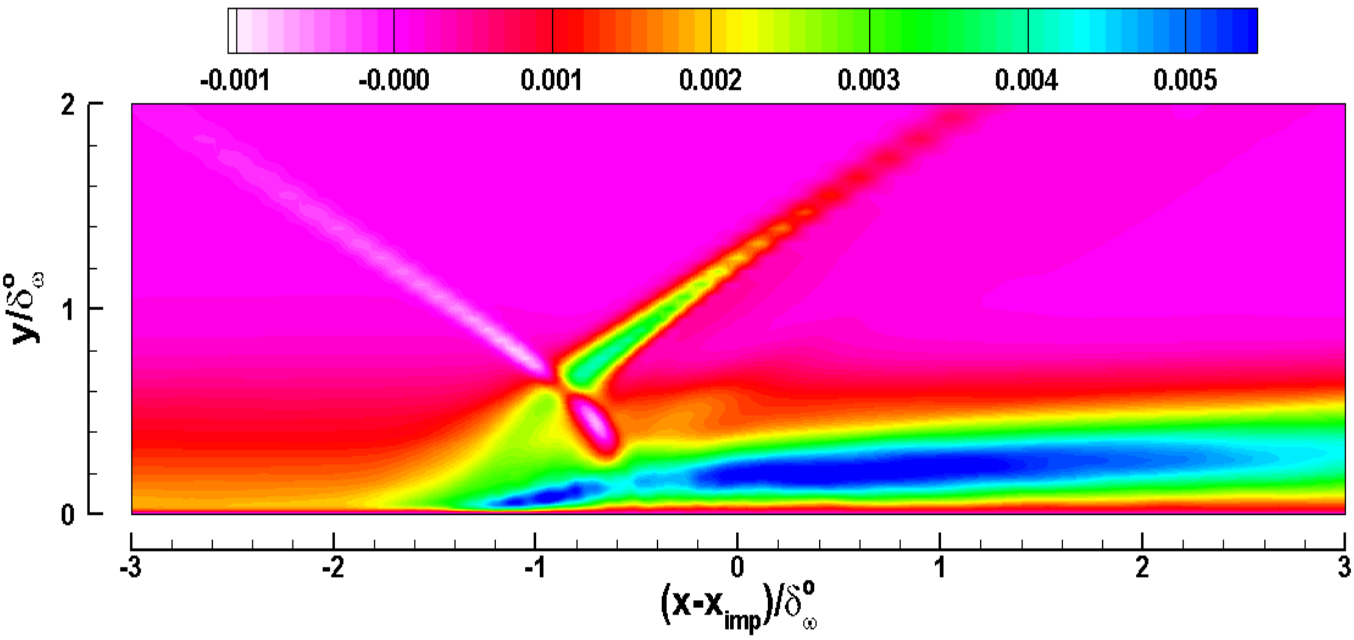

(a) Adiabatic Case

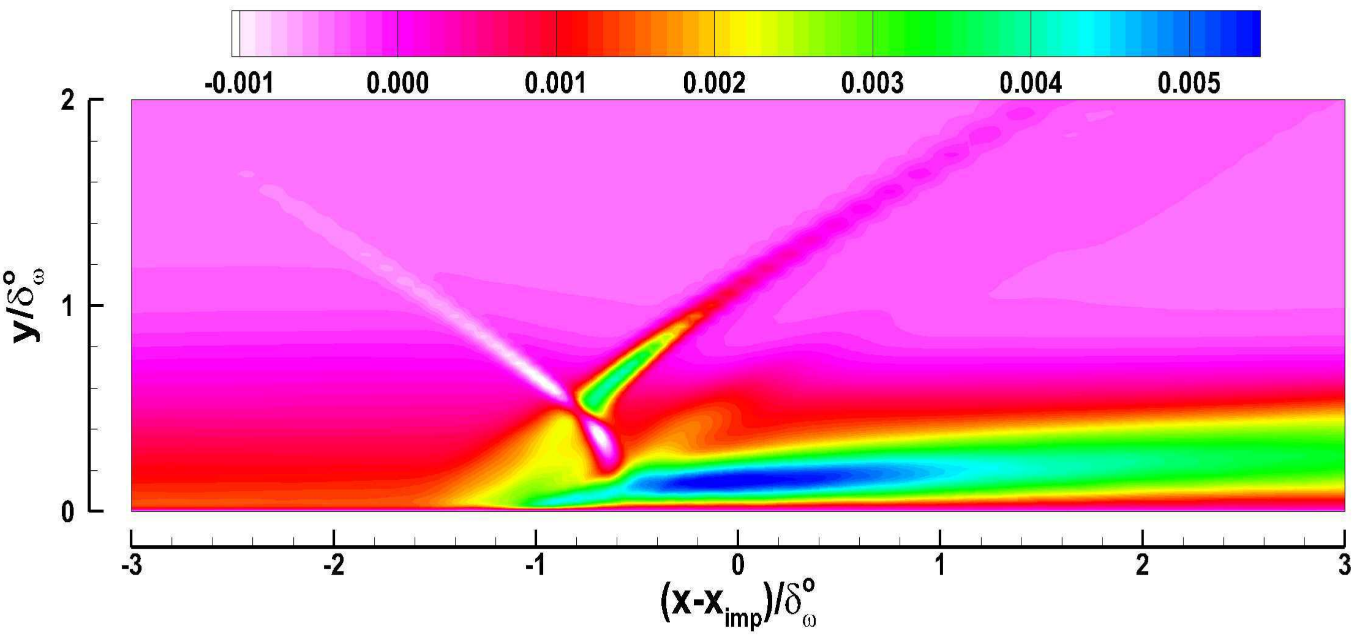

(b) Isothermal Case

Figure VI.17 – Evolution of Reynolds shear stress, $\overline{u_1'u_2'}/U^2_{\infty,bi}$, along the interaction region:(a) Adiabatic Case; (b) Isothermal Case

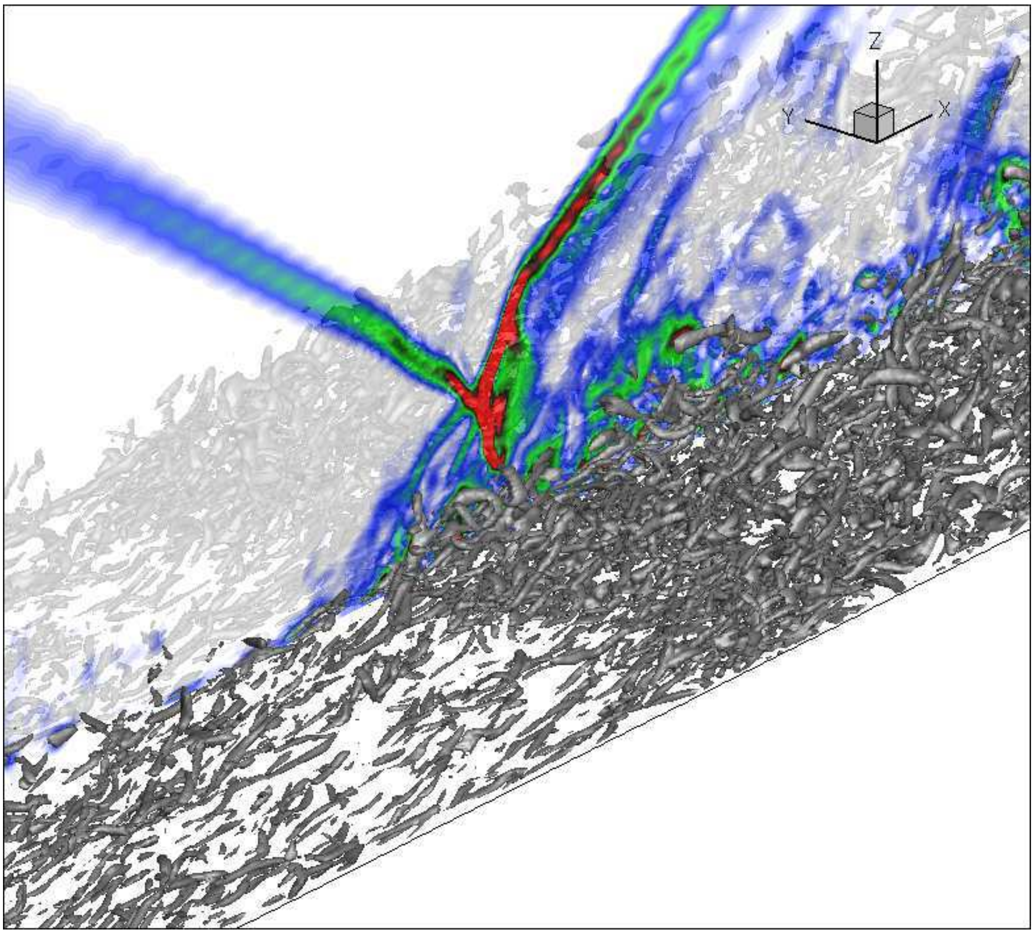

Figure VI.18 – Three-dimensional view of the interaction field. Grey structures represent the iso-surfaces of the Q-criterion $(0.5(W_{ij}W_{ij} - S_{ij}S_{ij}))$ and color contours represents the relative position of the shock-system in terms of the magnitude of the pressure gradient $|\nabla P|$

VI.2.3 Evolution of Turbulent Thermal Field

An analysis of the properties of the turbulent thermal field shows the major changes observed along the interaction region for the two different types of wall thermal boundary conditions. Contours representing the behavior of temperature variance ($\overline{T'T'}/T^2_{\infty,bi}$) distribution along the interaction region are presented in Fig. VI.19 for both cases. In comparison with the adiabatic wall conditions, the temperature variance magnitude observed for the isothermal case is significantly lower and is attributed to the fact that the isothermal wall conditions significantly dampen the fluctuations of the thermal field. Similar to the velocity field, an effect of the interaction is to displace the position of the maximum values of the quantities from very near-wall region to a position away from the wall. One can note that the temperature fluctuations in the near-wall region, bounded by the incident and reflected shocks, are quite small. In addition to the maximum temperature variance values observed in the region $-1.4 < X^* < -0.5$ (marked with blue levels), a thick layer of elevated temperature fluctuation levels is observed downstream of the interaction region $0.2 < y/\delta^o_\omega < 0.6$ (marked with green levels). The qualitative trends are similar to the ones observed by Garnier [66] for an impinging shock boundary layer interaction problem. For the isothermal case, relative to the values observed upstream of the interaction, slightly higher levels of temperature fluctuations are found downstream of the interaction $0.2 < y/\delta^o_\omega < 0.4$ (marked with red levels).

The evolution of density fluctuations ($\overline{\rho'\rho'}/\rho^2_{\infty,bi}$) along the interaction region for the adiabatic and isothermal cases are plotted in Fig. VI.20. The density variance contours, showing high levels of density fluctuations, are observed in the region just above the refracted part of the incident shock and below the reflected shock. In this region, relative to the values upstream of the interactions, the density fluctuation levels are amplified by a factor of ≈ 10 and can be attributed to the strong compressibility effects induced by the shock-system. Downstream of the interaction $X^* > 0$, amplified fluctuating density levels are also observed but their corresponding magnitudes are not that large relative to the values upstream of the interaction. Similar behavior is observed for the isothermal case; however, the relative magnitudes with respect to the adiabatic case are less. Evolution of pressure variance ($\overline{p'p'}/P^2_{\infty,bi}$) is presented in Fig. VI.21 for the adiabatic and isothermal cases and trends similar that of density variance are observed.

The distributions of streamwise ($\overline{-u'_1T'}/(UT)_{\infty,bi}$) and wall-normal ($\overline{u'_2T'}/(UT)_{\infty,bi}$) components of the turbulent heat flux for the adiabatic and isothermal cases are shown in Fig. VI.22 and Fig. VI.23, respectively. For the adiabatic case the maximum values of the streamwise component lies in the region just after the onset of interaction $-1.6 < X^* < -1.2$. While the region

$1.0 < X^* < -1.2$ contains elevated levels of $\overline{-u_1'T'}/(UT)_{\infty,bi}$ at a position farther away the wall. Downstream of this region, the levels drop rapidly to significantly lower values. Similar to the shear stress distribution, local peaks of $\overline{u_2'T'}/(UT)_{\infty,bi}$ are observed along the shock-system and negative values are identified along the incident shock. Again, similar to the shear stress distribution, two regions of elevated values of wall-normal heat flux are identified. An argument similar to that for the shear stresses can be made here as well. The first augmentation is attributed to the amplification of the turbulence across the reflected shock, while the second corresponds to the convection of large-eddies downstream of the shock-system. For the isothermal case, the magnitude of both components is significantly reduced due to the suppression of temperature fluctuations. As a result of the interaction, negative levels of $\overline{-u_1'T'}/(UT)_{\infty,bi}$ and $\overline{u_2'T'}/(UT)_{\infty,bi}$ are observed in the very near-wall region (for clarity of the above argument see Fig. V.37b and Fig. V.38b).

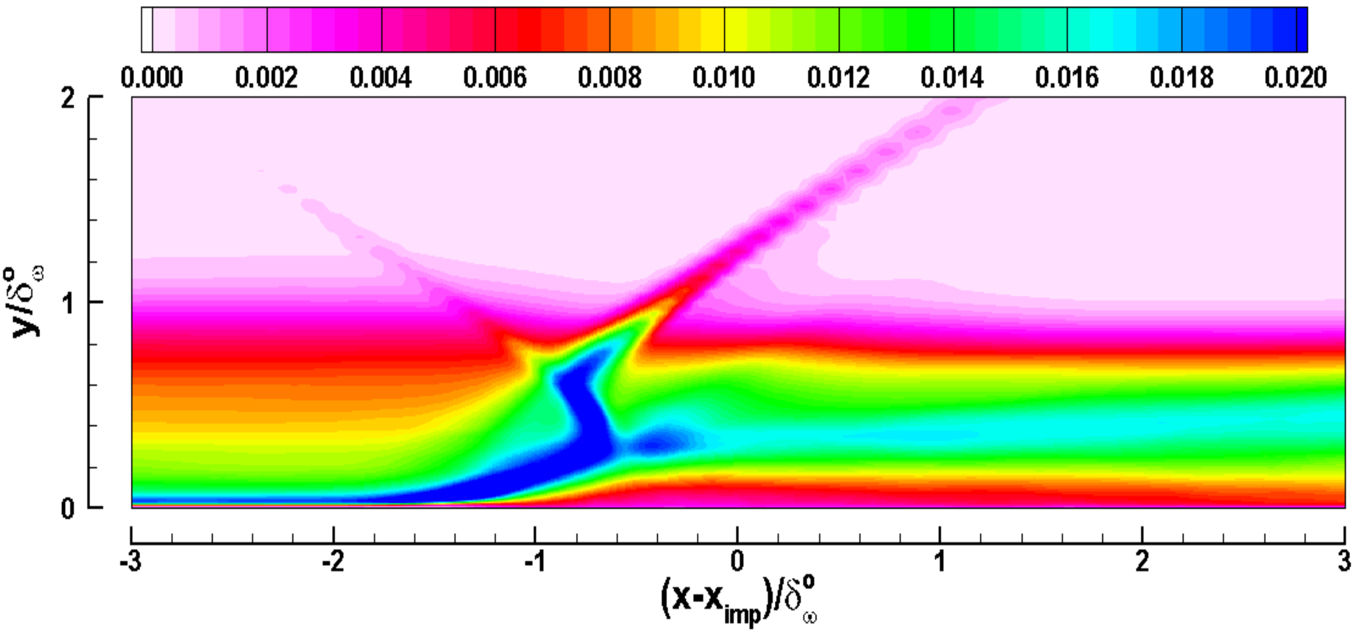

(a) Adiabatic Case

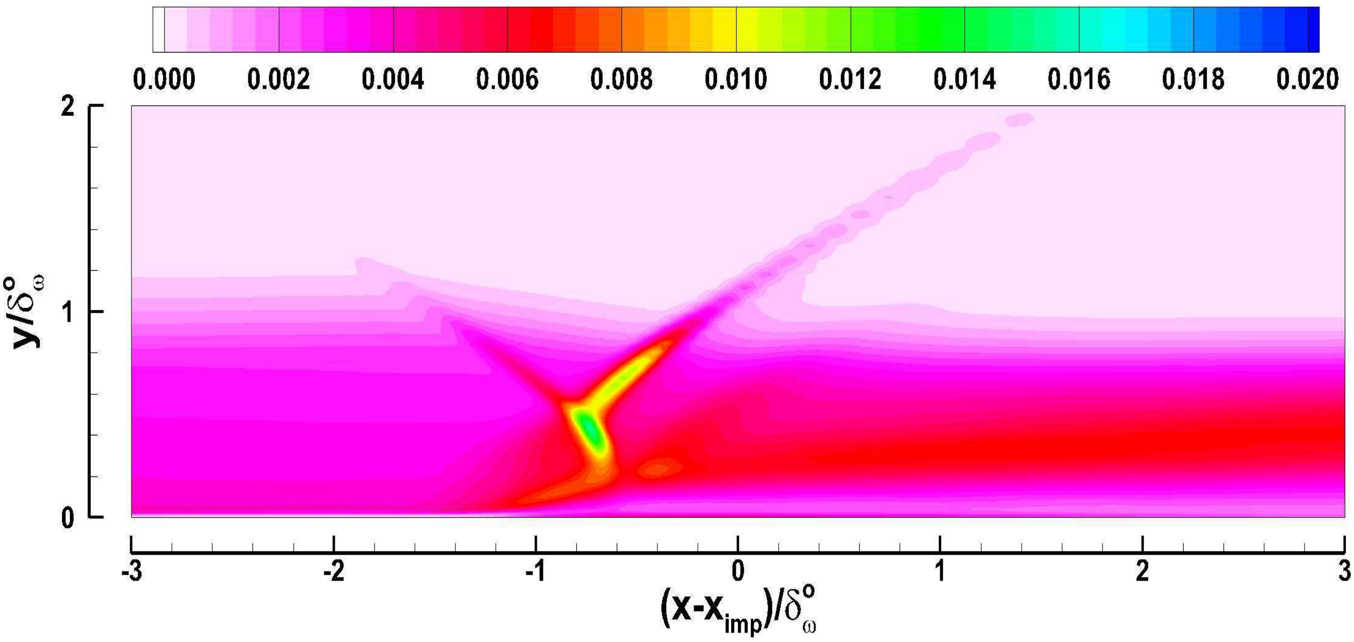

(b) Isothermal Case

Figure VI.19 – Evolution of temperature variance, $\overline{T'T'}/T^2_{\infty,bi}$, along the interaction region:(a) Adiabatic Case; (b) Isothermal Case

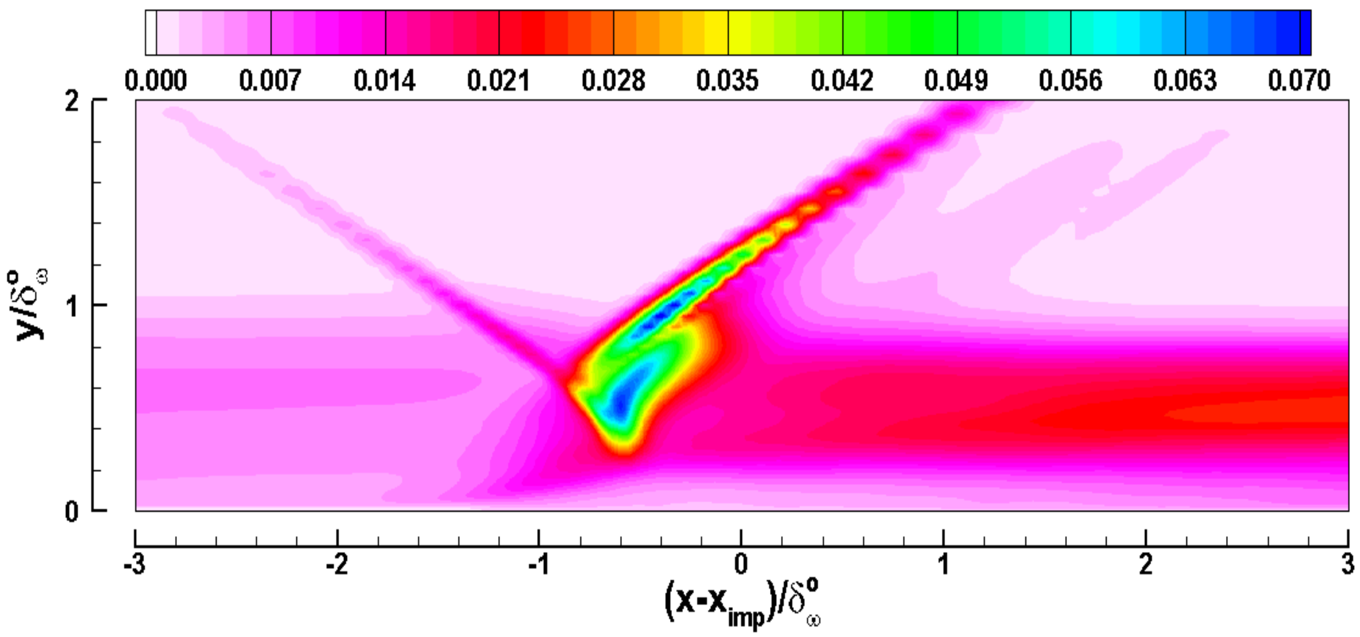

(a) Adiabatic Case

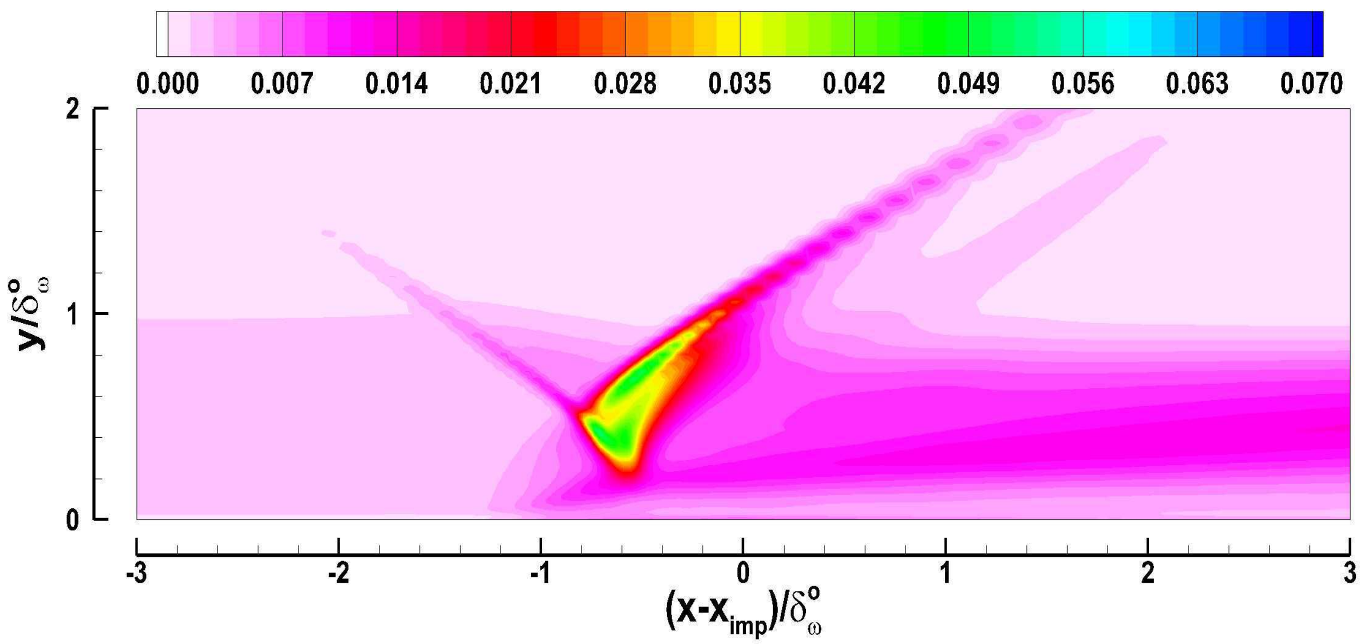

(b) Isothermal Case

Figure VI.20 – Evolution of density variance, $\overline{\rho'\rho'}/\rho^2_{\infty,bi}$, along the interaction region:(a) Adiabatic Case; (b) Isothermal Case

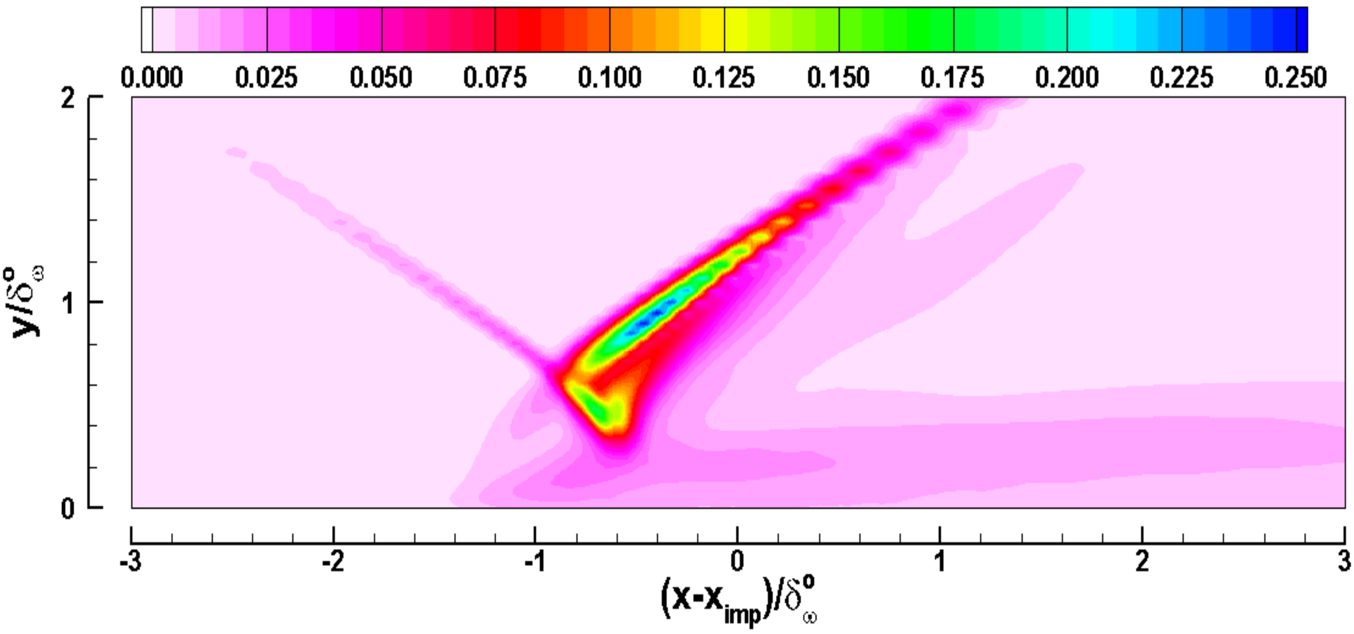

(a) Adiabatic Case

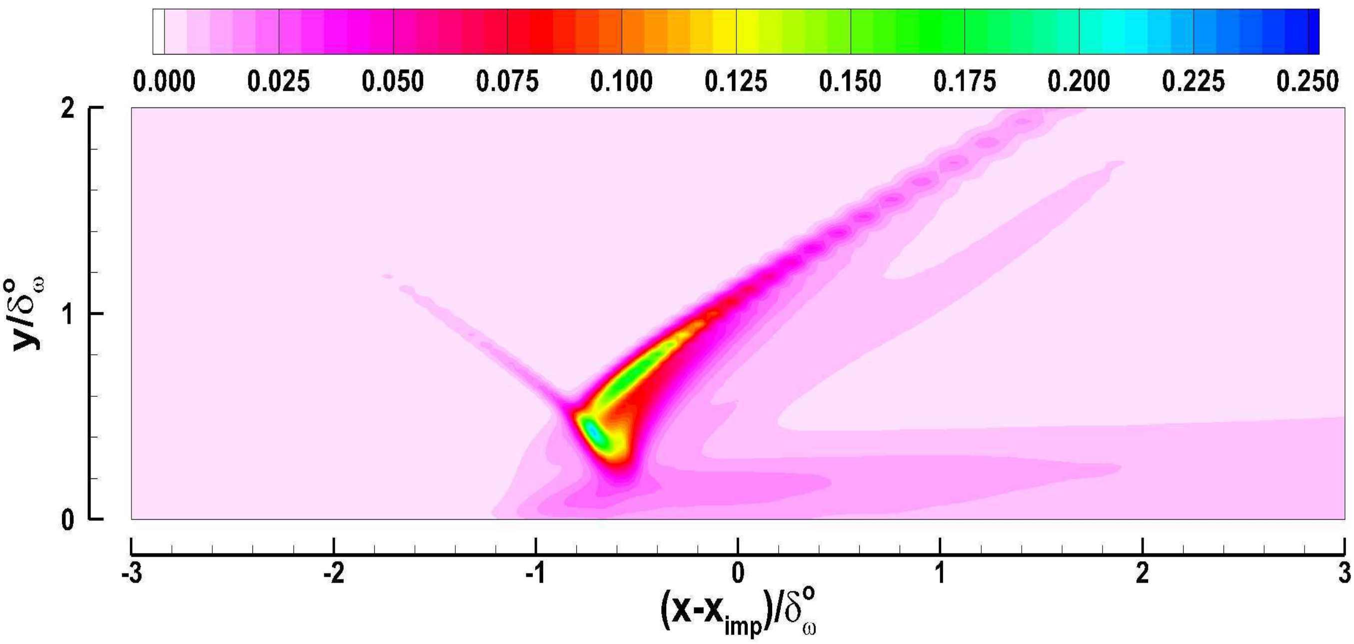

(b) Isothermal Case

Figure VI.21 – Evolution of pressure variance, $\overline{p'p'}/P_{\infty,bi}^2$, along the interaction region:(a) Adiabatic Case; (b) Isothermal Case

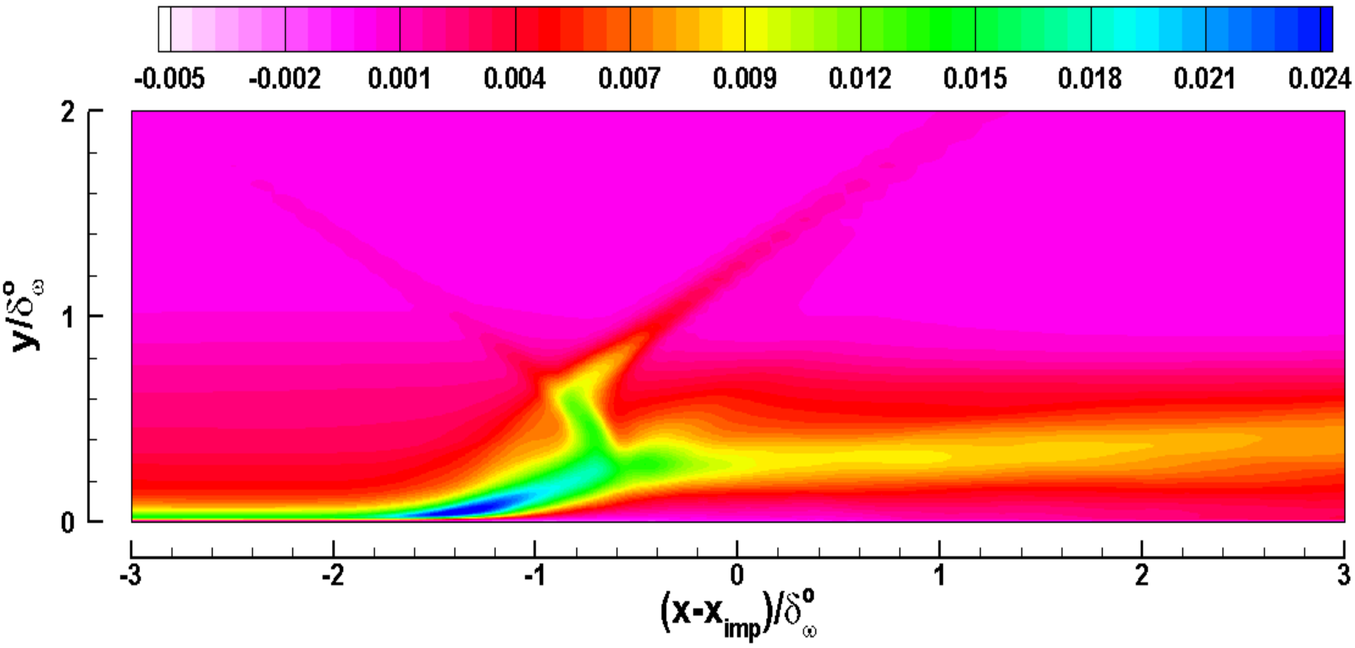

(a) Adiabatic Case

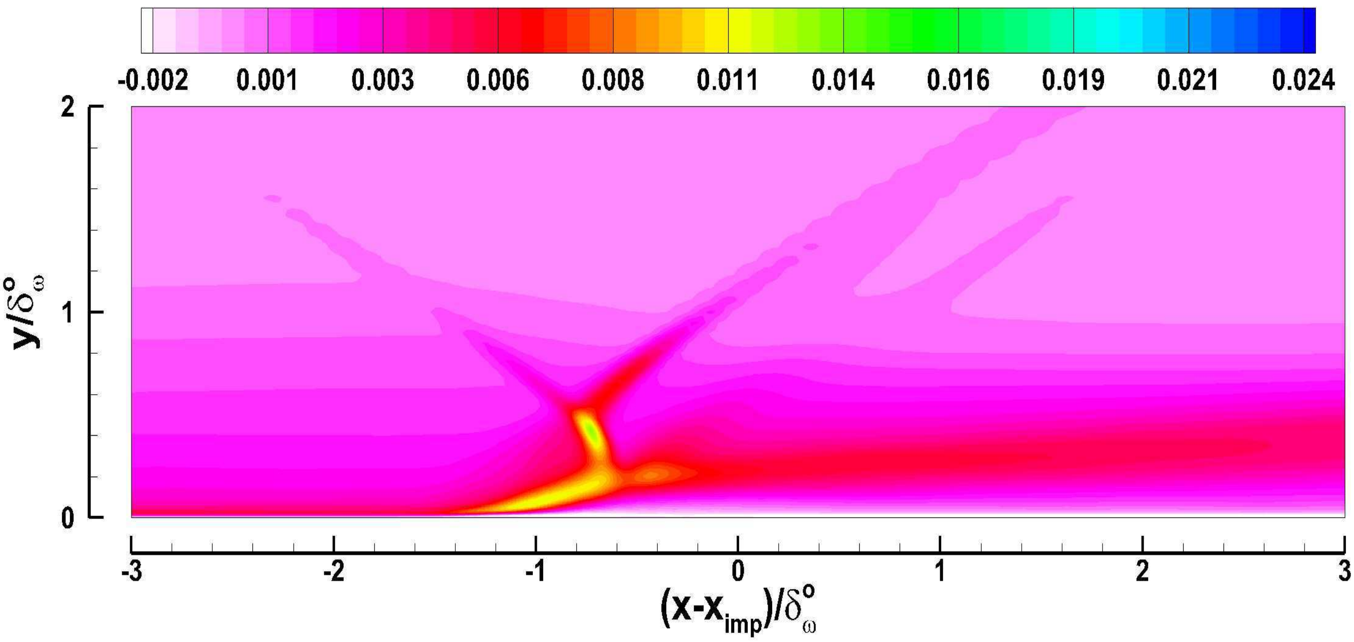

(b) Isothermal Case

Figure VI.22 – Evolution of streamwise component of turbulent heat flux, $\overline{-u_1'T'}/(UT)_{\infty,bi}$, along the interaction region:(a) Adiabatic Case; (b) Isothermal Case

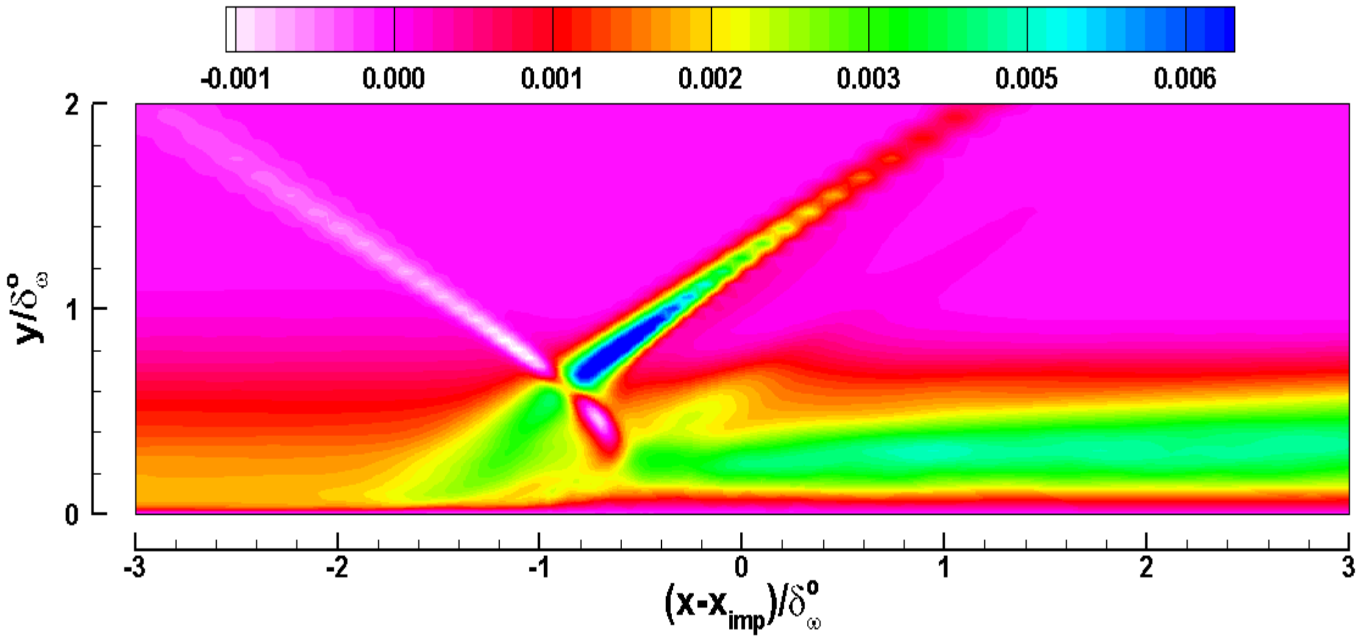

(a) Adiabatic Case

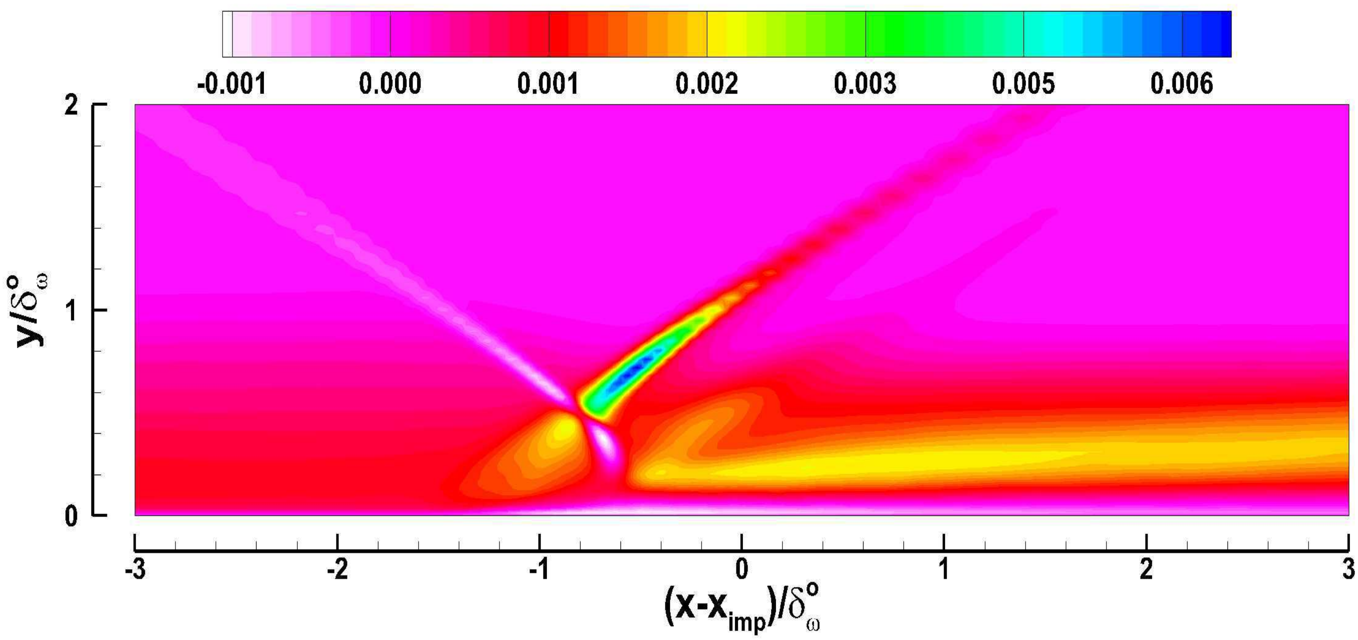

(b) Isothermal Case

Figure VI.23 – Evolution of wall-normal component of turbulent heat flux, $\overline{u_2'T'}/(UT)_{\infty,bi}$, along the interaction region:(a) Adiabatic Case; (b) Isothermal Case

VI.3 Summarizing Comments

In order to further understand the complex dynamics of interaction, an analysis describing the influence on the whole flow-field in the region bounded by the legs of the shock-system and in its immediate vicinity is presented. Again, the effects of two different thermal wall conditions are also taken into account. It has been observed that due to the effect of wall cooling relatively shorter upstream influence and separation lengths are identified when compared to the adiabatic case. An investigation of the compressible and incompressible integral parameters of the boundary layer revealed that the incompressible shape factor increases steeply in the interaction region and attains a maximum value that is in close agreement with the commonly found values for the case of turbulent separations. This significant increase in the incompressible shape factor value is due to the presence of highly decelerated velocity profiles in this region. For the isothermal case, instead of a very steep rise, a slightly more progressive rise in the value of the incompressible shape factor is observed and the maximum value obtained is less than the one observed for the adiabatic case. The distribution of compressible shape factor along the interaction region is different than the incompressible one. After attaining the maximum value, due to the mutual effect of the decrease in velocity and rise in density a large dip in the distribution is observed. In contrast to the incompressible value, the maximum compressible shape factor value for the isothermal case is higher than the adiabatic one. Due to the interaction, the incompressible displacement thickness rapidly increases in the interaction region, while a moderate increase in the values of incompressible momentum thickness is also observed. For the isothermal case, the maximum rise in the values of incompressible displacement thickness is slightly less than the one obtained for the adiabatic case. Also it is noted that the compressible displacement and momentum thickness evolution follows the same trends as that of incompressible ones.

An investigation of the evolution of the mean flow profiles suggest that as a result of the interaction (due to the presence of high gradients of pressure and density) significantly retarded velocity profiles are observed downstream of the onset of the interaction and the corresponding thickness of the subsonic layer also increases. In addition, in this region the flow experience an upward motion which is characterized by the positive values of wall-normal component of the velocity. It has been observed that due to the decrease in local Mach number in the boundary layer the tip of the incident shock is significantly curved within the boundary layer. For the isothermal case, the relatively thinner subsonic layers are observed downstream of the onset of interaction. Moreover, it has been noticed that the effect of wall cooling shifts the position of shocks cross-over point to a relatively lower position in the boundary layer and the impinging shock reflects with a less acute angle in comparison to the adiabatic case. Furthermore, relative to the adiabatic case, a clear difference in the mean static temperature and density fields have been observed for the isothermal case.

In order to identify the effects of the interaction on the state of the developing boundary layer. The evolution of normalized maximum shear stress evolution is traced against the equilibrium shape parameter. In the interaction region, due to the presence of significant perturbation effects, the deviation of the boundary layer from the equilibrium locus is clearly observed. A progressive recovery of the boundary layer to regain the undistorted state similar to the one observed upstream of the interaction is also depicted.

A quantitative description of the turbulent velocity and thermal fields along the interaction region has also been presented. It has been found that the velocity fluctuations level are amplified within the interaction region and their maximum locations shifted away from the wall. In addition, downstream of the shock-system, elevated fluctuation levels are identified in the evolutions of the wall-normal, spanwise and shear stress components. This is considered to be the characteristic signature of the large-scale eddies that are convected downstream of the shock-system. Along the entire interaction length the effect of wall cooling significantly dampens the magnitude levels of all the thermal turbulent quantities relative to the adiabatic wall conditions.

Chapter VII

Conclusions and Perspectives

The results of direct numerical simulations of an impinging shock/turbulent boundary layer interaction at Mach 2.25 and at two different thermal wall boundary conditions, adiabatic and isothermal (cold) wall, have been comparatively analyzed. To the best of our knowledge, the present study probably proposes one of the reference analysis of spatially developing supersonic boundary layer with both cooling and shock interaction effects. The evolution of mean and turbulent, velocity and thermal fields were extensively investigated. In order to establish the foundation for the understanding of this complex phenomenon, the characteristics of the compressible turbulent boundary layer in the absence of shock were examined. The study was extended to the next level of complexity where the influence of the shock-system was incorporated and the results analyzed. In the following, the main findings of the present work are discussed. For each specific field or parameter, any marked effect of the different thermal boundary conditions on the characteristics of the boundary layer is discussed first and then the mutual effects of shock interaction and heat transfer are discussed next.

An analysis of the streamwise evolution of the mean flow profiles showed that as a result of the shock interaction (due to the presence of high pressure and density gradients) significantly retarded velocity profiles occurred downstream of the onset of the interaction and the corresponding thickness of the subsonic layer was increased. In addition, in this region the flow experienced an upward motion that is characterized by positive values of wall-normal velocity. For the isothermal case, relatively thinner subsonic layers were observed downstream of the onset of shock interaction. Moreover, the effect of wall cooling shifts the position of the shocks cross-over point to a relatively lower position in the boundary layer and the impinging shock reflects with a less acute angle in comparison to the adiabatic case.

For the undisturbed boundary layer upstream of the interaction, there was a decrease in the value of the compressible shape factor in the isothermal case relative to the adiabatic case while, in contrast, the skin-friction coefficient increases in the isothermal case relative to the adiabatic case. Due to the effect of adverse pressure gradient, a significant increase in the values of compressible and incompressible shape factors has been observed in the interaction zone. For the incompressible shape factor, the maximum value found for adiabatic case is slightly higher than the isothermal one. In contrast, for the compressible shape factor the maximum value observed for the adiabatic case is much lower than the isothermal one. An analysis of the skin-friction coefficient and wall-pressure distribution in the separation region revealed that, due to the effect of wall cooling, upstream influence and separation lengths are reduced when compared to the adiabatic case.

There are significant effects of the shock interaction and heat transfer on the turbulent field. In an analysis of the upstream undisturbed boundary layer, for different thermal wall conditions, a semi-local type scaling proved to be quite effective in collapsing the profiles of the turbulent stresses. In the interaction region, all the components of the Reynolds stress tensor were anisotropically amplified and their maximum values shifted away from the wall due to the upward motion experienced by the flow. The maximum amplification was found in the wall-normal component while the streamwise component amplified the least. For the isothermal case, the Reynolds stresses were comparatively less amplified. Downstream of the shock-system, the magnitude of streamwise velocity fluctuations rapidly decreased; however, elevated fluctuations levels were identified in the evolution of the wall-normal, spanwise and shear stress components. This was as a characteristic signature of the large-scale eddies which convected downstream of the shock-system. Another important observation is that, in the distributions of the conditionally averaged shear stresses due to the effect of the interaction, the extent on the boundary layer over which the sweep contributions dominate over ejections was increased.

The higher-order moments of the velocity fluctuations were only slightly effected by the different wall conditions used. However, it has been found that due to the interaction, the skewness factor for the streamwise fluctuations changes sign from negative to positive in the inner part of the boundary layer with respect to the trends observed upstream of the interaction, suggesting a higher frequency of positive streamwise velocity fluctuations than negative ones. For the skewness factor of the wall-normal velocity fluctuations an opposite effect is observed. The effect of the interaction is also shown in the distribution of the streamwise flatness factor which increases in the near-wall region.

The major effects of the isothermal wall boundary condition on the developing turbulent boundary streamwise evolution were seen through the analysis of the thermal field. With respect to the adiabatic case, significantly different distributions of the mean and the turbulent thermal fields were observed for the isothermal case. Downstream of the shock-system, similar to the velocity field, the maximums of the turbulent quantities were shifted away from the wall with respect to the wall proximity positions observed upstream of the interaction. Moreover, for the isothermal case the magnitude of all the thermal turbulent quantities were significantly dampened and in the near-wall region, a secondary peak in the distributions of the static temperature variance, total temperature variance and density variances was also observed. Also, a sign reversal was identified for the streamwise and wall-normal turbulent heat flux components.

The turbulent Prandtl number variation across the boundary layer was determined from the diffusivities ratio definition, and from the extended SRA. For the upstream undisturbed boundary layer, qualitatively similar results in the log-layer were obtained using the two approaches. In contrast, for the case of perturbed boundary layer (downstream of the shock-system), a significant deviation between the two was observed in the inner part of the boundary layer and suggested that the HSRA does not hold in the perturbed regions across a large portion of the boundary layer.

A progressive recovery of the boundary layer has been observed when analyzing the results farther downstream of the shock-system. However, within the limits of the computational domain, for both adiabatic and isothermal simulations, the perturbed fields were not able to recover back their undistorted states observed upstream of the interaction. In addition, for the isothermal case, a relatively faster recovery process is put into evidence with reference to its adiabatic counterpart.

From the results obtained in this study, some perspective on future directions can be offered. As it has been observed, the effect of wall cooling moderately reduced the extent of upstream influence and separation length and also significantly dampens the levels of thermal fluctuations. It can be anticipated that the wall cooling at higher temperature ratio can control the dynamics of the flow along the interaction region and the unique details obtained here can be useful for developing active flow control strategies. Since direct numerical simulations can be considered to be a most accurate numerical tool due to their independence of scale modeling terms, important information about the structure of the turbulence can be gained. The DNS database that has been generated here can be used to develop new, and hopefully improved, turbulence/subgrid scale models for the RANS/LES applications of compressible wall-bounded flows. Even though the present study is necessarily limited to fixed freestream Mach number, shock impingement angle and wall temperature ratio conditions, a significant amount of information on the dynamic interactions between the velocity and thermal fields has been learned. In the future, the study can then be extended to investigate the effects on the dynamic interactions by changing various key parameters (such as shock angle, Mach number, wall-temperature ratio).

Chapter VIII

Synthèse de l'étude

Contexte et objectifs

Les interactions entre ondes de choc et couches limites turbulentes se rencontrent dans un grand nombre de configurations aérodynamiques, aussi bien en écoulements confinés (entrées d'air ou tuyères supersoniques, par exemple) qu'en aérodynamique externe (notamment sur les profils d'ailes supercritiques). Ces types d'interactions sont à l'origine de charges thermiques et aérodynamiques instationnaires, qui peuvent fortement dégrader les performances des divers systèmes considérés, voire endommager leurs éléments structurels. Les mécanismes physiques associés à ces phénomènes instationnaires à grande échelle, hors équilibre, restent encore aujourd'hui mal connus et très difficiles à appréhender numériquement.

Ce travail de thèse propose une investigation par simulation numérique directe d'un écoulement de ce type, dans la configuration canonique de couche limite turbulente en développement spatial sur une plaque plane, pour un nombre de Mach à l'infini amont de 2,25, soumise à l'influence d'une onde de choc oblique incidente (d'angle égal à une trentaine de degrés), et/ou d'un refroidissement pariétal (à une température inférieure d'un tiers environ à la température de recouvrement adiabatique). Ce jeu de conditions physiques permet d'examiner en premier lieu une situation critique d'apparition de décollement naissant au niveau de la paroi dans la zone d'interaction et de comparer la dynamique de la turbulence dans une situation similaire de refroidissement rapportée dans la littérature pour le cas du canal turbulent supersonique. L'analyse proposée permet de revisiter et prolonger la grande majorité des conclusions des études numériques et expérimentales antérieures effectuée sur ce cas d'étude.

Introduction

Une introduction générale des problématiques scientifiques adressées est tout d'abord donnée dans le premier chapitre. Celle-ci précise les choix effectués qui ont mené à la mise au point de la stratégie numérique choisie.

Etat de l'art

Une revue générale des contributions publiées dans la littérature ouverte est donnée dans le second chapitre. Les éléments de compréhension du phénomène étudié sont présentés avec une perspective historique en séparant d'une part les éléments apportés par l'évolution des moyens de mesures expérimentales de ceux apportés par le développement relativement récent des moyens de calculs hautes performances.

Stratégie numérique

Le troisième chapitre présente la méthodologie numérique utilisée.

Les équations en formulation compressible conservatives sont tout d'abord détaillées en précisant les quantités de référence choisies pour adimensionner le problème.

Les approximations spatiales et temporelles permettant la discrétisation de ces équations sont ensuite présentées. Un schéma d'intégration de type méthode des lignes (découplage espace-temps) a été préféré aux schémas d'intégration qui couplent le temps et l'espace. Les algorithmes utilisés reposent sur des schémas WENO (Weighted Essentially Non-Oscillating) à l'ordre 7 pour les termes convectifs, des schémas compacts à l'ordre 4 pour les termes visqueux et un algorithme de Runge-Kutta explicite à l'ordre 4 pour l'intégration en temps. Les détails d'écriture sont reportés en annexe.

La définition du domaine de calcul et la construction du maillage sont ensuite détaillées. Les conditions aux limites (Dirichlet en amont, paroi adhérente et frontières ouvertes non-réfléchissantes) et leur implémentation sont ensuite décrites.

Une des richesses de la présente contribution repose sur la simulation du développement spatial complet de la turbulence, en amont de la zone d'étude, à partir d'une solution laminaire, une transition forcée par une loi de soufflage/aspiration en paroi déterminée par une étude de stabilité (modes PSE) effectuée au préalable, jusqu'au développement de la turbulence. Cette approche permet ainsi d'observer un état de turbulence plus réaliste, complètement développé et non simplement entretenu comme dans la plupart des cas d'étude rencontrés dans la littérature.

Influence du refroidissement de la paroi sur le développement de la couche limite supersonique

Le quatrième chapitre se concentre sur l'analyse de l'influence d'un refroidissement de la paroi sur la structure de la turbulence dans la couche limite en mettant en exergue les différences observées par rapport au cas adiabatique. Le cas de référence étudié correspond à un écoulement à un nombre de Mach $M = 2,25$ et une température statique de $T_\infty = 170K$, soit une température de paroi de l'ordre de $323K$ dans le cas adiabatique. La température de paroi dans le cas isotherme est choisie égale à $230K$ de façon à se placer dans des conditions de refroidissement similaires à celles étudiées par Tamano et Morinishi et Morinishi et al en canal turbulent compressible et incompressible respectivement. L'influence du refroidissement est tout d'abord caractérisée de façon globale et les résultats de la simulation comparés à des estimations théoriques classiques. Des comparaisons statistiques plus détaillées sont ensuite effectuées à partir de données collectées dans des plans où une épaisseur de quantité de mouvement similaire est obtenue ($Re_\theta = 3706$ et 3798 respectivement pour les cas adiabatique et isotherme). L'ensemble des résultats sont validés notamment à partir de :

i/ la vérification de la perte de cohérence dans la direction de l'envergure à partir des fonctions de corrélation en deux points indiquant que la distance retenue dans l'envergure est suffisante pour éviter tout biais statistique lié à la présence d'effets tridimensionnels,

ii/ des spectres de puissance présentant une décroissance monotone sur au moins quatre décades, au-delà de la zone de décroissance inertielle en $-5/3$ (sauf pour la composante de vitesse normale à la paroi qui présente de façon attendue un pic d'énergie à la fréquence correspondant à l'espacement moyen entre structures longitudinales),

iii/ une confrontation favorable des résultats à ceux obtenus pour diverses études numériques ou expérimentales dans le cas adiabatique.

Le type de moyenne utilisée (moyenne de Reynolds ou moyenne de Favre avec pondération par la moyenne de la masse volumique) s'avère n'avoir qu'une influence négligeable sur les diverses observations réalisées sur cet écoulement canonique. Dans le cas adiabatique, une différence maximale de l'ordre de 2%, $0,7\%$ et 6% sont par exemple observées entre les deux types d'évaluation pour les champs de vitesse longitudinale, de température statique et de contrainte de cisaillement respectivement. Ces niveaux tombent à $0,8\%$, $0,2\%$ et 5% respectivement dans le cas isotherme. Ces différences apparaissent de façon plus marquée à la jonction entre la sous-couche visqueuse et le début de la zone tampon et sont fortement réduite dans l'ensemble de la zone logarithmique dans le cas isotherme. Une différence plus marquée (de l'ordre de

8%) et plus uniformément répartie à travers la couche limite est mise en évidence entre les estimations de flux de chaleur. Une remise à l'échelle semi-locale (vitesse de frottement standard mais viscosité cinématique locale) est également introduite afin de permettre une représentation plus universelle des lois d'évolution des contraintes turbulentes à travers la couche limite en compensant les effets moyens induit par le refroidissement sur le champ de masse volumique (réalignement des profils de contraintes entre les cas adiabatique et isotherme). Les analogies de Reynolds ont par ailleurs été revisitées. Des différences relativement marquées apparaissent entre les évolutions du nombre de Prandtl turbulent évalué par analogie ou à partir de viscosité et conductivité turbulente estimée par hypothèse de Boussinesq, une valeur moyenne de l'ordre de 0,9 étant observée à la fois pour les cas isotherme et adiabatique.

Les principales différences observées sur le champ cinématique dans le cas isotherme par rapport au cas adiabatique sont :

i/ un profil de vitesse sensiblement plus plein (associé à une diminution typiquement de l'ordre de 20% du facteur de forme, en accord avec les estimations analytiques générales de correction d'effets de compressibilité sur les solutions intégrales de couche limite),

ii/ une augmentation de $8,5\%$ du coefficient de frottement (en relativement bon accord avec une estimation analytique basée sur la relation de Karman-Schoenherr avec correction compressible) suggérant une augmentation sensible de la vitesse de frottement,

iii/ une diminution de la pente de vitesse dans la zone logarithmique associée à une augmentation du paramètre de sillage,

iv/ la perte de monotonie de l'évolution de la température statique associée à une sensible accumulation de chaleur au début de la zone tampon mais une température totale adimensionnée par la température de référence, suivant toujours une évolution logarithmique,

v/ un épaississement de la couche interne caractérisé notamment par un décalage vers la zone extérieure de la position du pic de contraintes normales et de cisaillement (pour lesquelles l'utilisation d'une normalisation par échelle semi-locale permet néanmoins d'avoir une représentation plus universelle),

vi/ un renforcement du niveau de fluctuations longitudinales conduisant notammant à une modification sensible de la distribution des invariants d'anisotropie (éloignement plus marqué de la limite bidimensionnelle axisymétrique le long de la frontière 2D du triangle de Lumley),

vii/ un rétrécissement associé à un accroissement d'activité de la sous-couche visqueuse, caractérisé en autre par un rapprochement vers la paroi des pics de contributions au bilan d'énergie cinétique turbulente, associé à une augmentation significative de leur amplitude (sans toutefois observer de changement qualitatif sur l'équilibre global observé),

viii/ un accroissement d'effets de ballayage (amortissement des fluctuations positive et augmentation des fluctuations négatives dans la direction normale à la paroi) qui revettent un caractère plus intermittent (forte réduction du facteur d'aplatissement) et une structure plus compacte des tourbillons longitudinaux, moins espacés dans la direction de l'envergure (diminution de la distance de corrélation en deux points dans la direction de l'envergure).

Le champ thermique a été par ailleurs caractérisé plus en détails. Dans le cas isotherme, par rapport au cas adiabatique, on observe :

i/ une forte diminution de l'amplitude des fluctuations de température statique (associée à une diminution significative de l'amplitude des flux de chaleur ou de masse longitudinaux et une diminution plus modérée des flux normalement à la paroi) et une distribution plus uniforme à travers la couche limite au lieu d'un déclin progressif à travers la zone logarithmique,

ii/ une légère diminution des niveaux de fluctuations de la température totale dans la zone logarithmique associée à l'apparition d'un pic au niveau de la zone de raccordement,

iii/ un flux de chaleur longitudinal qui contribue désormais négativement au bilan d'énergie totale, localement dans la sous-couche visqueuse,

iv/ une inversion en proche paroi, pour le transport de ce flux de chaleur longitudinal, des rôles dynamiques du terme de dissipation thermique visqueuse, dont la contribution au bilan global devient positive et du terme de transport turbulent dont la contribution devient négative, le comportement des autres contributions restant qualitativement similaire.

Modification de la turbulence pariétale en aval de la zone d'interaction avec un choc

L'analyse de la couche limite turbulente en aval de l'interaction avec un choc est présentée dans le cinquième chapitre. L'accent est porté sur la caractérisation de la relaxation vers l'état d'équilibre caractéristique de l'état amont.

Le résultat principal de cette partie de l'étude concerne la caractérisation de la forte diminution de la longueur d'influence du choc dans le cas de paroi refroidie, associée à une relaxation beaucoup plus rapide vers l'état d'équilibre énergétique.

Les effets des conditions de température en paroi (adiabatique ou isotherme, paroi froide) sont étudiés par comparaison des résultats. L'évolution des champs moyens de vitesse, température et masse volumique, des composantes du tenseur de Reynolds, des flux de chaleur turbulents et des facteurs d'aplatissement et de dissymétrie sont également revus en proposant une analyse des comportements consistante avec les approches proposées dans la littérature.

Cette analyse est complétée par l'étude, d'une part, de l'évolution de l'anisotropie entre les composantes de vitesse, et d'autre part, des composantes du tenseur des contraintes turbulentes. Un conditionnement par la méthode des quadrants est également mis en oeuvre afin de distinguer l'origine des contributions aux tensions de Reynolds. Une modification des mécanismes de transfert d'énergie au sein de la couche limite en aval de l'interaction est ainsi mise en exergue et reliée à la présence d'un accroissement de l'étendue de la zone de cisaillement.

Il est montré par ailleurs que la composante longitudinale des contraintes turbulentes est nettement moins amplifiée que la composante dans la direction normale à la paroi à travers la zone d'interaction. Ces composantes sont relativement moins amplifiées dans le cas isotherme tandis que les niveaux maximum restent localisés plus haut au sein de la couche limite du fait de son épaississement à travers la zone d'interaction. Tandis que les niveaux de contraintes dans la direction longitudinale décroissent relativement rapidement, les contributions restent plus actives dans la direction normale à la paroi. Ce comportement semble marquer la signature caractéristique de tourbillons à grande échelle qui sont convectés en aval du système de chocs. Il est par ailleurs montré que l'interaction conduit à une augmentation significative des contributions relative des mécanismes de ballayage, qui dominent les contributions des mécanismes d'éjection dans leur apport global aux contraintes turbulentes.

La variation du nombre de Prandtl est finalement commentée. Il est montré, comme attendu, que l'analogie de Reynolds n'est plus valable au sein de la couche limite perturbée proche de la paroi.

Etude de la zone d'interaction

Le sixième chapitre s'intéresse à l'analyse des caractéristiques de la couche limite dans la zone d'interaction au voisinage du système de chocs) afin de mieux clarifier la dynamique de l'interaction et de discuter l'influence du refroidissement de paroi.

Les modifications de la distribution des coefficients de frottement et des paramètres intégraux (à la fois compressibles et incompressibles) de couche limite sont discutés, ainsi que leur relation à travers l'équation intégrale de quantité de mouvement. Il est montré que le refroidissement de la paroi conduit à la fois à une augmentation du coefficient de frottement et une diminution du facteur de forme compressible, mais que ces coefficients augmentent significativement à travers la zone d'interaction.

Les champs de vitesse, température et masse volumique moyennes, des tensions de Reynolds, des flux de chaleur turbulents et des variances de pression, température et densité sont par ailleurs présentés afin de préciser la topologie de l'écoulement. Les zones de production de turbulence sont plus précisément identifiées.

L'analyse du portrait de phase d'équilibre est finalement donnée afin de caractériser l'influence du refroissement sur l'écart à la situation d'équilibre énergétique.

Conclusions et perspectives

Le septième chapitre liste les conclusions marquantes de l'étude. Les bases de données originales constituées au cours de la thèse permettent d'envisager le développement de travaux de modélisation par analyse a priori de modèles, à la fois pour les approches moyennées et les approches de simulation des grandes échelles. Au cours de cette étude, il a été montré que le refroidissement de la paroi n'affectait que peu la structure globale du champ cinématique, et que les modifications pouvaient en premier lieu s'interpréter globalement par l'altération du champ moyen. Cependant, une modification majeure du champ thermique et turbulent dans une zone relativement confinée près de la paroi reste également mise en exergue et laisse entrevoir la possibilité de modifier plus largement la dynamique de l'écoulement dans des cas où le flux de chaleur imposé à la paroi serait plus intense. Des études complémentaires dans de telles situations offriraient donc la possibilité d'examiner le possible contrôle actif, par ce biais, de la structure de ces écoulements.

Appendix 1

A.1 Elements of WENO Formulation

In the following, the details for some of the elements described in section III.2.1 (see chapter III) are described.

A.1.1 Roe Averaging Procedure

The Roe averaging procedure for the calculation of intermediate states at the zone boundary ($x_{i+1/2}$) using the variables values at the left (x_i) and right states (x_{i+1}), is given as

$$
\begin{aligned}
u_{i+\frac{1}{2}} &= \frac{ru_{i+1}+u_i}{1+r} \\
v_{i+\frac{1}{2}} &= \frac{rv_{i+1}+v_i}{1+r} \\
w_{i+\frac{1}{2}} &= \frac{rw_{i+1}+w_i}{1+r} \\
H_{i+\frac{1}{2}} &= \frac{rH_{i+1}+H_i}{1+r} \\
c_{i+\frac{1}{2}} &= \sqrt{(\gamma-1)(H_{i+\frac{1}{2}}-\frac{1}{2}(u^2_{i+\frac{1}{2}}+v^2_{i+\frac{1}{2}}+w^2_{i+\frac{1}{2}}))}
\end{aligned}
$$

where,

$$
\begin{aligned}
r &= \sqrt{\frac{\rho_{i+1}}{\rho_i}} \\
H &= \gamma E - \frac{\gamma-1}{2}(u^2+v^2+w^2)
\end{aligned}
$$

A.1.2 Eigenvectors and Eigenvalues

The left ($\boldsymbol{L}_d$) and right ($\boldsymbol{R}_d$) ($1 \leq d \leq 3$) eigenvectors matrices, evaluated on the basis of intermediate states determined by the Roe averaging formulation for all space directions are presented below (here, for the sake of simplicity of notation the subscripts $(i+1/2)$, $(j+1/2)$ and $(k+1/2)$ are intensionally omitted).

A.1.2.1 Left Eigenvectors Matrices

$$[\boldsymbol{L}_x]_{i+\frac{1}{2}} = \begin{bmatrix} \frac{1}{2}\left(\frac{(\gamma-1)M^2}{2}+\frac{u}{c}\right) & -\frac{1}{2}\left(\frac{(\gamma-1)u+c}{c^2}\right) & -\frac{1}{2}\left(\frac{(\gamma-1)v}{c^2}\right) & -\frac{1}{2}\left(\frac{(\gamma-1)w}{c^2}\right) & \frac{1}{2}\left(\frac{\gamma-1}{c^2}\right) \\ \left(1-\frac{(\gamma-1)M^2}{2}\right) & \frac{(\gamma-1)u}{c^2} & \frac{(\gamma-1)v}{c^2} & \frac{(\gamma-1)w}{c^2} & -\frac{\gamma-1}{c^2} \\ \frac{1}{2}\left(\frac{(\gamma-1)M^2}{2}-\frac{u}{c}\right) & -\frac{1}{2}\left(\frac{(\gamma-1)u-c}{c^2}\right) & -\frac{1}{2}\left(\frac{(\gamma-1)v}{c^2}\right) & -\frac{1}{2}\left(\frac{(\gamma-1)w}{c^2}\right) & \frac{1}{2}\left(\frac{\gamma-1}{c^2}\right) \\ -v & 0 & 1 & 0 & 0 \\ -w & 0 & 0 & 1 & 0 \end{bmatrix}_{i+\frac{1}{2}}$$

$$[\boldsymbol{L}_y]_{j+\frac{1}{2}} = \begin{bmatrix} \frac{1}{2}\left(\frac{(\gamma-1)M^2}{2}+\frac{v}{c}\right) & -\frac{1}{2}\left(\frac{(\gamma-1)u}{c^2}\right) & -\frac{1}{2}\left(\frac{(\gamma-1)v+c}{c^2}\right) & -\frac{1}{2}\left(\frac{(\gamma-1)w}{c^2}\right) & \frac{1}{2}\left(\frac{\gamma-1}{c^2}\right) \\ \left(1-\frac{(\gamma-1)M^2}{2}\right) & \frac{(\gamma-1)u}{c^2} & \frac{(\gamma-1)v}{c^2} & \frac{(\gamma-1)w}{c^2} & -\frac{\gamma-1}{c^2} \\ \frac{1}{2}\left(\frac{(\gamma-1)M^2}{2}-\frac{v}{c}\right) & -\frac{1}{2}\left(\frac{(\gamma-1)u}{c^2}\right) & -\frac{1}{2}\left(\frac{(\gamma-1)v-c}{c^2}\right) & -\frac{1}{2}\left(\frac{(\gamma-1)w}{c^2}\right) & \frac{1}{2}\left(\frac{\gamma-1}{c^2}\right) \\ -w & 0 & 0 & 1 & 0 \\ -u & -1 & 0 & 0 & 0 \end{bmatrix}_{j+\frac{1}{2}}$$

$$[\boldsymbol{L}_z]_{k+\frac{1}{2}} = \begin{bmatrix} \frac{1}{2}\left(\frac{(\gamma-1)M^2}{2}+\frac{w}{c}\right) & -\frac{1}{2}\left(\frac{(\gamma-1)u}{c^2}\right) & -\frac{1}{2}\left(\frac{(\gamma-1)v}{c^2}\right) & -\frac{1}{2}\left(\frac{(\gamma-1)w+c}{c^2}\right) & \frac{1}{2}\left(\frac{\gamma-1}{c^2}\right) \\ \left(1-\frac{(\gamma-1)M^2}{2}\right) & \frac{(\gamma-1)u}{c^2} & \frac{(\gamma-1)v}{c^2} & \frac{(\gamma-1)w}{c^2} & -\frac{\gamma-1}{c^2} \\ \frac{1}{2}\left(\frac{(\gamma-1)M^2}{2}-\frac{w}{c}\right) & -\frac{1}{2}\left(\frac{(\gamma-1)u}{c^2}\right) & -\frac{1}{2}\left(\frac{(\gamma-1)v}{c^2}\right) & -\frac{1}{2}\left(\frac{(\gamma-1)w-c}{c^2}\right) & \frac{1}{2}\left(\frac{\gamma-1}{c^2}\right) \\ -u & 1 & 0 & 0 & 0 \\ -v & 0 & 1 & 0 & 0 \end{bmatrix}_{k+\frac{1}{2}}$$

A.1.2.2 Right Eigenvectors Matrices

$$[\boldsymbol{R}_x]_{i+\frac{1}{2}} = \begin{bmatrix} 1 & 1 & 1 & 0 & 0 \\ u & u-c & u+c & 0 & 0 \\ v & v & v & 1 & 0 \\ w & w & w & 0 & 1 \\ H-uc & \frac{|\vec{U}|^2}{2} & H+uc & v & w \end{bmatrix}_{i+\frac{1}{2}}$$

$$[\boldsymbol{R}_y]_{j+\frac{1}{2}} = \begin{bmatrix} 1 & 1 & 1 & 0 & 0 \\ u & u & u & 0 & -1 \\ v-c & v & v+c & 0 & 0 \\ w & w & w & 1 & 0 \\ H-vc & \frac{|\vec{U}|^2}{2} & H+vc & w & -u \end{bmatrix}_{j+\frac{1}{2}}$$

$$[\boldsymbol{R}_z]_{k+\frac{1}{2}} = \begin{bmatrix} 1 & 1 & 1 & 0 & 0 \\ u & u & u & 1 & 0 \\ v & v & v & 0 & 1 \\ w & w & w+c & 0 & 0 \\ H-wc & \frac{|\vec{U}|^2}{2} & H+wc & u & v \end{bmatrix}_{k+\frac{1}{2}}$$

A.1.2.3 Eigenvalues Matrices

The real eigenvalues matrices, $\boldsymbol{\Lambda}_d$ $(1 \leq d \leq 3)$, corresponding to the Jacobian of system of Euler equations in all space directions are given as

$$[\boldsymbol{\Lambda}_x]_i = \begin{vmatrix} |\text{u-c}| & & & & \\ & |\text{u}| & & & \\ & & |\text{u+c}| & & \\ & & & |\text{u}| & \\ & & & & |\text{u}| \end{vmatrix} \quad [\boldsymbol{\Lambda}_y]_j = \begin{vmatrix} |\text{v-c}| & & & & \\ & |\text{v}| & & & \\ & & |\text{v+c}| & & \\ & & & |\text{v}| & \\ & & & & |\text{v}| \end{vmatrix} \quad [\boldsymbol{\Lambda}_z]_k = \begin{vmatrix} |\text{w-c}| & & & & \\ & |\text{w}| & & & \\ & & |\text{w+c}| & & \\ & & & |\text{w}| & \\ & & & & |\text{w}| \end{vmatrix}$$

A.1.3 Weights and Smoothness Estimators

The following listed the constants $a^r_{k;j}$ (table A.1), the optimal weights C^r_k (table A.2) and the formulations for the estimation of smoothness estimators IS^r_k (table A.3) defined in section III.2.1 (see chapter III) for order of accuracy between $r=2$ and $r=4$. It is to be noted that the function f used in the formulation of smoothness estimators IS^r_k is defined in section III.2.1 as $\mathbf{f}^+_{s;i+1/2}$ and $\mathbf{f}^+_{s;i+\frac{1}{2}}$ and here for the sake of simplicity of notation the subscripts ($+$ and $-$) and the superscripts $(s;i+1/2)$ are intentionally omitted.

Table A.1 – Constants $a^r_{k;j}$

r	$a^r_{k;j}$	j=1	j=2	j=3	j=4
2	$k=0$	-1/2	3/2		
	$k=1$	1/2	1/2		
3	$k=0$	1/3	-7/6	11/6	
	$k=1$	-1/6	5/6	1/3	
	$k=2$	1/3	5/6	-1/6	
4	$k=0$	-1/4	13/12	-23/12	25/12
	$k=1$	1/12	-5/12	13/12	1/4
	$k=2$	-1/12	7/12	7/12	-1/12
	$k=3$	1/4	13/12	-5/12	1/12

Table A.2 – Optimal weights C^r_k

C^r_k	k=0	k=1	k=2	k=3
r=2	1/3	2/3		
r=3	1/10	3/5	3/10	
r=4	1/35	12/35	18/35	4/35

Table A.3 – Smoothness estimator IS^r_k

r	k	IS^r_k
2	0	$(f_i - f_{i-1})^2$
	1	$(f_{j+1} - f_j)^2$
3	0	$\frac{13}{12}(f_{j-2} - 2f_{j-1} + f_j)^2 + \frac{1}{4}(f_{j-2} - 4f_{j-1} + 3f_j)^2$
	1	$\frac{13}{12}(f_{j-1} - 2f_j + f_{j+1})^2 + \frac{1}{4}(f_{j-1} - f_{j+1})^2$
	2	$\frac{13}{12}(f_j - 2f_{j+1} + f_{j+2})^2 + \frac{1}{4}(3f_j - 4f_{j+1} + f_{j+2})^2$
4	0	$f_{j-3}(547f_{j-3} - 3882f_{j-2} + 4642f_{j-1} - 1854f_j) + f_{j-2}(7043f_{j-2} - 17246f_{j-1} + 7042f_j) + f_{j-1}(11003f_{j-1} - 9402f_j) + 2107f_j^2$
	1	$f_{j-2}(267f_{j-2} - 1642f_{j-1} + 1602f_j - 494f_{j+1}) + f_{j-1}(2843f_{j-1} - 5966f_j + 1922f_{j+1}) + f_j(3443f_j - 2522f_{j+1}) + 547f_{j+1}^2$
	2	$f_{j-1}(547f_{j-1} - 2522f_j + 1922f_{j+1} - 494f_{j+2}) + f_j(3443f_j - 5966f_{j+1} + 1602f_{j+2}) + f_{j+1}(2843f_j - 1642f_{j+2}) + 267f_{j+2}^2$
	3	$f_j(2107f_j - 9402f_{j+1} + 7042f_{j+2} - 1854f_{j+3}) + f_{j+1}(11003f_{j+1} - 17246f_{j+2} + 4642f_{j+3}) + f_{j+2}(7043f_{j+2} - 3882f_{j+3}) + 547f_{j+3}^2$

References

[1] J. D. Anderson Jr. *History of Aerodynamics: And its impacts on flying machines.* Cambridge University Press, USA (1999). xix, 6

[2] D. Arnal and J. Délery. Laminar-turbulent transition and shock-wave / boundary layer interaction. Technical report, Rhodes Saint-Genese, Belgium (May, 2004). xix, 8, 10

[3] J. Délery and J. P. Dussauge. *Some physical aspects of shock wave/boundary layer interactions.* Shock Waves **19**, 453–468 (2009). xix, 7, 11

[4] D. R. Chapman, D. M. Kuehn, and H. K. Larson. Investigation of separated flows in supersonic and subsonic streams with emphasis on the effect of transition. Technical Note 3869 NACA (1957). xix, 5, 12, 14, 15, 31

[5] J. S. Shang, W. L. Hankey Jr., and C. H. Law. *Numerical simulation of shock wave-turbulent boundary-layer interaction.* AIAA J. **14**(10), 1451–1457 (1976). xix, 15

[6] G. S. Settles, T. J. Fitzpatrick, and S. M. Bogdonoff. *Detailed study of attached and separated compression corner flowfields in high Reynolds number supersonic flow.* AIAA J. **17**(6), 579–585 (1979). xix, 14, 16, 17, 26, 31

[7] D. S. Dolling and M. T. Murphy. *Unsteadiness of the separation shock wave structure in a supersonic compression ramp flowfield.* AIAA J. **21**(12), 1628–1634 (1983). xix, 14, 16, 17, 25, 26, 27, 31

[8] A. J. Smits and K. Muck. *Experimnetal study of three shock wave/turbulent boundary layer interactions.* J. Fluid Mech. **182**, 291–314 (1987). xx, 8, 14, 16, 17, 18, 26, 31, 85, 87, 90, 146

[9] M. S. Selig, J. Andrepoulos, K.C Muck, J.P. Dussauge, and A. J. Smits. *Turbulence structure in a shock-wave/turbulent boundary-layer interaction.* AIAA J. **27**, 862–869 (1989). xx, 8, 14, 19, 26, 88

[10] J. Deleuze. *Structure d'une couche limite turbulente soumise à une onde de choc incidente*. Thèse de Doctorat, Université de la Mediterranee Aix - Marseille (1995). xx, 9, 14, 19, 20, 21, 25, 26, 30, 31, 51, 52, 53, 54, 84, 85, 86, 87, 88, 89, 92, 93, 94, 95, 97, 101, 108, 110, 146

[11] S. J. Beresh, N. T. Clemens, and D. S. Dolling. *Relationship between upstream turbulent boundary-layer velocity fluctuations and separation shock unsteadiness*. AIAA J. **40**(12), 2412–2422 (2002). xx, 8, 14, 20, 22, 31

[12] P. Dupont, C. Haddad, and J. F. Debiève. *Space and time organization in a shock-induced separated boundary layer*. J. Fluid Mech. **559**, 255–277 (2006). xx, 21, 23, 30

[13] S. Pirozzoli and F. Grasso. *Direct numerical simulation of impinging shock wave/turbulent boundary layer interaction at $M = 2.25$*. Phys. Fluids **18**, DOI: 10.1063/1.2216989 (2006). xx, 27, 28, 85, 92, 111, 114, 121, 133

[14] M. Wu and M. P. Martin. *Direct numerical simulation of supersonic turbulent boundary layer flow over a compression ramp*. AIAA J. **45**, 879–889 (2007). xx, 8, 25, 27, 29, 87

[15] S. Priebe, M. Wu, and M. P. Martin. *Direct numerical simulation of a reflected shock wave / turbulent boundary layer interaction*. AIAA J. **47**, 1173–1185 (2009). xx, 9, 14, 25, 29, 30, 31, 48, 85, 87, 121, 122

[16] R. A. Humble. *Unsteady flow organization of a shock wave / boundary layer interaction*. Thèse de Doctorat, Delft University of Technology (2008). 5, 9, 14, 22, 31, 52, 85, 92, 93, 94, 133, 144, 145, 146

[17] A. Ferri. Experimental results with airfoils tested in the high speed tunnel at guidonia. Report No. TM–946 NACA (1940). 5

[18] T. C. Adamson Jr. and A. F. Messiter. *Analysis of two-dimensional interactions between shock waves and boundary layers*. Ann. Rev. Fluid Mech. **12**, 103–138 (1980). 5, 7

[19] D. S. Dolling. *Fifty years of shock-wave/boundary-layer interaction research: What next ?* AIAA J. **39**(8), 1517–1531 (2001). 5, 7

[20] C. DuP. Donaldson. Effects of interaction between normal shock and boundary layer. Report No. CB–4A27 NACA (1944). 5

[21] H. W. Liepmann. *The interaction between boundary layer and shock waves in transonic flow*. Journal of Aerospace Sciences **13**(12), 623–638 (1946). 5

[22] A. Fage and R. F. Sargent. Shock wave and boundary layer phenomena near a flat surface. In *Proceedings of the Royal Society of London*, Series A: Mathematical and Physical Sciences, 190, pages 1–20 (1947). 5

[23] J. Ackeret, F. Feldmann, and N. Rott. Investigations of compression shocks and boundary layer in gases moving at high speed. Report No. TM–1113 NACA (1947). 5

[24] J. H. Allen, M. A. Heaslet, and G. E. Nitzberg. The interaction of boundary layer and compression shock and its effect upon airfoil pressure distributions. Report No. RM–A7A02 NACA (1947). 5

[25] O. Bardsley and W. A. Mair. *The interaction between an oblique shock wave and a turbulent boundary layer*. Philosophical Magazine **42**(324), 29–36 (1951). 5

[26] F. W. Barry, A. H. Shapiro, and E. P. Neumann. *The interaction of shock waves with boundary layers on a flat surface*. Journal of Aerospace Sciences **18**(4), 229–238 (1951). 5

[27] W. H. Liepmann, A. Roshko, and S. Dhawan. On reflection of shock waves from boundary layers. Report No. TN–1100 NACA (1952). 5

[28] G. E. Gadd and D. W. Holder. The interaction between an oblique shock wave and a turbulent boundary layer on a flat plate. Part I–results for M=2. Report No. 14–848 British Aeronautical Research Council (1952). 5

[29] N. H. Johannesen. Experiments on two-dimensional supersonic flow in corners and over concave surfaces. Report No. 14–607 British Aeronautical Research Council (1952). 5

[30] C. DuP. Donaldson and R. H. Lange. Study of the pressure rise across shock-waves required to separate laminar and turbulent boundary layers. Report No. TN–2770 NACA (1952). 5

[31] G. E. Gadd, D. W. Holder, and J. D. Regan. The interaction between an oblique shock wave and a turbulent boundary layer on a flat plate. Part II–interim note on the results for M=1.5,2,3 and 4. Report No. 15–591 British Aeronautical Research Council (1953). 5

[32] D. W. Holder, H. H. Pearcey, and G. E. Gadd. The interaction between shock waves and boundary layers. Current Paper 180 British Aeronautical Research Council (1955). 5

[33] H. H. Pearcey. Shock-induced separation and its prevention by design and boundary layer control. In G. V. Lachmann, editor, *Boundary layer and flow control*, pages 1166–1344, New York (1961). Pergamon. 6

[34] K. Stewartson and P. G. Williams. Self-induced separation. In *Proceedings of the Royal Society of London*, Series A, 312, pages 181–206 (1969). 6

[35] V. Ya Neiland. *Theory of laminar boundary layer separation in supersonic flow*. Fluid Dyn. **4**(4), 33–35 (1969). 6

[36] A. L. Kistler. *Fluctuating wall pressure under a separated supersonic flow.* Journal of Acoustic Society of America **36**(3), 543–550 (1964). 6

[37] J. E. Green. *Interactions between shock waves and turbulent boundary layers.* Prog. in Aerosp. Sci. **11**, 235–341 (1970). 7, 9, 15

[38] R. Korkegi. *Survey of viscous interactions associated with high Mach number flight.* AIAA J. **9**(5), 771–784 (1971). 7

[39] E. Stanewsky. Shock-boundary layer interaction in transonic and supersonic flows. In *Transonic flows in turbomachinery*, Lecture Series 59, Rhodes Saint-Genese, Belgium (1973). Von Karman Institute. 7, 15

[40] W. L. Hankey Jr. and M. S. Holden. Two-dimensional shock-wave boundary layer interactions in high speed flows. AGARDograph No. 203 (1975). 7

[41] J. Delery and J. G. Marvin. Shock-wave boundary layer interactions. AGARDograph No. 280 NATO (1986). 7, 9, 15, 128, 130, 131, 142, 143

[42] G. S. Settles and D. S. Dolling. Swept shock-wave/boundary-layer interactions. In *Progress in Astronautics and Aeronautics*, Tactical Missile Aerodynamics: General Topics, 141, pages 505–574, Washington (1992). AIAA. 7

[43] D. Knight, H. Yan, A. G. Panaras, and A. Zheltovodov. *Advances in CFD prediction of shock wave turbulent boundary layer interaction.* Prog. in Aerosp. Sci. **39**, 121–184 (2003). 7, 24

[44] A. J. Smits and J.-P. Dussauge. *Turbulent Shear Layers in Supersonic Flow.* Springer, New York, second edition (2006). 7, 9, 15, 51, 93, 112, 114

[45] J. R. Edwards. *Numerical simulations of shock/boundary layer interactions using time-dependent modeling techniques: A survey of recent results.* Prog. in Aerosp. Sci. **44**, 447–465 (2008). 7, 24, 25

[46] T. B. Gatski and J.-P. Bonnet. *Compressibility, Turbulence and High Speed Flow.* Elsevier, Oxford (2009). 7, 56, 70

[47] Pascal L. Ardonceau. *The structure of turbulence in a supersonic shock-wave/boundary-layer interaction.* AIAA J. **22**(9), 1254–1262 (1984). 8, 14, 16, 31, 146

[48] J. Andreopoulos and K. C. Muck. *Some new aspects of the shock-wave/boundary layer interaction in compression-ramp flows.* J. Fluid Mech. **180**, 405–428 (1987). 8, 14, 18, 31

[49] D. W. Kuntz, V. A. Amatucci, and A. L. Addy. *Turbulent boundary-layer downstream of the shock-wave/boundary-layer interaction.* AIAA J. **25**(5), 668–675 (1987). 8, 14, 18, 31, 93, 146

[50] M. E. Erengil and D. S. Dolling. *Correlation of separation shock motion with pressure fluctuations in the incoming boundary layer.* AIAA J. **29**(11), 1868–1877 (1991). 8, 14, 19, 31

[51] N. A. Adams. *Direct simulation of the turbulent boundary layer along a compression ramp at $M = 3$ and $Re_\theta = 1685$.* J. Fluid Mech. **420**, 47–83 (2000). 8, 14, 25, 26, 31, 87, 97, 111, 115, 121

[52] A. J. P. Fletcher, A. I. Ruban, and J. D. A. Walker. *Instabilities in supersonic compression ramp flow.* J. Fluid Mech. **517**, 309–330 (2004). 8

[53] B. Ganapathisubramani, N. T. Clemens, and D. S. Dolling. *Effects of upstream boundary layer on the unsteadiness of shock-induced separation.* J. Fluid Mech. **585**, 369–394 (2007). 8, 14, 22, 31

[54] P. Bookey, C. Wyckham, A. J. Smits, and M. P. Martin. New experimental data of STBLI at DNS/LES accessible reynolds numbers. Paper No. 2005-0309 AIAA (2005). 8, 9, 14, 20, 26, 27, 31

[55] M. Wu and M. P. Martin. *Analysis of shock motion in shockwave and turbulent boundary layer interaction using direct numerical simulation data.* J. Fluid Mech. **594**, 71–83 (2008). 8, 14, 27, 31

[56] L. H. Back and R. F. Cuffel. *Shock wave/turbulent boundary-layer interactions with and without surface cooling.* AIAA J. **14**(4), 526–532 (1976). 9, 14, 16, 31, 128, 134

[57] H. Laurent. *Turbulence d'une interaction onde de choc/couche limite sur une paroi plane adiabatique ou chauffée.* Thèse de Doctorat, Université de la Méditerranée Aix - Marseille (1996). 9, 14, 19, 20, 25, 26, 30, 31, 85, 88, 111, 115, 121

[58] E. Garnier, P. Sagaut, and M. Deville. *Large eddy simulation of shock/boundary-layer interaction.* AIAA J. **40**(10), 1935–1944 (2002). 9, 25, 82

[59] S. Poponniau, J. P. Dussauge, J. F. Debiève, and P. Dupont. *A simple model for low-frequency unsteadiness in shock-induced separation.* J. Fluid Mech. **629**, 87–108 (2009). 9, 23

[60] E. Touber and N. D. Sandham. *Large-eddy simulation of low-frequency unsteadiness in a turbulent shock-induced separation bubble.* Theor. Comput. Fluid Dyn. **23**, 79–107 (2009). 9, 14, 29, 31

[61] C. H. Law. *Supersonic turbulent boundary-layer separation.* AIAA J. **12**(6), 794–797 (1974). 14, 15, 31

[62] C. Haddad. *Instationnarités mouvements d'onde de choc et tourbillons a grandes échelles dans une interaction onde de choc / couche limite avec décollement.* Thèse de Doctorat, Université de Provence Aix - Marseille I (2005). 14, 21, 31

[63] S. Poponniau. *Instationnarités dans les décollements compressible cas des couches limites soumises à ondes de choc.* Thèse de Doctorat, Université de Provence Aix - Marseille I (2009). 14, 23, 31, 145, 146

[64] L. J. Souverein. *On the scaling and unsteadiness of shock induced separation.* Thèse de Doctorat, Université de Provence Aix - Marseille I (2010). 14, 24, 31

[65] D. Hunt and D. Nixon. A very large eddy simulation of an unsteady shock wave/turbulent boundary layer interaction. Paper No. 95–2122 AIAA (1995). 14, 25

[66] E. Garnier. *Simulation des grandes échelles en régime transsonique.* Thèse de Doctorat, Université PARIS XI ORSAY (2000). 14, 25, 85, 88, 111, 115, 145, 153

[67] S. Stolz, N. A. Adams, and L. Kleiser. *The approximate deconvolution model for large-eddy simulations for compressible flows and its application to shock-turbulent-boundary-layer interaction.* AIAA J. **13**(10), 2985–3000 (2001). 14, 25, 26

[68] D. P. Rizzetta and M. R. Visbal. *Application of large-eddy simulation to supersonic compression ramps.* AIAA J. **40**(8), 1574–1581 (2002). 14, 25, 26, 31

[69] S. Dubos. *Simulation des grandes échelles d'écoulements turbulents supersoniques.* Thèse de Doctorat, L'Institut National des Sciences Appliquées de Rouen (2005). 14, 26, 31

[70] P. Bookey, M. P. Martin, and A. J. Smits. Analysis of shockwave/turbulent boundary layer interaction using DNS and experimental data. Paper No. 2005-2145 AIAA (2005). 14, 26, 31

[71] S. Pirozzoli, F. Grasso, and T. B. Gatski. DNS analysis of shock wave/turbulent boundary layer interaction at $M = 2.25$. In *Proceedings of the Fourth International Symposium on Turbulent Shear Flow Phenomena*, pages 1207–1211 (2005). 14, 27, 45

[72] M. Loginov. *Large-eddy simulation of shock wave/turbulent boundary layer interaction.* Thèse de Doctorat, Technishe Universität München Lehrstuhl für Aerodynamik (2006). 14, 27

[73] A. Hadjadj, J. Larsson, B. E. Morgan, J. W. Nichols, and S. K. Lele. Large-eddy simulation of shock/boundary-layer interaction. In *Proceedings of the Summer Program*, pages 141–152. Centre for Turbulence Research (2010). 14, 30

[74] B. Morgan, S. Kawai, and S. K. Lele. Study of Mach lines and acoustic waves in a jet using Rayleigh scattering. Paper No. 2010–4467 AIAA (2010). 14, 30, 85

[75] A. F. Charwat. *Supersonic flows with imbedded separated regions.* Adv. Heat Transfer **6**, 1–132 (1970). 15

[76] R. A. HUMBLE, G. E. ELSINGA, F. SCARANO, and B. W. VAN OUDHEUSDEN. *Three-dimensional instantaneous structure of a shock wave/turbulent boundary layer interaction.* J. Fluid Mech. **622**, 33–62 (2009). 22

[77] D. Knight and G. Degrez. Shock wave boundary layer interactions in high Mach number flows– a critical survey of current CFD prediction capabilities. Vol No. 2 AGARD AR-319 (1998). 24

[78] E. Lenormand, P. Sagaut, L. TaPhuoc, and P. Comte. *Subgrid-scale models for large-eddy simulation of compressible wall bounded flows*. AIAA J. **38**(8), 1340–1350 (2000). 25

[79] G. Urbin and D. Knight. Compressible large eddy simulation using unstructured grid: Unstructured boundary layer. In *Second AFOSR Conference on DNS/LES*, pages 443–458, Norwell, MA (1999). Kluwer Academic. 25

[80] M. Loginov, N. A. Adams, and A. A. Zheltovodov. *Large-eddy simulation of shock-wave/turbulent-boundary-layer interaction*. J. Fluid Mech. **565**, 135–169 (2006). 27

[81] A. A. Zheltovodov, V. M. Trofimov, E. Schülein, and V. N. Yakovlev. An experimental documentation supersonic turbulent flows in the vicinity of forward- and backward-facing ramps. Tech Rep No. 2030 Institute of Theoretical and Applied Mechanics, USSR Academy of Sciences, Novosibirsk (1990). 27

[82] J. CH. Robinet. *Bifurcations in shock-wave/laminar-boundary-layer interactions: Global instability approach*. J. Fluid Mech. **579**, 85–112 (2007). 30

[83] E. Touber and N. D. Sandham. *Low-order stochastic modelling of low-frequency motions in reflected shock-wave/boundary-layer interactions*. J. Fluid Mech. **671**, 417–465 (2011). 30

[84] P. Dupont, J. F. Debiève, J. P. Dussauge, J. P. Ardissonne, and C. Haddad. Unsteadiness in shock wave/boundary layer interaction. Technical Report 2003 ATAC working group, ONERA (2003). 30

[85] R. A. Humble, F. Scarano, and B. W. van Oudheusden. *Particle image velocimetry measurements of a shock wave/turbulent boundary layer interaction*. Exp. Fluids **43**, 173–183 (2007). 31

[86] C. W. Shu. Essentially non-oscillatory and weighted essentially non-oscillatory schemes for hyperbolic conservation laws. ICASE Report No. 97-95 NASA (1997). 34

[87] A. Harten, B. Engquist, S. Osher, and S. R. Chakravarthy. *Uniformly high order accurate essentially non-oscillatory schemes, III*. J. Comput. Phys. **71**, 231–303 (1987). 34

[88] X. D. Liu, S. Osher, and T. Chan. *Weighted essentially non-oscillatory schemes*. J. Comput. Phys. **115**, 200–212 (1994). 34

[89] S. K. Lele. *Compact finite difference schemes with spectral-like resolution.* J. Comput. Phys. **103**, 16–42 (1992). 39

[90] F. M. White. *Viscous Fluid Flow.* McGraw-Hill, Boston, second edition (1991). 41, 47

[91] M. M. Rai, T. B. Gatski, and G. Erlebacher. Direct simulation of spatially evolving compressible turbulent boundary layers. Paper No. 95–0583 AIAA (1995). 42

[92] S. Pirozzoli, F. Grasso, and T. B. Gatski. *Direct numerical simulation and analysis of a spatially evolving supersonic turbulent boundary layer at $M = 2.25$.* Phys. Fluids **16**(3), 530–545 (2004). 42, 45, 50, 114

[93] S. Tamano and Y. Morinishi. *Effect of different thermal wall boundary conditions on compressible turbulent channel flow at $M = 1.5$.* J. Fluid Mech. **548**, 361–373 (2006). 45, 46, 57, 66, 101, 104

[94] Y. Morinishi, S. Tamano, and K. Nakabayashi. *Direct numerical simulation of compressible turbulent channel flow between adiabatic and isothermal walls.* J. Fluid Mech. **502**, 273–308 (2004). 45, 59, 60, 64

[95] G. N. Coleman, J. Kim, and R. D. Moser. *A numerical study of turbulent supersonic isothermal-wall channel flow.* J. Fluid Mech. **305**, 159–183 (1995). 45, 50

[96] P. G. Huang, G. N. Coleman, and P. Bradshaw. *Compressible turbulent channel flows: DNS results and modeling.* J. Fluid Mech. **305**, 185–218 (1995). 45, 59, 76, 121

[97] S. E. Guarini, R. D. Moser, K. Shariff, and A. Wray. *Direct numerical simulation of a supersonic turbulent boundary layer at Mach 2.5.* J. Fluid Mech. **414**, 1–33 (2000). 45, 48, 116, 121

[98] T. Maeder, N. A. Adams, and L. Kleiser. *Direct simulation of turbulent supersonic boundary layers by an extended temporal approach.* J. Fluid Mech. **429**, 187–216 (2001). 45, 48, 55

[99] M. P. Martin. *Direct numerical simulation of hypersonic turbulent boundary layers. Part 1. Initialization and comparison with experiments.* J. Fluid Mech. **570**, 347–364 (2007). 45, 51, 52, 53, 54

[100] M. F. Shahab, G. Lehnasch, T. B. Gatski, and P. Comte. Statistical characteristics of the interaction of an impinging shock wave and turbulent boundary layer. In *Proceedings of the Sixth International Symposium on Turbulent Shear Flow Phenomena*, pages 1351–1356 (2009). 45

[101] Y. Morinishi, S. Tamano, and E. Nakamura. *New scaling of turbulent statistics for incompressible channel flow with different total heat flux gradients.* Int. J. Heat Mass Tran. **50**, 1781–1789 (2007). 46

[102] J. Cousteix. *Turbulence et Couche Limite*. Cepadues-Editions, Toulouse (1989). 48

[103] M. J. Ringuette, M. P. Martin, A. J. Smits, and M. Wu. Characterization of the turbulent structure in supersonic boundary layers using DNS data. Paper No. 2006-3359 AIAA (2006). 48

[104] M. J. Ringuette, M. Wu, and M. P. Martin. Coherent structures in DNS of turbulent boundary layers at Mach 3. Paper No. 2007-1138 AIAA (2007). 48

[105] S. Stolz and N. A. Adams. *Large-eddy simulation of high-Reynolds number supersonic boundary layers using the approximate deconvolution model and a rescaling and recycling technique*. Phys. Fluids **15**, 2398–2412 (2003). 48

[106] E. R. van Driest. *The problem of aerodynamic heating*. Aero. Engr. Rev. **15**, 26–41 (1956). 48

[107] E. J. Hopkins and M. Inouye. *An evaluation of theories for predicting turbulent skin friction and heat transfer on flat plates at supersonic and hypersonic Mach numbers*. AIAA J. **9**, 993–1008 (1971). 49

[108] A. E. Perry, S. Henbest, and M. S. Chong. *A theoretical and experimental study of wall turbulence*. J. Fluid Mech. **165**, 163–199 (1986). 51

[109] R. A. Humble, G. E. Elsinga, F. Scarano, and B. W. van Oudheusden. *Three-dimensional instantaneous structure of a shock wave/turbulent boundary layer interaction*. J. Fluid Mech. **622**, 33–62 (2009). 52, 53, 54

[110] L. P. Erm. *Low Reynolds number turbulent boundary layers*. Thèse de Doctorat, University of Melbourne (1988). 52, 53, 54, 97, 101

[111] P. R. Spalart. *Direct simulation of a turbulent boundary layer up to $R_\theta = 1410$*. J. Fluid Mech. **187**, 61–98 (1988). 52, 53, 54, 94, 96

[112] X. Wu and P. Moin. *Direct numerical simulation of turbulence in a nominally zero-pressure-gradient flat-plate boundary layer*. J. Fluid Mech. **630**, 5–41 (2009). 52, 53, 54

[113] M. V. Morkovin. Effects of compressibility on turbulent flows. In A. Favre, editor, *Mecanique de la Turbulence*, pages 367–380. CNRS (1962). 52, 75, 89, 115, 121

[114] E. R. van Driest. *Turbulent boundary layer in compressible fluids*. J. Aeronaut. Sci. **18**, 145–160 (1951). 55

[115] P. G. Huang and G. N. Coleman. *Van Driest transformation and compressible wall-bounded flows*. AIAA J. **32**, 2110–2113 (1994). Errata AIAA J. 33, 1756. 55, 56

[116] T. Cebeci and P. Bradshaw. *Momentum Transfer in Boundary Layers*. Hemisphere Publishing, Washington (1977). 56

[117] C. Carvin, J.-F. Debiève, and A. J. Smits. The near-wall temperature profile of turbulent boundary layers. Paper No. 88–0136 AIAA (1988). 58

[118] J. F. Debiève, P. Dupont, D. R. Smith, and A. J. Smits. *Supersonic turbulent boundary layer subjected to step changes in wall temperature.* AIAA J. **35**(1), 51–57 (1997). 58, 116

[119] C. Brun, M. P. Boiarciuc, M. Haberkorn, and P. Comte. *Large eddy simulation of compressible channel flow: Arguments in favour of universality of compressible turbulent wall bounded flows.* Theor. Comput. Fluid Dyn. **22**, 189–212 (2008). 58

[120] P.-Å. Krogstad and L. E. Torbergsen. *Turbulent stress invariant analysis: Clarification of existing terminology.* Flow Turbul. Combust. **64**, 161–181 (2000). 62

[121] J. Kreuzinger, R. Friedrich, and T. B. Gatski. *Compressibility effects in the solenoidal dissipation rate equation: A priori assessment and modeling.* Int. J. Heat Fluid Flow **27**, 696–706 (2006). 63

[122] J. L. Lumley. *Stochastic Tools in Turbulence.* Academic Press, New York (1970). 66

[123] J. Kim, P. Moin, and R. Moser. *Turbulence statistics in fully developed channel flow at low Reynolds number.* J. Fluid Mech. **177**, 133–166 (1987). 68, 101, 106, 108

[124] K. Abe, T. Kondoh, and Y. Nagano. *A two-equation heat transfer model reflecting second-moment closures for wall and free turbulent flows.* Int. J. Heat Fluid Flw. **17**, 228–237 (1996). 77

[125] Y. Nagano and M. Shimada. *Development of a two-equation heat transfer model based on direct simulations of turbulent flows with different prandtl numbers.* Phys. Fluids **8**, 3379–3402 (1996). 77

[126] Y. Nagano. Modelling heat transfer in near-wall flows. In B. E. Launder and N. D. Sandham, editors, *Closure Strategies for Modelling Turbulent and Transitional Flows*, pages 188–247, Cambridge (2002). Cambridge University Press. 77, 78

[127] C. Béguier, I. Dekeyser, and B. E. Launder. *Ratio of scalar and velocity dissipation time scales in shear flow turbulence.* Phys. Fluids **21**, 307–315 (1978). 78

[128] K. Abe, T. Kondoh, and Y. Nagano. *A new turbulence model for predicting fluid flow and heat transfer in separating and reattaching flows – II. Thermal field calculations.* Int. J. Heat Mass Tran. **38**, 1467–1481 (1995). 78

[129] L. H. Jin, R. M. C. So, and T. B. Gatski. *Equilibrium states of turbulent homogeneous buoyant flows.* J. Fluid Mech. **482**, 207–233 (2003). 78

[130] F. Ducros, V. Ferrand, F. Nicoud, C. Weber, D. Darracq, C. Gacherieu, and T. Poinsot. *Large-eddy simulation of the shock/turbulence interaction.* J. Comput. Phys. **152**, 517–549 (1999). 82

[131] S. Pirozzoli, M. Bernardini, and F. Grasso. *Direct numerical simulation of transonic shock/boundary layer interaction under conditions of incipient separation.* J. Fluid Mech. **657**, 361–393 (2010). 82

[132] J.H. Agui Y. Andreopoulos and G. Briassulis. Shock Wave Turbulence Interactions. In *Annual Review of Fluid Mechanics*, pages 309–345. Annual Reviews, New York (2000). 86

[133] P.S. Klebanoff. Characteristics of turbulence in a boundary layer with zero pressure gradient. Report No. TR–4467 NACA (1955). 92, 93, 97

[134] P. E. SkÅre and P. Å. Krogstad. *A turbulent equilibrium boundary layer near separation.* J. Fluid Mech. **272**, 319–348 (1994). 92, 93, 94, 96, 97, 101

[135] M. Elena and J. P Lacharme. *Experimental study of a supersonic turbulent boundary layer using a laser doppler anemometer.* J. MEC. THEOR. APPL. **7**(2), 175–190 (1988). 92, 93, 101

[136] E. M. Fernando and A. J. P Smits. *A supersonic turbulent boundary layer in an adverse pressure gradient.* J. Fluid Mech. **211**, 285–307 (1990). 92, 93, 95

[137] P. Bradshaw. *The turbulent structure of equilibrium turbulent boundary layers.* J. Fluid Mech. **29**, 625–645 (1967). 95

[138] A. D. Cutler and J. P. Johnston. *The relaxation of a turbulent boundary layer in an adverse pressure gradient.* J. Fluid Mech. **200**, 367–387 (1989). 95

[139] K. Shiloh, B. G. Shivaprasad, and R. L. Simpson. *The structure of a separating turbulent boundary layer part 3. transverse velocity measurements.* J. Fluid Mech. **113**, 75–90 (1981). 97

[140] J. L. Lumley. *Computational modeling of turbulent flows.* Advances in Applied Mechanics **18**, 123–176 (1978). 97

[141] B. Frohnapfel, P. Lammers, J. Jovanović, and F. Durst. *Interpretation of the mechanism associated with turbulent drag reduction in terms of anisotropy invariants.* J. Fluid Mech. **577**, 457–466 (2007). 100

[142] A. J. Simonsen and P. Å. Krogstad. *Turbulent stress invariant analysis: Clarification of existing terminology.* Phys. Fluids **17** (2005). 100

[143] A. K. Gupta and R. E. Kaplan. *Statistical characteristics of Reynolds stress in a turbulent boundary layer.* The physics of fluids **15**, 1981–1985 (1972). 101, 104

[144] H. P. Kreplin and H. Eckelmann. *Behavior of the three fluctuating velocity components in the wall region of a turbulent channel flow.* Phys. Fluids **22**(7), 1233–1239 (1979). 101, 104

[145] H. Ueda and J. O. Hinze. *Fine-structure turbulence in the wall region of a turbulent boundary layer.* J. Fluid Mech. **67**, 125–143 (1975). 101, 104

[146] R. L. Simpson, Y. T. Chew, and B. G. Shivaprasad. *Fine-structure turbulence in the wall region of a turbulent boundary layer.* J. Fluid Mech. **113**, 58–73 (1981). 101, 104

[147] S. S. Lu and W. W. Willmarth. *Measurements of the structure of the Reynolds stress in a turbulent boundary layer.* J. Fluid Mech. **60**, 481–511 (1973). 105, 108

[148] J. Deleuze, N. Audiffren, and M. Elena. *Quadrant analysis in a heated-wall supersonic boundary layer.* Phys. Fluids **6**(12), 4031–4041 (1994). 106, 108

[149] J. M. Wallace, H. Eckelmann, and R. S. Brodkey. *The wall region in turbulent shear flow.* J. Fluid Mech. **54**, 39–48 (1972). 106, 108

[150] J. P. Dussauge and J. Gaviglio. *The rapid expansion of a supersonic turbulent flow: role of bulk dilatation.* J. Fluid Mech. **174**, 81–112 (1987). 121

[151] J. Gaviglio. *Reynolds analogies and experimental study of heat transfer in the supersonic boundary layer.* Int. J. Heat Mass Transfer **30**(4), 911–926 (1987). 121

[152] F. W. Spaid and J. C. Frishett. *Incipient separation of a supersonic, turbulent boundary layer including effects of heat transfer.* AIAA J. **10**(7), 915–922 (1972). 128

[153] L. F. East and W. G. Sawyer. An investigation of the structure of equilibrium turbulent boundary layers. AGARDograph No. CP-271 NATO (1979). 142

[154] J. Délery. *Experimental investigation of turbulence properties in transonic shock/boundary-layer interaction.* AIAA J. **21**(2), 180–185 (1983). 143

Dans l'optique de développer à terme des modèles pertinents et in fine améliorer le design de véhicules supersoniques, cette étude propose une analyse détaillée de l'influence d'un choc et d'un transfert de chaleur sur la structure de la turbulence au sein d'une couche limite supersonique. La stratégie numérique utilisée repose sur des simulations numériques directes des équations de Navier-Stokes à l'aide de schémas WENO et compact d'ordre élevé. Le développement complet de la couche limite est simulé à l'aide d'un forçage amont à la paroi afin de s'assurer du plus haut degré de réalisme dans la zone d'étude. Des conditions de séparation naissante et deux conditions thermiques de paroi (adiabatique et refroidie) sont considérées. L'analyse se concentre sur l'altération des caractéristiques moyennes et turbulentes à travers la zone d'interaction et au sein de la zone de relaxation, sur la base de profils moyens et de paramètres intégraux. L'amplification anisotrope des variables turbulentes est quantifiée tandis que les évènements turbulents associés à la modification de la structure globale sont identifiés. La forte modification des champs thermiques moyens et turbulents par le refroidissement est mise en exergue, notamment la diminution significative des quantités turbulentes à travers la couche. Par ailleurs, la réduction à la fois des longueurs d'influence amont, de séparation et de relaxation est mise en évidence.

<u>Mots clés :</u> Simulation numérique directe, Ecoulement supersonique, Couche limite turbulente, Ondes de choc, Transfert de chaleur, Décollement des écoulements

As a prerequesite for relevant model development and improvement of design methodologies for supersonic vehicles, this study aims at investigating the influence of wall heat-transfer and shock interaction on the turbulence structure of supersonic boundary layers. The numerical strategy relies on the full resolution of three-dimensional compressible Navier-Stokes equations by means of state-of-art high-order WENO and compact schemes. A fully-developped turbulent boundary layer is simulated by means of upstream wall perturbations triggering the transition in order to dispose of fully-reliable data upstream of the analysis region. Insipient separation conditions and two different wall thermal boundary conditions (adiabatic and cold) are considered. The analysis focuses on the evolution of mean and turbulent flow properties along the interaction region and in the relaxation region downstream of the shock-system. The strong influence of the mean pressure gradient is quantified through the analysis of mean flow profiles and boundary layer integral parameters. The anisotropic amplification of turbulent quantities through the interaction region is characterized and the turbulent events associated with the modification of the turbulence structure of the perturbed boundary layer are identified. The mean and turbulent thermal fields are shown to be strongly modified by the wall cooling which significantly dampens more particularly the turbulent thermal quantities levels across the boundary layer. In addition, a reduction of the upstream influence and separation lengths by the wall cooling are evidenced along with a faster recovery process downstream of the shock-system.

<u>Keywords :</u> Direct numerical simulation, Supersonic flow, Turbulent boundary layer, shock waves, Heat transfer, Separated flows